Atomic layer processing and its applications

Dissertation

zur Erlangung des Doktorgrades
an der Fakultät für Mathematik, Informatik und Naturwissenschaften
Fachbereich Physik
der Universität Hamburg

vorgelegt von

Jun Peng

Hamburg
2024

Weitere Identifier: urn:nbn:de:gbv:18-ediss-126111

Gutachter/innen der Dissertation:	Prof. Dr. Robert Blick Dr. Robert Zierold
Zusammensetzung der Prüfungskommission:	Prof. Dr. Daniela Pfannkuche Prof. Dr. Patrick Huber Prof. Dr. Christian Schroer Prof. Dr. Robert Blick Dr. Robert Zierold
Vorsitzende/r der Prüfungskommission:	Prof. Dr. Daniela Pfannkuche
Datum der Disputation:	21.10.2024
Vorsitzender des Fach-Promotionsausschusses PHYSIK:	Prof. Dr. Markus Drescher
Leiter des Fachbereichs PHYSIK:	Prof. Dr. Wolfgang J. Parak
Dekan der Fakultät MIN:	Prof. Dr.-Ing. Norbert Ritter

Eidesstattliche Versicherung

Hiermit versichere ich an Eides statt, die vorliegende Dissertationsschrift selbst verfasst und keine anderen als die angegebenen Hilfsmittel und Quellen benutzt zu haben.

Sofern im Zuge der Erstellung der vorliegenden Dissertationsschrift generative Künstliche Intelligenz (gKI) basierte elektronische Hilfsmittel verwendet wurden, versichere ich, dass meine eigene Leistung im Vordergrund stand und dass eine vollständige Dokumentation aller verwendeten Hilfsmittel gemäß der Guten wissenschaftlichen Praxis vorliegt. Ich trage die Verantwortung für eventuell durch die gKI generierte fehlerhafte oder verzerrte Inhalte, fehlerhafte Referenzen, Verstöße gegen das Datenschutz- und Urheberrecht oder Plagiate.

Declaration on oath

I hereby declare and affirm that this doctoral dissertation is my own work and that I have not used any aids and sources other than those indicated.

If electronic resources based on generative artificial intelligence (gAI) were used in the course of writing this dissertation, I confirm that my own work was the main and value-adding contribution and that complete documentation of all resources used is available in accordance with good scientific practice. I am responsible for any erroneous or distorted content, incorrect references, violations of data protection and copyright law or plagiarism that may have been generated by the gAI.

Datum Date	Unterschrift der Doktorandin / des Doktoranden Signature of doctoral candidate

Preface

How to describe a hand? This question can describe my entire research philosophy. One can say that a hand has five fingers. One can say that a hand can be opened and clenched into a fist. One can say that a hand can be used to grab things. From different perspectives, the hand can be described in completely different ways. However, each perspective cannot fully describe a hand. But at the same time, you will also find that no matter what perspective, from anthropology, physics, biology, art, or sociology, the description of the hand gives us different understandings. However, it is still a hand. Such a philosophical question, to a certain extent, laid the foundation for my doctoral research in terms of thinking. Look at the same thing from different perspectives, be as innocent and curious as a child, ask some questions that seem superficial, and then seriously try to find the answers. Throughout my doctoral research, the starting point was to use atomic layer deposition (ALD) to deposit VO_2. During this process, many questions kept emerging. For example, what are the characteristics of VO_2? What can it be used for? Why is ALD special? What will happen if I adjust the parameter combination of ALD? If ALD is possible, how about atomic layer etching?

It is these divergent questions that led to this cumulative paper, which consists of one first-authored book chapter and four first-authored manuscripts. The original manuscript of the book chapter is integrated into the background chapter, and four complete research manuscripts constitute the main body of the paper. In addition, there is a co-authored review manuscript is also partly cited in the Background chapter. The specific information of the manuscripts involved in this cumulative dissertation is as follows:

The first-authored book chapter:

[1] **Peng, J**. and R. Zierold, *Atomic layer deposition of materials*, in *Encyclopedia of Condensed Matter Physics (Second Edition)*, T. Chakraborty, Editor. 2024, Academic Press: Oxford. p. 716-728. DOI: 10.1016/B978-0-323-90800-9.00206-7.

The four first-authored research manuscripts:

[2] **J. Peng**, D. Hensel, R. Venugopal, L. Rave, C. Schormann, S. Koch, R. H. Blick, R. Zierold, *ALD-assisted VO_2 for memristor application*. Advanced Engineering Materials, 2025. 2402614. DOI: 10.1002/adem.202402614.

[3] **J. Peng**, J. Brandt, M. Pfeiffer, L. G. Maragno, T. Krekeler, N. T. James, J. Henf, C. Heyn, M. Ritter, M. Eich, A. Yu. Petrov, K. P. Furlan, R. H. Blick, R. Zierold, *Switchable 3D photonic crystals based on the insulator-to-metal transition in VO_2*. ACS Applied Materials & Interfaces, 2024. 16(49): p. 67106-67115. DOI: 10.1021/acsami.4c13789.

[4] **J. Peng**, R. Venugopal, R. Blick, R. Zierold, *Atomic layer etching of SiO_2 using sequential SF_6 gas and Ar plasma*. DOI: 10.48550/arXiv.2412.20653.

[5] **J. Peng**, P. Zhao, R. Venugopal, K. Deneke, S. Haugg, R. Blick, R. Zierold, *Thermal Sight: A Position-Sensitive Detector for a Pinpoint Heat Spot*. Small Science, 2024. 4(8): p. 2400091. DOI: 10.1002/smsc.202400091.

The co-authored review manuscript:

[6] C. Hao, **J. Peng**, R. Zierold, R. H. Blick, *Atomic layer deposition films for resistive random-access memories*. Advanced Materials Technologies, 2024. 9(16): p. 2301762. DOI: 10.1002/admt.202301762.

Abstract

Nanotechnology has revolutionized electronics, energy, and healthcare over the past few decades, significantly enhancing our daily lives. Atomic layer processing (ALP), which includes atomic layer deposition (ALD) and atomic layer etching (ALE), enables precise manipulation of material deposition and etching at the atomic level, further driving the advancement of nanotechnology and its associated applications. This dissertation focuses on the study some aspects of ALP, encompassing both ALD and ALE, and explores its applications. Firstly, an ALD-assisted method for synthesizing VO_2 was developed through a combination of a non-stoichiometric vanadium oxide (VO_x) ALD process and a tailor-made annealing process. The ALD-assisted VO_2, characterized by its insulator-to-metal transition properties, was extended to two-dimensional and three-dimensional device applications to investigate its potential from both electrical and optical perspectives. Electrically, thin-film memristors and Si-Al_2O_3/VO_2 core/shell memristors based on ALD-assisted VO_2 demonstrated excellent switching performance and high sensitivity to temperature variations. Optically, three-dimensional inverse opal photonic crystals based on VO_2 were prepared using ALD-assisted VO_2 synthesis with polystyrene opal sacrificial templates. These photonic crystals displayed remarkable control over the photonic bandgap in the near-infrared (NIR) region, which can be reversibly switched by adjusting the external temperature. They also exhibited a temperature-dependent transition from a narrow-band NIR reflector to a broadband absorber. In addition, a novel thermoelectric-based position-sensitive detector (T-PSD) was proposed, along with a corresponding decoding strategy. This innovation has been proven effective for detecting single hot spots originating from various energy sources, including electromagnetic radiation, electrons, and macroscopic mechanical heat. Finally, a directional ALE process was developed for etching SiO_2 using SF_6 gas and Ar plasma near room temperature. This process achieved 100% synergy and a stable etching rate of approximately 1.4 Å per cycle. These studies have already demonstrated significant practical potential and may contribute to the further development of ALP-related nanotechnologies and applications. Additionally, the findings may provide deeper insights in turns into the underlying physics, materials science, and engineering principles involved.

Keywords:

Atomic layer processing, atomic layer deposition, atomic layer etching, vanadium dioxide, memristor, photonic crystal, position sensitive detector

Kurzfassung

Nanotechnologie hat in den letzten Jahrzehnten die Bereiche Elektronik, Energie und Gesundheitswesen revolutioniert und unsere Lebensqualität erheblich verbessert. Die Atomlagenverarbeitung (ALP), die sowohl die Atomlagenabscheidung (ALD) als auch das Atomlagenätzen (ALE) umfasst, ermöglicht die präzise Manipulation von Materialabscheidung und -ätzen auf atomarer Ebene und treibt so die Weiterentwicklung der Nanotechnologie und deren Anwendungen voran. Diese Dissertation konzentriert sich auf die Untersuchung von verschiedenen Aspekten der ALP und erforscht deren Anwendungen. Zunächst wurde eine ALD-basierte Methode zur Synthese von VO_2 entwickelt, die eine Kombination aus einem ALD-Prozess von nicht-stöchiometrischen Vanadiumoxid (VO_x) und einem maßgeschneiderten Temperverfahren umfasst. Das ALD-basierte VO_2, das durch seine Phasenübergangseigenschaften von einem Isolator zu einem Metall gekennzeichnet ist, wurde auf zwei- und dreidimensionalen Geräteanwendungen angewendet, um dessen Potenzial sowohl aus elektrischer als auch aus optischer Perspektive zu untersuchen. Elektrisch zeigten ALD-basierte VO_2 Dünnschicht-Memristoren und Si-Al_2O_3/VO_2 Kern/Schale-Memristoren hervorragende Schalteigenschaften und eine hohe Empfindlichkeit gegenüber Umgebungstemperaturschwankungen auf. Optisch wurden dreidimensionale inverse opaline photonische Kristalle unter Verwendung von ALD-basierter VO_2-Synthese sowie Polystyrol-Opal-Opfermaterialien hergestellt. Diese photonischen Kristalle zeigten eine bemerkenswerte Kontrolle über das photonische Stoppband im nahen Infrarotbereich (NIR), das durch Veränderung der Außentemperatur reversibel geschaltet werden kann. Sie wiesen zudem auch einen temperaturabhängigen Übergang von einem schmalbandigen NIR-Reflektor zu einem Breitbandabsorber auf. Darüber hinaus wurde ein neuartiger thermoelektrischer positionssensitiver Detektor (T-PSD) zusammen mit einer entsprechenden Dekodierungsstrategie vorgeschlagen. Diese Innovation ermöglicht die Erkennung einzelner thermischer Hotspots, die aus verschiedenen Energiequellen stammen können, einschließlich elektromagnetischer Strahlung, Elektronen und makroskopischer mechanischer Wärmequellen. Schließlich wurde ein gerichteter ALE-Prozess zum Ätzen von SiO_2 unter Verwendung von SF_6-Gas und Ar-Plasma nahe Raumtemperatur entwickelt. Dieser Prozess erreichte eine 100%ige Synergie und eine stabile Ätzrate von etwa 1,4 Å pro Zyklus. Die hier aufgezeigten Studien haben bereits ein signifikantes praktisches Potenzial gezeigt und könnten zur weiteren Entwicklung von ALP-bezogenen Nanotechnologien und Anwendungen beitragen. Darüber hinaus könnten die Ergebnisse wertvolle Einblicke in die zugrunde liegenden physikalischen, materialwissenschaftlichen und ingenieurtechnischen Prinzipien bieten.

Schlüsselwörter:
Atomlagenverarbeitung, Atomlagenabscheidung, Atomlagenätzen, Vanadiumdioxid, Memristor, Photonischer Kristall, positionsempfindlicher Detektor

Contents

Abbreviations and symbols

1D	one- dimensional
2D	two-dimensional
3D	three-dimensional
AFM	atomic force microscopy
ALD	atomic layer deposition
ALE	atomic layer etching
ALP	atomic layer processing
AZO	aluminum-doped zinc oxide
CVD	chemical vapor deposition
DRAM	dynamic random-access memory
ECM	electrochemical mechanism
EPC	etching per cycle
FEA	finite element analysis
GIXRD	Grazing Incidence X-ray Diffraction
GPC	growth per cycle
HF	hydrofluoric acid
HRS	high resistance state
ICP	inductively coupled plasma
IMT	insulator-to-metal transition
IO	inverse opal
ITO	indium tin oxide
k	dielectric constant
LRS	low resistance state
MEMS	microelectromechanical systems
MIM	metal–insulator–metal
NIR	near-infrared
PBG	photonic bandgap
PEALD	plasma enhanced atomic layer deposition
PhC	photonic crystal
PS	polystyrene
PSD	position-sensitive detector
PVD	physical vapor deposition
RRAM	resistive random-access memory
SAED	Selected area electron diffraction

SEM	scanning electron microscopy
SRAM	static random-access memory
TCM	thermochemical memory
TDMAV	tetrakis(dimethylamino)vanadium
TEM	Transmission Electron Microscopy
TMA	trimethylaluminum
T-PSD	thermoelectric-based position-sensitive detector
VCM	valence change mechanism
VO_2	vanadium dioxide
VO_2 (M)	monoclinic phase VO_2
VO_2 (R)	rutile metallic phase VO_2
V-RRAM	vertical RRAM
XRD	X-Ray diffraction analysis

1. Introduction

1.1. Motivation

Nanotechnology has revolutionized electronics, energy, and healthcare over the past few decades by developing devices with unprecedented performance and functionality, significantly improving our daily lives. At the heart of these advances is micro-nano manufacturing. How can we push development further? The answer may lie in manipulating materials at the sub-nanometer level or the atomic scale. Such advanced manipulation often involves deposition and etching, leading to two advanced technologies: atomic layer deposition (ALD) and atomic layer etching (ALE), which can control film thickness at the sub-nanometer scale. The earliest reports of both technologies appeared in patent documents. ALD was independently invented twice: once in the 1970s for electroluminescent flat panel displays in Finland,[1] and once in the Soviet Union in the 1960s, described as "molecular layering reactions".[2] ALE was first disclosed in a patent application by Max Yoder for crystalline diamond etching in 1988.[3] However, despite their high precision, both ALD and ALE initially lacked application demand and did not receive much attention. Since semiconductor technology has advanced over the past two decades, both techniques have become increasingly prominent in various applications.

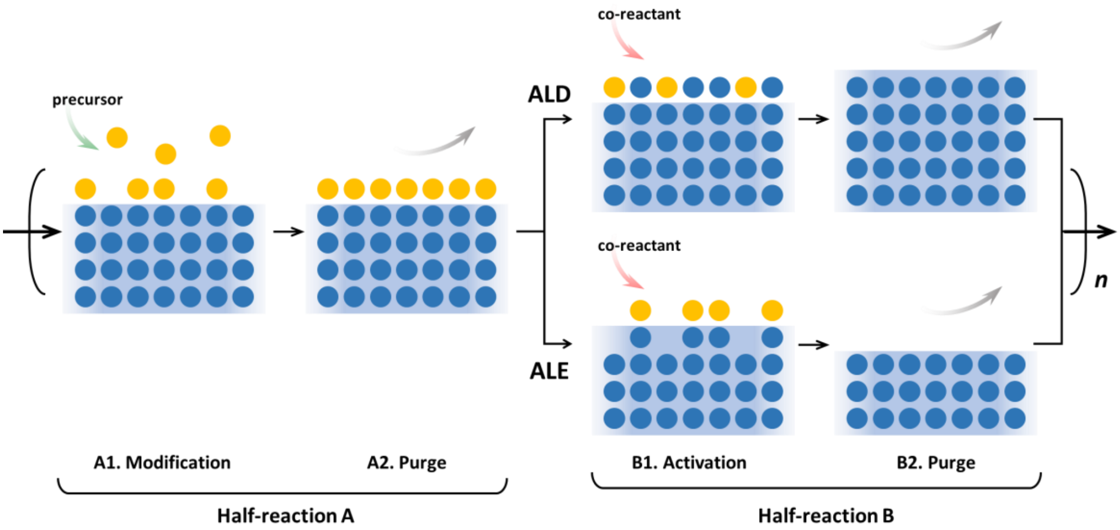

Figure 1.1. Schematic diagram of the ALP process.

ALD and ALE are highly similar. For example, (1) both involve a repetition of multiple half-reactions, (2) both are gas-solid reactions occurring on the surface, (3) both require a self-limiting nature, and (4) both provide thickness control over material at the atomic scale. Therefore, Atomic Layer Processing (ALP), as referred to in this dissertation, means processing materials at the atomic layer level, specifically involving ALD and ALE. Figure 1.1 shows the similarities between ALD and ALE via the typical two-half-cycle form process from a process setup perspective. In the first half-cycle (A), the surface is modified by the adsorption of an incident precursor, which is usually a chemical in the gas phase (A1.

modification step). This is followed by a purge to remove excess precursors and byproducts (A2. purge step). In the second half-cycle (B), the modified surface is exposed to a different co-reactant, which is either another type of chemical, plasma, electrons, or some other energy forms such as infrared light, to activate the reaction on the solid surface (B1. activation step). The key difference between ALD and ALE lies in the subsequent process: ALD will add another layer of material that contains at least one element from precursor and reactant, whereas ALE involves the desorption of the modified surface, resulting in the removal of a monolayer from the surface. When this cycle is repeated *n* times, *n* layers of material will be added/removed from the sample. ALP currently has a great track record in tackling challenges in the nanoelectronics field. For example, Intel began using ALD to prepare high-k metal gate stacks in logic circuits starting with the 45 nm node, and manufacturing 10 nm devices involves about 70 ALD steps.[4] ALE has also been used to produce logic devices since the advent of the 10 nm node.[5, 6] Such achievements come not only from their true atomic scale control, but also from their compatibility with wafer-scale fabrication and high-volume manufacturing. Additionally, ALD has demonstrated its utility in packaging for flexible displays and in creating nanolayers for photovoltaic cells.[7-10] What’s more, in the next-generation advanced devices and quantum circuits,[11-13] ALP is playing an increasingly important role, further solidifying its significance in cutting-edge technology development.

Technological progress often drives development across various fields. Although some applications have been achieved, the development of ALP is in its early stages, with so far impacting a limited number of areas. However, it is anticipated that ALP will lead to a broader range of applications in many more fields. My original motivation was to deposit vanadium dioxide (VO_2) via ALD to expand the range of materials that ALD can handle, as VO_2's insulator-to-metal transition (IMT) near room temperature is intriguing for both physicists and engineers.[14-19] Yet fabricating VO_2, especially into complex structures, is still challenging due to vanadium's multiple valence states.[20, 21] It is foreseeable that successfully combining VO_2 and ALD holds immense potential for electrical and optical applications. During the exploration of VO_2 films, I realized that the conformality characteristic of ALD-deposited films could greatly reduce the thermal resistance at the interfaces between the ALD film and the substrate. By combining the thermoelectric properties of VO_2, the thermoelectric-based position-sensitive detector (T-PSD) was developed. Due to the concerns about the variable valence properties and the inherent phase transition of VO_2, the more stable Al-doped ZnO (AZO) using ALD was used to build this sensor. Delving deeper into ALD, I naturally became interested in the emerging sister technology, ALE, which led to exploratory work on ALE based on the knowledge gained from ALD research. This dissertation thus represents a multi-perspective exploration of ALP, showcasing its potential and providing examples for future innovations in atomic layer processing.

1.2. Scope of the work

This dissertation is arranged as follows:

Chapter 2 introduces the general theoretical knowledge of ALP and its applications, specifically focusing on ALD and its related applications in the main topics of this dissertation—memristors, photonic crystals, and position-sensitive detectors (PSDs).

Chapter 3 details the VO_2 synthesis process, beginning with the deposition of VO_x via ALD followed by a tailored annealing process. The chapter also provides an in-depth study of the electrical properties, especially the current-voltage characteristics, of the synthesized VO_2. Additionally, this ALD-assisted VO_2 synthesis strategy is adapted to coat nanowires made of different materials, such as Al_2O_3-coated Si nanowires and carbon nanotubes, to explore the potential of ALD-assisted VO_2 synthesis in 3D memristors.

Chapter 4 extends the ALD-assisted VO_2 synthesis strategy to more complex nanostructures, specifically opal structures, resulting in the creation of switchable 3D photonic crystals with an inverse opal structure. This chapter systematically studies the temperature-dependent properties of the ALD-assisted VO_2 thin film and photonic crystal, including both structural and optical properties.

Chapter 5 presents the invention of the T-PSD. The chapter includes the mathematical model, the finite element model, and prototype studies of the T-PSD, which are cross-validated. It also demonstrates and verifies the theoretical derivation and practical operation of two decoding methods.

Chapter 6 demonstrates the ALE process for precise SiO_2 etching. This chapter explores the etching process using SF_6 and Ar plasma, systematically studying all related key parameters, including discussions of its synergy effect and different "ALE windows".

Chapter 7 provides a final summary of the four works carried out in the paper around the theme of ALP and discusses potential directions for continued development based on existing research results.

2. Background

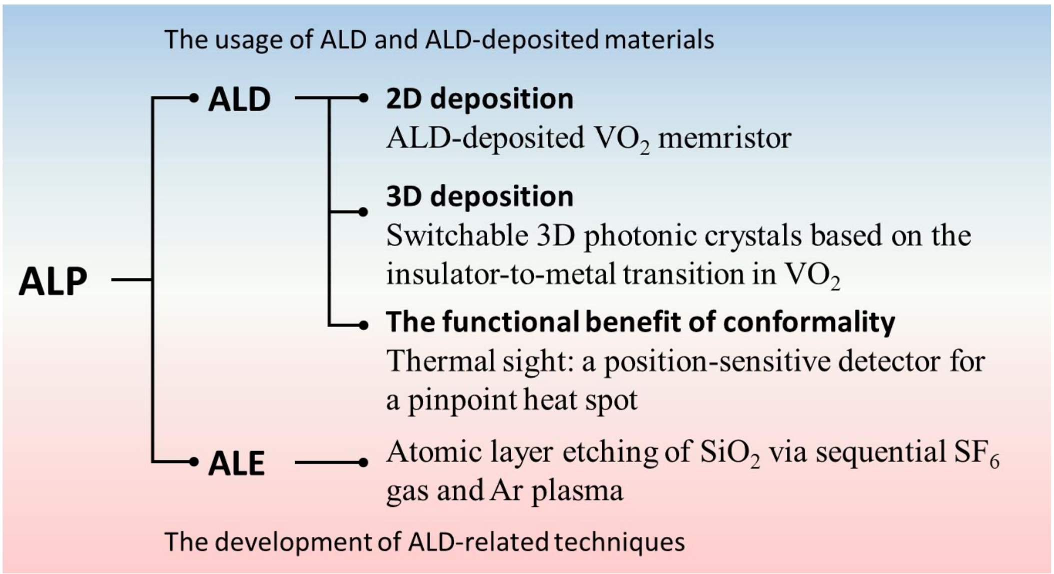

This doctoral dissertation primarily focuses on ALP, encompassing both ALD and ALE, along with their applications. It can be divided into two dimensions: On the one hand, it is the extension and application of ALD technology, which is relatively mature in experimental and theoretical aspects under the framework of ALP. Specifically, the process of ALD-assisted VO_2 deposition was developed, and this technology was explored for its applications in VO_2-based memristors, PhC, and T-PSD. Among them, T-PSD finally uses AZO film deposited by ALD for performance optimization. On the other hand, based on the understanding of ALD, the dissertation further extends to ALD's sister technology, ALE. As ALE is much less mature than ALD, this dimension focuses on exploring new ALE processes to understand the underlying physical and chemical mechanisms.

In this context, Chapter 2 first introduces ALD in Section 2.1, via a first-authored book chapter entitled "Atomic layer deposition of materials". Since the state-of-the-art for each application has been covered independently in the main chapters, Section 2.2 serves as a background supplement to memristors (Chapter 3), photonic crystals (Chapter 4), and position sensors (Chapter 5). Section 2.2.1 discusses the current role of ALD in memristor development, drawing from parts of a co-authored review article. Section 2.2.2 introduces the physical principles underlying photonic crystal structures. Section 2.2.3 explains the working principle of mainstream PSDs to differentiate the T-PSD from a fundamental physical perspective. Finally, Section 2.3 compares ALE and ALD, emphasizing the similarities and differences between the two techniques.

2.1. Atomic layer deposition①

2.1.1. Abstract

As a chemical vapor deposition technique that can achieve outstanding coating conformality on complex structures, atomic layer deposition (ALD) has received great attention in both academic research and industrial applications since its invention in the 1960s and 1970s. Herein, the basic principle of ALD—based on a sequence of self-limiting gas-solid-surface reactions—and different ALD approaches, namely temporal vs. spatial and thermal vs. plasma-enhanced, are summarized. Subsequently, the variety of materials deposited by ALD is highlighted and some ALD-coated nanostructures are presented. Finally, a short but comprehensive introduction is given to the most recent developments and achievements in ALD or closely related methods.

2.1.2. Introduction to and general principle of ALD (history of ALD)

Atomic layer deposition (ALD) is a coating technique to deposit thin films and is closely related to the chemical vapor deposition (CVD) method. In contrast to CVD where one or more precursors are decomposed or reacted in the gas phase, ALD bases on sequential, separated self-limiting gas-solid surface reactions of two or more gaseous precursor species. A binary ALD cycle consisting of two half-reactions is sketched in Figure 2.1a.

Four steps can be identified:

(1) *Pulse 1:* The substrate's surface is occupied by certain surface groups. Vapor of precursor α is brought to the substrate's surface.

(2) *Purge 1:* After the completed, self-terminating surface reaction, the non-used precursor α molecules as well as the reaction by-products are pumped away and the reaction chamber is purged.

(3) *Pulse 2*: At this point, the substrate remains in an intermediate surface state. The second precursor β is pulsed into the ALD chamber and reacts in a self-limiting manner with the residues of precursor α chemisorbed to the substrate.

(4) *Purge 2*: After the completed gas-solid surface reaction, the reaction chamber is purged from the by-products and the non-used precursor β molecules.

If the two precursors α and β are well-chosen, the surface groups after one ALD cycle allow for repeating the cycle. In every ideal ALD cycle, the same amount of material—a fraction of the material's monolayer— is deposited depending on the accessible surface sites, the precursor size, and the precursor and the substrate. Typical growth rates observed for ALD processes range from 0.1 to 1.5 Angstrom per ALD cycle. Thus, the total deposited film thickness can be defined by the number of cycles during an ALD process (Figure 2.1b). Note, the thin film growth via ideal ALD is not limited by the absolute mass transport of precursor molecules as long as self-termination of the surface reactions is reached. In general, ALD is

---

① This section comes completely from the published first-authored book chapter:

Peng, J.; Zierold, R. Atomic layer deposition of materials. In *Encyclopedia of Condensed Matter Physics (Second Edition)*, Chakraborty, T. Ed.; Academic Press, 2024; pp 716-728. *Copyright © 2024 Elsevier Ltd.*

diffusion-limited which means on the one hand, no line-of-sight from the precursor source to the substrate is required (Figure 2.1c). On the other hand, the molecules need sufficient time for diffusion and surface-side reaction. Consequently, homogeneous and conformal coatings with controlled sub-nm thickness can be achieved even on three-dimensional (3D) features at the expense of extended process times. Depending on the precursors chosen, a plethora of materials can be deposited by ALD, ranging from oxides, nitrides, fluorides, sulphides, and phosphides as well as selenides, tellurides to pure elements or mixtures of the aforementioned materials. In the "[…] case study for the trimethylaluminum/water process", Puurunen describes the most important features and main characteristics of ALD in detail in her review article in 2005.[22] An updated version of the review including more than 2300 references and focusing on the crystallinity of ALD deposited film has been published in 2013.[23] In general, ALD has the capability to provide continuous, pinhole-free films with a low content of residual impurities. However, by employing the different surface chemistry of precursors on various materials, ALD can be tailored in such a way that deposition of nanoparticles and clusters or in an area-selective fashion is feasible.[24, 25] Note, Steve George's review[26] summarizes in a short and comprehensive manner the major trends and developments in ALD in the last two decades. Specifically, the review addresses new ALD process technologies, such as plasma-enhanced ALD (PEALD), atmospheric-pressure ALD, spatial ALD, area-selective ALD (AS-ALD), and (polymer) molecular layer deposition (MLD), to name a few of them.

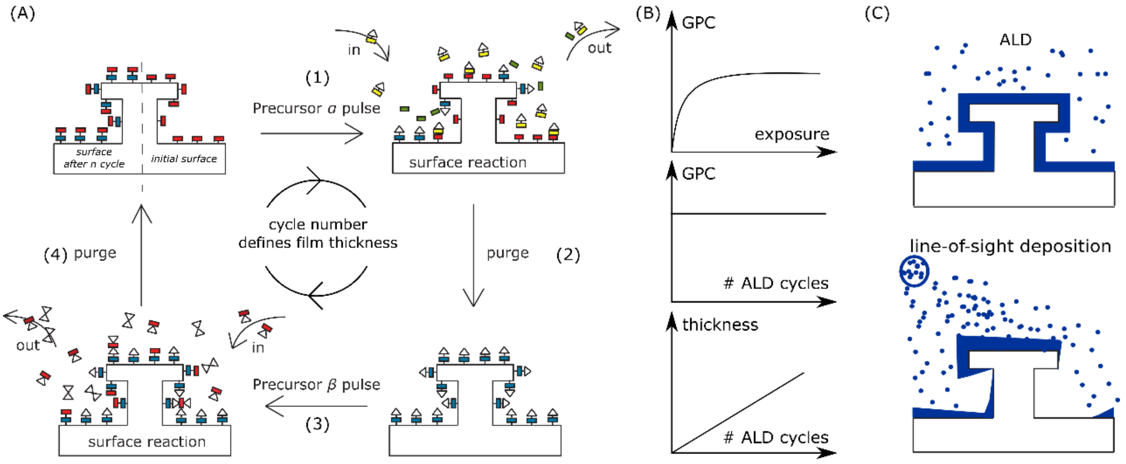

Figure 2.1. (A) Schematic of an ALD cycle with two different precursor species. One ALD cycle consists of a pulse of precursor α which reacts in a self-limiting manner with surface groups. After purging the reaction chamber, the precursor β is brought to the substrate presenting an intermediated surface. Precursor β reacts there again in self-terminating behavior, and deposits the desired material. Subsequently, the reaction chamber is purged again. Since the (resulting) surface groups after one ALD cycle can react with precursor α again, a sequential deposition routine allows for exact thickness control by adjusting the number of cycles. (B) Due to the self-limiting nature of the ALD reactions, a constant growth per cycle (GPC) and thus a linear growth as the function of cycle number is achieved. (C) Schematic comparison of a conformal surface reaction-limited ALD process and a deposition process which is mass flux limited by a line-of-sight coating, e.g., sputtering.

The origin of ALD dates back to the 1960s and 1970s when the principle of ALD was developed and investigated in parallel in the former Soviet Union and Finland under the name ‘Molecular layering’ and ‘Atomic Layer Epitaxy’, respectively. However, the initial ALD research activities in the Soviet Union went unnoticed for a long time and are still poorly cited compared to the fundamental studies in Finland.[27] An ALD community-driven virtual project on the history of ALD (VPHA)[28] summarizes 22 publications—voted by the community as significant early achievements in the field of ALD— in chronological order. Note, ‘early’ is defined therein as before 1986 when a review article about ALD/ALE was published by authors not treated as the pioneers of ALD. In detail, Shevjakov, Aleskovskii, and Kol'tsov reported on metal chloride reactions with water for the deposition of TiO_2, GeO_2, and later SiO_2 and PO_x from 1965 to 1975. At that time, Suntola and Antson[1] patented the principle of atomic layer epitaxy for depositing compound films from elemental precursors, e.g., ZnS from Zn and S. However, other materials such as SnO_2 and GaP are listed, as well, and H_2S as potential hydrogen source is suggested. In the follow-up patents and applications molecular inorganic precursors were introduced, e.g., $TaCl_5$ and $AlCl_3$ with H_2O for depositing Ta_2O_5 and Al_2O_3, respectively, as well as ZnS from $ZnCl_2$ and H_2S. Note, the first industrial application of ALD or atomic layer epitaxy was in fact ZnS which was used for the fabrication of thin film electroluminescence displays employed at Helsinki airport from 1982 until 1998. In the mid of the 80s, metal-organic precursors were introduced in ALD for the first time to deposit III-V semiconductors GaAs and AlAs by utilizing AsH_3 with $Ga(CH_3)_3$ and $Al(CH_3)_3$, respectively. In the early 1990s, the more general term atomic layer deposition gained acceptance over atomic layer epitaxy because many ALD reactions did not result in epitaxial or even crystalline growth. Due to the high purity of the deposited materials, the ability to coat even complex structures without shadowing effect, and the precise control of the film thickness, ALD came into the focus of the semiconductor industry in the 1990s for the deposition of "high-κ" dielectrics. The usage of materials with higher dielectric constant than the classical silicon dioxide allowed for further miniaturization of metal-oxide-semiconductor field-effect transistors (MOSFET) structures. Together with the industrial interest in ALD, the research landscape also revived and great progress was made in the last 20 years in precursor and reaction chemistry. As of 2022, a community-driven process database hosted and maintained by Kessel’s group at Eindhoven University of Technology gives a tabular literature overview of the published processes.① Moreover, a regularly updated list of review articles related to ALD can be found there as well. ALD is outstandingly suited for the coating of (nano)structures with high aspect ratios— the ratio of geometrical characteristic length and diameter—because of its self-limiting nature. In such substrates, e.g., opals, nanoporous membranes, biomaterials, and nanoparticles, ALD is often the only suitable technique to reach a conformal coating without shadowing effects.[29-31] Besides basic research in physics, chemistry, and material science, ALD is a state-of-the-art technique in different industry fields, such as semiconductor and solar cell energy.

2.1.3. Overview

In order to offer a more comprehensive understanding of ALD, this section firstly presents the several basic forms of ALD, namely thermal and plasma-enhanced ALD as well as temporal and spatial ALD in Section 2.1.3.1 and Section 2.1.3.2, respectively. Since ALD has received

---

① https://www.atomiclimits.com [accessed 02.04.2022] attention from basic research to industry in recent years, a variety of ALD processes utilizing various precursor types have been explored to deposit materials comprising the majority of elements in the periodic table as summarized in Figure 2.2. However, one of the most important points for a successful ALD is the metal precursors used. A typical metal precursor contains one type of metal atom per precursor and several characteristics, namely high reactivity, volatility, and good thermal stability over a wide temperature range have to be fulfilled whereas state of aggregation, costs, ease of handling, and toxicity are side aspects but not to be neglected. Note, the ligands's properties determine the properties of the metal precursor and thus can be used to tailor the precursor chemistry. Although the potential advantages of organometallic precursors are their high volatility and low growth temperature, one of the disadvantages is their thermal decomposition often already at low temperatures which may induce non-self-limiting CVD components besides the ALD growth and high impurity contents. Main material classes deposited by ALD, e.g., oxides, nitrides, metal, etc. are presented in Section 2.1.3.3 ~ Section 2.1.3.7. Subsequently, approaches to synthesize multi-component films (Section 2.1.3.8) and, following *in situ* characterization methods in ALD processes (Section 2.1.3.9) are discussed. Finally, a selection of applications profiting from the unrivaled ability of ALD to deposit conformal coatings on nanostructures will be presented.

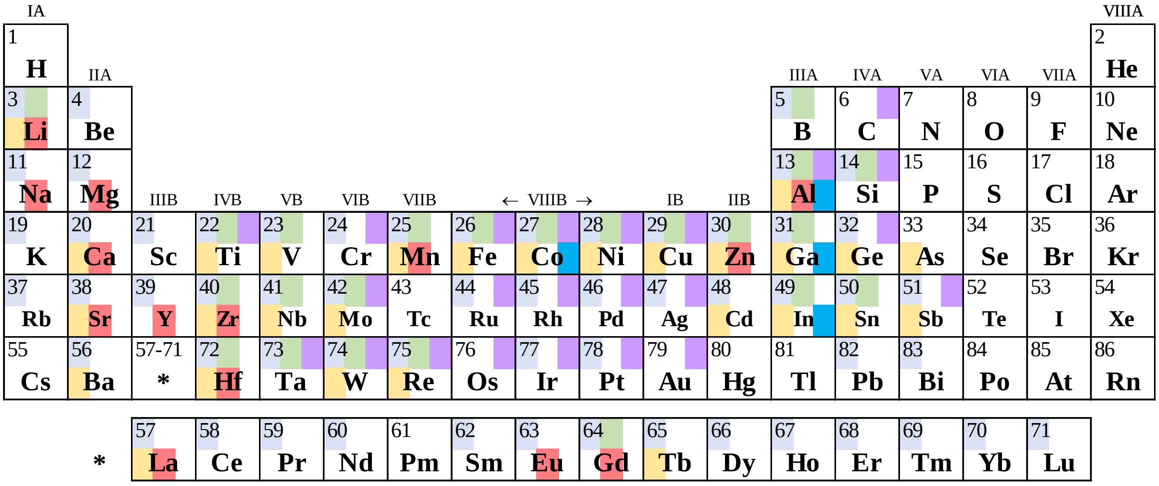

IA	IIA	IIIB	IVB	VB	VIB	VIIB	← VIIIB →			IB	IIB	IIIA	IVA	VA	VIA	VIIA	VIIIA
1 H																	2 He
3 Li	4 Be											5 B	6 C	7 N	8 O	9 F	10 Ne
11 Na	12 Mg											13 Al	14 Si	15 P	16 S	17 Cl	18 Ar
19 K	20 Ca	21 Sc	22 Ti	23 V	24 Cr	25 Mn	26 Fe	27 Co	28 Ni	29 Cu	30 Zn	31 Ga	32 Ge	33 As	34 Se	35 Br	36 Kr
37 Rb	38 Sr	39 Y	40 Zr	41 Nb	42 Mo	43 Tc	44 Ru	45 Rh	46 Pd	47 Ag	48 Cd	49 In	50 Sn	51 Sb	52 Te	53 I	54 Xe
55 Cs	56 Ba	57-71 *	72 Hf	73 Ta	74 W	75 Re	76 Os	77 Ir	78 Pt	79 Au	80 Hg	81 Tl	82 Pb	83 Bi	84 Po	85 At	86 Rn

*	57 La	58 Ce	59 Pr	60 Nd	61 Pm	62 Sm	63 Eu	64 Gd	65 Tb	66 Dy	67 Ho	68 Er	69 Tm	70 Yb	71 Lu

Figure 2.2. Periodic table of elements illustrating the reported materials deposited by ALD, e.g. oxides, nitrides, pure elements, sulphides, phosphides, and fluorides. The compounds are displayed with cerulean, olive, purple, straw, red, and blue background squares, respectively, at the element's panel.

2.1.3.1. Thermal and plasma-enhanced ALD

ALD bases on (at least) two binary reactions of a precursor α with a precursor β, often denoted as reactants, to prepare the desired material. A common example is the deposition of aluminium oxide by reaction of trimethylaluminum (TMA, $Al(CH_3)_3$) with water. The two half-reactions can be written as:

(1st half-reaction) $AlOH^* + Al(CH_3)_3 \rightarrow AlOAl(CH_3)_2^* + CH_4$

(2nd half-reaction) $AlCH_3^* + H_2O \rightarrow AlOH^* + CH_4$

summing up to $2Al(CH_3)_3 + 3H_2O \rightarrow Al_2O_3 + 3CH_4$.

The driving force of this exothermic reaction is the formation of a strong Al-O chemical bond. Similarly, other thermal oxide processes, such as those for TiO_2 and ZnO, are also driven by a conducive change in the Gibbs free energy. However, other ALD reactions might require additional energy, such as heat, to overcome the energy barrier for the chemical reaction of the precursor with the surface. In the ideal ALD, a temperature range, the so-called *ALD window*, can be defined in which the growth per cycle is constant (Figure 2.3). Below the ALD temperature window either CVD caused by precursor condensation or a suppressed growth can be identified; whereas, above the ALD window, precursor decomposition and desorption or loss of functional groups can lead to CVD and reduced growth, respectively. Note, the applicable reaction temperatures are generally limited by constraints in precursor vapor pressure and stability, reaction chamber design, and substrate. To overcome this thermodynamic obstacle without excessive heating, additional external energy is needed which can be provided, e.g., by a highly reactive species delivered from plasma or radical source in at least one half-cycle of the ALD reaction. In addition to the inherent higher reactivity of the plasma radical, the ions' kinetic energy, surface recombination rates and energies, and the total energy flux of the plasma radiation contribute to the additional energy term in a PEALD process.

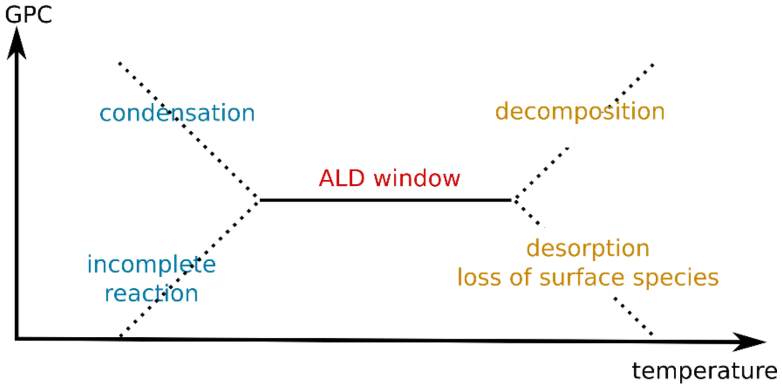

Figure 2.3. Sketch of the ALD window including the processes when the ALD window is left to lower and higher temperatures.

Already in the first ALD review by Suntola and Hyvärinen in 1985,[32] the authors predicted the occurrence of plasma-supported ALD to render new reaction pathways. Six years later, a first plasma-enhanced, also called plasma-activated, ALD process of GaAs employing hydrogen radicals prepared in a plasma source was reported. However, it lasted almost one decade until the ALD community took up the topic when PEALD has been used for the deposition of Ti and Ta. From there, novel processes and precursors as well as plasma sources and reactor types have been developed, enabling ALD scientists to deposit materials hardly achievable by thermal ALD, e.g., elemental metals and semiconductors, or to improve the quality and to reduce the impurity content of the deposited films. The reviews of Profijt in 2011[33] and Knoops in 2019[34] present a comprehensive summary of the development of PEALD in the past 20 years.

On the one hand, PEALD reveals several advantages compared to thermal ALD: First, as aforementioned, the plasma with its highly reactive species provides an additional energy contribution. Consequently, the thermal energy, i.e., the temperature, needed to deposit an ALD thin film with the same properties as in a thermal ALD process can be lowered. Such a reduction in temperature is of special interest if temperature-sensitive substrates, e.g., polymeric ones, need to be coated. Second, several publications report on improved material properties deposited by PEALD compared to thermal ALD, such as impurity content, density, and optical or electronic characteristics, to name a few. Third, metal-organic precursors not usable in thermal ALD and thus novel ALD reaction pathways are conceivable. For instance, some metal-organic compounds, with sufficient vapor pressure and thermal stability, reveal a vanishing or negligible reactivity to water rendering them unsuitable for thermal ALD. However, by utilizing a highly reactive oxygen plasma, these compounds can be employed as ALD precursors, opening new reaction schemes. Additionally, hydrogen plasma can provide highly reducing species to allow for depositing metals not feasible by thermal ALD reductants. Fourth, due to the highly reactive plasma species, more reactive surface sites can be prepared during the ALD plasma half-cycle leading to an overall increased growth rate for some processes.

On the other hand, PEALD also has some drawbacks compared to thermal ALD. The major disadvantage is the non-usability of PEALD to coat high aspect ratio nanostructures or highly porous substrates conformally. Recombination of radicals at the surface with other species or radicals is accompanied by losing their high reactivity. Since the probability of surface collision and, consequently, recombination is significantly increased for these kinds of high surface area substrates, the local flux of radicals inside the porous structure or at 3D structures is reduced as a function of the diffusion depth and geometry, respectively; thus, the deposition becomes non-conformal. By varying the plasma parameters, such as power, duration, pressure, to name a few of them, the conformality of the PEALD process can be controlled and improved for aspect ratios up to ~30. However, PEALD cannot compete with thermal ALD where aspect ratios of 1000 and more or even branched porous substrates with non-ballistic transport paths can be coated conformally at sufficiently long diffusion and purge times. Another impediment of PEALD is the possibility of damage or surface alteration upon the plasma half-reaction. The highly reactive species of the reactant can alter the chemical properties of the substrate surface via oxidation and nitridation leading to an unwanted interface. Energetic ions impinging on the surface during the plasma may lead to bond-breaking and defects in the deposited materials or on the substrate, as well as to charge accumulation in the thin film. Another source of plasma-induced damage is the highly energetic ultraviolet (UV) radiation occurring during the plasma. This radiation can alter the properties of polymeric substrates but also potentially introduce defects and degrade surface passivation. Lastly, the plasma source and the control of which render the ALD system much more complex, prone to error, and expensive. Furthermore, the parameter space for process optimization, e.g., temperature, (partial) pressure, precursor dose, is expanded by the plasma parameters, e.g., power and duration.

2.1.3.2. Temporal vs spatial ALD

The invention and development of ALD sparked several concepts of ALD reactor designs from the beginning. The scientists in the former Soviet Union started their research on ALD in a reactor chamber with a stationary substrate which is exposed to a sequence of different precursors. In contrast, Suntola drafted in his initial patent[1] a concept of a rotating disc holding the substrate which crosses areas of stationary precursor vapors during spinning. Thus, two different major operation modes can be defined, namely temporal and spatial ALD (Figure 2.4).

In temporal ALD, a heated reactor is loaded with a stationary substrate and stationary valves control the precursors flow by opening and closing one after the other, separated by a purge/pump time. Adjusting the duration of the individual steps in the ALD cycle is needed to achieve sufficient precursor doses to saturate all surface groups but also to remove all non-used precursors and reaction by-products to avoid reduced growth and CVD, respectively. Scale-up of thermal temporal ALD processes is achieved in so-called batch reactors in which several substrates are stacked over each other and coated simultaneously. Of course, precursor doses and purge times have to be increased according to the increased surface area of reactor and substrate. Note, PEALD in batch reactors is hampered because of the stacked arrangements of the substrates (see Figure 2.4). Specifically, the long diffusion paths without line-of-sight between substrate and plasma source increase the probability of surface collision and recombination; thus, reducing the number of reactive species deep inside the batch.

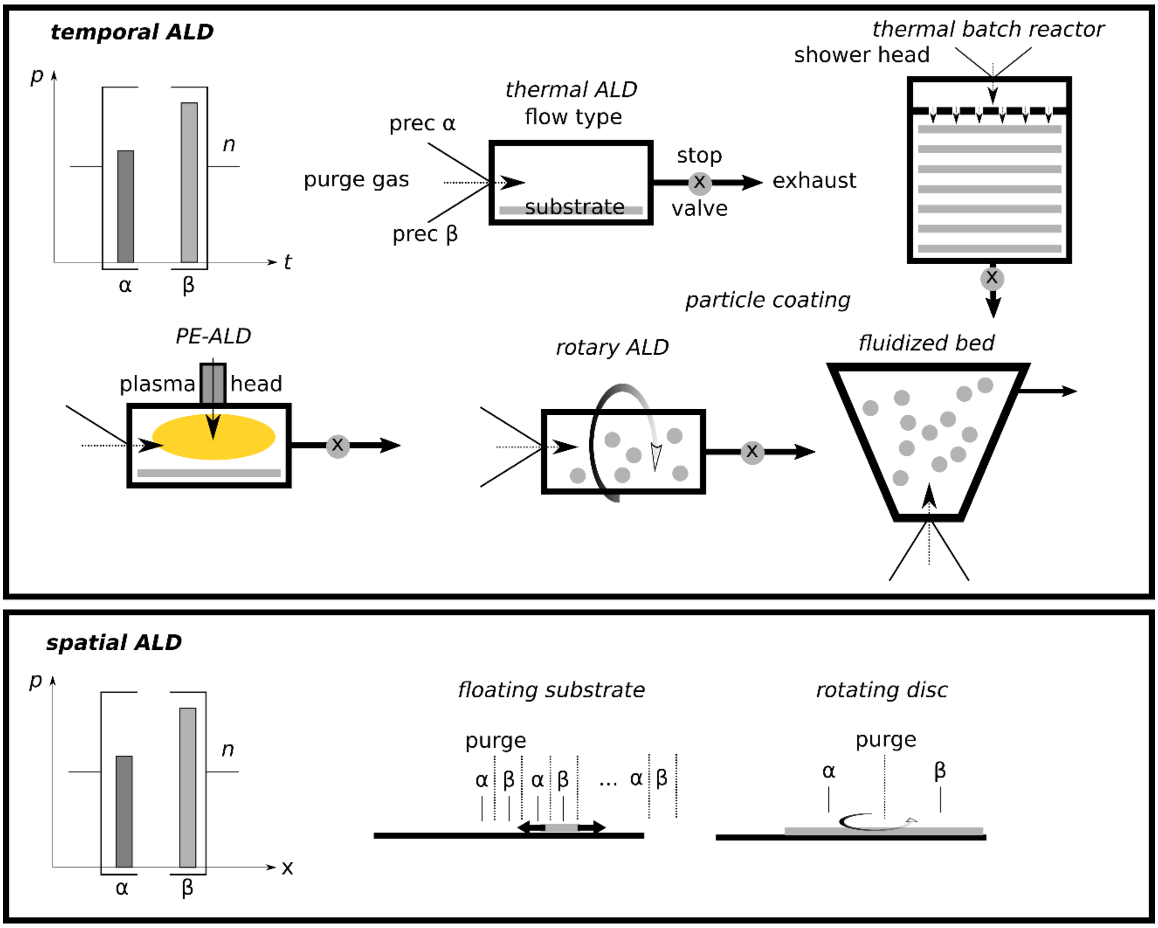

Figure 2.4. Schematic overview for different reactor types. Upper box: Types of ALD reactors operating in a temporal fashion, e.g., thermal and thermal batch ALD, PEALD, but also ALD systems for particles coatings. Lower box: ALD reactor types working in the spatial regime, such as floating substrate or rotating disc reactors.

In spatial ALD, the substrate is moving through different fixed and stationary precursor zones separated by a zone in which the purging occurs. This could be a rotating substrate as in the Suntola patent[1], for instance, but it could also be a substrate transported (back and forth) through a line of different precursor zones separated by an inert gas zone (see Figure 2.4). A fixed substrate with a movable precursor injection head is another concept of spatial ALD. Note, in all cases, not only thermal ALD but also PEALD operation is feasible. The main advantage of spatial ALD compared to temporal ALD is the absence of purge time which is needed in temporal ALD to empty the reaction chamber. Since the chemical surface reaction typically occurs in the millisecond time range, only the mechanical transfer time between two separated precursor zones limits the total cycle time of ALD. Of course, at more complex structures the exposure time — which is the time the substrate has to remain in one precursor zone — has to be extended to fulfil the ALD criterion of self-limitation at all available and accessible surface groups. A good overview of different concepts of spatial ALD, such as roll-to-roll reactors where a flexible substrate is moved from one roll to another roll by guide rollers running several times through two different precursor zones chamber, rotating discs reactors, and drum reactors, to name a few of them, is given by Poodt *et al.*[35] terms of economic aspects, spatial ALD comes with a more complex reactor design with mechanical parts compared to temporal ALD. On the other hand, the reactor wall is coated in temporal ALD and usually, much more precursor than absolutely needed for the self-limiting surface reaction is provided. However, the precursor excess, which is not reacted, is then purged and thus wasted. In other words, the efficiency of precursor utilization is increased for spatial ALD concepts compared to temporal one. Consequently, the running costs of the spatial ALD coating, namely the expenses for precursors, could be significantly reduced compared to temporal ALD. Moreover, complex gas abatement systems for cleaning the exhaust gas of non-used (and potentially explosive or toxic) precursor are superfluous.

2.1.3.3. ALD of oxides

Metal oxides have been deposited from a huge variety of inorganic and organic molecular precursors, such as halides, alkoxides, alkyls, amides, beta-diketonates, just to name a few. As reactants, water, ozone, and oxygen plasma have been mainly used.[23] Note, processes with water often bases on a protonation reaction of the precursor ligands, whereas reactions with ozone and oxygen plasma are often combustion-like. Alternative oxidant precursors such as hydrogen peroxide, alcohols, and N_2O, have been reported in literature as well. Furthermore, special ALD processes have been explored which do not contain a separate dedicated oxygen reactant but use another metal precursor as oxygen source. Specifically, metal alkoxides or carboxylates have been employed for such processes that are treated as gentler to the underlying substrate since a highly oxidizing reactant is waived.

Historically, the major driving force for ALD of oxides was the need for advanced high-κ dielectrics as gate oxides in MOSFET and as capacitor dielectrics in dynamic random-access memories (DRAM). Nowadays, ALD is recognized as a state-of-the-art deposition technique in the industrial fabrication of complex logic and memory devices due to its inherent conformality and film thickness control often outperforming other deposition techniques, such as CVD and sputter coat.[36] Within the last decades, the device structures changed from 2D to nanostructured 3D rendering ALD the method of choice. The majority of the deposited dielectrics by ALD are binary oxides, e.g., HfO_2, Al_2O_3, ZrO_2, to name a few of them.Also, doped oxides, e.g., Sr- or Ba-doped TiO_2 ($SrTiO_3$, STO; $BaTiO_3$, BTO) or nanolaminates consisting of zirconia and alumina are of particular interest for DRAM applications.[37]

Recently, ALD in general has aroused interest in more fields and applications: Special attention has been paid to moisture diffusion barrier layers, e.g., Al_2O_3, ZrO_2, and SiO_2, to encapsulate and to protect organic-light emitting diodes (OLED). Other transition-metal oxides, namely MO_3, WO_3, and V_2O_5 have been employed as hole contact in OLEDs. Further, lithium oxide compounds have already been deposited for battery applications. Besides, in organic and flexible electronics and displays, ALD of transparent conducting oxides, for instance, Sn-doped In_2O_3 (ITO) and Al-doped ZnO (AZO), has taken hold in industry.

Other properties of oxide thin films, e.g., magnetism, ferroelectricity, or multiferroics, deposited by ALD have been investigated in detail in basic research but also for applications. For example, multiferroic (doped) hafnia layers have been studied as potential resistive RAM (ReRAM).

Apart from binary oxides, plenty of doped oxides, e.g., In_2O_3:Zr, SnO_2:Sb, ZnO:Ga, and other ternary or quaternary oxides (for further information see Section 2.1.3.7), such as $PbTiO_3$, $SrTa_2O_6$, $SrBi_2Ta_2O_9$, $La_{1-x}Ca_xMnO_3$, to name a few of them, have also been produced via ALD.

2.1.3.4. ALD of nitrides

Typically, metal nitrides are hard, chemically resistant, sometimes catalytically active, and often electrically conductive materials. Since the pioneering work of ALD-deposited metal nitride published in 1988,[38] they have become the material class with the 2nd most number of ALD publications after ALD oxide. Metal nitrides, such as Si_3N_4, TaN, TiN, and WN_x, are often used as diffusion barriers for water as well as oxygen and metal diffusion, respectively, in the microelectronics industry. Another increasing interest for ALD of nitrides exists in research on superconductivity, e.g., TiN, NbN, or mixtures of them. The reported nitrides deposited by ALD can be generally divided into two categories according to their electrical properties: (1) Nitride dielectrics or semiconductors such as BN, AlN, GaN, Si_3N_4, Ta_3N_5, Cu_3N, InN, Zr_3N_4, Hf_3N_4, LaN, LuN; (2) metallic nitrides such as TiN, Ti-Si-N, TaN, NbN, MoN, Ti-Al-N, WN_x, WN_xC_y, Co_xN, Sn_xN.

The most typical ALD nitride processes are based on the reaction of metal chloride (or other halide) precursors with NH_3 as a reactant. A prime example is the reaction of $TiCl_4$ with NH_3 to deposit TiN. However, these processes need relatively high temperatures (typically in the range of 350−500 °C) and suffer from residual impurities of the respective halogens. Both issues can be addressed simultaneously by replacing the halide precursor with a metal-organic precursor. Specifically, metal-organic alkylamide-based compounds can be used for metal nitride deposition, e.g., TiN, ZrN_x, MoN_x, HfN_x, TaN_x, and WN, at lower temperatures (150−250°C) compared to the halide-based processes and avoiding halogen residues at the same time but at the cost of additional carbon impurities.[23] To grow nitrides containing main Group III elements, namely Al, Ga, and In, by ALD, alkyls which contain a direct metal-carbon bond have been used.

NH_3 serves as a reductant of the metal center in the precursor during the ALD reaction. Generally, NH_3 leads to the stable nitride with the highest metal oxidation state. For instance, to achieve the conductive TaN over the dielectric Ta_3N_5 an additional reducing agent to NH_3, such as elemental Zn or Me_3Al needs to be implemented during the ALD process.[23] Different reducing agents such as hydrazine (Me_2NNH_2) and tert-butylamine have been employed for the deposition of TaN and TiN as well.

PEALD can ease the deposition of metal nitrides with lower oxidations state and often reduced amount of impurities compared to thermal ALD. The deposition temperature can be lowered, novel precursor chemistries could be used, e.g., $Nb(N^tBu)(NEtMe)_3$ instead $NbCl_5$ for depositing NbN, and the number of tunable process parameters, e.g., plasma power, pressure, and gases, can be increased to improve and tune the thin film properties. Instead of using gaseous NH_3, nitrogen-hydrogen mixtures with adjustable ratio have been exploited in PEALD. The hydrogen-plasma serves as reductant during the ALD process whereas the nitrogen-plasma resembles the nitrogen source. Note, amide compounds, i.e., $Ti[NMe_2]_4$, in combination with reducing hydrogen (plasma) have been studied to deposit the corresponding nitride, i.e., TiN, without the need of an additional nitrogen source.

2.1.3.5. ALD of metals and elements

Metals deposited by ALD are often more challenging to achieve high quality compared to oxides and nitrides. Consequently, relatively less research—and even fewer industrial applications—utilizing metal ALD has been carried out compared to ALD of metal oxides in the past. However, in order to fulfill Moore's law, CMOS devices need to be further downs-scaled and the architecture becomes more complex. Hence, increased demands for the precision and conformality of the deposition process are set. These requirements can be easily met by ALD leading to a number of potential applications in the device fabrication not only for oxides and nitrides as aforementioned, but also for metal deposition. Tungsten and copper are important metals for plugs and interconnects, respectively, in CMOS technology and have been in focus for ALD for a while. Whereas, tungsten layers can be deposited by the reducing WF_6 with diborane, silanes, or hydrogen (plasma) for years. The reliable deposition of metallic copper remained challenging until novel reaction pathways have been developed, e.g., $Cu(dmap)_2$ or $Cu(hfac)_2$, in combination with a plethora of reductants including H_2, H_2 plasma, diethyl zinc, formic acid, formaldehyde, etc. Other applications of metals (Ru, Co, Ta, Ni, and Ti) deposited by ALD in barriers and liners for interconnects or electrical contacts and gate electrodes are conceivable nowadays. Note, the introduction of 3D gate structures, such as fin- or nanowire-based gate-all-around FETs makes the use of ALD processes inevitable for reliable device fabrication.[36, 39]

Noble metals, especially in form of (nano)particles, are of interest for catalysis applications. In contrast to electronic device preparation in which continuous— ideally pinhole-free—thin films are aimed for, isolated particles and islands are often preferred for maximum catalytic performance. By employing the difference in surface energy of the metal to be deposited and the substrate, the ALD process parameters can be tuned to adjust particle-size distribution. Especially, platinum-group metals, e.g., Pt, Ru, Pd, Ir, are comparably easy to reduce in their oxidation state—after precursor adsorption of the metal precursor at the substrate's surface—and thus can be deposited in their metallic state without the need of high temperatures or strong reducing agents.

Three different types of reaction schemes for the reduction step have been mainly explored: First, 'normal' reducing agents, e.g., H_2, NH_3, and N_2/H_2 as well as plasma of which, have been applied not only on platinum group metals but also on some more reactive metals. Molecular H_2 has been widely used for the ALD of some highly reactive metals, e.g., Cu, Ta, Ti, and Sn, by reaction with their halides. NH_3 or nitrogen/hydrogen plasma was employed to deposit metallic films of cobalt and nickel. Second, metal deposition via an intermediated surface oxidation step by utilizing oxygen, ozone, water, or air as reactant for combustion of the adsorbed precursor. In other words, firstly a metal oxide film is produced, followed by a subsequent reduction to metal by the next metal precursor pulse. This reaction is often supported by self-catalytic effects of the metallic thin films as well as a limited stability of the intermediated oxides. Third, other less common reducing agents have been investigated to deposit metals, such as zinc vapor, silanes, and boranes.

Note, further developing and optimizing processes for metals remain an important aspect in ALD. Specifically, metal-organic precursor development and the search for matching reductants are still ongoing for reliable metal deposition. Current materials of interest are the deposition of gold and silver. Moreover, understanding the interplay between substrate properties, e.g., surface energy, texture, and oxidation state, with the metal deposition process, specifically its initial nucleation, is essential to control and to tune the growth of metallic particles but also continuous thin films.

2.1.3.6. ALD of sulfides, phosphides, fluorides

Apart from the widely investigated oxides, nitrides, and metals discussed above, other binary compounds have also been explored and some of which have even been alput to applications.

As previouslymentioned, the development of ALD was driven by the need for an optimized fabrication method for thin film electroluminescent displays containing ZnS. In detail manganese- as well as rare and alkaline earth-doped ZnS films have been used for monochromatic (yellow) and multicolor displays, respectively. Most recently, the development of advanced structures for 'green' energy-related applications, such as photovoltaics or batteries, have been a driving force for ALD of sulfide materials. Especially the unique ability of ALD to conformally coat complex structures is advantageous to coating these (often porous) devices with a large surface area and to tailor the interfaces. For example, CdS and InS can be employed to deposit a buffer layer for energy band alignment in Cu(In,Ga)Se_2 (CIGS) solar cells. The first deposition of ZnS based on elemental Zn and S. However, halides and, much more prominent, metal-organic precursors can easily react with hydrogen sulfide (H_2S) to form a metal sulfide at lower temperatures than needed for elemental precursors.

ALD of phosphides has been rarely reported: Only CoP has been developed as a catalyst to enable efficient water splitting, whereas AlP, GaP, and InP have gotten their position in semiconductor applications. Phosphorus is customarily delivered by its hydrides, e.g., PH_3 plasma. However, PH_3 decomposes seriously during plasma treatment so that excess P remains, which is hard to eliminate in the following purge step and leads to an undesirable deposition. Therefore, the subsequent removal—for instance, by an additional H_2 plasma step—of the excess P would be the key to achieve ALD of phosphides.[40]

Metal fluorides, e.g., CaF_2, SrF_2, MgF_2, LaF_3, ZnF_2, are important optical coating materials because they possess not only a low refractive index but also a high transmission at both UV and infrared (IR) wavelengths. The conformal characteristic of ALD coating renders it a perfect method to produce three-dimensionally shaped optical components. Furthermore, other metal fluorides, e.g., AlF_3, have been employed as a protective coating on Li-ion battery electrodes. Similarly to phosphides, only a decent number of processes for ALD of fluorides has been reported because vaporous HF reacts with metal-organic precursors to form fluorides, e.g., AlF, MgF, NaF, ZrF_4, etc., but it is highly toxic and corrosive, and thus needs dedicated ALD and laboratory equipment with high safety requirements. Nonetheless, alternatives have been explored: On the one hand, the *in situ* thermal decomposition of NH_4F to only locally create the HF and to avoid handling dangerous HF vapor has been suggested. On the other hand, vaporous TiF_4 and TaF_5 have been used as fluorine reactants in combination with a variety of metal-thd precursors. Unlike HF, these reactants are low vapor pressure solids and can thus be handled and stored more safely with fewer restrictions. Note, even the reactant carries another metal center, the impurity content of Ti and Ta is reported to be of minor nature.

2.1.3.7. ALD of ternary and quaternary components

The basic principle of ALD is based on two half-reactions forming a binary material. Hence, traditional applications of ALD rely on binary oxides. However, the binary process can be combined to form complex tailor-made materials containing three, four, and more elements often referred to as ternary, quaternary, and quinary materials, respectively. Strategies to synthesize such complex materials by ALD include so-called supercycle schemes, co-dosing approaches, and multistep approaches[41, 42] as illustrated in Figure 2.5.

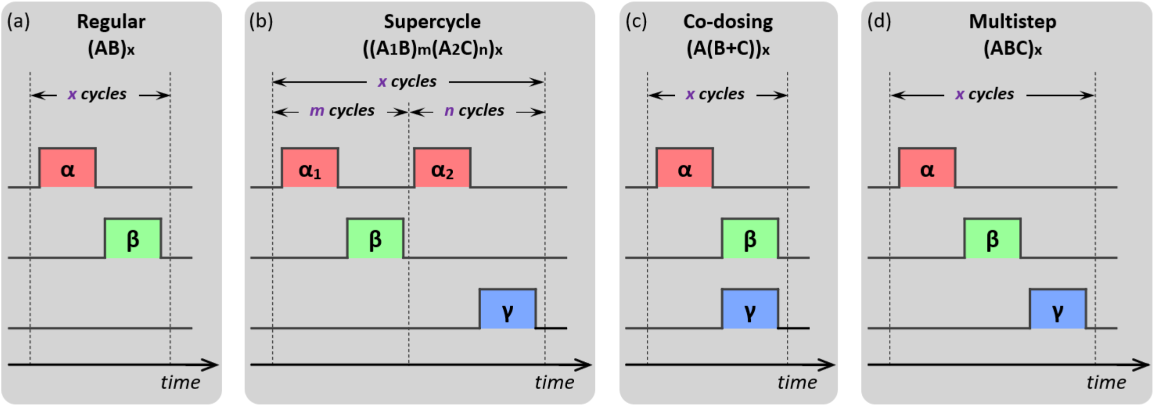

Figure 2.5. Schematic overview of strategies leading to complex materials constituting more than two elements. Here, precursor α, β, γ are containing the target deposited elements A, B, C, respectively. Precursor α_1 and α_2 in (b) can stand for the same precursor or two different precursors that contribute to the same deposited element A.

A regular binary ALD cycle (Figure 2.5a) usually consists of sequential precursor pulses, exposure, or carrier gas purge for each half-reaction to form one ALD cycle. In a so-called supercycle deposition scheme, two or more binary ALD processes (running *m*- and *n*-times, etc.) are put together into a "larger" loop which itself is then repeated *x*-times (Figure 2.5b). Depending on the number of *m* and *n*, the achieved compound can be tailored and can be divided as follows:

1. *m* and *n* are comparably small and equal (e.g., 1:1, 1:2, etc.): A ternary oxide, $A_xB_yC_z$, which is uniform and well-mixed in the deposited composition. The ratio between the different constituents can be slightly tailored.
2. *m* >> *n*, or vice versa (e.g., 1:20, 1:50): A doped material can be achieved.
3. *m* and *n* are close but large (e.g., 20:20, 40:50, etc.): A so-called nanolaminate consisting of separated continuous thin layers is formed.

Accordingly, in the example of the reactions with diethylzinc (precursor β), trimethylaluminum (precursor γ), and water (precursor α) for depositing ZnO and Al_2O_3, one can deposit by varying *m* and *n*: (1) a $Zn_xAl_yO_z$ ternary oxide thin film with tailor-made stoichiometry, (2) an Al-doped ZnO thin film which can be employed as transparent conductive oxide, and (3) a multilayer film of separated Al_2O_3 and ZnO layers. Also, the accordingly management of trimethylaluminum (precursor β) and O_3 (precursor α_1) plus titan(IV)isopropoxid (precursor γ) and water (precursor α_2) can respectively lead to $Al_xTi_yO_z$, Al-doped TiO_2, "Al_2O_3 + TiO_2" nanolaminate too.

In the co-dosing approach, as shown in Figure 2.5c, at least two precursors (e.g., β, γ) are injected simultaneously into the reaction chamber. Alternatively, two precursors or reactants can be mixed in varying proportions in the precursor container or a dedicated volume, and then injected together. A typical example of the co-dosing scheme is the ALD process for ZnO_xS_y. Both reactants, namely, H_2O and H_2S, are pulsed at the same time. By varying the concentration ratio of them, the resulting composition of the deposited materials can be tailored.

Supercycling and co-dosing can both be used for the deposition of multicomponent thin films. However, each of them has specific advantages and downsides. On the one hand, better mixing of the constituents in the sub-monolayer regime can be achieved by co-dosing compared to the supercycle approach. On the other hand, the simultaneous competing chemical reactions of the two precursors on the substrate — with different (and often not well-known) kinetics, reactivity, diffusivity, and adsorption behavior — complicate the prediction for process optimization and may vary in complex architectures like trenches. In contrast, such a potential drawback is avoided in the supercycle approach since the individual ALD reactions are separated. To which degree any of these effects play a role and to which extent they impact the properties of the prepared film varies from case to case.

The multistep approach (Figure 2.5d) is also used to deposit multi-component materials in ALD. Within this manner, a regular ALD process consisting of two half-cycle (AB-type) is extended by adding one or more steps (ABC-, ABCD-type, etc.). These additional steps can introduce an additional constituent to the material, resulting in the deposition of a multicomponent material. Besides, the multi-step scheme is often used to extend the operating window of ALD processes or modify the properties of a material. For example, in the low-temperature Pt ALD process using $PtMe_3CpMe$ and O_2 plasma, the regular ALD process results in PtO_x at low temperatures. Low-temperature deposition of metallic platinum can be achieved by a multistep approach adding an H_2 plasma as a third step to reduce the PtO_x to metallic Pt.

Note, different process schemes can be combined with each other, e.g., the plasma-enhanced deposition of TiNbN uses the supercycle approach for varying the Nb/Ti ratio and the co-dosing approach during the plasma half-reaction of nitrogen and hydrogen to replace NH_3.

2.1.3.8. *In situ* characterization of ALD processes

Optimization and characterization of ALD processes are typically performed as follows in daily lab routine: One of the ALD parameters, such as precursor or reactants, temperatures (chamber, precursor), characteristic times (pulse, exposure, purge), plasma parameters (power, duration), to name a few of them, is altered and a process of *x*-cycles is run. Subsequently, the properties of the deposited thin film, e.g., composition, morphology, thickness, crystallinity, are *ex situ* characterized and based on these results the process is adapted. This procedure is repeated until the desired properties are achieved. However, such an approach could be rather time-consuming and the chemical reactions occurring at the surface during the process remain unknown.

Hence, *in situ* operation of characterization methods typically used afterward, but also other techniques not applied for thin film analysis can speed up the optimization process and may shed light onto the ALD reaction itself. Note, the self-limiting nature of the ALD half-reactions is beneficial for these kinds of studies, since the surface remains for long time in the same state allowing for long measuring/integration times without altering the surface. Most of the *ex situ* characterization methods used in the ALD community to characterize the deposited thin film or the process can also be employed *in situ* after modification of the ALD reaction chamber.
A summary of selected *in situ* methods and the targeted thin film and reaction analysis is given in Table 2.1.[43-45]

Table 2.1. In situ methods and their targets

Classification	**Method**	**Target**
Gravimetry/Mass	Quartz crystal microbalance to study the mass up-take/loss during half-reactions	• GPC • Conclusion to chemistry • Characteristic times (saturating and purging behavior) • Determination of precursor decomposition and surface etching reaction
Optical	Fourier-transform infrared spectroscopy	Molecular species during half-reactions in gas pahse and on surface
	(Surface-enhanced) Raman	Molecular species on surface
	(Spectroscopic) Ellipsometry	Film thickness evolution and refractive index
	Optical emission spectroscopy	Only for PEALD: species during plasma pulse
X-ray Analysis	Absorption Spectroscopy	Probing the local atomic environment
	Diffraction	Crystallinity and grain size
	Fluoresence	Film composition (and thickness)
	Grazing-incidence small-angle scattering	Surface morphology
	Photoelectron spectroscopy	Surface composition and oxidation state
	Reflectivity	Thickness, roughness, density
Charge/Mass	Quadrupole mass spectrometry	Gas phase molecules
Electron	Reflection high-energy electron diffraction	Growth mode and film thickness
Electrical/thermal	Resistance measurements	Conductivity and growth mode
	Thermopile	Heat, reaction enthalpy

2.1.3.9. Nanostructures (high aspect ratio)

The separated self-limiting gas-solid chemical reactions of ALD feature two important aspects: (1) thickness control in the sub-nm regime and (2) conformal deposition in non-line-of-sight fashion. Hence, ALD is ideally suited to overcoat complexly shaped nano- and microstructures because the gaseous precursor can easily penetrate into complex substrates, and the same film thickness at any position of the sample is deposited. ALD has proven its value in applications of conformal thin film deposition inside complicated geometries and 3D nanostructures, e.g., deep trenches, grooves, narrow pores, and aerogels, etc. All of which are difficult to coat conformally by other deposition techniques such as sputter, pulsed laser deposition, and CVD.

Depending on the template structure, which needs to be coated, ALD can be used in exposure/stop mode operation. In detail, a valve between chamber and vacuum pump is closed immediately before the precursor is pulsed into the chamber. Then the reaction chamber rests in this state, and the precursor molecule can diffuse into the template structure. After a time t, the valve is opened again and the chamber is purged. Note, determining the minimum duration of t—which can span even to a few minutes—is not trivial since several aspects such as sticking probability, temperatures, pressures, precursor doses, and aspect ratio, to name a few of them, influence the time needed to achieve full coverage of the surface.[46]

A plethora of nanostructured templates such as free-standing nanowires and -tubes, porous membranes, 3D printed scaffolds, assembled spheres/blocks, polymeric networks, CNT forests, and even biological substrates, e.g., viruses and butterfly wings, have been coated by ALD for various applications.[29-31, 47] A selection of templates are highlighted in Figure 2.6. Moreover, prominent applications of ALD and nanostructures used therein are summarized in Table 2.2.

In general, ALD on these nanostructured templates can serve several tasks:

(i) Adding a “functional” layer to a non-active template that provides support, e.g., metal electrodes, photoactive layer, magnetic layers.
(ii) Stabilization of underlying substrate, e.g., resistive coating against harsh environments, increase mechanical stability, encapsulation.
(iii) Changing the electrical nature of the surface, e.g., ionic conductivity, capacity enhancement, work function adaptation.
(iv) Spacer layer or sacrificial layer between functional layers of interest.

A conformal coating of individual particles which are assembled on a substrate is hampered by the contact points between the particles but also between particle and substrate. (Miniaturized) Fluidized bed and rotary reactors agitate the particles in such a way that surface reactions all around the particles are achieved during the exposure to the precursor gases.[48] The coated particles can be later assembled to composite materials for application in similar fields as aforementioned, e.g., catalysis, electrode materials, and encapsulation, to name a few of them.

Table 2.2. Application overview of ALD-coated complex nanostructures.

Application	Nanostructured Templates	References
Solar cells	• inorganic nanorod/-wires/-tubes • (inverse) opals • porous membranes (anodic aluminum oxide (AAO), anodized titania)	[49]
Energy Storage (supercaps, batteries, etc.)	• inorganic nanorod/-wires/-tubes • inverse opals • Ni foam, Pt/AAO • carbon nanotubes (CNTs) scaffold, multiwalled CNTs (MWCNTs) sponge, graphene foam & expanded graphite (GF)	[50]
Photocatalyst	• nanorod/-particles/-wires/-tubes • nanosheets, membranes • AAO • mesoporous silica • CNTs • zeolites	[51]
Solid Oxide Fuel Cells	• nanostructured (porous) silicon • AAO • porous solid electrodes (LSC – LaSrCoO, LSCF-GDC – LaSrCoFeO, Ag)	[52, 53]
Gas sensing	• CNTs, CNT foams • polymeric fibers, nanocellulose • AAO • self-assembled porous blockcopolymer • porous Au, Si • inorganic nanorod/-wires • inverse opals	[54]
(Micro)Fluidics	• pores in SiN • nanochannels in Si • AAO • ion track-ecthed polymeric membranes • porous blockcopolymer	[55, 56]
Bio-medical applications	• AAO • nanowires • nanoporous silicon nitride membrane • porous polymer particles • nanocellulose aerogels • porous biotemplates, ie. tobacco mosaic virus and ferritin • 3D-printed scaffolds	[47, 57]

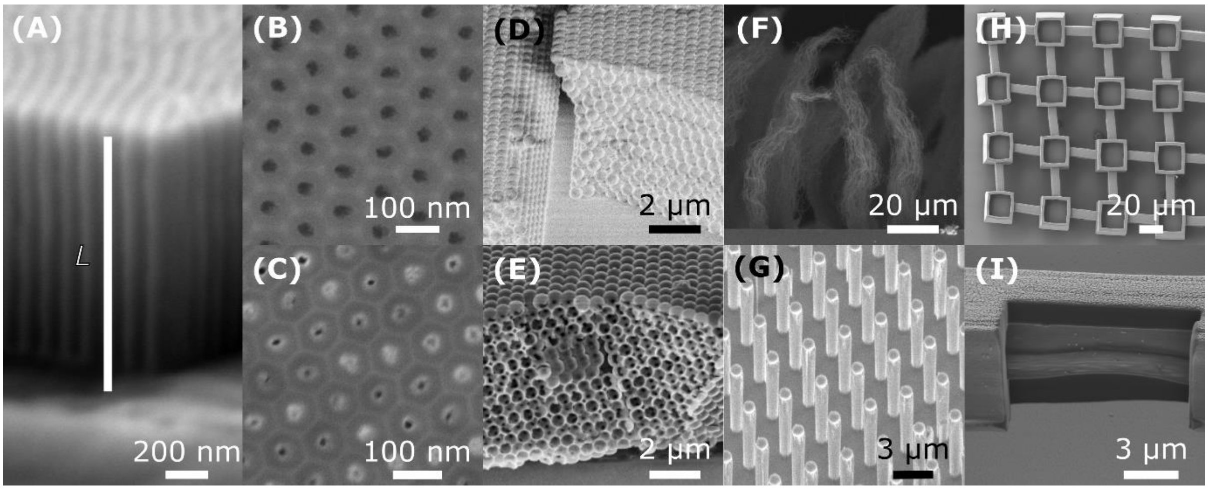

Figure 2.6. Scanning electron microscopy (SEM) images of nanostructures that have been employed as templates for ALD. AAO facilitates the growth of nanotubes by ALD: The length, L, shown in the (A) cross-sectional image along the hole direction; the diameter and the interpore distance of the pore (B) can be controlled by the anodization process; the bright ring inside the pores in (C) are ZnO nanotubes embedded in the AAO membrane after ALD and Ar^+ sputtering removing the interconnecting layer on top. Pores appearing blocked are filled by redeposited material during the sputtering process. (D) Opal template from self-assembled polystyrene beads and (E) inverse opal achieved after ALD and calcination of the opal template. (F) CVD-grown CNTs and (G) nanorods prepared by a combination of lithography and reactive ion etching have been employed as templates for ALD. SEM images of (H) a 3D-printed scaffold structure utilized for cell culturing after ALD coating and (I) a cross-sectional image after focused ion beam cutting of the connecting tunnel.

2.1.4. Summary and future directions

As discussed and shown above, ALD is a versatile tool that allows for the deposition of thin films of a plethora of materials, e.g., metals, oxides, nitrides, ternary ones, etc., with sub-nm precision even on complex nanostructures.

The conformality is an ALD-inherent property which is usually treated as an advantage of ALD. However, in industrial applications deposition on specified areas and no growth on others would ease the processing much because complex further lithography-(deposition-) etching steps can be saved. Since ALD bases on chemical (gas-solid surface) reactions, one could locally tailor or can employ the given surface chemistry in a sense to enable or to inhibit the growth.[58] Such an AS-ALD could be achieved by either selective precursor/reactant adsorption on the growth area or surface deactivation to define the non-growth area. A prime example of selective precursor adsorption is the different chemical nature of OH- and H-terminated surfaces, i.e., oxides can be easily deposited at hydroxyl-groups but hardly at H-terminated surface sites. On the other hand, self-assembled monolayers or small inhibitor molecules, such as acetylacetone (Hacac), could be used to deactivate surface sites for reaction with the precursor. However, none of these processes could fully suppress the growth in the non-growth areas leading to a reduced selectivity. Hence, correction steps are introduced into the AS-ALD cycle, similar to the supercycle ALD approach mentioned before. For instance, repeated functionalization of the non-growth area or a (selective) etching step which removes deposited material in the non-growth area are experimental pathways to tackle the selectivity problem.

Especially, the combination of AS-ALD with atomic layer etching — the counterpart of atomic layer deposition — is a promising approach. Similar to ALD, an atomic layer etching process (abbreviated in literature with ALE but not to be confused with atomic layer epitaxy) consists of (at least) two self-limiting steps. The first step modifies the top surface layer in a way that the surface binding energy is weakened. In the 2nd half cycle — the etching step — the topmost layer is removed. Hence, a layer-by-layer etching is achieved. The etch rate per cycle is constant, and by setting the cycle number, the etched film thickness is defined. The lowered binding energy in the 1st step can be overcome by either using a plasma (ion bombardment) or a thermal chemical reaction in the 2nd step to remove the topmost layer. ALE has been invented in the late 80s but with further pushing Moore's law an upswing has been taken in the last decade.[59] A prime example of ALE is the etching of Si: Therein, the silicon surface is exposed to a chlorine species — either thermally or by plasma chlorination — forming Si-Cl bonds at the top. In the etching step, energy in form of an Ar plasma is transferred to the substrate to form gaseous $SiCl_2$ with an evaporation energy of ~2.3 eV which is significantly lower than the binding energy of 4.7 eV for pure Si. The plasma energy has to be chosen in such a way that the ion bombardment does not harm the bulk silicon but only the chlorinated surface. Hence, the etching stops once all chlorine species have been removed. Since a plasma etching step is used, the etching behavior is directionally similar to reactive ion etching. Most recently, significant progress in the development of thermal ALE processes has been achieved by introducing the isotropic, conformal behavior well-known form ALD by employing thermally driven chemical reactions in the 2nd step. Note, other energy sources to remove the modified surface layers are conceivable as well, such as photons and temperature or a combination of both as well as neutral beams of Ne.[5, 60] Up to now, a variety of materials ranging from semiconductors, such as Si or GaAs, to metals, nitrides, and oxides can be etched by ALE. A database for ALE processes is available on the atomic limits blog, similar to the ALD database.①

All the processes mentioned above target the deposition (and etching) of inorganic materials. However, the general principle of ALD based on separated self-limiting reaction steps can also be used to deposit organic thin films or even hybrid organic/inorganic structures in combination with ALD. These processes are then called MLD.[61, 62] Compared to ALD, MLD is much younger and dates back to the early 1990s. In combination with ALD in the 2000s organic/inorganic hybrid materials—metal centers covalently bonded to organic molecules—could be prepared for the first time with versatile and tunable material properties. MLD allows for the deposition of polymeric thin films, such as amides, imides, ureas, urethanes, and esters, etc.

By its origin and definition, ALD utilizes gaseous precursor molecules to conduct the self-limiting reaction. However, it has been shown that ALD can be conducted also from liquid precursors in fluidic reactors, so-called liquid- or solvent-based ALD (lALD/sALD).[63].

---

① https://www.atomiclimits.com/aledatabase/ [accessed, 02.03.2022]

Herein, the same pre-requisites as for ALD from the gas phase have been defined, namely self-terminating, sequential surface reactions with a defined growth per cycle. On the one hand, lALD widens the field of applicable precursors and materials. Specifically, precursors which have no or only very few vapor pressures or are thermally not stable could be potentially employed to design lALD reactions. On the other hand, the setups as well as the purging step are more complex compared to the ALD based on gaseous precursors since the reaction chamber has to be rinsed with a solvent. As a consequence, the duration of the cycle times as well as consumptions costs for the purge medium, if not circulated, are higher than for conventional ALD but with the perspective of the utilization of cheaper precursors.

In summary, ALD and neighboring techniques, namely AS-ALD, MLD, ALE, and lALD, will be essential to push the limits in downscaling semiconductor devices further, to develop novel process schemes, to create and synthesize materials with tailor-made properties, and to open up new applications in various, such as ‘green’ energy, semiconductors, biology & medicine, optics, and sensors, to name a few of them.

2.2. ALD and devices

2.2.1. Memristor①

Data storage has always been a hotspot with the development of the digital age and predominantly affects the future direction of data analysis and security. Recent memories, including static random-access memory (SRAM), dynamic random-access memory (DRAM), and flash memory, amalgamate their strengths and weaknesses, thereby influencing their overall performance and utility.[64] SRAM is a fast-speed memory but is more expensive than the other.[65] It is a volatile memory, meaning that this type of memory should be refreshed constantly to maintain information storage, leading to undesirable energy consumption.[66] DRAM exhibits higher capacity and density.[67] However, DRAM is also a volatile memory like SRAM; hence, it permanently needs electrical power to store information. For flash memory, a typical nonvolatile memory, the stored data are retained even after removing the power supply.[68] Due to its affordability and high density, flash memory is now widely used mainly for embedded devices. However, it suffers from lower operation speed (write/erase time: 1 ms/0.1 ms) and high operation voltage (~10 V).[69, 70] In contrast, resistive random-access memory (RRAM) offers distinct advantages over existing technologies. With its nonvolatility, high speed (~ns level fast switching rate), low power consumption (~pJ), scalability, endurance, and compatibility with complementary metal-oxide-semiconductor (CMOS) technology,[69, 71, 72] RRAM facilitates a wide range of applications. These include consumer electronics,[73, 74] Internet of Things (IoT) devices,[75, 76] artificial intelligence,[77] in-memory computing,[78-80] and hardware security.[81, 82] For example, RRAM arrays can function as synaptic weights in neuromorphic computing architectures,

---

① This section comes from part of the published co-authored review manuscript:

Hao, C.; **Peng, J.**; Zierold, R.; Blick, R. H. Atomic layer deposition films for resistive random-access memories. *Advanced Materials Technologies* 2024, 2301762. *Copyright © 2024 The Authors. Advanced Materials Technologies published by Wiley-VCH GmbH.*

simulating synaptic behavior in the human brain. This positions RRAM as a promising candidate for developing energy-efficient hardware accelerators for artificial intelligence and machine learning tasks, enhancing the speed and efficiency of processing large datasets.[83, 84] Moreover, RRAM technology enables the construction of three-dimensional (3D) cross-point memory arrays, where memory cells are stacked vertically. This configuration enhances memory density and scalability compared to traditional planar memory architectures, making it suitable for applications requiring substantial memory capacities, such as data centers and high-performance computing systems.[85-87] Benefiting from RRAM's unique attributes, numerous cutting-edge applications are poised to achieve elevated levels of performance, efficiency, reliability, and security across various fields.

The phenomenon of a sudden resistance change under an applied voltage on metal oxides was already found in the 1960s.[88-90] It is a form of memory achieving resistance switching (RS) performance between a high-resistance state (HRS) and a low-resistance state (LRS) based on an electrically stimulated change, usually applied by two-terminal devices: metal–insulator–metal (MIM).[91] The switching behavior is not only relevant to the material type but also to the electrical operation as well as the type of electrode, which could determine the mechanism of the resistance change to either an electrochemical mechanism (ECM), valence change mechanism (VCM), thermochemical memory (TCM), or a mixture mechanism.[92] In ECM-based resistive switching, the resistance change is induced by the migration of metallic ions (e.g., Ag or Cu) within the solid electrolyte material. Application of a voltage bias causes the migration of ions, leading to the formation and dissolution of conductive filaments. These filaments alter the resistance state of the material, which usually occurs in chalcogenides, SiO2, amorphous materials, etc. In contrast, the counter electrode in ECM is typically inert, such as Pt, Au, W, etc.[93-95] VCM is based on the change in the oxidation state within the resistive switching material. When a voltage is applied, oxygen vacancies can migrate, leading to a change in the valence state of the material, consequently, a change in resistance. Oxide-based resistive switching devices often exhibit valence change behavior, usually occurring in metallic oxides, such as HfO_2, Al_2O_3, Ta_2O_5, and TiO_2.[96-99] It has also been observed on two-dimensional (2D) materials such as graphene oxide, degraded black phosphorus, and MoS2.[100-104] TCM involves resistive switching induced by temperature changes. Heating or cooling the resistive switching material can cause reversible changes in its structural or chemical properties, leading to variations in resistance.

Both unipolar and bipolar switching behaviors are important characteristics in resistive switching devices, and the specific behavior can depend on the materials used, device structures, and fabrication techniques. Bipolar switching is indeed common in both ECM and VCM devices. In ECM, conductive filaments can form or dissolve under both positive and negative voltage biases, influencing the bipolar switching behavior. Similarly, in VCM, changes in the oxidation state often occur in response to both polarities. Unipolar switching may be associated with TCM devices in some cases, such as TiO_2 and NiO.[105, 106] The reversible changes induced by temperature variations could lead to a more unipolar switching behavior, with alterations occurring primarily in one direction. The understanding of these mechanisms is crucial for the development of next-generation non-volatile memory technologies. Researchers and engineers explore these mechanisms to design memory devices with improved performance, energy efficiency, and reliability.[71, 91, 92, 107-111]

RRAM seamlessly integrates with CMOS technology, the standard fabrication process utilized in semiconductor manufacturing. This compatibility not only simplifies the integration of RRAM into existing chip designs and facilitates cost-effective production of memory devices but also enables the utilization of various fabrication methods employed in integrated circuits for RRAM production. Several popular film deposition methods have already been applied to fabricate RRAM. Firstly, normal chemical vapor deposition (CVD)[112, 113] offers good conformality and can coat a wide range of substrate geometries, allowing the deposition of various materials, including oxides, nitrides, and metals, thus providing versatility in memory device fabrication. However, CVD typically requires high temperatures, which limit its compatibility with temperature-sensitive substrates or devices. Additionally, its control over film thickness and composition is limited. Secondly, physical vapor deposition (PVD) techniques, such as sputtering, evaporation, and pulsed laser deposition, provide good adhesion and uniformity in thin film deposition. They can deposit metals and other materials with high purity, making them suitable for certain memory device applications with relatively simple structures. However, PVD suffers limitations in uniformly depositing thin films on complex structures, particularly in high-aspect-ratio features or recessed regions. Spin coating is also a popular, simple, and cost-effective method for depositing uniform thin films. Although it is suitable for small-scale or research-oriented memory device fabrication processes, it may not offer precise control over film thickness or composition. In addition, electrochemical deposition is also a practical method for fabricating RRAM, offering conformal coatings on complex structures and effective filling of trenches, vias, and other features. It is compatible with a wide range of materials and can achieve high deposition rates. However, it faces challenges in achieving precise control over film properties, such as thickness and composition, necessitating further process optimization.

As 2D or 3D integration memory arrays with significantly scaled feature sizes continue to downscale,[114, 115] the allowed thickness for the deposition of multiple metals and oxide layers in bit-line holes or trenches is only a few nanometers, as shown in the structure in Figure 2.7.[116] When compared to other deposition methods for fabricating RRAM, atomic layer deposition (ALD) [34, 39, 41, 46, 117] offers several distinct advantages, making it a compelling choice. (1) ALD provides exceptional conformality, depositing thin films with atomic-scale precision and uniformity even on complex and high aspect ratio structures. This conformal nature is critical for RRAM devices, which often feature intricate architectures and require uniform coatings on both planar and 3D surfaces. (2) ALD offers precise control over film thickness at the atomic level due to its self-limiting surface reactions. This level of control is also crucial for RRAM devices, where the thickness of the insulating or resistive layers directly impacts device performance, such as switching speed and endurance. (3) ALD offers excellent uniformity and reproducibility in thin film deposition, ensuring consistent device characteristics across wafers and fabrication runs. This reliability is essential for RRAM manufacturing, where device-to-device variations can affect yield and performance metrics. (4) ALD can be performed at relatively low temperatures (usually <400 °C) compared to some other deposition methods, making it compatible with temperature-sensitive substrates and allowing for integration with CMOS processes, which facilitates the integration of RRAM with existing semiconductor technologies. (5) ALD is compatible with a wide range of materials, including oxides, nitrides, metals, and other compounds. This versatility allows for the deposition of various layers in RRAM devices, such as switching materials, electrodes, and insulating layers, enabling the optimization of device performance and reliability. Overall, ALD's combination of conformal coating, precise thickness control, uniformity, reproducibility, low-temperature processing, and material versatility makes it a superior option for fabricating RRAM devices compared to other deposition methods. These advantages contribute to improved device performance, reliability, and manufacturability, positioning ALD as a high-potential candidate in the advancement of RRAM and other emerging memory technologies.

In addition, while ensuring the above advantages, the ALD family offers various ALD forms, including thermal ALD, plasma-enhanced ALD (PEALD), temporal ALD, and spatial ALD,[34, 39, 41, 46, 117] each providing unique contributions to the fabrication process. Thermal ALD provides precise control over film thickness and excellent conformality, making it suitable for depositing critical layers in RRAM devices, such as insulating oxides and switching materials. Compared to thermal ALD, PEALD utilizes plasma to enhance chemical reactions, leading to improved film quality, lower defect density, and enhanced densification. It offers a wider range of material options and can deposit critical layers with improved performance and reliability. Temporal ALD involves pulsing different precursors sequentially to deposit multi-component or multi-layer films, enabling precise control over film composition and facilitating the deposition of complex materials with tailored properties for RRAM applications. In contract, spatial ALD utilizes multiple precursor sources and separate gas phase reactions to deposit thin films spatially on substrates, enabling high-throughput and large-area deposition, suitable for scaling up RRAM fabrication for mass production. These different types of ALD techniques offer distinct advantages in RRAM fabrication, ranging from precise thickness control and excellent conformality to enhanced film quality, material versatility, and scalability. By leveraging the strengths of these ALD techniques, manufacturers can develop advanced RRAM devices with improved performance, reliability, and scalability, driving innovation in memory technologies.

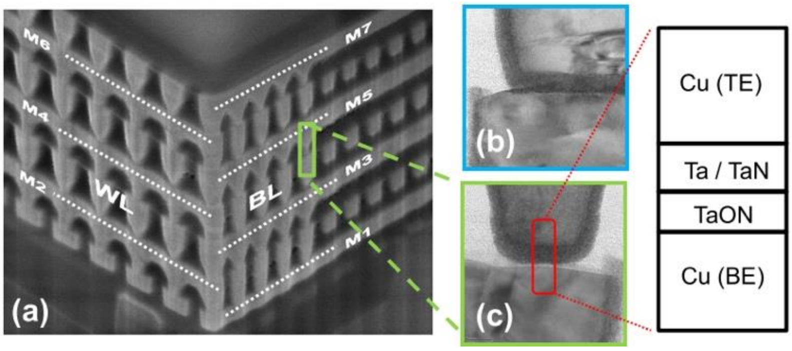

Figure 2.7. (a) Scanning electron microscopy (SEM) image of 28 nm TaON-based cross-point 3D Via RRAM. (b, c) Transmission electron microscopy (TEM) image of an RRAM cell with a 30 nm x 30 nm cell size. Reproduced with permission from ref [116]. *Copyright © 2013, IEEE*.

2.2.2. Photonic crystals

2.2.2.1. Basic for the formation of photonics

PhCs are materials in which the dielectric function is periodic in 1D, 2D, or 3D as shown in Figure 2.8. The propagation properties of photons in these periodic media are analogous to the behavior of electrons in crystalline solids. The periodicity leads to the formation of photonic bandgaps, where certain wavelengths of light are prohibited from propagating through the material.

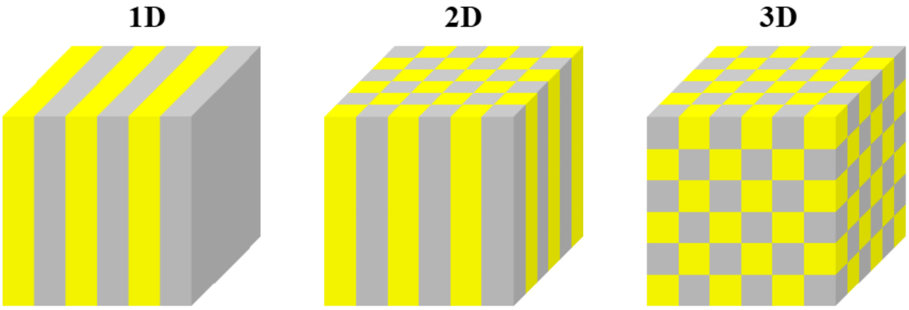

Figure 2.8. Simple example of 1D, 2D and 3D PhCs. The different colors present materials with different dielectric constants.

The interaction of light with materials as well as the propagation of light within the materials, are described by the macroscopic Maxwell's equations in SI unit:[118]

$$\begin{aligned} \nabla \cdot \boldsymbol{B} &= 0 \qquad & \nabla \times \boldsymbol{E} + \frac{\partial \boldsymbol{B}}{\partial t} &= 0 \\ \nabla \cdot \boldsymbol{D} &= \rho \qquad & \nabla \times \boldsymbol{H} - \frac{\partial \boldsymbol{D}}{\partial t} &= \boldsymbol{J} \end{aligned} \tag{2.1}$$

where $\boldsymbol{E}$ and $\boldsymbol{H}$ are the macroscopic electric and magnetic fields, $\boldsymbol{D}$ and $\boldsymbol{B}$ are the displacement and the magnetic induction field, and ρ and $\boldsymbol{J}$ are the free charge and current densities. This approach assumes that propagation within the mixed dielectric medium systems, i.e., PhCs, is as a function of the Cartesian position vector r, in which the structure does not vary with time, and there are no free charges or currents ($\rho = 0, \boldsymbol{J} = 0$). In addition, assuming that the studied PhCs are in the linear regime, that means the material is macroscopic and isotropic, and ignoring any explicit frequency dependence of the dielectric constant, without considering any nonlinear optical effects, the constitutive material equations to:[119]

$$\begin{aligned} \boldsymbol{D} &= \varepsilon_0 \varepsilon(\boldsymbol{r}) \boldsymbol{E}(\boldsymbol{r}) \\ \boldsymbol{B} &= \mu_0 \mu(\boldsymbol{r}) \boldsymbol{H}(\boldsymbol{r}) \end{aligned} \tag{2.2}$$

where ε_0 is the vacuum permittivity; $\varepsilon(\boldsymbol{r})$ is a scalar dielectric function known as relative permittivity, μ_0 and $\mu(\boldsymbol{r})$ are the vacuum permeability and the relative magnetic permeability. For most dielectric materials, $\mu(\boldsymbol{r})$ is close to 1. And in general, from Snell's law,[120] $\varepsilon = n^2$, where n is the refractive index. Then the Maxwell equations become:

$$\begin{aligned} \nabla \cdot \boldsymbol{H}(\boldsymbol{r}, t) &= 0 \qquad & \nabla \times \boldsymbol{E}(\boldsymbol{r}, t) + \mu_0 \frac{\partial \boldsymbol{H}(\boldsymbol{r}, t)}{\partial t} &= 0 \\ \nabla \cdot [\varepsilon(\boldsymbol{r})] \boldsymbol{E}(\boldsymbol{r}, t) &= \rho \qquad & \nabla \times \boldsymbol{H}(\boldsymbol{r}, t) - \varepsilon_0 \varepsilon(\boldsymbol{r}) \frac{\partial \boldsymbol{E}(\boldsymbol{r}, t)}{\partial t} &= \boldsymbol{J} \end{aligned} \tag{2.3}$$

Magnetic and electric fields are a function of both time and space and can be write as:

$$\begin{aligned} \boldsymbol{H}(\boldsymbol{r},t) &= \boldsymbol{H}(\boldsymbol{r})e^{-i\omega t} \\ \boldsymbol{E}(\boldsymbol{r},t) &= \boldsymbol{E}(\boldsymbol{r})e^{-i\omega t} \end{aligned} \tag{2.4}$$

Substitute equation (2.4) into equation (2.3), two curl equations related to $\boldsymbol{E}(\boldsymbol{r})$ and $\boldsymbol{H}(\boldsymbol{r})$ are:

$$\begin{aligned} \nabla \times \boldsymbol{E}(\boldsymbol{r}) - i\omega\mu_0\boldsymbol{H}(\boldsymbol{r}) &= 0 \\ \nabla \times \boldsymbol{H}(\boldsymbol{r}) + i\omega\varepsilon_0\varepsilon(\boldsymbol{r})\boldsymbol{E}(\boldsymbol{r}) &= \boldsymbol{J} \end{aligned} \tag{2.5}$$

where ω is the frequency.[118, 121] These two equations can be decoupled to formulate an equation entirely in $\boldsymbol{H}(\boldsymbol{r})$, giving a master equation describing the propagation of the magnetic field ($\boldsymbol{H}(\boldsymbol{r})$) of a photon:

$$\nabla \times \left(\frac{1}{\varepsilon(\boldsymbol{r})}\nabla \times \boldsymbol{H}(\boldsymbol{r})\right) = \left(\frac{\omega}{c}\right)^2 \boldsymbol{H}(\boldsymbol{r}) \tag{2.6}$$

In this equation, vacuum light speed $c = 1/\sqrt{\varepsilon_0\mu_0}$. [119]

2.2.2.2. Photonic band diagram

According to the periodicity of PhC, $\varepsilon(\boldsymbol{r})$ can be written as

$$\varepsilon(\boldsymbol{r}) = \varepsilon(\boldsymbol{r} + \boldsymbol{R}) \tag{2.7}$$

$\boldsymbol{R}$ is a lattice-translation vector, equal to $l_1\boldsymbol{a_1} + l_2\boldsymbol{a_2} + l_3\boldsymbol{a_3}$, where l_1, l_2, and l_3 are integers, and $\boldsymbol{a_1}$, $\boldsymbol{a_2}$, and $\boldsymbol{a_3}$ are the primitive lattice vectors.[121, 122] This periodicity requires the solution of equation (2.6) to satisfy the Floquet–Bloch theory.[123, 124] According to this theory, the solutions to the equations for periodic media take the form of plane waves modulated by a periodic function with the same periodicity as the lattice. This can be expressed as:

$$\boldsymbol{H}(\boldsymbol{r}) = h_{\boldsymbol{k}}(\boldsymbol{r})e^{i\boldsymbol{kr}} \tag{2.8}$$

where k is the wave vector, which is contained within the first Brillouin zone, a region of reciprocal space that is closer to the origin than to any other reciprocal lattice point. The function $h_{\boldsymbol{k}}(\boldsymbol{r})$ is the periodic function of position, often referred to as the Bloch function, which reflects the periodicity of the underlying lattice.

$$h_{\boldsymbol{k}}(\boldsymbol{r}) = h_{\boldsymbol{k}}(\boldsymbol{r} + \boldsymbol{R}) \tag{2.9}$$

Solving the master equation (equation (2.6)) can be accomplished by various computational methods, with the plane-wave expansion method being the most commonly used. This can reduce the master equation to a matrix equation, with eigenvalues in the form $\omega_n(\boldsymbol{k})$ with n = 1, 2, …, corresponding to the photonic bands. This band structure illustrates all the frequencies in which the optical modes are allowed for a given wave vector $\boldsymbol{k}$. A photonic bandgap (PBG) is defined as a range of ω for which no propagating eigensolutions exist for any $\boldsymbol{k}$ within the crystal. This means that within the PBG, light cannot propagate through the material, while it can propagate at frequencies above and below the gap. Opal and inverse opal are both typical photonic crystal structures. Examples of their structures and corresponding photonic band diagrams characteristics are shown in Figure 2.9.

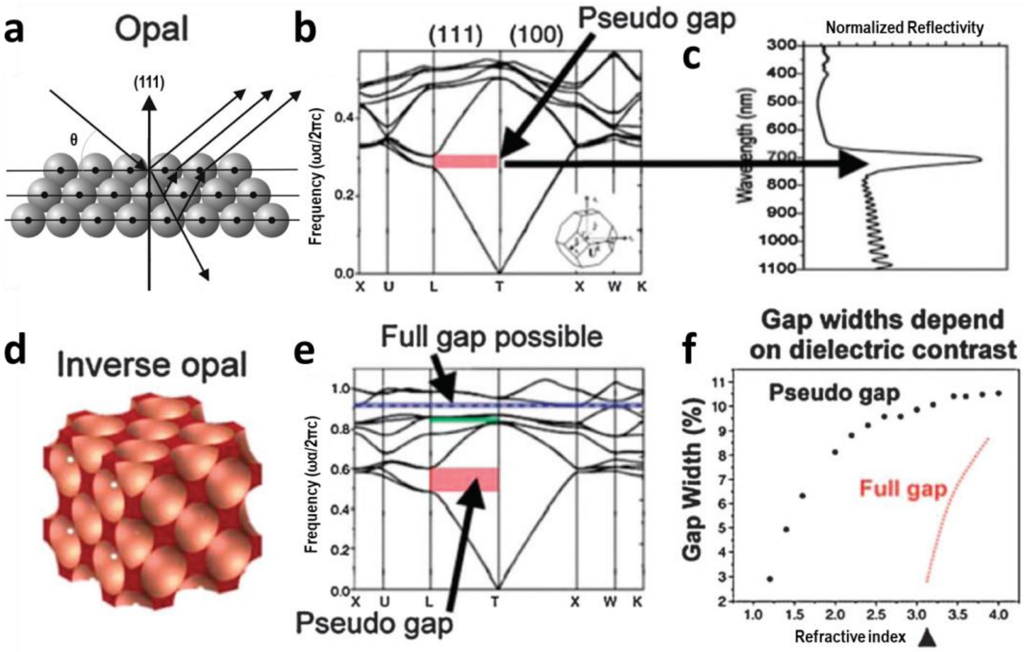

Figure 2.9. Optical bandgap for opal and inverse opal. (a) Opal structure. (b) Photonic bandstructure calculation for a silica opal. (c) Reflectance measurement along the $L–\Gamma$ (111) direction, as a proof of the PBG. (d) Inverse opal structure. (e) photonic bandstructure calculation for a silicon inverse opal. (f) Gap widths plotted over index of refraction. The stop band in (b) and (e) is marked in red. The complete photonic band gap in (e) is marked in blue. Adapted from ref [122, 125]. *Copyright © 2012 Wiley-VCH Verlag GmbH & Co. KGaA.*

2.2.2.3. Bragg's law in photonic structures

A Bragg stack, also known a Bragg reflector or Bragg mirror, typically comprises alternating layers of materials with high and low refractive indices. The diffraction behavior of periodic arrays, e.g., a Bragg stack, can be accurately described by the Bragg-Snell law, which applies to normal incidence and non-absorbing materials.[126]

$$m\lambda = 2(n_l d_l + n_h d_h), \tag{2.10}$$

where m is the diffraction order, n_l and n_h are the refractive indices of the low- and high-refractive-index materials, and d_l and d_h are the respective thicknesses. The reflectivity R of the Bragg stack is influenced by the refractive index contrast and the number of bilayers (N) that make up the stack, which is

$$R = \left[\frac{n_0 - n_s (n_l/d_h)^{2N}}{n_0 + n_s (n_l/d_h)^{2N}}\right]^2, \tag{2.11}$$

where n_0 and n_s are the refractive indices of the surrounding medium and the substrate, respectively. If we assume the central wavelength of the photonic band is λ_0, the bandwidth $\Delta\lambda_0$ of the photonic stop band can also be calculated:

$$\Delta\lambda_0 = \frac{4\lambda_0}{\pi}\arcsin\left(\frac{n_h - d_l}{n_h + d_l}\right), \tag{2.12}$$

Similar analyses can be extended to more complex systems, such as 3D colloidal PhCs. Light of a specific wavelength is diffracted according to Bragg's law:

$$m\lambda = 2nd\sin\theta, \tag{2.13}$$

where m, λ, n, d, and θ are the order of diffraction, the wavelength of incident light, the mean refractive index of the system composed of colloids and voids, the spacing between the planes in lattice, and the glancing angle between the incident light and diffraction crystal planes, respectively. In practical applications, the colloidal spheres are often embedded in matrix materials such as solvents and polymers. Consequently, by taking into account the effective refractive index of the system, Bragg's law can be approximately expressed as below:

$$m\lambda = \sqrt{\frac{8}{3}} D\left(\sum_i n_i^2 V_i - \sin^2\phi\right)^{1/2}, \tag{2.14}$$

where D is the center-to-center distance between nearest spheres, n_i and V_i correspond to the refractive index and volume fraction of each component, respectively. And ϕ denotes the angle between the incident light and the sample normal.

2.2.3. Position-sensitive detectors

2.2.3.1. State of the art

A position-sensitive detector (PSD) is traditionally defined as a photodetector used to measure the position of a light spot in one or two dimensions. Based on their working principles, PSDs can be categorized into two types: isotropic and discrete. An isotropic PSD is essentially a photodiode that operates on the lateral photoelectric effect, providing continuous position data in either 1D or 2D forms, as illustrated in Figure 2.10a. In contrast, a discrete PSD is a segmented photodetector that determines the position using data from multiple pixels. Examples of discrete PSDs include dual-segment photodiode, four-quadrant photodiode PSDs (Figure 2.10b), and CCD- or CMOS-based PSDs (Figure 2.10c (iii)), which measure light intensity across several or even numerous spatial locations (pixels). Based on this pixel data, the position of the light spot can be calculated. For infrared detection, independent thermopile elements can also serve as pixels in this type of PSD (Figure 2.10c (iv)).

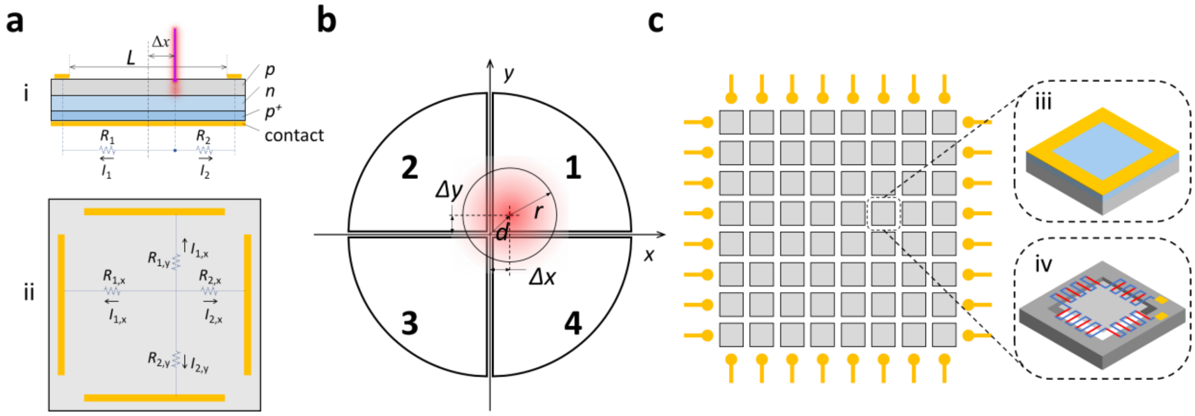

Figure. 2.10. Existing PSD forms. (a) Isotropic PSD based on lateral photoelectric effect. Inset (i) the structure of 1D PSD. The red line in the top panel is the incident laser. Inset (ii) Top view of a 2D PSD. The cross-section is the same as the structure in inset (i). (b) Quadrant photodiode PSD. The red dot represents the location of the incident laser, and the red area diffused from it represents the range of the laser intensity. This intensity usually has the characteristics of a Gaussian distribution. (c) Discrete PSD based on CMOS technology. Inset (iii) Open Electrode CCD single pixel for CCD chip. Inset (iv) Thermopile pixel for infrared sensor chip.

(1) Isotropic PSD

The active region of a 1D PSD based on the lateral photoelectric effect comprises a photodiode with two contacts for extracting different photocurrents and a common cathode (Figure 2.10a (i)). Lateral effect PSDs are typically fabricated as p-n or Schottky junctions. For p-n junction PSDs, the junction is formed by diffusing or implanting p-type dopants into an n-type substrate, or vice versa. In the case of a Schottky junction, a thin layer of metal is deposited on the substrate to create the rectifying contacts. The carriers generated by incident light diffuse through the bulk resistance, are separated by the junction field, and are distributed between the two contacts in proportion to the resistance.[127] This kind of PSD can determine the incident light position but is relatively insensitive to the shape or size of the light spot. The total current generated by the PSD is equivalent to that of a photodiode and can be expressed as:[128]

$$I_P = I_L\left(e^{qV/kT} - 1\right) - I_{op}, \tag{2.15}$$

where q, V, k, and T are the electrical charge, the bias voltage, Boltzmann’s constant, temperature in degrees Kelvin, respectively. In this equation,

$$I_L = A \cdot q\sqrt{\frac{D_p}{\tau_p}\frac{n_i^2}{N_D}} + \frac{qn_iW}{\tau_e}, \tag{2.16}$$

$$I_{op} = qAg_{op}\left(L_p + L_n + W\right), \tag{2.17}$$

where A is the cross-sectional area of the device; τ_p and τ_e are the recombination lifetimes for holes and electrons; D_p, N_D, n_i, and W are the diffusion coefficient for holes, the doping concentration, the intrinsic carrier concentration, and the depletion width, respectively; g_{op} is the generation rate per volume and time (EHP/cm^{-3}·s); L_p and L_n are the lengths of the *n*- and *p*-type materials within a diffusion length from the depletion region.[129]

If the resistivity of the top p-layer is assumed to be perfectly uniform, the two equivalent resistances R_1 and R_2 will be directly proportional to the distances from the two contacts. Consequently, the ratio of I_1 and I_2 accurately indicates the location x_c of the photogenerated current distribution. Therefore, the centroid location, also the light spot position x_c, can be defined as the total lateral current distribution over the length L of the PSD.[130]

$$x_c = \frac{\int_{-L/2}^{L/2} x \cdot I_{psd}(x)dx}{\int_{-L/2}^{L/2} I_{psd}(x)dx}, \tag{2.18}$$

where I_{psd} is the lateral current distribution and *x* the position on the sensor. One can get a ratio,

$$\frac{I_1}{I_2} = \frac{R_2}{R_1} = \frac{L/2 - x_c}{L/2 + x_c}. \tag{2.19}$$

Therefore, the light spot position is

$$x_c = \frac{L}{2}\frac{(I_2 - I_1)}{I_1 + I_2}, \tag{2.20}$$

whose value ranges from – to + half the active length with the center defined as the zero position.

To measure the position of a light spot in two dimensions, the 1D detection area can be expanded to 2D by adding two additional contacts, allowing the generated photocurrent to be distributed among the four contacts. Figure 2.10a (ii) presents a schematic diagram of a 2D PSD along with a simplified equivalent circuit diagram, where the top resistive layer is modeled using four separate resistors. The determination of the x and y position components follows the similar principle (equation (2.20)) and can be expressed as:

$$\begin{cases} x = \frac{L_x}{2}\frac{(I_{2x}-I_{1x})}{I_{1x}+I_{2x}} \\ y = \frac{L_y}{2}\frac{(I_{2y}-I_{1y})}{I_{1y}+I_{2y}}, \end{cases} \tag{2.21}$$

where L_x and L_y are the lengths of the PSD in the x and y directions and I_{1x}, I_{2x}, I_{1y} and I_{2y} are the currents measured from each contact.

(2) Discrete PSD

A quadrant photodetector is a widely used discrete PSD composed of four single sub-photodetectors arranged in quadrants on the sensing surface, primarily used for tracking incident low power laser beams.[131] When a laser spot illuminates the quadrant photodetector, each sensor element provides an analog signal proportional to the optical power it receives. The principle of this PSD is illustrated in Figure 2.10b, where four regions correspond to each sub-photodetector (i = 1, 2, 3, 4), and an incident laser spot is depicted as a circle of radius r. The spot center is located at a distance d from the sensor center. In this scenario, each sub-photodetector captures a portion of the total energy incident on the device. The power density at each point on the sensor depends on the profile and position of the laser spot.[132, 133] Assuming an ideal circular Gaussian spot, the incident beam can be mathematically expressed as follows:

$$p(d) = \frac{2P_{\text{beam}}}{\pi r} e^{-2d^2/r^2}, \tag{2.22}$$

where $p(d)$ is the density of incident power at distance d from the spot center, P_{beam} is total incident power, and r is the spot radius, defined as the distance from the spot center, from where the power density downfalls by a factor of $1/e^2$. With this configuration, the power received by each sub-photodetector (i) can be computed as:

$$P_i = \frac{2P_{\text{beam}}}{\pi r} \int_{S_i} e^{-2d^2/r^2}\, dS_i, \tag{2.23}$$

Considering that in Figure 2.10b the distance d follows $d^2 = x^2 + y^2$, the solution for the sub-photodetector 1 can be:

$$P_1 = \frac{2P_{\text{beam}}}{\pi r} \int_{x=-\Delta x}^{\infty} \int_{y=-\Delta y}^{\infty} e^{-2\frac{x^2+y^2}{r^2}}\, dx \cdot dy, \tag{2.24}$$

Simplify and extend to all sub-photodetector, we have:

$$\begin{cases} P_1 = \frac{P_{\text{beam}}}{4}\left[1 + erf\left(\Delta x \frac{\sqrt{2}}{r}\right)\right]\left[1 + erf\left(\Delta y \frac{\sqrt{2}}{r}\right)\right] \\ P_2 = \frac{P_{\text{beam}}}{4}\left[1 - erf\left(\Delta x \frac{\sqrt{2}}{r}\right)\right]\left[1 + erf\left(\Delta y \frac{\sqrt{2}}{r}\right)\right] \\ P_3 = \frac{P_{\text{beam}}}{4}\left[1 + erf\left(\Delta x \frac{\sqrt{2}}{r}\right)\right]\left[1 - erf\left(\Delta y \frac{\sqrt{2}}{r}\right)\right], \\ P_4 = \frac{P_{\text{beam}}}{4}\left[1 - erf\left(\Delta x \frac{\sqrt{2}}{r}\right)\right]\left[1 - erf\left(\Delta y \frac{\sqrt{2}}{r}\right)\right] \end{cases} \tag{2.25}$$

When the spot center is perfectly aligned with the quadrant photodetector center, each sub-photodetector receives 1/4 of the total incident power over the sensor. However, if the spot moves, the power received by each element varies, and the displacement can be deduced from:

$$\begin{cases} \Delta x = \frac{r}{\sqrt{2}} erf^{-1}\left[\frac{(P_1+P_4)-(P_2+P_3)}{P_{\text{beam}}}\right] \\ \Delta y = \frac{r}{\sqrt{2}} erf^{-1}\left[\frac{(P_1+P_2)-(P_3+P_4)}{P_{\text{beam}}}\right], \end{cases} \tag{2.26}$$

Usually, the received power is presented by photocurrent using the below equation:[131]

$$I = k \iint_{\Sigma} P_{\text{beam,G}}\, dS, \tag{2.27}$$

where I is the output current signal from each quadrant, $P_{\text{beam,G}}$ is the spot average illumination intension, and k is the photoelectron conversion efficiency of the detector.

In addition to quadrant photodetectors, standard pixel detectors can also be employed for position determination. The most common types include image sensors such as CCD, CMOS, and thermopile infrared arrays. These sensors are divided into multiple pixels, with the position of the light being determined by comparing the signals from all the pixels. The advantages of using pixel detectors include easier removal of stray light and the ability to measure multiple light sources simultaneously. However, these detectors also come with disadvantages, such as more complex readout electronics and the necessity for image processing to accurately determine the position of the light source.

2.2.3.2. Interfaces and thermal conduction in ALD films

Heat transfer is the transfer of thermal energy due to a temperature difference in space. Whenever there is a temperature difference in or between media, heat transfer will occur. Generally, it takes three forms: heat conduction in the medium; heat convection between the surface and the flowing fluid; and heat radiation, which occurs on all surfaces. In the case of a 1D steady-state, the heat conduction can be described by Fourier's law,

$$q_x = -kA\frac{dT}{dx}, \tag{2.28}$$

where the heat flow, q_x (W), is the exchange of thermal energy between connected solids, which is a constant in steady-state. Furthermore, k, A, and $\frac{dT}{dx}$ are the thermal conductivity (W/m·K), the contact area and the temperature gradient, respectively.[134, 135] Consequently, the temperature here is a function of length and can be used for positioning applications.

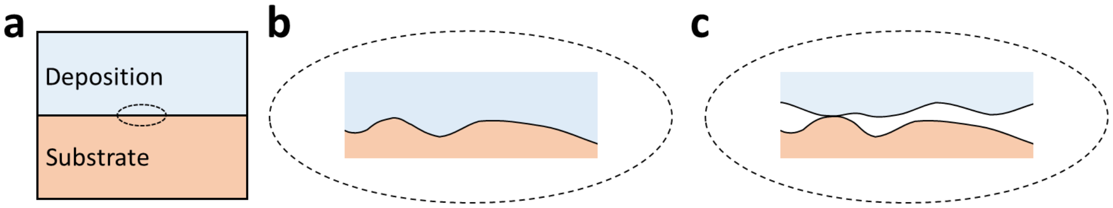

Figure 2.11. Joint-roughness model for thermal contact resistance. (a) Sketch of the substrate and deposition on top. The interface for (b) ALD deposition and (c) other thin film deposition technique.

One of the most significant advantages of ALD is its exceptional conformality, meaning that the deposited film can uniformly and completely cover the substrate being coated. In contrast, other mainstream large-area coating methods, such as CVD and sputtering, often result in gaps at the interface (Figure 2.11).[136, 137] These gaps have a significant impact on properties including the thermal conductivity between the deposited film and the substrate.[138-140] As a result, the conformal interface created by ALD can be simply approximated as heat conduction between solids. In contrast, other coating methods leave void spaces filled with trapped gas, making the (local) variations in heat transfer at the interface non-negligible.

2.3. Atomic layer etching

ALE is another important branch of ALP. Similar to ALD, ALE decomposes the etching process into two or more individually controlled, self-limiting, surface reaction steps that remove material only when run in sequence.[5] The first report for ALE came about in 1988 via a patent application by Max Yoder.[3] In this patent, nitrogen dioxide and a beam of ions mixed with noble gases and hydrogen were introduced to the diamond surface in sequence to remove “a single atomic layer from the surface of crystalline diamond”.[3] This etching manner, which repeats two separate steps, laid the foundation for later ALE processes. However, such a precise etching technique was beyond the requirement of that era, resulting in little attention in either academia or industry. Until the past 10 years, as the technology nodes of the semiconductor industry have continued to shrink, ALE has gradually been taken seriously because of the increasing demands for controlled and accurate processing techniques in integrated circuit fabrication. Fox example, ALE has be used for the production of logic devices since 10 nm technology node.[5]

2.3.1. Comparison between ALE and ALD

Intuitively, the ALE process can be considered the opposite of the ALD process, essentially "reverse ALD." This terminology accurately captures the relationship between ALE and ALD to a certain extent. ALE is a layer-by-layer etching method with these defining characteristics: (1) it is cyclic, (2) each cycle involves several steps, and (3) it is based on self-limiting surface chemistry. Note, the "layer" in ALE, similar to ALD, does not refer to a strictly crystallographic monolayer but typically to a fixed thickness of about or less than a monolayer, achieving atomic precision per cycle and an atomically smooth surface due to self-limitation. Although ALE processes are limited and less developed compared to ALD, their similar characteristics have led to the creation of an ALE process database like the ALD database on the Atomic Limits blog.[141]

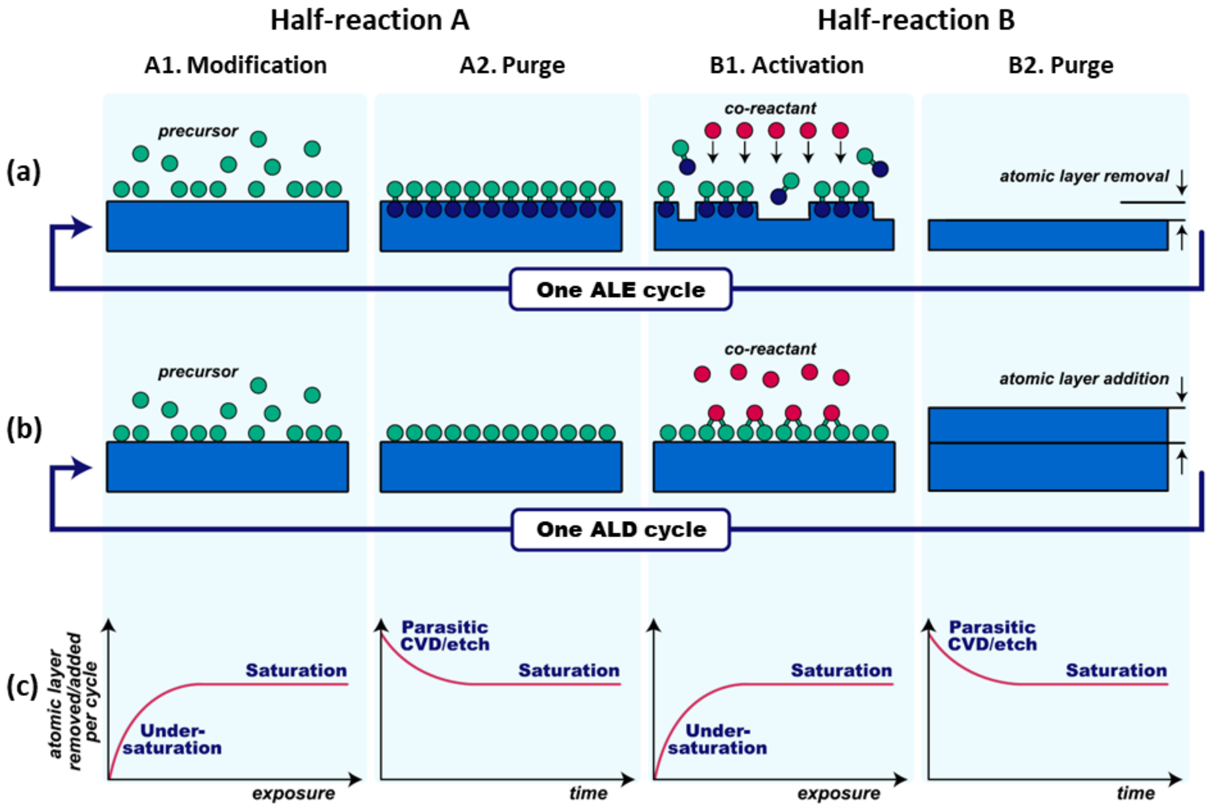

Figure 2.12. Schematic representations of a complete, generalized cycle for (a) ALE and (b) ALD. In (c), the so-called saturation curves for the various steps in the ALE and ALD processes are schematically illustrated. These processes consist of two Half-reactions, A and B, with the total cycle divided into four distinct process steps. During these steps, the surface is exposed to reactants—referred to as the "precursor" in step A1 "Modification step" and the "co-reactant" in step B1 "Activation step". Steps A2 and B2 are "Purge steps". These cycles, and therefore the process steps, are repeated multiple times during etching or film deposition. In ALE, each cycle removes an atomic layer, while in ALD, each cycle adds an atomic layer to the film. The saturation curves illustrate that the exposure times to the reactants in steps A1 and B1 must be sufficiently long to reach saturation. Additionally, the purging steps between these exposures must be sufficiently long to prevent parasitic CVD or etch reactions, which could compromise the ALE or ALD processes. Adapted from ref [142]. *Copyright © 2015 The Electrochemical Society.*

To better understand ALE, it helps to compare it to ALD, as shown in Figure 2.12. For simplicity, we compare processes with two half-reactions and four steps per cycle, which can be considered the most basic reaction setup. In half-reaction A, both ALE and ALD modify the exposed substrate surface in a self-limiting manner during the modification step (A1. Modification). This is followed by a purge step (A2. Purge) to remove excess precursor material and reaction products. As for the activation in half-reaction B (B1. Activation), after another purge step (B2. Purge), the co-reactant in ALD reacts with the modified surface to add a layer of material with GPC thickness. In contrast, the co-reactant in ALE reacts with the modified surface to remove a layer of material with GPC thickness. Therefore, from a process design perspective, the main differences between ALD and ALE are found in the surface modification step and the activation step. While ALD focuses on material addition, ALE focuses on material removal, with both cyclic processes relying on precise control over these reactions to achieve atomic-level precision in a self-limiting manner. Note, the precursors or co-reactants differ significantly between ALD and ALE. In ALD, precursors in both the surface modification and deposition steps contain the element to be deposited. In ALE, the precursor in the surface modification step typically forms volatile reaction products with the material to be etched. However, in the activation step (B1. Activation), it can be ions, electrons, high-energy neutral particles, or photons, and may involve substrate temperature changes.

In addition to comparing ALE and ALD cycles and their process steps, it is important to focus on the key characteristics desirable for these processes. Ideally, if the sample surface is exposed to the precursor and co-reactant doses for a sufficient duration, surface chemical saturation will be achieved across all surface areas. This self-limitation guarantees uniformity for both methods when processing large areas at the wafer level. However, there is currently a clear difference in the desired results for ALE and ALD when processing complex 3D surfaces. ALD can produce highly conformal films on complex 3D structures, such as trenches or holes with high aspect ratios. In contrast, for ALE, the desired etching outcome depends on the specific co-reactants used. The etching effect can be directional ("non-conformal") or isotropic ("conformal"), offering flexibility based on the application requirements. This distinction is discussed in more detail in Section 2.3.2.2.

Similar to the GPC for ALD, the term “etching per cycle” (EPC) is defined to present the etching rate for ALE. The EPC is expressed in nm/cycle or Å/cycle because the process is cyclic and removes a well-defined amount of material every cycle. Because almost all early ALE schemes involved plasma, people's understanding of ALE is closely related to plasma etching, such as reactive ion etching (RIE). In 1979, Coburn and Winters[143] discovered that Si etching was insignificant when exposed solely to an energetic Ar ion beam or a reactive neutral gas (such as XeF_2 or Cl_2), while the coexistence of ions and reactants enhanced the etch rate significantly. This observation led to the proposal of the “ion-neutral synergy” concept that plasma etching is synergistic because it “cannot be easily explained by simply superimposing a physical sputtering process onto the chemical etching process”,[143-145] which aims to understand the plasma-related etching process better. The ALE community expanded the synergy concept to ALE as the term “ALE synergy”.[146, 147] It can be quantified as a percentage relative to the total amount of material removed per cycle,

$$\text{ALE synergy \% } (S) = \frac{\text{EPC} - (\alpha + \beta)}{\text{EPC}} \times 100\%,$$

where the values of “α” and “β” are undesirable contributions from the individual surface modification steps and the removal step, respectively. In ALE, these two steps are separated, and ideally neither step alone should produce an etching effect, meaning that S approaches 100%. The concept of synergy is crucial for understanding the etching mechanisms in ALE. For instance, the self-limiting nature of the process explains why the removal step stops after a certain point, and it also accounts for the influence of competing reactions, such as physical sputtering or contamination. This self-limiting behavior is what gives ALE its key advantages: aspect ratio independence, uniformity, smoothness, and selectivity. Measuring synergy makes it easier to compare different ALE parameters or systems and provides a useful reference for evaluating the independence of each etch step.

2.3.2. Classification of ALE

2.3.2.1. From the process perspective

Etching, including ALE, involves breaking surface bonds of solid materials to remove atoms.[148] In ALE's cyclic process, the modification step first weakens bonds between surface atoms and the bulk material using an adsorbent. Then, energy is provided in the removal step to break these weakened bonds, removing the surface atomic layer. The accompanying Figure 2.13 illustrates interactions between chemically active adsorbed species and the solid surface. Here, E_A, E_S, and E_O represent the bond energy between the adsorbate and surface atoms, the bond energy between surface atoms and bulk atoms, and the bond energy between bulk atoms, respectively. The presence of E_A weakens E_S. When external energy is supplied, the weakest bond will break first. If "E_S < supplied energy < E_O and E_A", surface etching occurs, which is a prerequisite for an ALE process. However, if "E_A or supplied energy < E_S and E_O", no etching will happen; while if "E_A, E_S, and E_O < supplied energy", it results in sputtering or evaporation of the bulk material.[148-150] Although this simplified model does not account for surface structure, reaction kinetics, or activation energy barriers, it effectively demonstrates the energy relationship among the relevant important chemical bonds.

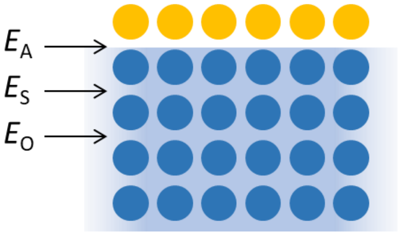

Figure 2.13. Sketch of the bond's position in a surface system with adsorbed atoms. E_A represents the bond energy between the adsorbate and surface atoms; E_S represents the bond energy between surface atoms and bulk atoms. E_O represents the bond energy between bulk atoms. The yellow spheres represent adsorbed atoms, and the blue spheres represent atoms in the solid.

In principle, there are a large number of schemes that can be used to deliver reactants to the surface to modify the bond energies involved in the surface modification step and the removal step, including reactants delivered by gas, plasma, liquid chemistry or other sources. The Figure 2.14 summarizes the classification ideas for ALE in these two key steps.[151]

In the surface modification step, there are at least four possible methods, depending on the changes in composition and structure: chemical adsorption, deposition, conversion, and extraction. In the first three cases, the reactants are introduced to the surface of a substrate with the thickness d to produce a modified layer with a thickness defined as d_m. In the case of chemisorption, d_m is equal to "zero" (or more precisely, a monolayer), while deposition case is able to add a modified layer with a thickness of d_m to the surface. These two are the current mainstream solutions. For example, the ALE process of SiO_2 using C_4F_8 gas and Ar plasma is to first deposit a fluorocarbon layer to modify the surface, and then use Ar plasma to remove the fluorocarbon layer and the modified surface.[152] For modification by deposition case, saturation must take advantage of the fact that the deposited activation layer only helps etching below a certain thickness. At the beginning of the removal step, the excess deposit will be removed from the surface without etching. Conversion and extraction methods extend the modified layer of d_m into the substrate based on the surface or remove the modified layer of d_m thickness. Among them, the extraction method involves etching the composite material, where one step removes a subset of the elements that make up the material, and the second step removes the remaining elements. The modification step deep into the bulk material achieves saturation through characteristics such as adsorption, diffusion, and implantation processes.

The removal step can also be performed in a variety of ways. The modified layer can be removed thermally (desorption, evaporation, or sublimation), chemically (e.g., by ligand exchange reactions or by dissolving the modified surface layer with liquid chemicals), by particle bombardment (ion or electron bombardment), or by extraction. In the case of thermal removal, the heat energy can be delivered by wafer heating, infrared light, laser radiation, or microwave coupling.

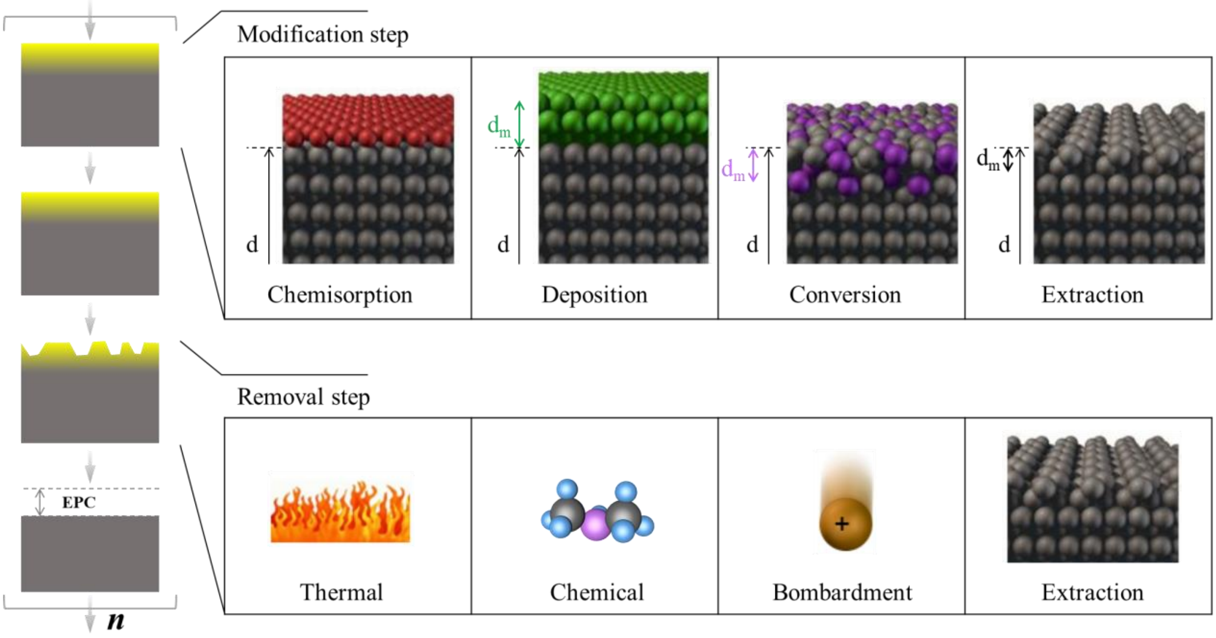

Figure 2.14. Classification of ALE from the process perspective. In the ALE process, both the modification step and the removal step can be implemented in a variety of ways, thus developing various types of ALE. Adapted from ref [151]. *Copyright © 2016 Taylor & Francis Group. Adapted with permission.*

2.3.2.2. From the etching effect: directional and isotropic ALE

Different from ALD, which emphasizes conformality, ALE can be categorized into directional and isotropic etching. In the semiconductor industry, most etching processes require directional etching, where the vertical etching rate is significantly higher than the horizontal rate. This requirement is a key reason why RIE has largely replaced wet etching in many processes. However, with the advent of 3D devices like fin field-effect transistors (FinFETs) and gate-all-around (GAA) devices, precise horizontal or isotropic etching has regained importance.[153] ALE offers potential adjustability between these etching modes. For ALE to be directional, at least one of the two steps, modification step or removal step, must be directional and involve momentum transfer (Figure 2.15). This can be achieved using plasma (perpendicular to the wafer plane) and ion bombardment with ions or neutral beams.[154] Typically, this kind of etching occurs along the line of sight. When ions are used in the surface modification step (such as through ion implantation), they create a thin modified layer with sufficient energy to penetrate the crystal lattice. This allows for deep saturation due to the projection range of the ions. Sputtering must be minimized to achieve controlled etching. Then the modified layer can be selectively removed by gas or liquid phase chemistry. Tamirisa *et al*.[155] reported this approach for etching copper by alternating chlorine and hydrogen plasmas. In the removal step, if ions are used, the surface is first modified by neutral species or free radicals. The modified surface layer is then removed by low-energy ion bombardment. Isotropic ALE requires that both the surface modification step and the removal step are isotropic. This is currently achieved mainly by thermal ALE.[156] However, as researchers gain more control over the plasma, ALE processes involving plasmas can now also be isotropic.[157, 158] When a plasma is ignited, free radicals are generated as well as ions and electrons. Plasma radicals are neutral species that do not orient in the plasma sheath but rather diffuse toward the substrate like thermal reactants. In addition, plasma radicals are more reactive than thermal reactants, resulting in lower activation barriers, allowing even higher etch rates at further reduced operating temperatures and etching of materials previously considered resistant to thermal ALE. Therefore, plasma-involved isotropic ALE is possible when directed ions are separated from the etch active species and only free radicals are used for etching.

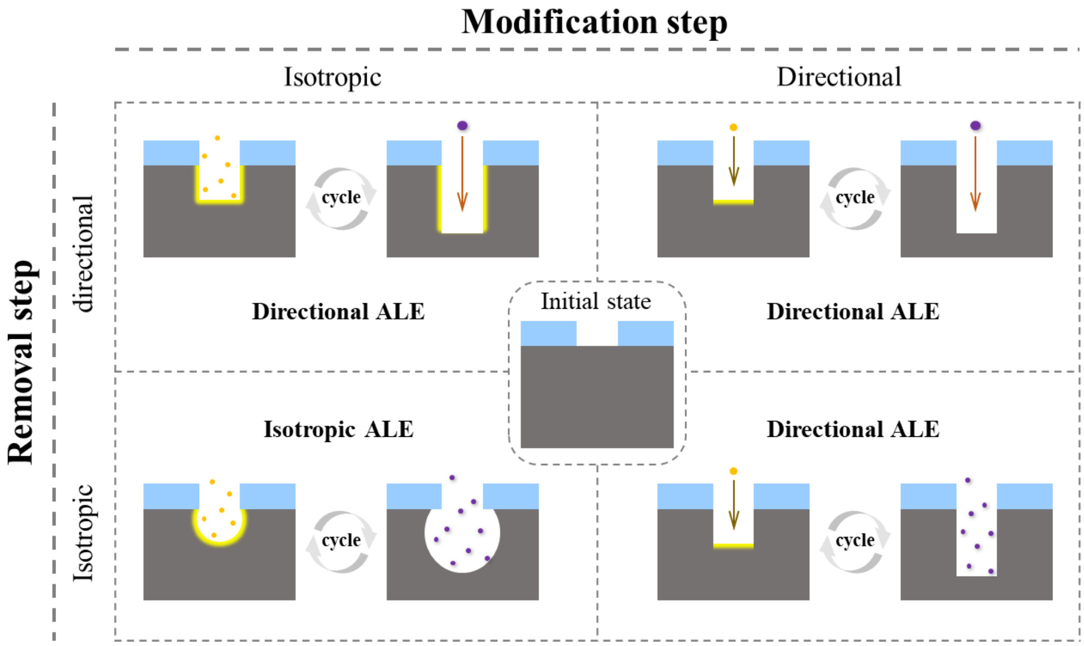

Figure 2.15. Classification of ALE from the etching result perspective. For the sample with a pattern defined by a mask (initial state, center), different etching effects (four quadrants) are shown during the ALE cyclic etching process. In the figure, the yellow balls represent the reactants in the modification step, the purple balls represent the reactants in the removal step, the blue area represents the mask material that is inert to the reactants, such as photoresist, the gray area represents the etched substrate, and the light yellow attached to the substrate surface represents the modified surface area. Adapted from ref [151]. *Copyright © 2016 Taylor & Francis Group. Adapted with permission.*

Both directional and isotropic ALE ensure precise etching and can be used in different scenarios, which is essential for developing advanced semiconductor devices. For instance, anisotropic ALE is ideal for etching fins in FinFETs, while isotropic ALE can be used for isotropic etching or "thinning" of nanosheets or nanowires in gate-all-around FETs.

3. ALD-assisted VO_2 for memristor application

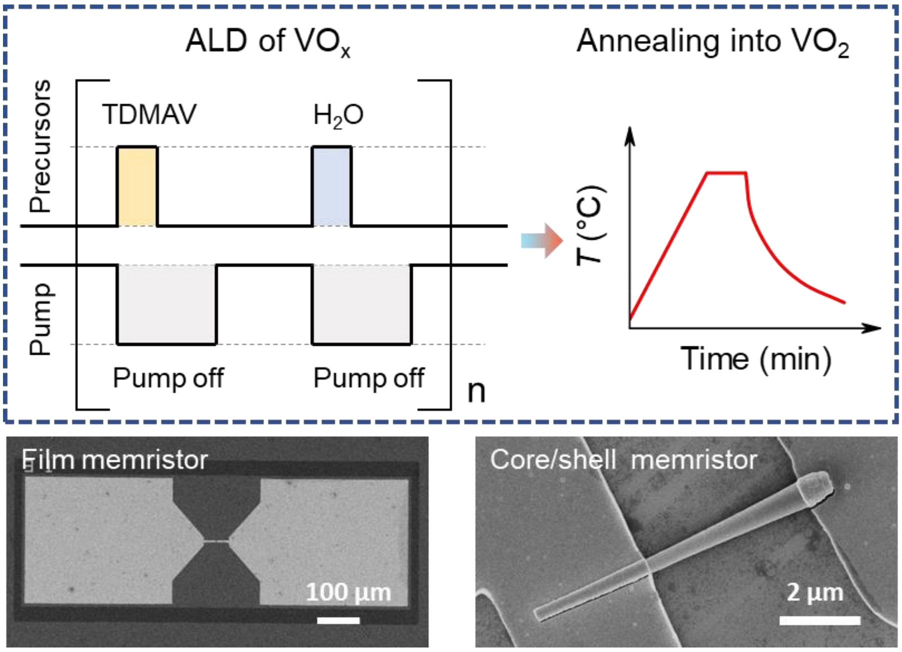

This work demonstrates a strategy for depositing VO_x using thermal atomic layer deposition (ALD) followed by thermal annealing to synthesize VO_2. The thin-film and core/shell wire memristors method exhibit excellent switching performance and are highly sensitive to ambient temperature. This ALD approach to preparing key memristor materials paves the way for future high-density hardware neural networks.

This chapter is adapted from a published first author's peer-reviewed article, with only the formatting changed, and the content remains unchanged.

J. Peng, D. Hensel, R. Venugopal, L. Rave, C. Schormann, S. Koch, R. H. Blick, R. Zierold, *ALD-assisted VO_2 for memristor application*. Advanced Engineering Materials, 2025. 2402614.

Manuscript title

ALD-assisted VO_2 for memristor application

Author list

Jun Peng[1], Daniel Hensel[1], Rakshith Venugopal[1], Lucas Rave[1], Colin Schormann[1], Sebastian Koch[1], Robert H. Blick[1,2], Robert Zierold[1]**

1 Center for Hybrid Nanostructures, University of Hamburg, Luruper Chaussee 149, 22607 Hamburg, Germany

2 DESY Photon Science, Deutsches Elektronen-Synchrotron DESY, 22607 Hamburg, Germany

Keywords

atomic layer deposition, vanadium dioxide, insulator-to-metal transition, memristor, unipolar threshold switching

Author contributions

J.P. and R.Z. designed experiments; J.P. and D. H. performed ALD growth and analyses; J.P., D.H. R. V., L. R., C. S., and S. K. fabricated and analyzed the memristors; All authors analyzed data; J.P. and R.Z. wrote the manuscript. All authors have approved the final version of the manuscript.

Acknowledgements

This work was funded by the Deutsche Forschungsgemeinschaft (DFG, German Research Foundation) – Projektnummer 192346071 – SFB 986 “Tailor-Made Multi-Scale Materials Systems”. We thank you Jann Harberts for providing us with the Si nanowire array samples. We acknowledge the use of the Hamburg-CRR cleanroom facility, jointly operated by UHH, DESY, and MPSD, which was instrumental for the work presented in this paper.

3.1. Abstract

Vanadium dioxide (VO_2) is a well-known candidate for memristor applications due to its insulator-to-metal transition (IMT) characteristics. The fabrication of memristor devices require highly controlled synthesis processes concerning the material chemistry and geometry. Atomic layer deposition (ALD) offers unique advantages for the fabrication of hardware neural networks, such as miniaturization, conformality, and sub-nm thickness control. Herein, an ALD process for non-stoichiometric vanadium oxide (VO_x) using tetrakis(dimethylamino)vanadium (TDMAV) and water as precursors is presented. Subsequently, a tailor-made annealing process converts VO_x into VO_2, which exhibits an IMT of about three orders of magnitude at around 70 °C, rendering it a promising memristor material. VO_2 thin film and Si-Al_2O_3/VO_2 core/shell memristors are fabricated and analyzed, both of which exhibited I-V hysteresis loops, indicating their suitability for memristor applications in both 2D and 3D morphologies. Additionally, these memristors are sensitive to the operation temperature, with the hysteresis loops narrowing and shifting toward lower voltages as temperature increases, eventually disappearing beyond VO_2's intrinsic phase transition temperature. This study highlights the viability of ALD-assisted VO_2 for memristor applications and demonstrates its potential for advancing the three-dimensionalization of neuromorphic chips.

3.2. Introduction

Recent advancements in artificial intelligence have significantly accelerated research in neuromorphic computing.[77, 159] Hardware neural networks, which emulate the neural architecture of biological brains, offer highly parallel computing solutions. Its most basic element is the memristor—a compact resistive device with a simple structure, that can replicate the multiple functions of a synapse, enabling ultra-high-density integration and low-cost manufacturing.[160] VO_2 is a special material due to its IMT, making it suitable for various applications, including electronic switches, smart windows, photonics, photodetectors, and batteries.[161-166] Recently, VO_2-based memristors have gained significant attention in the fields of neuromorphic computing and signal processing.[167-170] In addition, since its IMT characteristics can be regulated by environmental factors such as temperature, light, magnetic field, strain, and electric field,[171] similar to neurons that are affected by different triggers of the organism, VO_2-based neural networks also have certain sensing functions. Unlike most memristor materials, VO_2-based memristors can operate in two distinct modes: voltage-driven and current-driven, each offering unique neuron-like functions. For instance, voltage-driven VO_2 memristors have been successfully employed as compact leaky integrate-and-fire neurons, adaptive leaky integrate-and-fire neurons,[172] multisensory neurons that integrate touch and temperature sensing,[173, 174] and adaptive Hodgkin-Huxley neurons;[175] while current-driven VO_2 memristors exhibit all three classes of excitability and a wide range of known biological neuron dynamics due to their negative differential resistance.[176]

However, most of the demonstrated VO_2 as a key material for memristors thus far, have been fabricated using well-established physical vapor deposition methods such as molecular beam epitaxy,[177] pulsed laser deposition, and sputtering.[178] While these techniques can produce high-quality VO_2 films, they face challenges in scalability for large-area synthesis and 3D integration. [179] This has driven an increased interest in using ALD as an alternative to prepare key materials for memristors. On the one hand, ALD offers sub-nanometer control over film thickness, making the atomic-level memristors possible.[46, 180] On the other hand, its conformality characteristic is regarded as "the ultimate way to achieve high-density 3D synapses and memory arrays".[181] These two features are crucial to the miniaturization and energy efficiency of neural network hardware. In this work, VO_x is deposited onto silicon wafer substrates and Al_2O_3-coated Si nanowire arrays using TDMAV and water as the vanadium and oxygen sources, respectively. The annealing parameters for converting the VO_x to VO_2 are systematically examined. In the optimized annealing protocol, the sample is kept at 450 °C for 10 minutes in an approximately 1.4 Torr N_2 atmosphere with around 4% O_2 partial pressure content. The VO_2 films produced through this standard annealing process exhibited an IMT of about three orders of magnitude at around 70 °C (Figure S3.1). VO_2 thin-film memristors and Si-Al_2O_3/VO_2 core/shell memristors fabricated using this ALD-assisted VO_2 process demonstrated excellent switching performance, with temperature-sensitive tuneability. This study highlights the potential of ALD-assisted VO_2 deposition in advancing next-generation memristor applications, providing a promising path for high-density hardware neural networks.

3.3. Results and discussion

3.3.1. ALD-assisted VO_2 thin film

Controlling the oxidation state of vanadium is crucial in VO_2 material synthesis because a variety of vanadium oxides with oxidation states between +2 and +5 exist, e.g., V_2O_3, V_3O_5, V_4O_7, VO_2, and V_2O_5.[182] Tetrakis(dimethylamino)vanadium(IV) (TDMAV)[183, 184] is chosen for this work due to the vanadium oxidation state already being +4, which could facilitate the formation of VO_2 over other vanadium oxides. In this study water is chosen as the other reactant because its oxidative behavior is not as strong as ozone, as reported in other studies,[185, 186] to avoid the synthesis of higher oxidation state VO_x. As shown in Figure 3.1a, the VO_2 synthesis process contains two steps: (1) VO_x deposition via a binary ALD process; (2) post-deposition annealing. The ALD process is operated in exposure mode. In this configuration the pump-off time is always longer than the precursors' pulse time so that each precursor has enough time to diffuse in the reactor for the gas-solid-surface reaction in each ALD half-reaction. As indicated by Lv's report,[187] the ALD window for the TDMAV is about 50 °C to 200 °C. We verified that at 95 and 150 °C, the growth per cycle (GPC) remains stable at around 0.56 Å/cycle (Figure S3.2), matching well with the previous report.[187] Next, the as-deposited VO_x thin film is transferred into a vacuum chamber for post-deposition annealing. The standard annealing recipe for the VO_x deposited at 150 °C is fixed as: annealing temperature at 450 °C, annealing pressure at 1.4 Torr, partial oxygen at 4%, annealing time for 600 s. After annealing the roughness of a 33.6 nm thick as-deposited film increases from 0.55 nm to 1.64 nm (Figure 3.1b and Figure 3.1c). Raman spectra of the annealed film near room temperature in Figure 3.1d exhibit distinct peaks at 142.6, 195.1, 222.8, 263.5, 308.8, 337.8, 389.0, 441.6, 617.5 cm^{-1}, corresponding to the monoclinic VO_2 (M) phase which agrees well with previous reports on crystalline VO_2.[188] These Raman results prove that the as-deposited non-stoichiometric VO_x thin film turns into a VO_2-dominated thin film.

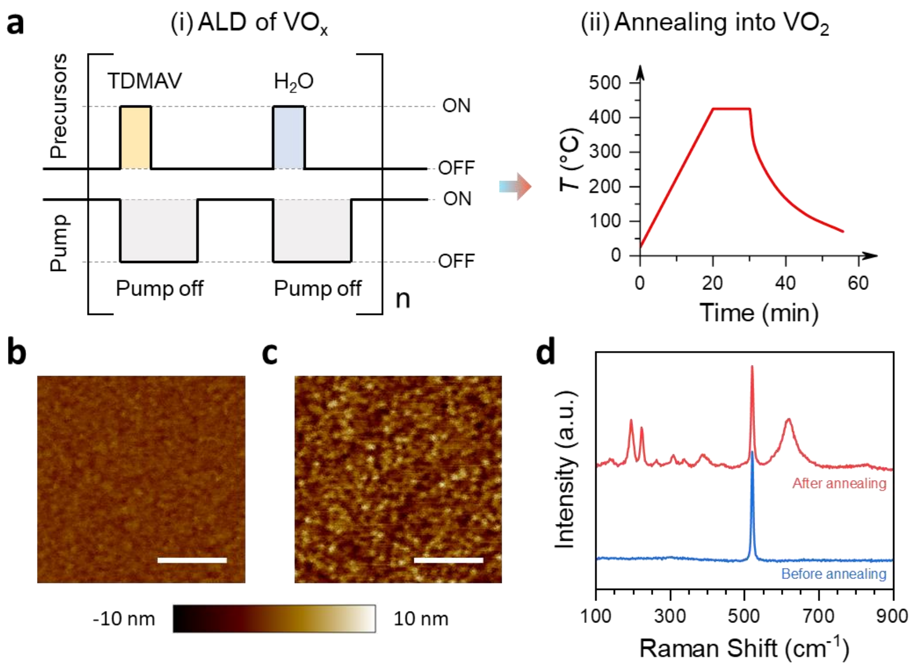

Figure 3.1. Fabrication process characteristics. (a) VO_2 synthesis using ALD. The synthesis process includes two steps: (i) ALD of VO_x and (ii) a followed post-deposition annealing. The reactor is operated in exposure mode, meaning that the unpumped periods are longer than the individual precursor pulses. This guarantees a complete precursor diffusion in the reactor. (b) The initial as-deposited VO_x film with a thickness of 33.6 nm is smooth and dense, characterized by a surface roughness R_a = 0.55 nm. (c) During the annealing, the VO_x film undergoes crystallization, transforming it into a crystallized VO_2 film, accompanied by an increase in surface roughness to R_a = 1.64 nm. Scale bars for (b) and (c) are 1 μm. (d) Raman spectra for the as-deposited VO_x film and the annealed VO_2 film. The strong Raman peak at 520 cm^{-1} comes from the silicon substrate.

3.3.2. The influence of the annealing parameters

The as-deposited VO_x thin film exhibits a resistance exceeding 10^5 Ω and shows no IMT phenomena near and above room temperature (Figure S3.3**Error! Reference source not found.**). The deposition temperature, the choice of substrate, and the annealing parameters, including partial oxygen pressure, annealing pressure, annealing temperature, and annealing duration, significantly influence the composition and crystallinity of the annealed films, which may affect the memristor device fabricated from it.[171] Therefore, it is necessary to understand the influence of the synthesis process parameters on the film, which can be reflected by the resistance-temperature hysteresis curves. Figure 3.2a and Table S3.1 display the deposition temperature influence on the resistance-temperature hysteresis curves. As the deposition temperature increases from 95 °C to 150 °C, the overall resistance decreases. This reduction in resistance can be attributed to a decrease in precursor residues, such as carbon and nitrogen elements at higher deposition temperatures,[184] hence reducing electron scattering at impurities leading to a lower resistance. The partial oxygen pressure is a critical factor in the annealing process of VO_x (Figure S3.4).[189-192] By tuning the ratio of the N_2 and O_2 flow, different partial oxygen pressures were created in our vacuum oven to explore its influence. The corresponding hysteresis curves are shown in Figure 3.2b and the analysis is displayed in Table S3.2. An increase in the O_2 content shifted the temperature-resistance hysteresis curves to higher temperatures and to increased overall resistances. The lowest transition width of 13.6 °C and the highest resistance change between the insulating and metallic phases were observed with a 4% partial oxygen pressure. A similar trend is observed for the annealing pressure: a higher overall pressure raises the transition temperature as well as the overall resistance (Figure 3.2c, Table S3.3). The resistance change is the sharpest when the pressure is set to the lowest pressure allowed, 1.4 Torr. Note that lower chamber pressures, not accessible, in our oven may further improve the resistance ratio. As shown in Figure 3.2d and Table S3.4, an increase in the annealing temperature had a significant effect on the measured curves. The temperature-resistance hysteresis curves are again shifted to higher temperatures and overall resistances at higher annealing temperatures. This phenomenon points to the fact, that there is an optimal temperature and might be a result of the increased grain size constituting the film.[187] Higher temperatures may induce dedrimental effects similar to the partial and absolute pressure dependences described previously, with a probable loss of the exact oxidation state. Increasing the annealing time from 300 s to 1200 s at a constant temperature of 450 °C has the same effect of shifting the temperature-resistance hysteresis curves to higher temperatures and resistances though it has less influence on the hysteresis (Figure 3.2e and Table S3.5). This is in agreement with assuming an optimal thermal load which acts on the thin film during the annealing process: higher temperatures or longer times should have similar effects. Additionally, we revealed a substrate dependency (Figure 3.2f and Table S3.6). which probably is a result of different thermal expansion coefficients of the substrates leading to internal strain. These results demonstrate that different preparation parameters significantly influence the performance of the VO_2 films. Previous studies have indicated that strain within VO_2—arising from factors such as doping,[193] O_2 vacancies,[15, 194] the difference to the substrates' thermal expansion coefficient,[195, 196] and lattice mismatch[197, 198]—can profoundly impact the IMT characteristics, including the position and the width of the hysteresis. The fabrication parameters explored in this work directly or indirectly contribute to these internal strains within the synthesized VO_2 films. However, a complete understanding of how individual or combined manufacturing parameters affect the IMT or memristor properties requires a more detailed and comprehensive evaluation, which might include an in-depth analysis of material structure, microcomposition, defects, internal stress, and corresponding electronic structures.

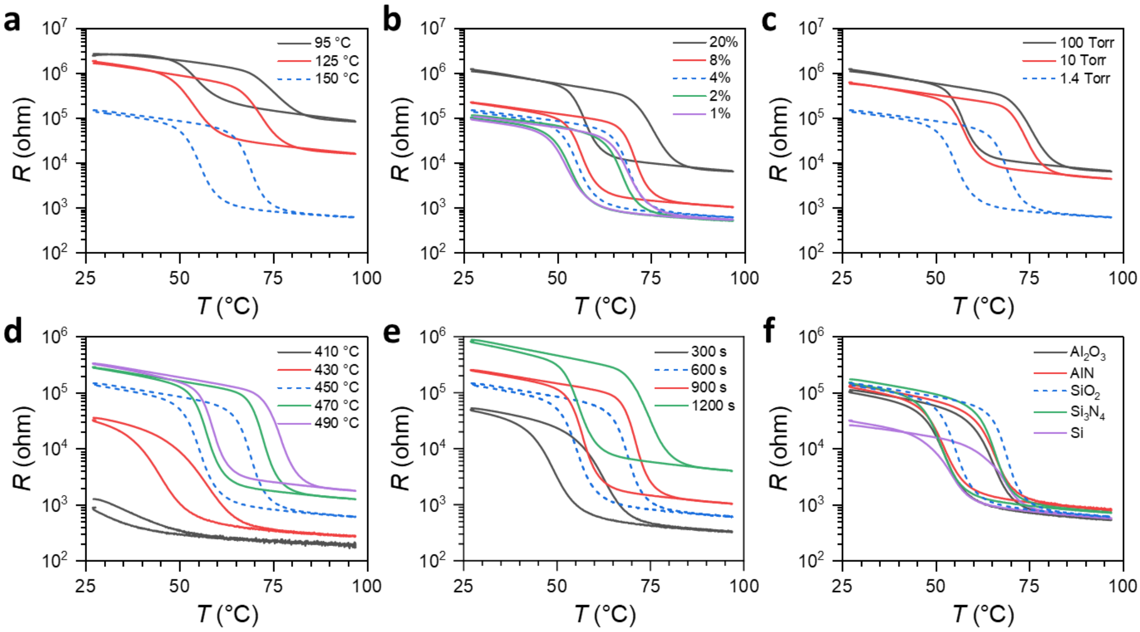

Figure 3.2. The influence of different parameters during the VO_2 synthesis on the IMT. (a) Deposition temperature. (b) Partial oxygen. (c) Annealing pressure. (d) Annealing temperature. (e) Annealing time. (f) Substrate. The blue dashed line is the result obtained with the standard process recipe: deposition temperature at 150 °C, annealing temperature at 450 °C, annealing pressure at 1.4 Torr, partial oxygen at 4%, and annealing time for 600 s.

3.3.3. VO_2 thin film memristor

In order to verify the potential of ALD-assisted VO_2 allowing for manufacturing a 3D memristor, a planar 2D device structure is first fabricated to analyze the memristor characteristics from the material perspective. As shown in the SEM image of Figure 3.3a, the memristor consists of a 33 nm thick ALD-assisted VO_2 film deposited on a silicon wafer and two Cr/Au electrodes, where the channel length between the two electrodes is about 2 μm. Its temperature-dependent resistance measurement reveals a resistance change of three orders of magnitude (Figure 3.3b), which is comparable to the results of the four-probe measurements on a thin film (Figure 3.2). This indicates that ALD-assisted VO_2 can undergo normal semiconductor CMOS processes including photolithography, lift-off, and sputtering. The voltage-driven and current-driven I-V curves of this two-terminal device are shown in Figure 3.3c, whose measurement circuit is depicted in Figure S3.5. From a material perspective, this result is similar to the I-V measurement results of VO_2 synthesized by other methods: (1) Voltage drive shows hysteresis when increasing and decreasing voltage; (2) Current drive reveals negative resistance phenomenon.[176, 199] Generally speaking, voltage-driven memristors are more widely used, so this study conducts a more detailed investigation into this aspect. When the applied voltage is gradually increased to the threshold voltage (V_{th}), the device jumps from a high resistance state (HRS) to a low resistance state (LRS); when the voltage is gradually reduced from a voltage higher than V_{th} to the holding voltage (V_{hold}), the device changes back to HRS. By applying a voltage scan, the resistance of the memristor device changes repeatedly between LRS and HRS. The I-V curve displayed by the device shows that the device can be used as a volatile unipolar threshold switch.[200] Temperature-dependent I-V measurements are shown in Figure 3.3d and Figure S3.6. The shape of the I-V curve changes significantly with increasing operation temperature. The higher the temperature, the less obvious the hysteresis of the I-V loop. Above the IMT temperature, the hysteresis completely disappears. Such changes are well reflected in the two parameters V_{th} and V_{hold} (Figure 3.3e). For the resistance value in the HRS, three orders of magnitude change occurred in the measured temperature range, while the resistance value in the LRS remained stable (Figure 3f). It is worth noting that the temperature-dependent resistance value transition of the HRS shows the same trend as that of the pure temperature-dependent resistance measurement but without hysteresis. This indicates that the IMT triggered by Joule heating is the essence of the switch between HRS and LRS.[177, 201, 202] In HRS, the IV measurement is dominated by the dielectric monoclinic VO_2 (M) phase, while in LRS, it is dominated by the metallic rutile VO_2 (R) phase. The transition from HRS to LRS requires the application of additional energy, for example, Joule heating or environmental temperature increase, to overcome the energy barrier for initiating the formation of conductive filaments or structural changes in the material. Consequently, the V_{th} is always higher than V_{hold} in this device. Moreover, the decrease in V_{th} and V_{hold} with increasing temperature in Figure 3.3d can also be attributed to this reason.

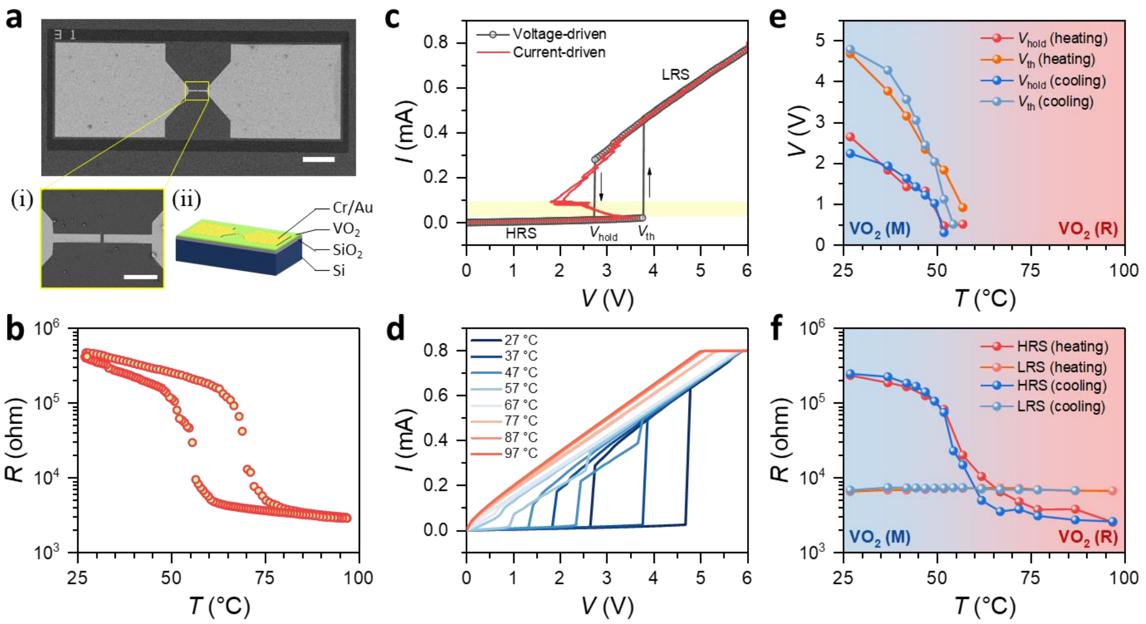

Figure 3.3. Memristor characterization for the VO_2 film memristor. (a) SEM images of the film memristor. Inset (i): A magnified view of the central area. The area between the two electrodes is 5 × 2 μm^2 (electrode line width × electrode spacing). Inset (ii): Sketch of the memristor stack. (b) Temperature-dependent resistance measurement for the memristor device. Scale bars for (a), inset (i) are 100 μm and 20 μm, respectively. (c) I-V measurements of the memristor in voltage- and current-driven mode. A hysteresis loop is observed in the voltage-driven I-V curve (indicated by black arrows), while an "S"-shaped negative differential resistance region (highlighted in yellow) appears in the current-driven I-V curve. (d) Voltage-driven I-V measurements as a function of the increased ambient temperature. (e) V_{hold} and V_{th} during the heating and cooling process. (f) Resistance in HRS and LRS during the heating and cooling process.

3.3.4. Si-Al_2O_3/VO_2 core/shell memristor

Then the method using ALD to synthesize VO_2 on a flat substrate is transferred to an array of standing nanowires, to explore the potential three-dimensionalization of memristor devices. Figure 3.4a and Figure S3.7 show the coated Si-Al_2O_3/VO_2 core/shell array and the cross-section of the nanowire setup. The fabricated Si-Al_2O_3/VO_2 memristor device and its electrical circuit is displayed in Figure 3.4b and Figure S3.5, respectively. The temperature-dependent resistance measurement for the Si-Al_2O_3/VO_2 core/shell memristor is shown in Figure 3.4c. The overall resistance change is smaller than that of the thin-film memristor, probably because of the difference in the substrate in direct contact with VO_2 that affects the internal stress. The temperature-dependent I-V measurement of this kind of memristor shows similar phenomena as the thin film device, but with lower threshold voltage and holding voltage (Figure 3.4d). This indicated that the Si-Al_2O_3/VO_2 core/shell memristor is more energy-efficient than the VO_2 thin film memristor. However, in actual measurements, it was found that the core/shell memristor was more easily burned (Figure S3.8). Note that when the device is operated, the induced Joule heating can hardly dissipate like in the thin film device. Therefore, heat dissipation can be one issue worth considering when three-dimensionalizing neural networks.

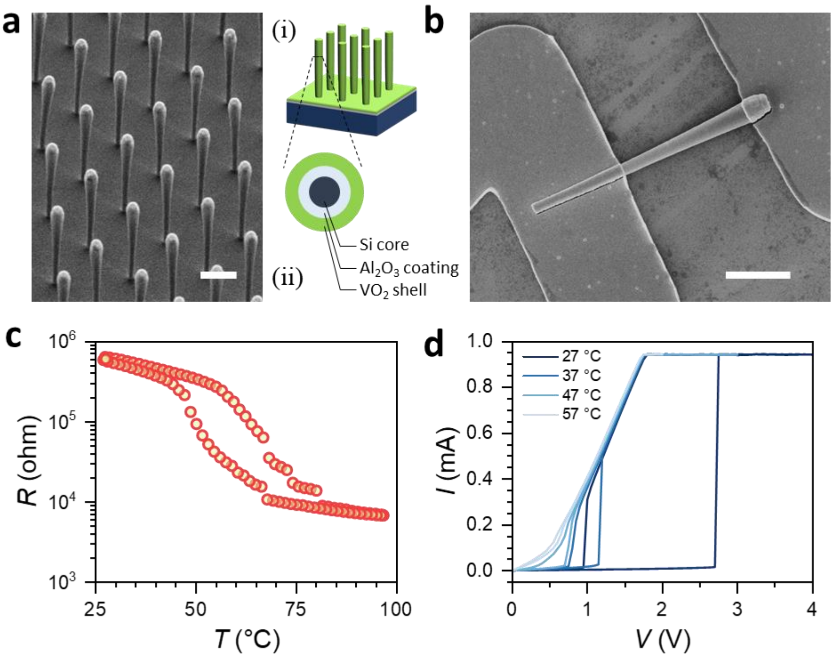

Figure 3.4. Memristor characterization for Si-Al_2O_3/VO_2 core/shell memristor. (a) SEM image of VO_2 and Al_2O_3 coated nanowire array. Sketch of the array (Inset (i)) and the cross-section of the Si-Al_2O_3/VO_2 core/shell nanowire (Inset (ii)). (b) SEM image of a typical Si-Al_2O_3/VO_2 core/shell memristor device. (c) Temperature-dependent resistance measurement for the Si-Al_2O_3/VO_2 core/shell two terminal memristor. (d) Voltage-driven I-V measurement of the device as a function of temperature. Scale bars for (a) and (b) are 2 μm.

3.4. Conclusions

By combining thermal ALD using TDMAV and water in a custom reactor with subsequent tailor-made thermal annealing, we successfully prepared high-quality polycrystalline VO_2 thin films that exhibited a resistance change of three orders of magnitude. The optimal annealing conditions were determined to be 450 °C for 10 minutes in a nitrogen atmosphere with an oxygen partial pressure of 4% at approximately 1.4 Torr. The VO_2 thin-film memristors and Si-Al_2O_3/VO_2 core/shell memristors fabricated through this ALD-assisted VO_2 process demonstrated excellent switching performance and displayed tunability that was highly sensitive to the operation temperature. This study highlights the scalability of 3D ALD-assisted VO_2 synthesis in memristor applications, particularly when integrated with micro- and nanostructures, offering a promising pathway for the development of future high-density hardware neural networks.

3.5. Materials and Methods

VO_2 synthesis: The VO_2 thin film was fabricated in two steps: Firstly, non-stoichiometric VO_x is deposited in ALD under an exposure mode using an in-house modified Savannah^{TM}100 reactor (Cambridge Nanotech). Tetrakis(dimethylamino)vanadium(IV) (TDMAV, Strem Chemicals, Inc., USA) precursor as vanadium source is heated to 70 °C to get sufficient vapor pressure. Deionized water (DIW) as oxygen source is kept at room temperature. The valves and manifold lines from the precursor containers to the reaction chamber are heated to 105 °C to ensure that the precursor gases do not condense. The deposition is performed at a temperature of 95~150 ℃, with a N_2 flow of 30~65 sccm serving as both carrier and purge gas, and an operating pressure maintained between 0.5 and 1.5 Torr. Different substrates, SiO_2 (300 nm)/Si wafers (SIEGERT WAFER GmbH), pure polished Si wafer (SIEGERT WAFER GmbH), and self-deposited Al_2O_3, AlN and Si_3N_4 on SiO_2 (300 nm)/Si wafers (SiMat Silicon Materials) are used for VO_x deposition. The “precursor pulse time / exposure time / purge time” combinations are set as 0.1/15.0/60.0 s and 1.0/15.0/60.0 s for DIW and TDMAV respectively. Next, the VO_x film is annealed at the target temperature with a heating rate at 1℃/min in a vacuum atmosphere with controlled oxygen partial pressure for a certain period, and then cooled down naturally in the furnace oven (MC050, ANNEALsys). The annealing gas flow starts before the temperature is ramped up and stops when the sample temperature cools down to room temperature. Si-Al_2O_3 core/shell nanowires are chosen as a base to fabricate the Si-Al_2O_3/VO_2 core/shell nanostructures. The silicon nanowire fabrication refer to the method previously reported in our group.[203] At first a nanowire substrate consisting of an array of free-standing Si nanowires is coated with an around 55 nm thick Al_2O_3 insulating layer to isolate the Si core from the later applied VO_x film. The Al_2O_3 deposition is carried out at 100 ℃ via thermal ALD using trimethylaluminum and DIW as precursors, with a N_2 flow of 30 sccm serving as both carrier and purge gas, and an operating pressure maintained between 0.5 and 1 Torr. A VO_x thin film is then deposited using the standard ALD recipe at 150 °C. To crystallize the amorphous non-stoichiometric VO_x film into the VO_2 stoichiometry, the standard annealing recipe is applied. After these steps a substrate with free standing Si-Al_2O_3/VO_2 core/shell nanotubes is produced. The Si-Al_2O_3/VO_2 core/shell nanotubes are then transferred onto silicon wafers for memristor fabrication using an in-house micro-manipulator. The Cr (8 nm) /Au (82 nm) electrode is defined by standard lithography process.

Characterization: The thickness of the deposited film was measured by profilometer (DektakXT, Bruker). The topology was characterized by an atomic force microscope (AFM, Dimension ICON, Bruker) and SEM (Supra55, Zeiss). The phases of the thin films were determined by grazing incidence Raman measurements were performed using a Renishaw inVia Raman Microscope with a 20× objective, 1200 grooves/mm grating, and excitation wavelength of 532 nm at a laser power of 1.7 mW. Electrical characterization was carried out in a physical property measurement system (VersaLab, Quantum Design).

3.6. Supporting Information

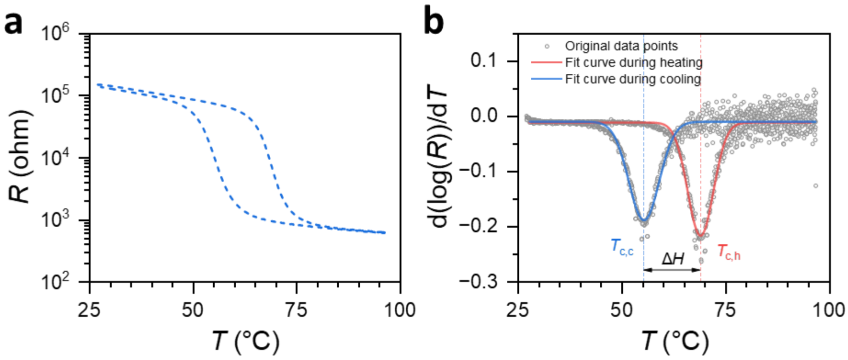

Figure S3.1. Characteristic parameters of the temperature-dependent resistance of VO_2. (a) temperature-dependent resistance of VO_2 using the standard annealing recipe. (b) Characteristic parameters of the IMT of VO_2 were determined by fitting a Gaussian curve to the derivation of the logarithmic resistance hysteretic curve for the heating and cooling branch. The critical temperatures for the transition from the insulating to the metallic phase or vice versa are defined as the minima of the heating branch $T_{c,h}$ or cooling branch $T_{c,c}$. The width of the transition ΔH can be calculated by subtracting both temperatures. Furthermore, the abruptness of a transition is defined by the full-width at half-maximum, FWHM, of the Gaussian fits, where lower numbers mean sharper transitions.

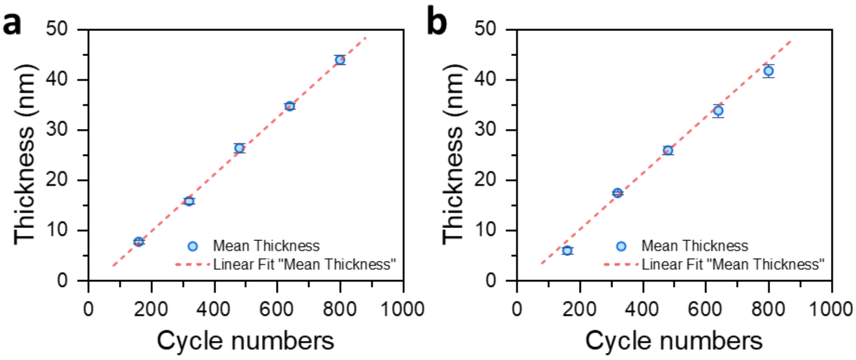

Figure S3.2. The GPCs at different temperatures. (a) 95 °C. (b) 150 °C. The GPC for the ALD process with TDMAV and H_2O was determined by measuring the film thickness using an AFM. Therefore, patterned films on Si/SiO_2 substrates were prepared using photolithography to create steps the AFM could measure. The thickness was then determined for different numbers of ALD cycles. Linear fits of the measured data yield an overall GPC of 0.56 Å/cycle for both deposition temperatures. This indicates that the deposition is well inside the ALD window.

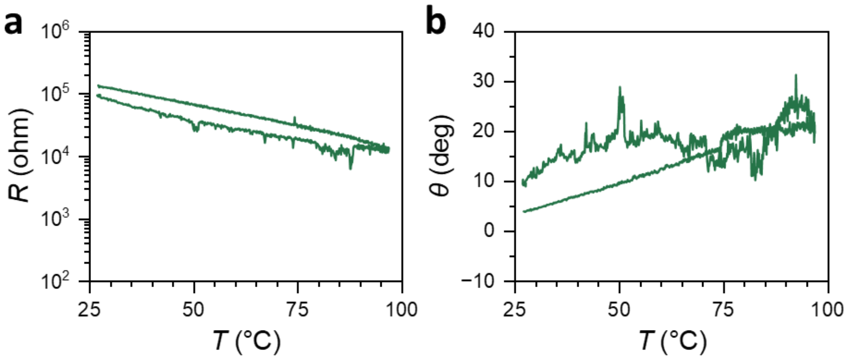

Figure S3.3. One example of the temperature-dependent measurement for the as-deposited VO_x film. (a) The resistance *R*. (b) The corresponding phase angle *θ*. For the originally deposited thin film, its resistance is generally in the order of 10^5~10^6 ohm.

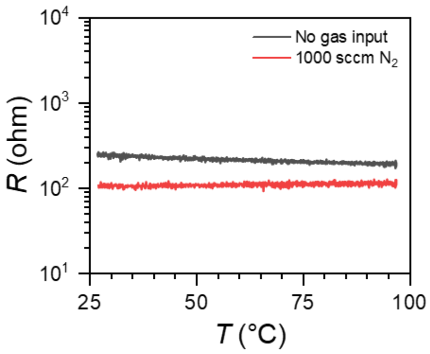

Figure S3.4. Annealing recipes without oxygen. When there is no oxygen partial pressure, the film obtained by annealing at 450℃ for 600s shows conductor properties in the temperature range of 25~90 °C, and there is no IMT phenomenon.

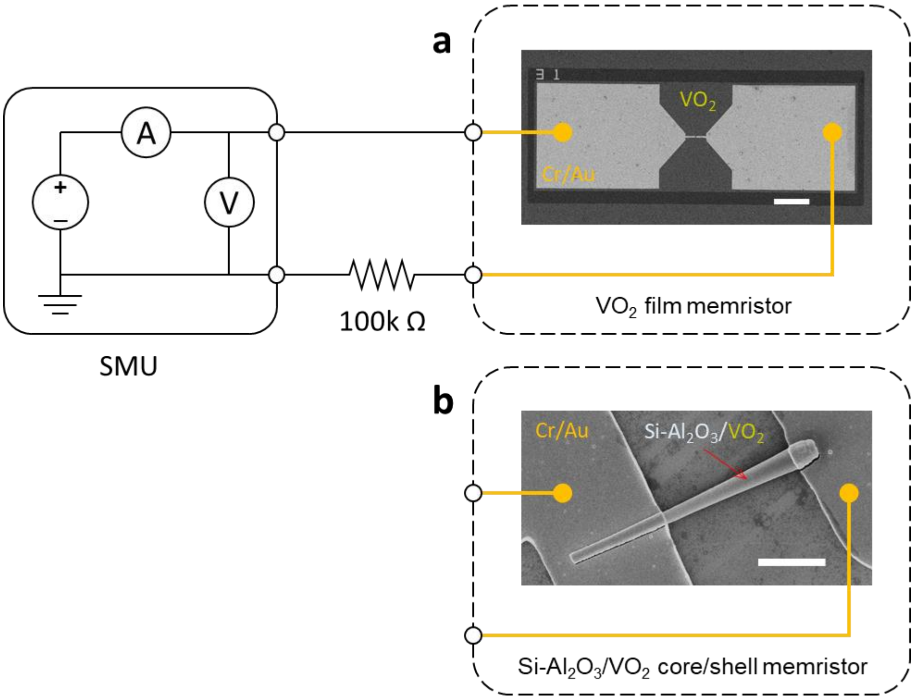

Figure S3.5. The electrical circuit of the measured memristor. (a) VO$_2$ film memristor. (b) Si-Al2O3/VO2 core/shell memristor. The source/monitor unit (SMU) is ADCMT 6241A DC voltage current source/monitor. The 100k Ω resistor is set to prevent the circuit from burning due to the instantaneous current change before and after HRS/LRS switching. The scale bars in (a) and (b) are 100 µm and 2 µm, respectively.

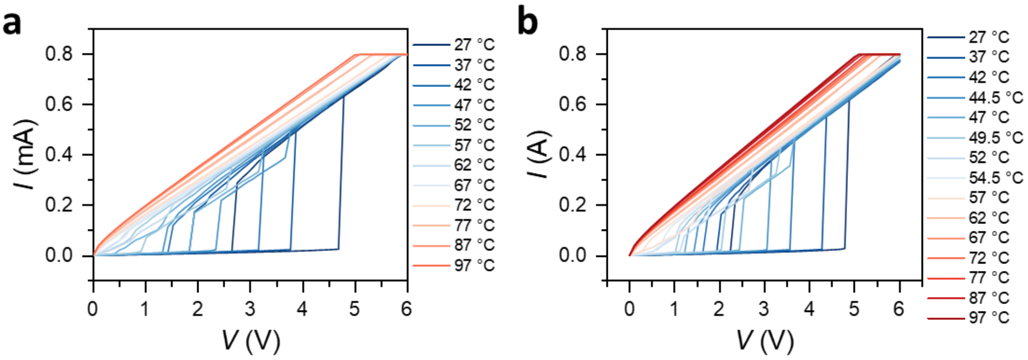

Figure S3.6. Voltage-driven I-V measurements as a function of temperature. (a) Heating process. (b) Cooling process.

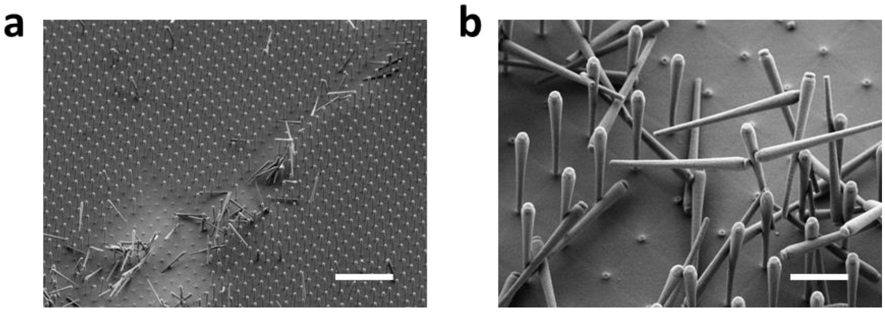

Figure S3.7. The VO_2 and Al_2O_3 coated silicon nanowire array. Scale bar for (a) and (b) are 15 μm and 3 μm, respectively.

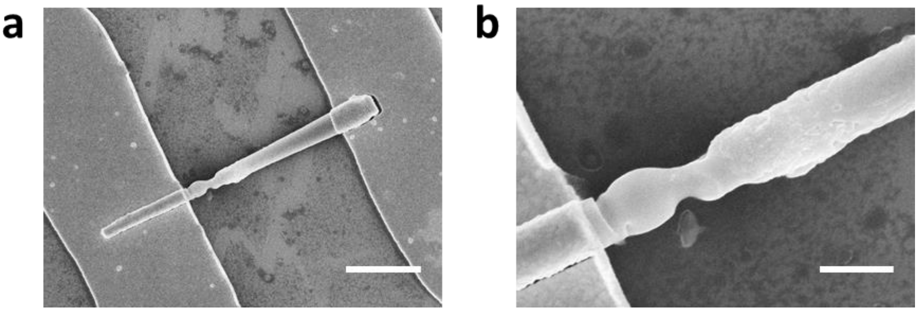

Figure S3.8. Thermal breakdown of the device. Scale bar for (a) and (b) are 2 μm and 200 nm, respectively.

Table S3.1. IMT characteristics for different ALD deposition temperatures.

Items	$T_{c,h}$ (°C)	$T_{c,c}$ (°C)	FWHM$_h$ (°C)	FWHM$_c$ (°C)	ΔH (°C)
95 °C	75.3	54.9	12.8	11.0	20.5
125 °C	71.6	53.7	10.3	11.8	18.0
150 °C	69.0	55.3	7.3	8.6	13.6

Table S3.2. IMT characteristics for different partial oxygen pressure.

Items	$T_{c,h}$ (°C)	$T_{c,c}$ (°C)	FWHM$_h$ (°C)	FWHM$_c$ (°C)	ΔH (°C)
20%	75.6	57.3	10.0	7.5	18.3
8%	70.8	56.5	6.9	7.7	14.3
4%	69.0	55.3	7.3	8.6	13.6
2%	67.1	53.4	7.9	9.4	13.7
1%	68.9	52.6	9.2	10.2	16.3

Table S3.3. IMT characteristics for different annealing pressure.

Items	$T_{c,h}$ (°C)	$T_{c,c}$ (°C)	FWHM$_h$ (°C)	FWHM$_c$ (°C)	ΔH (°C)
100 Torr	75.6	57.3	10.0	7.5	18.3
10 Torr	74.0	57.6	8.4	7.8	16.5
1.4 Torr	69.0	55.3	7.3	8.6	13.6

Table S3.4. IMT characteristics for different annealing temperatures.

Items	$T_{c,h}$ (°C)	$T_{c,c}$ (°C)	$FWHM_h$ (°C)	$FWHM_c$ (°C)	ΔH (°C)
410 °C	-	-	-	-	-
430 °C	56.2	44.4	16.5	13.2	11.8
450 °C	69.0	55.3	7.3	8.6	13.6
470 °C	72.4	57.3	7.1	7.6	15.1
590 °C	76.9	58.9	8.1	6.8	18.0

Table S3.5. IMT characteristics for different annealing durations.

Items	$T_{c,h}$ (°C)	$T_{c,c}$ (°C)	$FWHM_h$ (°C)	$FWHM_c$ (°C)	ΔH (°C)
300 s	86.5	53.4	18.3	16.7	33.1
600 s	69.0	55.3	7.3	8.6	13.6
900 s	71.1	56.9	6.8	7.4	14.2
1200 s	74.4	55.8	10.0	8.2	18.6

Table S3.6. IMT characteristics for different substrates.

Items	$T_{c,h}$ (°C)	$T_{c,c}$ (°C)	$FWHM_h$ (°C)	$FWHM_c$ (°C)	ΔH (°C)
Al_2O_3	65.0	52.3	10.4	10.6	12.8
AlN	65.6	52.1	9.3	9.9	13.5
SiO_2	69.0	55.3	7.3	8.6	13.6
Si_3N_4	65.8	51.4	8.3	9.7	14.3
Si	67.8	53.3	10.7	11.6	14.5

4. Switchable 3D photonic crystals based on the insulator-to-metal transition in VO_2

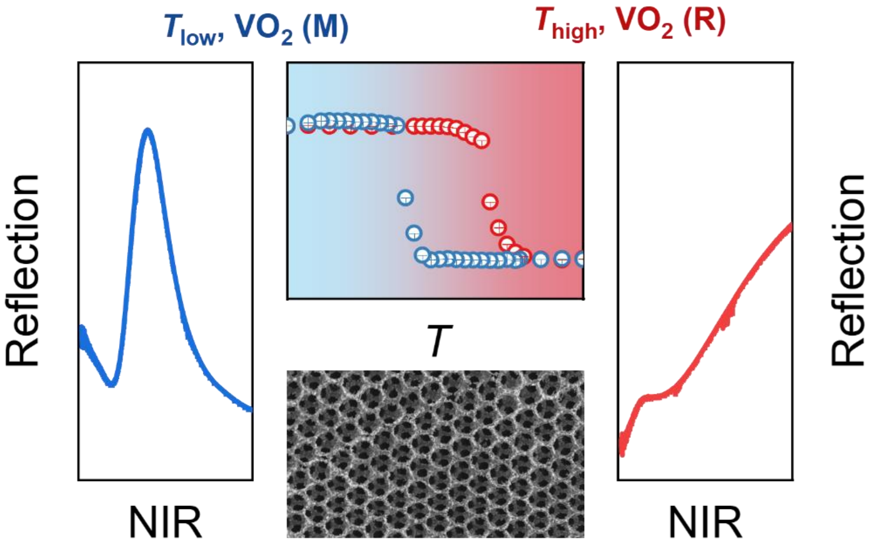

A switchable VO_2-based 3D photonic crystal inverse opal structure that exhibits substantial control over the photonic bandgap within the near-infrared region is demonstrated. The photonics is fabricated using a combination of self-assembly, atomic layer deposition, and tailored heat treatment for phase control. This switchable photonic crystal has the potential for developing advanced photonic devices with adaptable functionalities.

This chapter is adapted from a published first author's peer-reviewed article, with only the formatting changed, and the content remains unchanged.

> J. Peng, J. Brandt, M. Pfeiffer, L. G. Maragno, T. Krekeler, N. T. James, J. Henf, C. Heyn, M. Ritter, M. Eich, A. Yu. Petrov, K. P. Furlan, R. H. Blick, R. Zierold, *Switchable 3D photonic crystals based on the insulator-to-metal transition in* VO_2. ACS Applied Materials & Interfaces, 2024. 16(49): p. 67106-67115.
>
>

Manuscript title

Switchable 3D Photonic Crystals Based on the Insulator-to-Metal Transition in VO_2

Author list

*Jun Peng[1], Julia Brandt[2], Maurice Pfeiffer[2], Laura G. Maragno[3], Tobias Krekeler[4], Nithin T. James[3], Julius Henf[2], Christian Heyn[1], Martin Ritter[4], Manfred Eich[2,5], Alexander Y. Petrov[2,5], Kaline P. Furlan[3], Robert H. Blick[1,6], Robert Zierold[1]**

1 Center for Hybrid Nanostructures, Universität Hamburg, Luruper Chaussee 149, 22607 Hamburg, Germany

2 Institute of Optical and Electronic Materials, Hamburg University of Technology, 21073, Hamburg, Germany

3 Institute of Advanced Ceramics, Integrated Materials Systems Group, Hamburg University of Technology, 21073, Hamburg, Germany

4 Betriebseinheit Elektronenmikroskopie, Hamburg University of Technology, 21073, Hamburg, Germany

5 Institute of Functional Materials for Sustainability, Helmholtz-Zentrum Hereon, 21502 Geesthacht, Germany

6 Deutsches Elektronen-Synchrotron (DESY), Notkestr. 85, 22607 Hamburg, Germany

Keywords

switchable photonics, vanadium dioxide, insulator-to-metal transition, atomic layer deposition, inverse opal

Author contributions

J.P. and R.Z. designed experiments; J.P. performed ALD growth and analyses; L.M., N.J. and K.F. performed the template self-assembly experiments design and execution, XRD measurement and analyses; M.P. performed the ellipsometry measurements and analysis; J.B and J.H performed the FTIR measurement and the simulations; T.K. performed the TEM characterization and analysis. All authors analyzed the data, as well as wrote and improved the manuscript. All have approved the final version of the manuscript.

Acknowledgements

This work was funded by the Deutsche Forschungsgemeinschaft (DFG, German Research Foundation) – Projektnummer 192346071 – SFB 986 "Tailor-Made Multi-Scale Materials Systems". We thank Dassault Systèmes for providing us with their electromagnetic simulation software CST Studio Suite.

4.1. Abstract

Photonic crystals (PhCs) are optical structures characterized by the spatial modulation of the dielectric function, which results in the formation of a photonic band gap (PBG) in the frequency spectrum. This PBG blocks the propagation of light, enabling the filtering, confinement, and manipulation of light. Most of the research in this field has concentrated on static PhCs, which have fixed structural and material parameters leading to a constant PBG. However, the growing demand for adaptive photonic devices has led to an increased interest in switchable PhCs, where the PBG can be reversibly activated or shifted. Vanadium dioxide (VO_2) is particularly notable for its near-room-temperature insulator-to-metal transition, which is accompanied by significant changes in its optical properties. Here, we demonstrate a fabrication strategy for switchable three-dimensional (3D) PhCs, involving sacrificial templates and a VO_2 atomic layer deposition (ALD) process in combination with an accurately controlled annealing procedure. The resulting VO_2 inverse opal (IO) PhC achieves substantial control over the PBG in the near-infrared (NIR) region. Specifically, the synthesized VO_2 IO PhC exhibits PBGs near 1.49 µm and 1.03 µm in the dielectric and metallic states of the VO_2 material, respectively, which can be reversibly switched by adjusting the external temperature. Furthermore, a temperature-dependent switch from a narrow-band NIR reflector to a broad-band absorber is revealed. This work highlights the potential of the integration of VO_2 into 3D templates in the development of switchable photonics with complex 3D structures, offering a promising avenue for the advancement of photonic devices with adaptable functionalities.

4.2. Introduction

Photonics, the science and technology of generating, controlling, and detecting photons, has emerged as a cornerstone in modern engineering and scientific research. The manipulation of light has led to transformative advancements across various fields, including telecommunications, sensing, imaging, and computing. Central to many of these advancements are PhCs - periodic nanostructures that possess unique optical properties due to their ability to control light propagation through PBGs and resonant modes,[118, 204] which are essential to various cutting-edge applications including metasurfaces, photonic integrated circuits, and photonic diagnosis.[205-207] However, conventional static PhCs are limited by their lack of *in operando* tunability. This limitation restricts their adaptability and versatility, particularly in dynamic environments where the optical properties need to be adjusted in real-time in response to external stimuli.[208, 209] To address this challenge, researchers have focused on developing adjustable photonics, where the optical properties, such as the photonic band structure, resonance frequencies, and light propagation can be dynamically altered,[210, 211] enabling new possibilities for designing adaptive optical devices with enhanced functionality and performance.

Vanadium dioxide (VO_2) stands out as a promising material for switchable photonics because of its near-room-temperature insulator-to-metal transition (IMT), which is accompanied by significant changes in optical and electronic properties.[16, 19, 177, 212-215] In recent years, many studies have explored the use of VO_2 to construct periodic structures or to integrate VO_2 with such structures for various applications.[166, 216-218] For example, sol-gel infiltrated VO_2 integrated into core/shell 2D PhC has been used to adjust the color for thermochromic smart window applications.[219] Additionally, hybrids of crossed gold nanoantenna arrays and VO_2 thin films synthesized by chemical vapor deposition have achieved reversible switching for nanoscale optical memory functionalities.[220] Alternatively, sputtered VO_2 thin films integrated with metal metasurfaces have been utilized as optical switches, optical limiters with adjustable thresholds, and nonlinear optical isolators.[221] Despite these advancements, most VO_2 integrations have been limited to 1D or 2D structures, with little attention given to the potential of its integration with and within 3D structures.[222-224]

As an advanced and surface-limited coating technique, ALD offers precise conformality on 3D complex structures. Previous works have demonstrated the deposition of VO_2 thin films on a variety of planar substrates,[184, 186, 187, 192, 225-227] indicating the potential for integrating VO_2 into 3D photonic structures, like 3D PhCs. By exploiting the change in the optical parameters induced by the VO_2's IMT, the optical properties of integrated photonics can be dynamically modulated. In this work, we first demonstrate ALD-based VO_2 3D PhCs via a combination of ALD and followed post-deposition annealing. The temperature-dependent IMT in the annealed thin film, transitioning from a low-temperature dielectric monoclinic phase VO_2 (M) to a high-temperature rutile metallic phase VO_2 (R), is investigated from electrical, structural, and optical perspectives. Subsequently, we successfully fabricate a VO_2 IO PhC using a process adapted from the VO_2 thin film deposition process to a polystyrene (PS) opal template. The fabricated VO_2 IO PhC demonstrates PBGs at approximately 1.49 µm and 1.03 µm in the dielectric and metallic states of the VO_2 material, respectively. Significantly, these PBGs can be reversibly switched by altering the external temperature. Additionally, a switch from a narrow-band NIR reflector to a broad-band absorber is observed in the dielectric and metallic state, respectively. The successful realization of VO_2 IO PhC demonstrates the feasibility of integrating ALD-deposited VO_2 with complex 3D structures, which opens up new opportunities for switchable photonics in adaptive and versatile optical devices.

4.3. Results and discussion

4.3.1. Fabrication of ALD-deposited VO_2 thin film

The screening of suitable ALD precursors to later produce the 3D IO PhCs should meet two key conditions: (1) the precursor should not undergo chemical reactions with PS that would alter the polymer structure or degrade the template, and (2) ALD deposition should occur below the stable temperature for ALD processing of PS, which is approximately 100 °C. Attracted by the interesting IMT property, the ALD community has already reported several precursors for the successful synthesis of VO_x films, including $VOCl_3$, VCl_4, vanadium oxy-tri-isopropoxide [$VO(OC_3H_7)_3$], tetrakis(ethylmethylamino)vanadium ($V(NEtMe)_4$, TEMAV), tetrakis(dimethylamino)vanadium ($V(NMe_2)_4$, TDMAV).[224, 228, 229] Among them, TEMAV is the most studied in detail.[186, 192, 225, 226] However, in the reported literature, only the combination of TDMAV and H_2O has revealed a self-limited deposition of a dense VO_x film below 100 °C, which could then be converted into VO_2 via a post-deposition annealing process.[184, 187, 230] Therefore, we selected H_2O and TDMAV as precursors for oxygen and vanadium sources, respectively. According to the ligand-exchange mechanism which is commonly suggested for dimethylamino metal precursors, *e.g.*, $Zr(NMe_2)_4$, $Zr(NEtMe)_4$, $Hf(NMe_2)_4$, $Hf(NEtMe)_4$,[231, 232] the postulated deposition mechanism during the exposure ALD mode can be present in Figure 4.1a. During the first ALD half-cycle, the surface, saturated with hydroxyl groups (-OH) is exposed to and fully reacts with the TDMAV precursor, leaving -NMe_2-terminated groups at the surface. The by-product $HNMe_2$ and excessive TDMAV are pumped out in the following purging step. Then in the second half-cycle, the -NMe_2 groups connected to the V atom react with the second precursor, H_2O, forming a -OH group-terminated surface again after the H_2O pulse and purge step. As the deposition cycles continue, the thickness of VO_x increases linearly with the number of cycles.

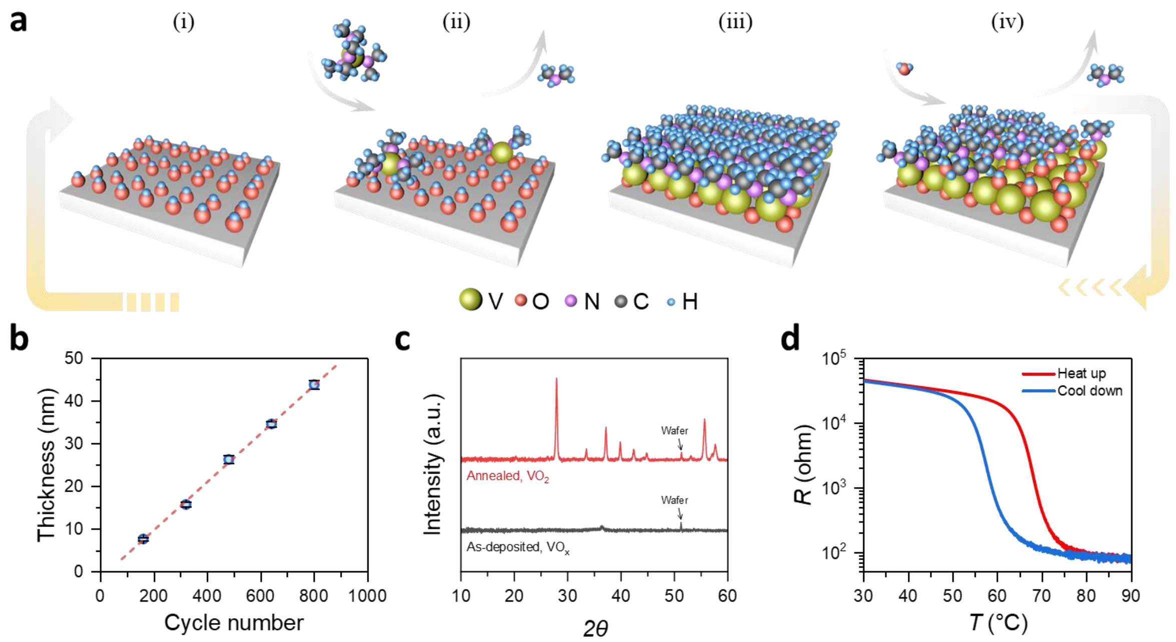

Figure 4.1. **ALD deposition of VO_2 thin film.** (a) Mechanism of VO_x film deposition via ALD. This diagram illustrates the ligand-exchange process during the ALD cycles, showing how the surface becomes terminated with (i) -OH groups and (iii) -NMe_2 groups after (iv) the H_2O and (ii) the TDMAV pulses, respectively. (b) Thickness of the deposited films as a function of the number of ALD cycles, demonstrating a constant GPC of 0.56 Å/c. (c) GIXRD spectra for the as-deposited VO_x film and annealed VO_2 film. In the annealed VO_2 film, the peak near $2\theta = 51°$ belongs to the substrate, while other peaks belong to VO_2. A more detailed labeling is shown in Figure S4.1. (d) Temperature-dependent resistance measurement of the annealed VO_2 film, revealing the IMT with over three orders of magnitude change in resistance.

The deposition temperature is set at 95 °C, where a constant deposition rate, usually termed growth per cycle (GPC), of 0.56 Å/c is obtained (Figure 4.1b). In agreement to earlier reports,[184, 187, 230] the as-deposited film is an amorphous VO_x film (Figure 4.1c and Figure S4.1a). After a post-deposition annealing process referring to the parameter's ranges used for thermal treatments of VO_x deposited by TEMAV (see Section 4.5),[192, 226] the VO_x film is converted into a polycrystalline VO_2 film in the monoclinic $P2_1/c$ space group (Figure 4.1c and Figure S4.1b). The annealing treatment not only adjusts the stoichiometry and crystallinity, but also causes changes in the film morphology, i.e., in roughness and thickness. Specifically, for a 33.6 nm thick as-deposited film, its roughness increases from 0.57 nm to 1.63 nm after annealing (Figure S4.2); and for a thicker as-deposited film of 140 nm thickness, a shrinkage of about 2% of the height was observed under the same annealing conditions (Figure S4.3). This slight change in morphology can be attributed to the more regular and orderly arrangement of atoms in polycrystalline VO_2 films compared with amorphous VO_x films after post-deposition annealing. The change in resistance over temperature is one of the most important indicators of VO_2 IMT performance. The temperature-dependent resistance measurement (Figure 4.1d) exhibits an IMT with over three orders of magnitude, accompanied by a hysteresis of 10.3 °C (Figure S4.4), which is comparable to VO_2 synthesized by other synthetic methods, such as pulsed laser deposition[233] and molecular beam epitaxy.[169, 234]

4.3.2. Structural characterization of the VO_2 thin film

The negligible morphological change and impressive electrical IMT performance indicate ALD's feasibility in constructing VO_2-based 3D structures. Furthermore, the quality of the ALD-deposited VO_2 thin films is verified by detailed Grazing Incidence X-ray Diffraction (GIXRD) and Raman characterization during *in situ* heating and cooling processes. In the *in situ* temperature-dependent GIXRD measurement shown in Figure 4.2a, a small shift of approximately 0.15° is observed at around 68 °C and 60 °C during heating and cooling, respectively, for the most intense peak near $2\theta = 28°$ representing the (011) plane of VO_2 (M). The shifted peak at elevated temperatures represents the (110) plane of VO_2 (R), indicating the expected reversible transition from the VO_2 (M) phase to VO_2 (R) phase.[14, 225, 235] To assure no other remanent phase changes occurred in the samples during the *in situ* experiments, the samples were also measured by GIXRD before and after the heating/cooling cycles covering a broader range of 2θ from 10° to 60°. The resulting diffractogram depicted in Figure S4.1b indicates a reversible IMT change without further irreversible phase transformation within the thin film.

Additionally, Raman spectra of the annealed thin film at near room temperature, i.e., $T_{\mathrm{start\_R}}$ = 19.4 °C and $T_{\mathrm{end\_R}}$ = 19.1 °C in Figure 4.2b, exhibit distinct peaks at 144.5, 195.0, 224.8, 261.6, 285.7, 310.3, 338.9, 390.28, 440.2, 499.6, 613.8 cm^{-1}, corresponding to the VO_2 (M) phase which agrees well with previous reports on crystalline VO_2.[182, 234, 236-238] The structural phase transition of the film has been monitored by temperature-dependent Raman spectroscopy (Figure 4.2c). Existing Raman peaks associated with the VO_2 (M) are expected to disappear above the transition temperature, i.e., when the film changes to the VO_2 (R) phase.[182] During the heating-up process, the intensity of all Raman peaks gradually decreases with increasing temperature. Above 65 °C up to the highest test temperature, $T_{\mathrm{max\_R}}$ = 103.4 °C all peaks belonging to VO_2 disappear, except the peaks at about 144.5 cm^{-1} and 520.0 cm^{-1}. The peak at 520.0 cm^{-1} belongs to the silicon substrate, and as expected, a linear redshift of this peak is observed as the temperature increases (Figure S4.5a). The peak at 144.5 cm^{-1} is associated with the VO_2 (M) and experiences a redshift below the transition temperature, while a significant blueshift is followed above the transition temperature, as displayed in Figure 4.2d. Noticeably, other VO_2 peaks also show similar red shifting behavior as shown in Figure S4.5b~c before disappearance. Subsequently, during cooling, the disappeared peaks start to appear again at around ~60 °C, and gradual increase in peak intensity with decreasing temperature. A similar pattern has been reported for single crystal VO_2.[188, 239] The temperature-dependent redshift can be explained by thermal lattice expansion which results in a decrease in the phonon frequency. However, the arising blueshift at the transition temperature points to an increase in phonon frequency which can be attributed to a lattice contraction.[237] Such a lattice contraction is associated with the phase transition between VO_2 (M) and VO_2 (R) phases, which is consistent with the *in situ* GIXRD results. Upon heating, the 144.5 cm^{-1} peak's intensity defined over the peak area also experiences an obvious decrease due to the IMT (Figure 4.2e). This observed behavior of the ALD-deposited VO_2 films is consistent with previous reports on strain studies of an epitaxial VO_2 film[234] and a single-crystal nanobeams.[188] Additionally, the overlapping curves from multiple temperature-dependent resistance tests on the same film sample, along with consistent Raman spectra before and after cyclic testing, indicate that the synthesized VO_2 exhibits excellent reversible switching durability in both performance and structural integrity (Figure S4.6).

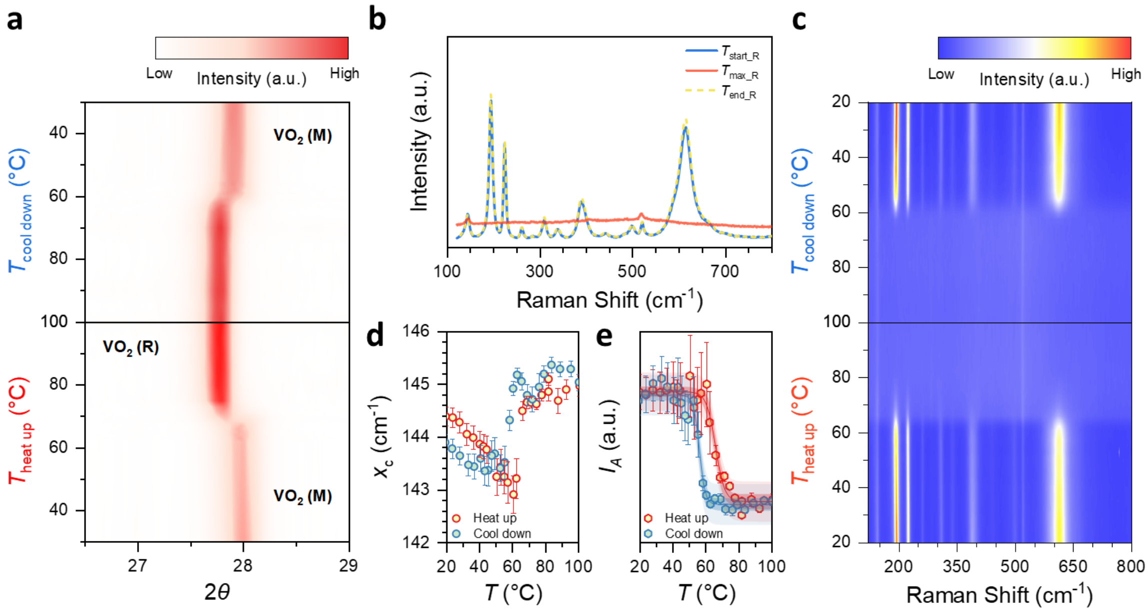

Figure 4.2. IMT characterization on thin film structure. (a) In situ temperature-dependent GIXRD measurement zoomed in near 2θ = 28° region. The peak shown belongs to the (011) plane of VO2 (M) at low temperature while the (110) plane of VO2 (R) at high temperature. (b) Raman spectra at low and high temperature. (c) Temperature-dependent Raman measurement. The peak at ~520 cm-1, which remains almost unaltered, is the signal from the SiO2/Si substrate. Lorentz fitting analysis for (d) the peak position shift and (e) the peak area as peak intensity at ~144.5 cm-1 as a function of temperature.

4.3.3. Optical properties of the VO_2 thin film

To better understand the optical properties of the ALD-deposited VO_2, *in situ* temperature dependent spectroscopic ellipsometry was used to characterize the change in complex permittivity $\tilde{\varepsilon}(\lambda) = \varepsilon' + i\varepsilon''$ of the thin film on the Si substrate over the wavelength λ during the IMT, where ε' and ε'' are the real part and the imaginary part of the complex permittivity $\tilde{\varepsilon}(\lambda)$, respectively. This measurement starts at room temperature $T_{\text{start\_E}}$ = 25.7 °C, heats to the temperature $T_{\text{max\_E}}$ = 88.4 °C, above the transition temperature, and finally cools down to near room temperature $T_{\text{end\_E}}$ = 27.8 °C again. Both ε' (Figure 4.3a) and ε'' (Figure 4.3b) reveal distinct differences between the low temperature ($T_{\text{start\_E}}$, $T_{\text{end\_E}}$) and the high temperature ($T_{\text{max\_E}}$) states. The typical value of ε' of a metal is negative, while that of a dielectric exceeds 1. At low temperatures, ε' of the thin film indicates an optically lossy dielectric behavior over the entire measured wavelength range. At high temperatures, ε' remains above 1 only for wavelengths shorter than 1 μm, meaning that the VO_2 thin film, despite the change in value, remains lossy dielectric characteristics in this wavelength range. For wavelengths longer than

1 µm, ε' becomes negative, revealing optically metallic characteristics. Limiting the discussion to this long wavelength range, these results demonstrate that the crystalline phase transition induces a pronounced change in optical properties. This is in good agreement with other reported VO_2 thin films produced by sputtering or sol-gel.[240-243] Specifically, the film begins its optical transition to the metallic VO_2 (R) phase at ~70 °C during heating and transitions back to the dielectric VO_2 (M) phase at ~60 °C during the cooldown process, as shown in the temperature-dependent colormaps of ε' and ε'' in Figure 4.3c and Figure S4.7a, respectively. In addition, similar to the resistive and structural transition, the optical transition also presents a hysteresis in the heating and cooling process. The film reflectance R_{film} can be mathematically obtained with the transfer-matrix method from the measured $\tilde{\varepsilon}(\lambda)$ (Figure S4.7b).[244] All the colormaps show a distinct IMT transition between VO_2 (M) and VO_2 (R) phases during the heating and cooling processes. When the R_{film} is plotted as line curves, the optical effect of the IMT transition on the reflection can be clearly seen (Figure 4.3d). The skin depth δ, which is the distance an electromagnetic wave travels through a material before its power is reduced to $1/e^2$, is used to explain the optical characteristics of VO_2. It can be calculated using the equation $\delta = \left(\frac{4\pi}{\lambda}k\right)^{-1}$ derived from the relation $\tilde{n}(\lambda) = \sqrt{\tilde{\varepsilon}(\lambda)}$ between $\tilde{\varepsilon}(\lambda)$ and $\tilde{n}(\lambda)$, where $\tilde{n}(\lambda) = n + ik$ is the complex refractive index, and n and k are its real and imaginary part, respectively.[245] The skin depth of the dielectric phase increases to longer λ as shown in Figure 4.3e. In contrast, the skin depth is relatively constant in the metallic phase and remains below 200 nm over the entire λ range considered. Moreover, the detailed n and k also reveal a distinct difference between VO_2 (M) and VO_2 (R) phases (Figure S4.8).

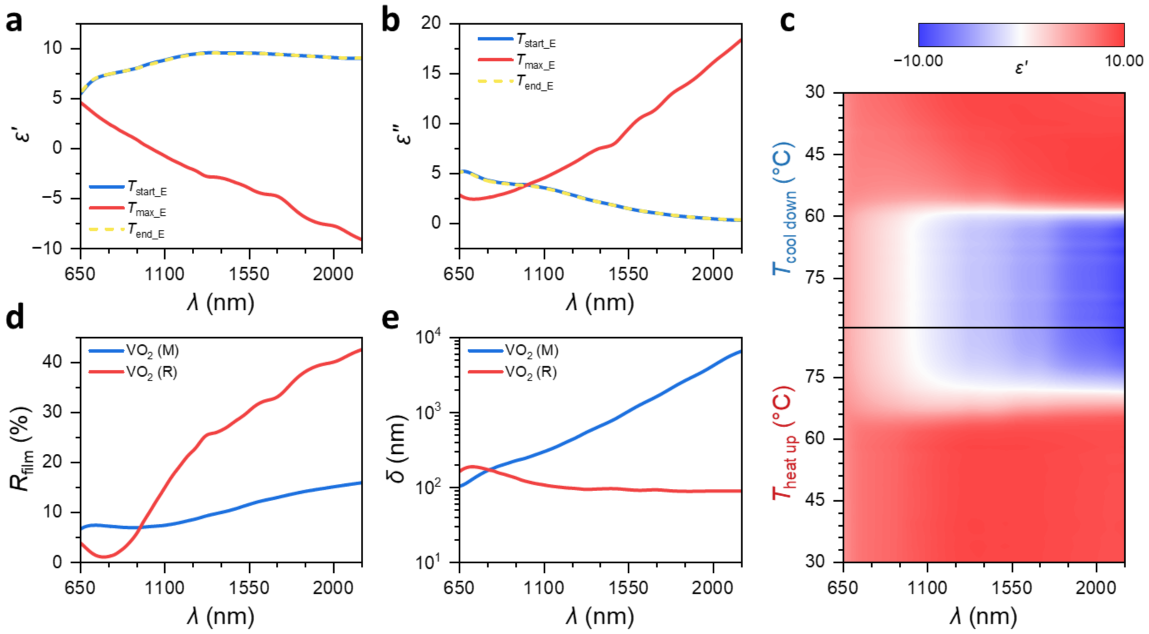

Figure 4.3. Optical characterization of ALD-deposited VO_2 thin film. (a) The real permittivity ε' and (b) the imaginary permittivity ε'' at the start ($T_{\mathrm{start\_E}}$), maximum ($T_{\mathrm{max\_E}}$), and end ($T_{\mathrm{end\_E}}$) temperatures during a continuous heating/cooling measurement obtained from spectroscopic ellipsometry as a function of wavelength λ. Note that the lines for $T_{\mathrm{start\_E}}$ and $T_{\mathrm{end\_E}}$, plotted as a solid blue line and a dashed yellow line in (a) and (b), overlap. This match indicates a fully reversible change in the optical properties of the film. (c) Colormap of ε' versus wavelength λ and temperature. (d) The film reflectance R_{film} converted from ε' and ε'',

taking the temperature at $T_{\mathrm{start\_E}}$ as VO_2 (M), and at $T_{\mathrm{max\_E}}$ as VO_2 (R). (e) Skin depth δ for the VO_2 (M) and VO_2 (R) phases plotted logarithmically. The skin depth increases significantly toward long wavelengths in the VO_2 (M) phase while remaining constant in the VO_2 (R) phase.

4.3.4. Fabrication of ALD-deposited VO_2 IO

All the above results, coupled with the inherent conformality and Angstrom-level controllability of ALD coatings, render the ALD-based VO_2 synthesis process a suitable candidate for fabricating switchable 3D photonic structures. By exploiting the pronounced reflectivity switching of VO_2 in the NIR region induced by temperature changes, alongside with the presence of a PBG of the PhC structure, we devised a controllable PhC with an IO structure. This structure allows for active control of PBGs through temperature switching, combining a narrow-band NIR reflector — determined by the PBG of the VO_2 IO — and a broad-band absorber given by the material's properties. The fabrication details are described in the Section 4.5. The successfully fabricated VO_2 IO PhC is shown in Figure 4.4. The VO_2 IO exhibits a 3D periodic and ordered multilayer porous structure throughout, from top to bottom, as presented in Figure 4.4a. This homogeneity demonstrates that the ALD coating is conformal within the opal structure. Figure 4.4b further highlights the high uniformity and regularity of the pore arrangement. Additionally, the stability of the IO structure is conserved upon heat treatment and crystallization. However, compared with the pristine PS opal template, the VO_2 IO experiences significant shrinkage (Figure S4.9). The center-to-center distance, $D_{\mathrm{Center-to-center}}$, between adjacent PS spheres or macropores at different stages in the fabrication process is statistically compared, as shown in Figure 4.4c. After the self-assembly process, the $D_{\mathrm{Center-to-center}}$ between adjacent PS spheres is 708.7 ± 9.66 nm. After VO_x ALD coating, the $D_{\mathrm{Center-to-center}}$ between adjacent VO_x-coated PS spheres is 708.6 ± 12.67 nm, remaining almost unchanged. But after removing the PS template performed at 390 °C in vacuum (Section 4.5, Figure S4.10), the $D_{\mathrm{Center-to-center}}$ between adjacent macropores decreases to 687.8 ± 27.05 nm, accounting to a shrinkage of approximately 3%. During the subsequent annealing process to adjust the IO shell composition from VO_x to VO_2, the $D_{\mathrm{Center-to-center}}$ between adjacent macropores further shrinks significantly to 566.7 ± 24.45 nm, resulting in a further shrinkage of approximately 17.6%. Overall, compared with the pristine PS opal template, the VO_2 IO shrinks by approximately 20%. This observed shrinkage is about double the value previously observed for zirconia, titania, and mullite IOs.[246-248] However, in our work, we expect that not only crystallization would occur, but also phase transitions between different vanadium oxide phases with associated shrinkage of the unit cell. Thus, the hereby observed shrinkage has the contribution from the thermal shrinkage related to crystallization as observed in other reports,[246-248] as well as the material phase change. In addition to the 3D morphology change in macropore size, the material itself undergoes a complex process and is successfully transitioned into VO_2 by a final post-deposition annealing step. The Raman spectrum of a such prepared IO is highly consistent with that of the VO_2 film as shown in Figure 4.4d, which indicates that the skeleton of IO is indeed pure VO_2 with the V oxidation state +4. Thus, the additional shrinkage from the calcined VO_x to the VO_2 phase is attributed to the change in oxidation state and not solely crystallization. However, determining the exact stoichiometry in all phases of fabrication is necessary to fully explore the volume shrinkage during the different heat treatments, and understand the differences between complex 3D structures fabrication and thin film preparation. Furthermore, a piece of an IO lamella (Figure S4.11) was prepared to further study the VO_2 IO structure using transmission electron microscopy (TEM). The radial distribution profile of the IO lamella's electron diffraction ring matches well with the same PDF card used for thin film XRD matching (Figure 4.4e, Figure S4.12). This agreement also confirms the successful fabrication of an IO made out of VO_2. In addition, the composition and microstructure of the VO_2 IO lamella remains unchanged after being heated to 100 °C and then cooled back to room temperature (Figure S4.12).

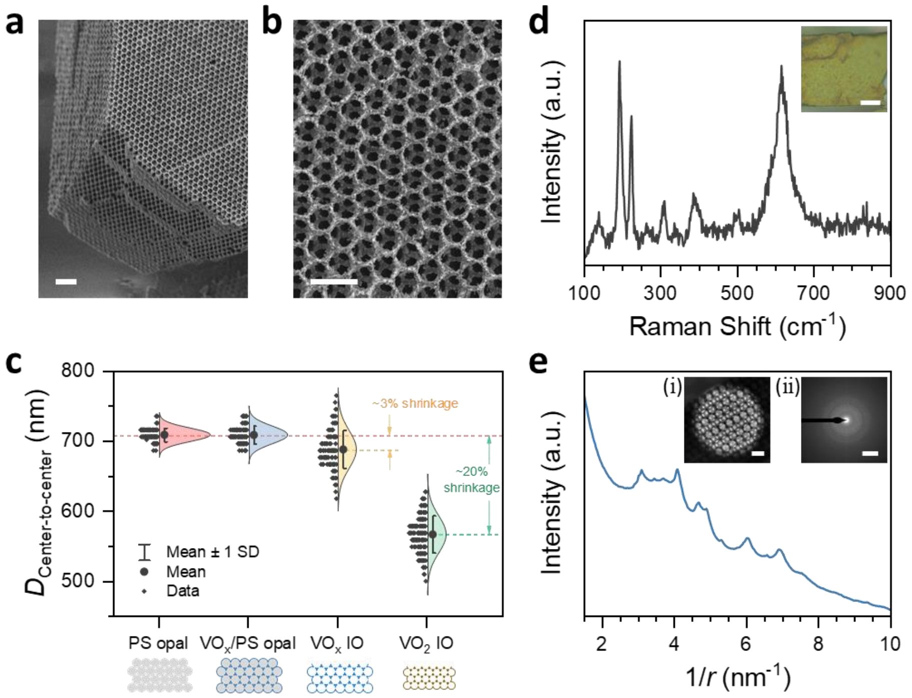

Figure 4.4. VO_2 IO PhC fabrication. SEM images of the VO_2 IO (a) from the side view at low magnification and (b) from the top view at higher magnification. (c) Statistics of center-to-center distance, $D_{\text{Center-to-center}}$, between adjacent PS spheres or macropores during the IO fabrication process: I. Pristine PS opal template, II. VO_x coated PS opal template (VO_x/PS opal), III. VO_x IO, and IV. VO_2 IO PhC. The $D_{\text{Center-to-center}}$ is measured using ImageJ software on the corresponding SEM images. The distribution curves were normalized according to the area under the curve. (d) Raman spectrum for the VO_2 IO. Inset: optical image of the VO_2 IO. (e) Radially averaged profiles of the IO lamella's electron diffraction ring using TEM before and after a heating/cooling cycle showing an unchanged VO_2 phase. Inset (i): TEM image for the VO_2 IO lamella. Inset (ii): corresponding electron diffraction pattern. Scale bars for (a), (b), (d-inset), (e-inset i), and (e-inset ii) are 2 µm,1 µm, 20 µm, 500 nm, and 5 nm^{-1}, respectively.

4.3.5. Switchable Photonics

Detailed reflection spectra R_{IO} of the VO_2 IO are recorded during *in situ* heating and cooling. At low temperatures, when the VO_2 is in the dielectric state (M), *e.g.*, at $T_{\text{start\_IO}}$ = 30 °C, a distinct PBG is identified in the NIR region with the center of Bragg peak position $\lambda_c \approx 1.49$ µm, as shown in temperature-dependent R_{IO} in Figure 4.5a. This PBG is induced by the IO structure consisting of face-centered cubic (FCC) stacked sphere-shaped air cavities embedded in the ALD-deposited VO_2 backbone, forming a periodic permittivity alteration. When the temperature rises above 80 °C, this peak in the NIR wavelength range vanishes due to the IMT of VO_2 into the VO_2 (R), which is metallic. A small peak at around $\lambda_c \approx 1.03$ µm is observed. The occurrence of this peak can be attributed to the transition in optical parameters due to the IMT, as estimated in Section 4.6.2. This peak is not as pronounced as that observed in the dielectric VO_2 (M) since the real part of the refractive index, n, of VO_2 in the VO_2 (R) phase is considerably lower than that in the VO_2 (M) phase, while the imaginary part, k, is higher (Figure S4.8). This implies that the reflection at each opal layer is small. Only a fraction of the incident light power is reflected, whereas the majority penetrates the structure and is absorbed. Moreover, due to increased absorption the peak spectrally widens making it less pronounced. In addition, similar to the R_{film} of the VO_2 (R) in Figure 4.3, the R_{IO} becomes broadband towards longer λ as the temperature increases. During the subsequent cooling process, the Bragg peak $\lambda_c \approx 1.49$ µm reappears as the dielectric state is restored, and the photonic structure reverts to being a narrow-band NIR reflector. Figure 4.5b shows in more detail the reflectivity curves corresponding to the starting temperature $T_{\mathrm{start\_IO}}$, maximum temperature $T_{\mathrm{max\_IO}}$, and end temperature $T_{\mathrm{end\_IO}}$ of the test. The weak peak at $\lambda_c \approx 1.03$ µm above the IMT transition temperature, *e.g.*, $T_{\mathrm{max\_IO}}$, is much more pronounced than when using the colormap diagram. In addition, the electromagnetic simulation results for the VO_2 IO in dielectric VO_2 (M) phase (corresponding to the low temperatures, $T_{\mathrm{start\_IO}}$, and $T_{\mathrm{end\_IO}}$) and metallic VO_2 (R) phase (corresponding to high temperature, $T_{\mathrm{max\_IO}}$) are compared with the experimental reflectance spectra here, showing a good agreement with the experimental data, particularly in the general position and relative intensity of the Bragg peaks in both states. Minor deviations between simulation and experiment mainly stem from the fact that the macropores' size has a certain distribution, the existence of cracks, and the roughening of the surface of the VO_2 shell due to the annealing, resulting in diffuse scattering beyond the microscope's aperture. The Bragg peak's position λ_c during the temperature-dependent measurement from Figure 4.5a is presented in processed form in Figure 4.5c, revealing a reversible switch with external temperature. Specifically, when VO_2 is in the VO_2 (M) phase (low temperature), only the PBG near 1.49 µm in IO exists. But it switches off at high temperatures when the VO_2 is in a VO_2 (R) phase. The situation of the PBG near 1.03 µm is just the opposite. Similarly, there is a hysteresis in this switching which is consistent with the other fixed positions of R_{IO} in Figure S4.13. Besides, the variation of R_{IO} with temperature also exhibits a hysteresis, which is wider than that observed in thin films (Figure S4.13). Early reports show that the hysteresis of VO_2 in thin films can be altered by introducing of either tensile or compressive strain, resulting in a narrower or wider hysteresis, respectively.[15, 197] The 20% shrinkage observed during synthesis likely introduced residual stresses, which may differ from the thin film due to the different underlying substrates. While the thin film sits on top of a silicon substrate, the IO is assembled on top of a microscope glass substrate. Moreover, they have different thicknesses of around 0.5 mm for the Si wafer against 1 mm of the glass, likely leading to a lower surface temperature of the IO during measurement in comparison to the thin film, since the heating plate heats them from underneath the substrate. All combined results in a wider IMT hysteresis in the VO_2 IO.

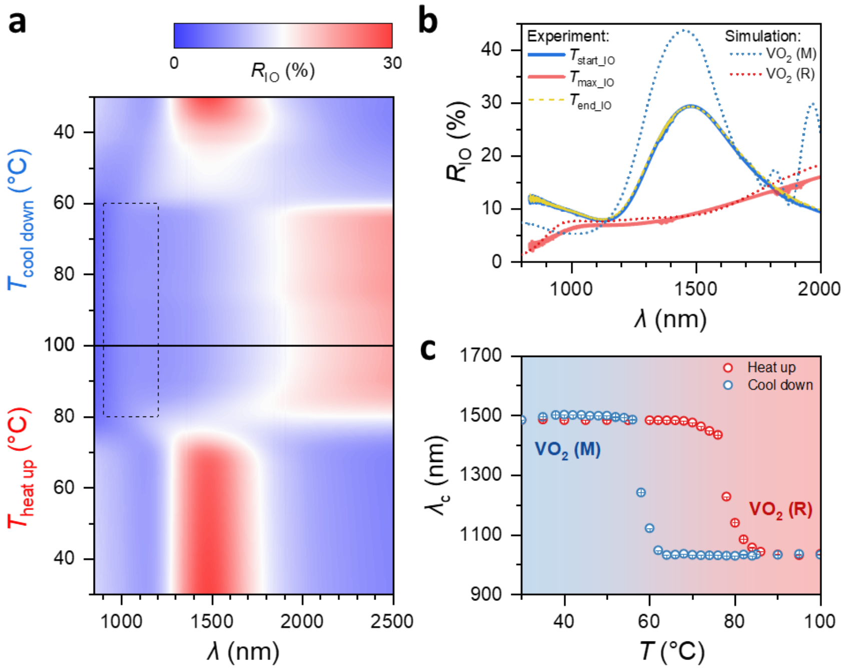

Figure 4.5. Switchable PBG of VO₂ IO PhC. (a) Reflection spectra R_{IO} during a heat-up and following cool-down measurement. (b) Experimental R_{IO} and simulated R_{IO} at high and low temperatures. The experimental results for T_{start_IO} and T_{end_IO} overlap. The small peak in the 900-1200 nm region of the curve marked as T_{max_IO} in (b) is highlighted in the roughly corresponding region with a black dashed box in (a). The oscillation in the simulated spectrum of the VO_2 (M) phase results from Fabry-Perot interference. (c) The Bragg peak position λ_c as a function of temperature, showing a switch function adapted to the external temperature. The Bragg peak position λ_c shifts from about 1.49 μm below the IMT transition temperature to about 1.03 μm above the IMT transition temperature.

4.4. Conclusions

We successfully prepared high-quality polycrystalline VO_2 thin films via ALD combined with a post-deposition annealing treatment. Furthermore, the synthesis route was then adapted to conformally coat opaline PS templates, resulting in the successful fabrication of switchable VO_2 IO PhCs. The VO_2 thin films demonstrated an IMT in structural, electrical, and optical properties at about 60~70 °C, similar to previously reported VO_2 thin films obtained by other methods, *e.g.*, magnetron sputtering, molecular beam epitaxy, and sol-gel. The integration of the VO_2's IMT properties with IO PhCs structure opens active capabilities other than conventional photonics. Our VO_2 IO exhibits a reversible switching between two different bandgaps at nearly 1.49 μm and 1.03 μm at low-temperatures dielectric state and high-temperature metallic state, respectively. This work provides a convincing example of the integration of ALD-based VO_2 coating and devices with complex structures, holding significant promise for further unleashing the potential of VO_2 as the route herein described can be applied to other low-temperature substrates, such as 3D-printed polymers.

4.5. Experimental Section

Thin film fabrication: The VO_2 thin film fabrication process involved two steps. Initially, a non-stoichiometric VOx layer was deposited via thermal ALD in exposure mode, utilizing a modified Savannah^{TM}100 reactor (Cambridge Nanotech). The deposition was conducted at 95 ℃ with 30 sccm (standard cubic centimeter per minute) nitrogen as carrier gas and purge gas. The working pressure during deposition was approximately 1.5 Torr. Various substrates including SiO_2/Si wafers and pure polished Si wafers (SIEGERT WAFER GmbH) were employed for coating. The precursors, deionized water and tetrakis(dimethylamino)vanadium(IV) (TDMAV, Strem Chemicals, Inc., USA) were utilized as oxygen and vanadium sources, respectively. The combination of "precursor pulse time / exposure time / purge time" was set as 0.1/15.0/60.0 s for deionized water and 1.0/15.0/60.0 s for TDMAV. Subsequently, the VO_x film was annealed at 425 ℃ in a vacuum oven (MC050, ANNEALsys) at 0.1 Torr for 10 min within a controlled atmosphere (10 sccm O_2, 100 sccm N_2).

VO_2 IO PhC fabrication: The vertical self-assembly of the 757 nm diameter polystyrene beads (Microparticles GmbH) into an opal structure with FCC stacking followed a previously published procedure.[248] Next, the template was placed in the ALD chamber and coated by VO_x at 95 ℃ with a prolonged exposure time and purge time, i.e., 0.1/60.0/90.0 s and 1.0/60.0/90.0 s, for deionized water and TDMAV, respectively. These parameters were set to enhance precursor penetration into the voids within the template, based on our previous studies on titania and mullite.[239, 249] Following this, a portion of the top layer of the coated sample was etched using a reactive ion etching system (SENTECH SI 500) via Ar ion sputtering. Afterward, template removal, coupled with a post-deposition annealing process, was conducted in the vacuum oven (MC050, ANNEALsys) to achieve VO_2 phase in the 3D structure of the inverse opal photonic crystal. The annealing cycle consisted of two steps: (1) Controlled PS template removal to avoid potential phase changes from VO_x phase to V_2O_5 phase or distortion of the 3D structure in the 2nd step. Specifically, the template removal was performed at 390 °C, near the polystyrene vaporization point, with a 1 °C/min heating rate in a vacuum of 0.01 Torr and maintained for 6 hours. (2) Then the temperature was tuned to 425 ℃, 100 sccm N_2 and 10 sccm O_2 were input, and the pressure was maintained at 0.1 Torr for 20 min for the subsequent post-deposition annealing process to achieve VO_2 phase.

Thin film characterization: Water-diluted HCl (20:1) is used to etch the as-deposited film to prepare a step-edge for thickness measurements by a profilometer (DektakXT, Bruker). Atomic force microscope (AFM, Dimension ICON, Bruker) was applied to determine the thin film’s roughness. Electrical characterization was carried out in a Physical Property Measurement System (VersaLab, Quantum Design). The crystalline phases of the thin films were determined by grazing incidence X-ray diffraction analysis (Bruker AXS D8 Advance, Bruker) using Cu Kα radiation. The incident angle was 0.5°, with the range, step size, and step time set to 26.5 to 29.0°, 0.01° and 2 s for the *in situ* measurements and 10° to 60°, 0.01° and 2 s for the *ex situ* measurements. The *in situ* measurements were performed using a high-precision hot stage (DHS 900, Anton Paar) and a heating controller (TCU 150, Anton Paar). Heating and cooling cycles were performed from 25 °C until 90 °C with increments of 5 °C per measurement. Before data collection, samples were allowed to equalize the temperature for 5 min at each temperature data point. To ensure that no other phase change occurred due to the heating/cooling cycles, the samples were analyzed *ex situ* at room temperature (25 °C) before and after the *in situ* measurements. Raman measurements were performed using Renishaw inVia Raman Microscope equipped with a 20× objective, 1200 grooves/mm grating, and an excitation wavelength of 532 nm at a laser power of 1.7 mW. The Raman system incorporated a home-made temperature controller comprising a thermoelectric power generator Peltier module (SP1848-27145, VGEBY), a copper water cooling unit, and a voltage source. The optical measurements of the thin films were performed with spectroscopic ellipsometer (SE-2000, SEMILAB) equipped with a heating chamber (Linkam). All measurements were performed at an incidence angle of 65° within the wavelength range of 650 nm to 2150 nm. The sample consisted of a 138.6 nm VO_2 layer on a 2 nm native SiO_2 layer on a Si substrate. The sample was heated in an open chamber in an air atmosphere to mitigate the influence of windows during data collection, reaching temperatures up to 88 °C in increments of approximately 2 °C with a 120 s holding time before starting the spectroscopy ellipsometry measurement. Temperature readings were calibrated using a thermoelement (NiCr-Ni) attached to the upper surface of the sample. The $\tilde{\varepsilon}(\lambda)$ of the VO_2 layer was obtained from the measured ellipsometry angles (Psi and Delta) by mathematical inversion method[250] and afterwards checked for consistency with Kramers-Kronig relations. Both methods are implemented by Semilab in their Spectroscopic Ellipsometry Analyzer (SEA) software.

Characterizations of VO_2 IO PhC: SEM images were taken via scanning electron microscopy (SEM, Supra 55 VP, Zeiss). FIB-preparation and transfer of the TEM-lamella to the *in situ* MEMS chip was done with a Thermo Fisher Helios G3 UC according to the standard lift-out procedure. Contacting of the lamella to the MEMS chip was performed with beam-induced platinum deposition. The *in situ* experiments were performed in a Thermo Fisher Talos F200X transmission electron microscope equipped with a Thermo Fisher NanoEx™-i/v *in situ* TEM sample holder. TEM micrographs were recorded in BF-TEM mode at 200 kV and 10 nA beam current. SAED patterns were recorded at a camera length of 840 mm. Intensity profiles were extracted using Velox TEM software (Thermo Fisher). Control of Temperature and heat rate were done with NanoEx-control software. The reflection spectra of the IO PhC samples were recorded using an FT-IR spectrometer Vertex 70 combined with a microscope Hyperion 2000 (Bruker Optics), and a Linkam Heating chamber TS1500. During heating, increments of 5 °C were applied for each measurement within the temperature ranges of 20 °C to 60 °C and 90 °C to 105 °C. Additionally, a smaller increment of 2 °C was applied near the IMT temperature, specifically within the range of 60 °C to 86 °C. In the cooling stage, increments of 5 °C were set within the temperature ranges of 105 °C to 85 °C and 84 °C to 20 °C. Furthermore, a smaller increment of 2 °C was applied within the temperature range of 60 °C to 38 °C.

Electromagnetic simulation: The simulations were performed using a Frequency Domain Solver with hexagonal unit cell boundary conditions from the CST Studio Suite (Dassault Systèmes). The simulation model (see Figure S4.14) is designed as follows: there are six consecutive layers of spheres of 566 nm diameter, which are assembled into an FCC lattice with the (111)-plane parallel to the surface. For VO_2, we applied the permittivity function obtained from the ellipsometry measurement of the thin film. Below the spheres, a glass substrate with $\varepsilon = 2.25$ was considered. The background is air.

4.6. Supporting Information

4.6.1. Supporting figures

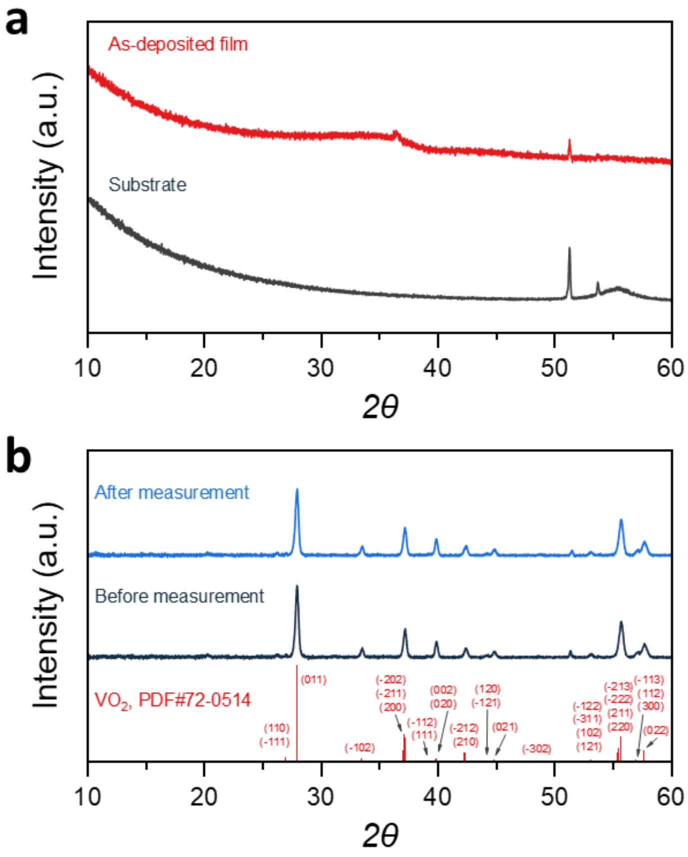

Figure S4.1. Comparisons of *ex situ* GIXRD measurements. (a) Comparison of the as-deposited film and the substrate's GIXRD signal. In the as-deposited film, the two peaks at $2\theta \approx 51.2°$ and 53.6° come from the substrate. The weak peak at $2\theta \approx 36.5°$ might be contributed by many vanadium oxides compounds such as V_2O_3, V_5O_9, V_6O_{13}, VO_2. (b) The full measurements of an annealed thin film before and after the *in situ* temperature-dependent measurements showing no alteration in the main phase due to the heating/cooling cycle. The dominant compound in the annealed film is VO_2 (PDF#72-0514, $P2_1/c$).

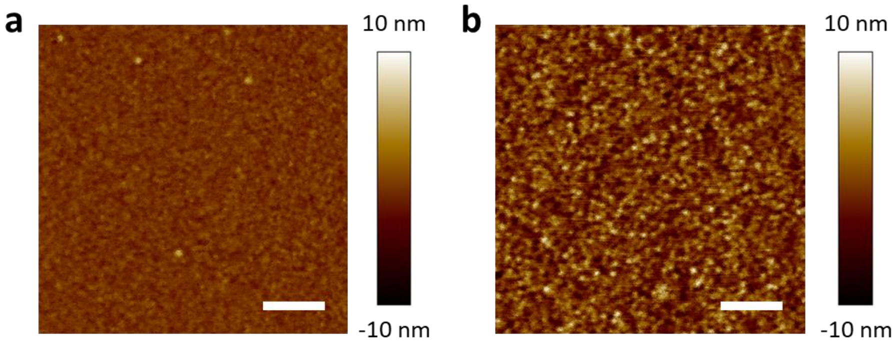

Figure S4.2. The surface morphology comparison for the same sample before and after post-deposition annealing using AFM. (a) The initial as-deposited VO_x film with a thickness of 33.6 nm is smooth and dense, characterized by a surface roughness (R_a) of 0.574 nm. (b) Subsequent to annealing, the VO_x film underwent crystallization, transforming into a crystallized VO_2 film, accompanied by an increase in surface roughness to 1.630 nm. Scale bars for (a), (b) are all 1 μm.

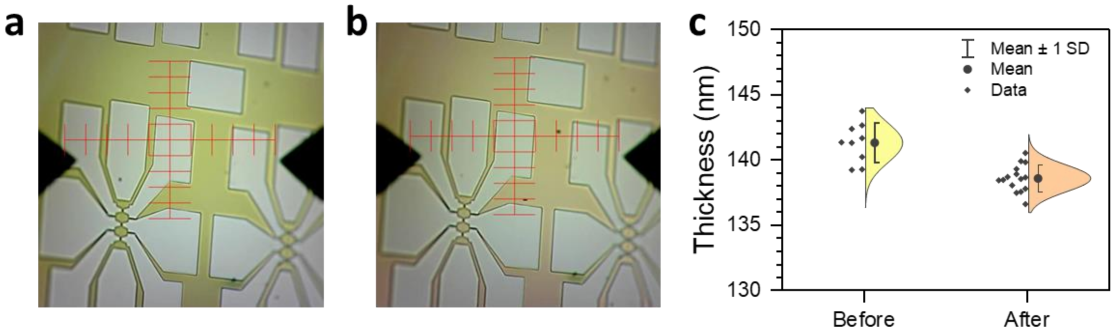

Figure S4.3. Optical microscope photos of the same thin film sample at the same position (a) before and (b) after annealing. The specific pattern on the sample has no meaning, it is generated during the process of constructing the step height for the step meter to measure. First, the pattern is defined on the VO_x film through a standard photolithography process, then the film within the developed area is etched with a chromium etching solution, followed by a clean process using acetone, isopropanol, and deionized water, resulting in a VO_x film with steps. These photos are derived from a file profilometer, and the length of each small transverse grid in the cross ruler is approximately 150 μm. After annealing, the color of the film becomes darker due to slight change in stoichiometry to the VO_2 phase. (c) Results of multiple thickness measurements on the same sample before and after annealing. Annealing reduces the thickness of the film from 141.3 ± 1.52 nm to 138.6 ± 1.03 nm, a decrease of approximately 2%.

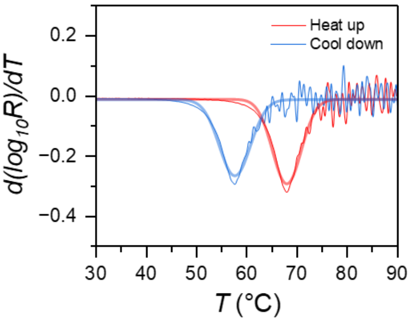

Figure S4.4. The corresponding Gaussian fitting of the derivation of the logarithmic *R* hysteretic curve in Figure 4.1d to determine the transition temperature and hysteresis. The transition temperature during heating is 68.0 °C, while during cooling is 57.7 °C, with a hysteresis of 10.3 °C. Taking the average value of the IMT temperatures during the heating and cooling processes as the IMT temperature of the sample, the IMT temperatures of the film during the electrical measurement is 62.85 °C.

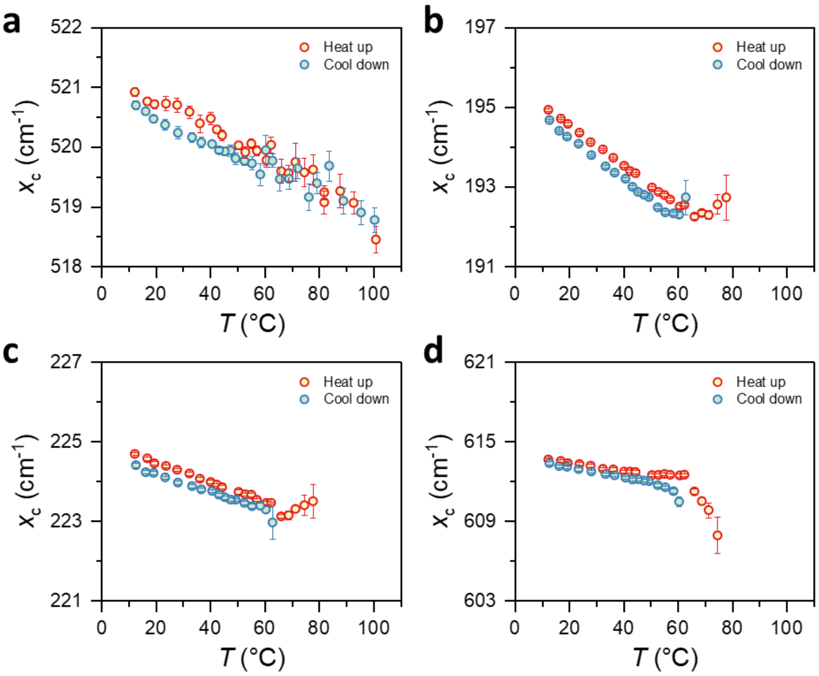

Figure S4.5. The shift of Raman peak position x_c peaks during the temperature-dependent Raman characterization in Figure 4.2c. (a) The Si signal from the substrate. It redshifts due to the lattice expansion with temperature. The three typical VO_2 signals at near (b) 194 cm^{-1}, (c) 244 cm^{-1}, and (d) 612 cm^{-1} when room temperature. The two characteristic peaks at near 194 cm^{-1} and 244 cm^{-1} both with A_g symmetry are assigned to V–V vibration modes, and the high-frequency peak at near 612 cm^{-1} with A_g symmetry relates to the V–O vibrations.[182] The three peaks show a slight redshift between RT and near 60 °C. However, the peaks near 194 cm^{-1} and 244 cm^{-1} show a significant blue shift at temperatures above 60 °C, while the peak near 630 cm^{-1} exhibits more pronounced red shift. After about 80 °C, all peaks disappear. These strong changes occur near the IMT temperature.

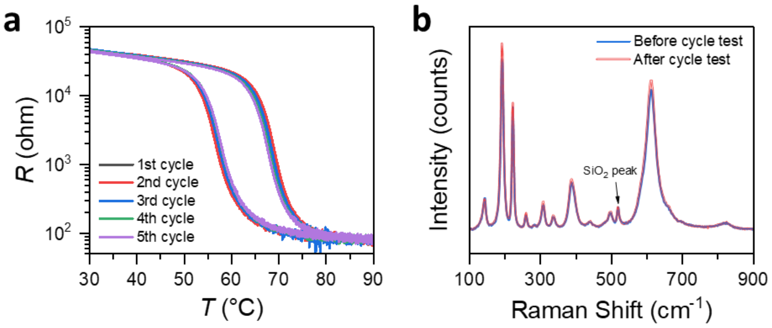

Figure S4.6. Reversible switching durability test of the VO_2 thin film. (a) Five consecutive temperature-dependent resistance tests. (b) Raman spectra comparison before and after the temperature-dependent resistance tests. The overlap character in both tests confirms the superior reversible switching properties of the ALD-assisted synthesized VO_2.

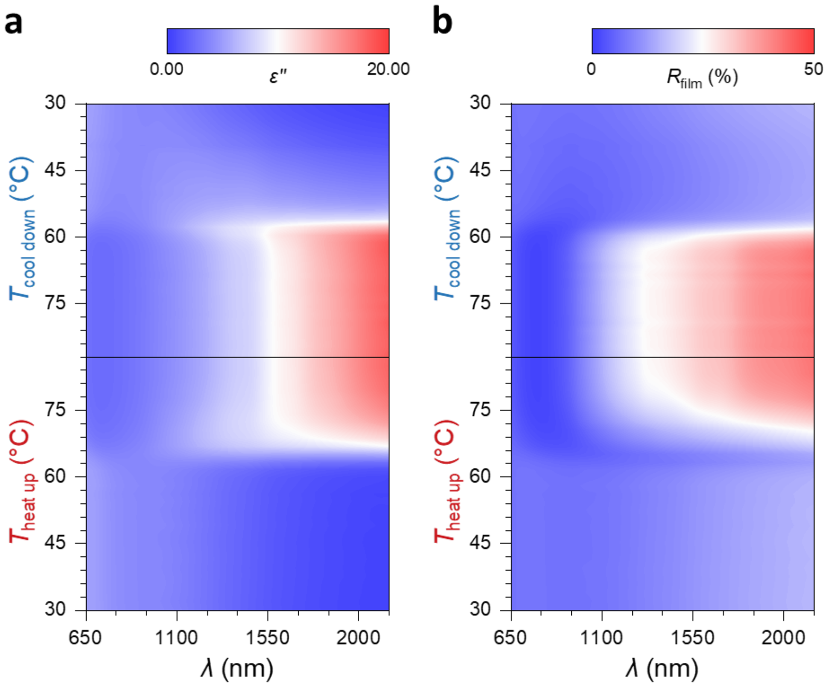

Figure S4.7. (a) Colormap of the temperature-dependent imaginary permittivity ε''. (b) Colormap of the film reflectance R_{film} converted mathematically from ε' and ε'' with the transfer-matrix method and plotted as a function of wavelength and temperature.

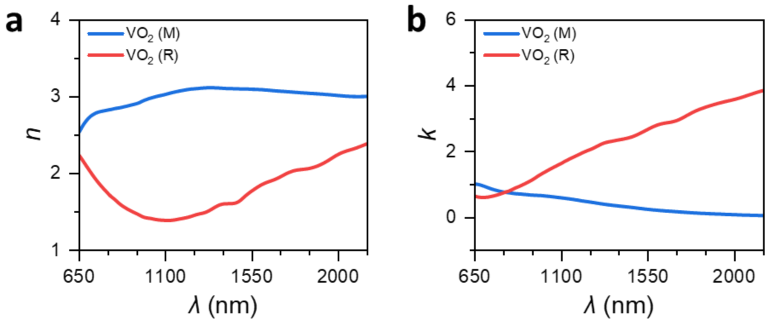

Figure S4.8. Complex refractive index of the VO_2 thin film. (a) *n*. (b) *k*.

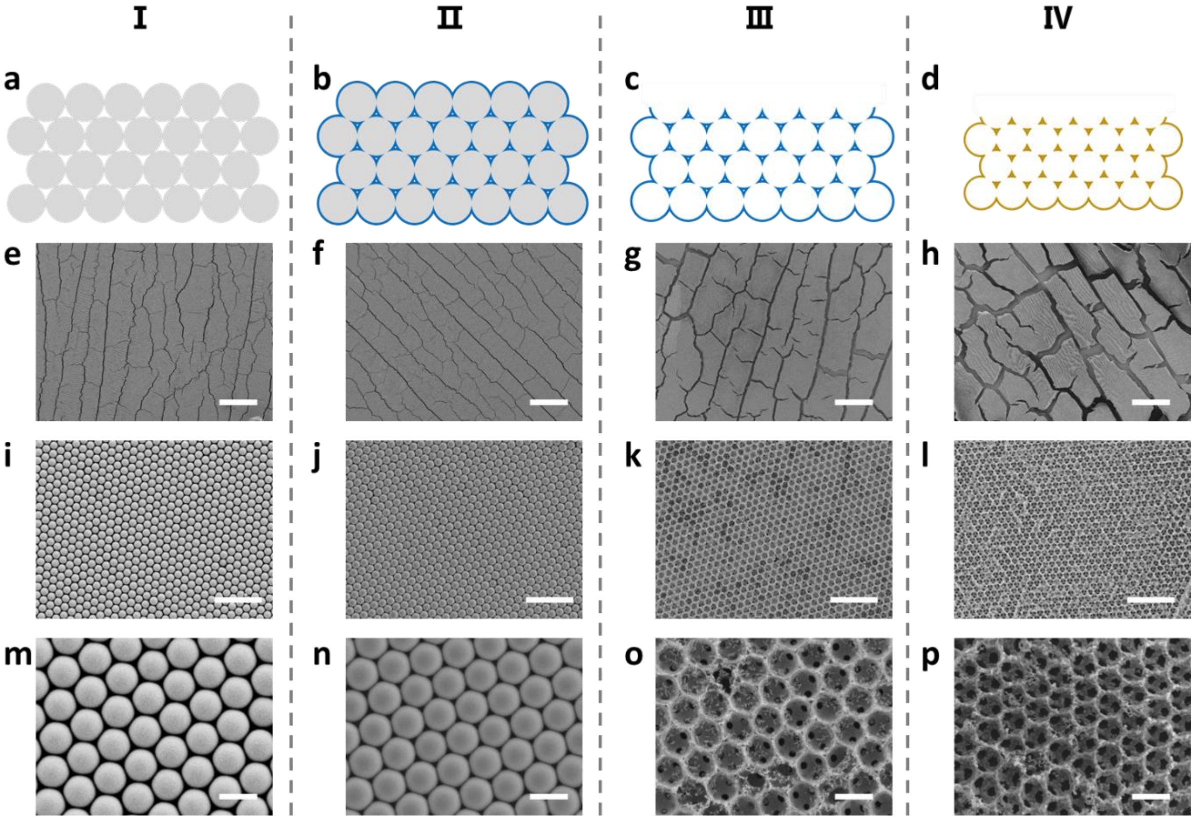

Figure S4.9. Shrinkage of the sample during preparation. Pristine PS opal template (column I), VO_x coated PS template (column II), VO_x IO (column III), and VO_2 IO PhC (column IV). (a~d) the side view sketch of the opal or IO layer at stages I, II, III, and IV. (e~h) SEM images for the samples at stages I, II, III, and IV. The scale bars are all 80 μm. (i~l) Zoomed-in SEM images for the samples at stages I, II, III, and IV. The scale bars are all 4 μm. (m~p) Further zoomed-in SEM images for the samples at stages I, II, III, and IV. The scale bars are all 800 nm. In (g) and (h), the gaps between opal blocks increase continuously compared to those in (e) and (f), and traces of the original pure PS template's location can even be seen in some large gaps. This maybe the results of the shrinkage.

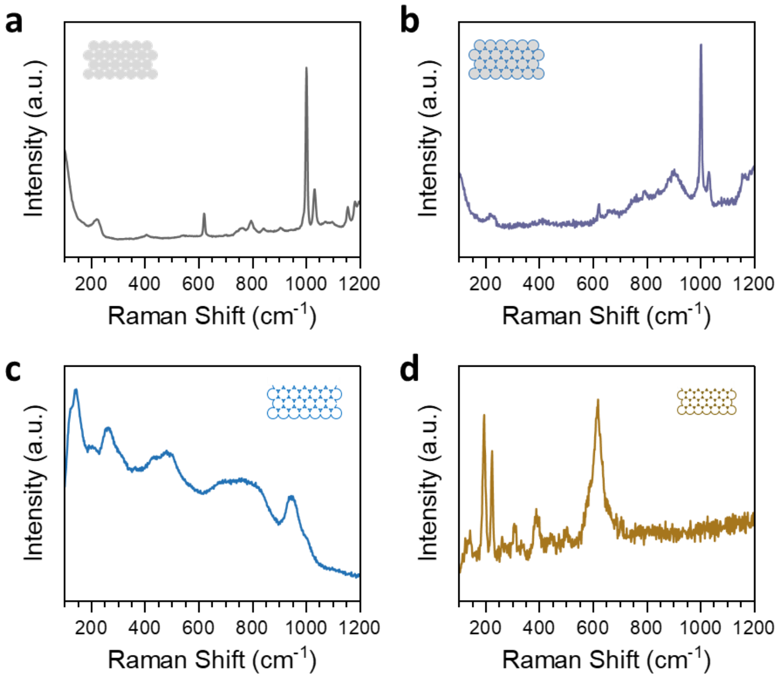

Figure S4.10. Raman curves of the main steps in the VO_2 IO process. (a) Pristine PS opal template. (b) VO_x coated PS template. After ALD deposition of VO_x, the curve is still dominated by PS signals, but a new peak belonging to vanadium oxide compounds appears around 700 ~ 950 cm^{-1}. (c) VOx IO. This curve does not contain the main peak of V_2O_5. (d) VO_2 IO PhC.

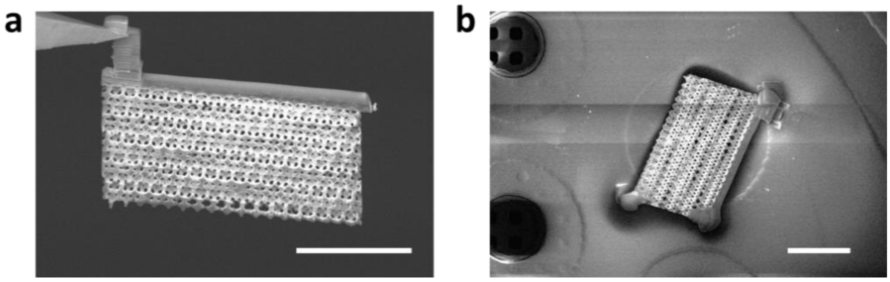

Figure S4.11. SEM images of the VO_2 IO lamella for the TEM characterization. Scale bars for (a), and (b) are all 5 µm.

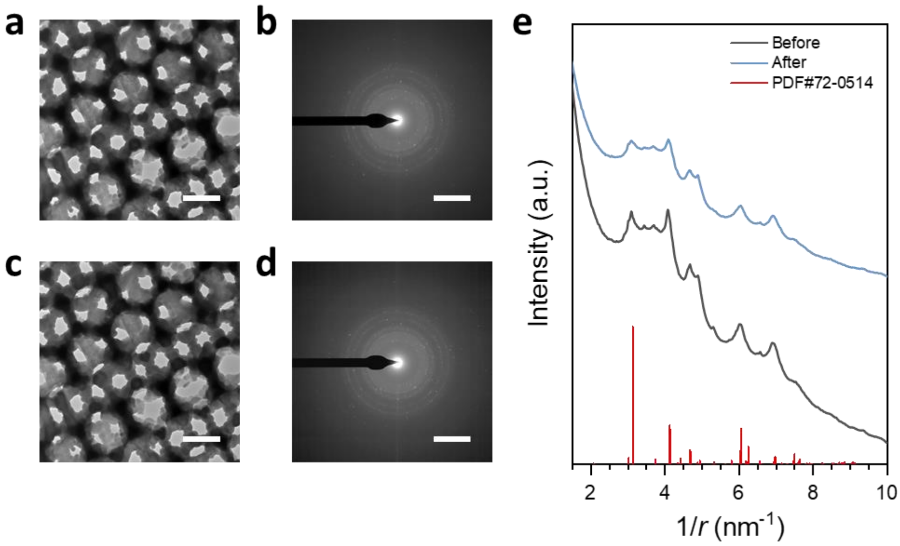

Figure S4.12. Detailed comparison of the TEM characterizations before and after heat-up and cool-down treatment. (a) TEM image and (b) corresponding diffraction ring pattern before heat-up treatment. (c) TEM image and (d) corresponding diffraction ring pattern after cool-down treatment for the same lamella at the same area. (e) Comparison of radial integrated diffraction patterns before and after heat-up and cool-down treatment. Peak position in the intensity profiles match well with values from PDF card (PDF#72-0514, $P2_1/c$), indicating the good structural integrity during the IMT phase transition. The faint peak near $1/r = 3.44\ \mathrm{nm}^{-1}$ can be explained with nanocrystalline gallium, which is a residue of FIB preparation of the lamella. The peak position corresponds to the (111) lattice plane distance in alpha-Ga (2.95Å). Scale bars from (a) to (d) are 500 nm, 5 nm^{-1}, 500 nm, and 5 nm^{-1}, respectively.

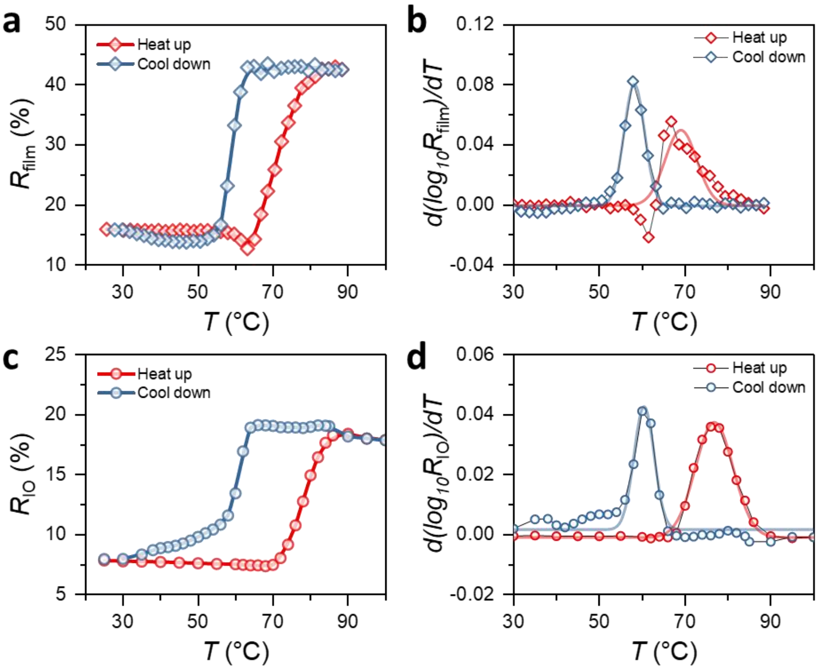

Figure S4.13. Comparison of the temperature-dependent reflectance between the VO_2 thin film and the VO_2 IO PhC at the wavelength of 2150 nm. (a) The VO_2 thin film reflectance R_{film} and (b) the corresponding Gaussian fitting of the derivative of the logarithmic R_{film} hysteretic curve to determine the transition temperature and hysteresis. (c) The VO_2 IO PhC reflectance R_{IO} and (d) the corresponding Gaussian fitting of the derivative of the logarithmic R_{IO} hysteretic curve to determine the transition temperature and hysteresis. This wavelength is picked because it is in the near IR region where the *R* of both thin film and IO are not affected by the structure judging from Figure 4.3c and Figure 4.5a. Remarkably, the hysteresis in the heating and cooling process is quite similar to the trend of the typical IMT on resistance as shown Figure 4.1d. The IO sample shows a higher transition temperature (76.8 °C) than that of the thin film sample (69.1 °C) during the heating process, while during the cooling process, the transition temperature of the IO sample (60.5°C) is comparable to that of the thin film sample (58.2°C). Taking the average value of the IMT temperatures during the heating and cooling processes as the IMT temperature of the sample for comparison, the IMT temperatures of the film and IO samples are 63.65 °C and 68.65 °C, respectively.

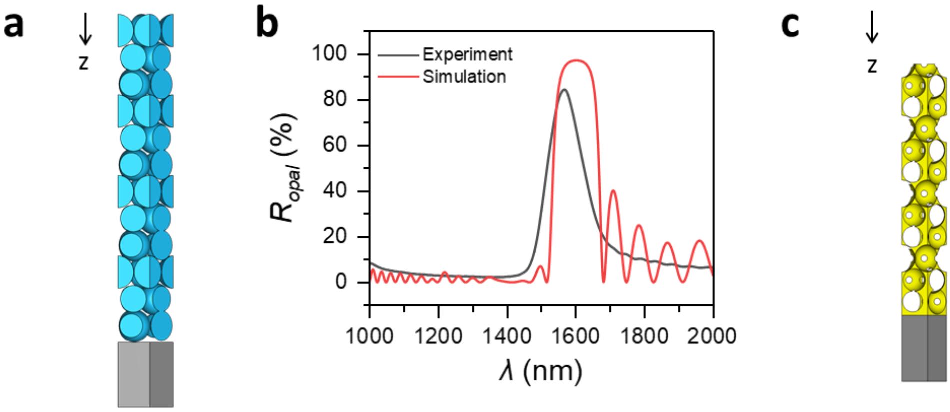

Figure S4.14. Simulation models. (a) Simulation model for the direct PS opal template. (b) Comparison of the opal reflection R_{opal} from the experiment and simulation. Both center positions of the peaks align well with each other. The oscillations in the simulated spectrum result from Fabry-Perot interference. The experimental spectrum does not show these oscillations due to slight variation of the opal thickness in the illuminated area. (c) The VO_2 IO PhC simulation model. The models in (a) and (c) consist of one unit cell of the FCC lattice with the (111)-plane oriented parallel to the surface. The light is incident along the z-axis.

4.6.2. Estimation of the Bragg peak

Bragg's law is applied to calculate the center spectral position of the Bragg peak, $\lambda_{\text{c}} = 2n_{\text{eff}}d_{111}$, where $d_{111} = \sqrt{\frac{2}{3}}d$ being the lattice constant along the [111]-direction in the FCC-stacked sphere-shape air within the VO_2 backbone and $n_{\text{eff}} = \sqrt{fn_1^2 + (1-f)n_2^2}$ the real part of the effective refractive index, with $f = 0.2$ as the filling fraction, $n_2 = 1$ as the refractive index of air, d as the diameter of the spherical motif and n_1 is the real part of the refractive index of VO_2. The applicability of Bragg's Law is constrained to non-dispersive and lossless dielectrics. Following the ellipsometry results shown in Figure 4.3 and Figure S4.7, we approximate the real part of the refractive index of VO_2 in its dielectric phase to be $n_1 = 3.05$. For a sphere diameter of 566 nm, the Bragg peak is at 1.5 µm. The real part of the refractive index in the metallic phase is $n_1 = 1.7$. Using the same parameters as before, we calculate the spectral position of the Bragg peak in the metal phase to be at 1.1 µm. Both calculated Bragg peak positions agree well with the experimental values, supporting the use of this simple model to describe the reflection behavior of the VO_2 IO.

5. Thermal sight: a position-sensitive detector for a pinpoint heat spot

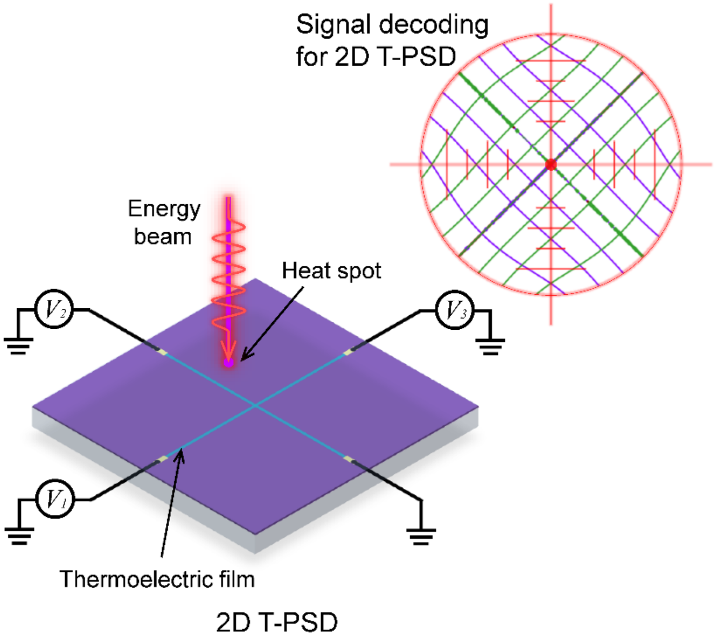

This study proposes a thermoelectric-based position-sensitive detector concept, providing an alternative but more versatile approach to high-precision position detection compared to existing detectors. Utilizing structured aluminum-doped zinc oxide thermoelectric thin film prepared via atomic layer deposition as an amplifier, the prototypes exhibit accurate detection of single heat spots originating from electromagnetic radiation, electrons, and macroscopic mechanical heat sources.

This chapter is adapted from a published first author's peer-reviewed article, with only the formatting changed, and the content remains unchanged.

J. Peng, P. Zhao, R. Venugopal, K. Deneke, S. Haugg, R. Blick, R. Zierold, *Thermal Sight: A Position-Sensitive Detector for a Pinpoint Heat Spot*. Small Science, 2024. 4(8): p. 2400091.

Manuscript title

Thermal Sight: A Position-Sensitive Detector for a Pinpoint Heat Spot

Author list

Jun Peng, Pai Zhao, Rakshith Venugopal, Kristian Deneke, Stefanie Haugg, Robert Blick, Robert Zierold**

Center for Hybrid Nanostructures, Universität Hamburg, 22761 Hamburg, Germany

Keywords

position-sensitive detector, thermoelectric, heat spot, atomic layer deposition, heat transfer

Author contributions

J.P. designed the sensor and experiments, fabricated the samples, and did the FEA analyses; J.P., P.Z., and S.H. set up the measurement system; J.P., R.V., and K.D. performed the measurements; R.Z. supervised the study; R.B. provided infrastructure to conduct the experiments. All authors analyzed data; J.P., R.B. and R.Z. wrote the manuscript. All authors have approved the final version of the manuscript.

Acknowledgements

This work was funded by the Deutsche Forschungsgemeinschaft (DFG, German Research Foundation) project numbers 192346071 – SFB 986 “Tailor-Made Multi-Scale Materials Systems” – and 469222030. Furthermore, we acknowledge financial support from the Open Access Publication Fund of Universität Hamburg.

Open Access funding enabled and organized by Projekt DEAL.

5.1. Abstract

Precise positioning is a never-ending goal in both fundamental science and technology. Recent decades of advancements in high-precision position detection have predominantly relied on photoelectric effects for light detection in semiconductors. Herein, a different approach is proposed: The thermoelectric-based position-sensitive detector (T-PSD) concept, designed to detect single heat spots arise from various energy sources, including electromagnetic radiation, electrons, and macroscopic mechanical heat. The T-PSD concept is initially derived mathematically from the fundamental principles of heat conduction and the Seebeck effect. Subsequently, it is proved by finite element simulation in both 1D and 2D configurations. Following this theoretical groundwork, T-PSD prototypes are fabricated and subjected to positional detection using various stimuli such as CO_2 laser beam, hot soldering tip, and electron beam. In the prototypes, structured aluminum-doped zinc oxide thermoelectric thin films, prepared via atomic layer deposition, are outfitted with voltage probes, enabling the measurement of thermoelectric voltages as a function of position and the intensity or temperature of the heat spot. Furthermore, practical decoding strategies are introduced to infer the position from the measured signals. The T-PSD in this article showcases considerable promise in high-precision position detection such as (quasi-)particle tracking and precision machinery, offering an alternative concept in PSD design.

5.2. Introduction

Position-sensitive detectors (PSDs) are devices that can determine the position of incident radiation or (quasi-)particles in a spatially sensitive manner. These devices serve as fundamental components in modern industry and science. They hold a significant prominence throughout numerous applications, such as motion tracking[251, 252], 3D printing[253, 254], robotic[255, 256], machining[257, 258], and (quasi-)particle detection[259-261]. State-of-the-art PSDs are often based on the lateral photoelectric effect in a semiconductor junction (Figure 5.1a,b)[262-264]. Following the existing main PSD design principles, they can be primarily classified into two groups. The first category involves the lateral photoelectric effect on an isotropic sensor surface, supplying continuous position data. Typical representatives of this design are lateral PSD[127] and quadrant PSD[132]. They detect the light spot position by estimating the photocurrents measured by several electrodes. Such PSDs are widely used in ranging systems or high-precision instruments[265-267], etc. The second principle is to integrate discrete detection units together as a PSD to extract position information via pixel imaging, albeit at an expensive cost and inevitably sacrificing resolution. In the consumer market, for instance, complementary metal–oxide–semiconductors (CMOS) chips[252] incorporate millions of small discrete pixels, so-called PIN diodes, as detection units to determine the light position. However, these detectors, relying on silicon-based materials, impose strict requirements, *i.e.*, limited operating temperature range and wavelength detection range[268-270]. Other more complex discrete PSDs, e.g., thermopile arrays[271] and bolometer arrays[272], can work in wider operating temperatures and spectral range, but still suffer from the complex fabrication process and low resolution.

This work introduces an innovative concept for a PSD derived from the heat transfer principles, that detects the position of a single heat spot (HS) on the detection surface precisely. Isotropic heat conduction on a homogeneous substrate results in a uniform temperature gradient distribution around a HS. Consequently, the HS position on the surface of the substrate can be determined based on the thermoelectric voltages generated from the temperature differences between HS and pre-defined electrodes (Figure 5.1c,d). Based on this idea, we developed a new type of PSD, realized in one-dimensional (1D) and two-dimensional (2D) devices, for single-point HS detection, termed the thermoelectric-based PSD (T-PSD). Since the arising thermoelectric voltages determine the signal strength, a thermoelectric thin film is incorporated into the detector design to amplify the measured signal. The herein proposed mathematical model for T-PSD is validated through both finite element analysis (FEA) and experiments on the 1D and 2D T-PSD prototypes. Furthermore, an approach for decoding the measured voltage signals to obtain a specific position is demonstrated. As the T-PSD relies on temperature differences for detection, this work demonstrates its capabilities in detecting HSs converted from various energy forms.

5.3. Results and discussion

5.3.1. Design principle for T-PSD

The T-PSDs developed herein rely on the basic principles of heat conduction and the Seebeck effect, enabling accurate determination of a HS on the detector surface. Assuming an ideal situation where only heat conduction is considered, a HS is introduced to an isotropic plate surface. On the one hand, energy is transferred from hotter regions near the HS to those farther away and at lower temperatures. The temperature distribution on the plate is described by Fourier's law of heat conduction[134, 135]

$$q_x = -kA\frac{dT}{dx}. \tag{5.1}$$

where, q_x represents the rate of heat transfer, k denotes the thermal conductivity, A corresponds to the cross-sectional area through which the heat flows, and $\frac{dT}{dx}$ indicates the temperature gradient in the direction of the heat flow. On the other hand, a thermoelectric voltage arises when a temperature difference exists across two points within the plate, a phenomenon known as the Seebeck effect[273, 274], expressed as

$$S = -\left(\frac{dV}{dT}\right). \tag{5.2}$$

In the above equation, S is the Seebeck coefficient, while dV represents the thermoelectric voltage arising from the temperature difference dT between the two points. The relationship between dV and dx can be quantitatively concluded from equation (5.1) and equation (5.2) if k and S are independent of temperature. The resulting relation builds the core principle of our T-PSDs, allowing precise derivation of the HS position on the detector surface. By appropriately extending Fourier's law, mathematical models for 1D and 2D T-PSDs can be derived.

The realization of T-PSD requires a meticulous selection of the fabrication materials involved. For the substrate material, in addition to being thermally isotropic, it also needs a significant S to make the detected thermoelectric signal more sensitive to a temperature change. Therefore, we developed a strategy for using an isotropic substrate with a thermoelectric thin film on top. In this way, k and S is mainly determined by the substrate and the thermoelectric thin film, respectively. Here, a silicon wafer with a 300 nm oxide insulating layer is used as the substrate, and an alumina-doped zinc oxide (AZO) film[275, 276], with stable chemical properties in air, is selected to be the thermoelectric film. To minimize the potential contact thermal resistance[277] between the substrate and the film, atomic layer deposition (ALD), with its inherent conformal coating characteristic[46, 117] is chosen to deposit the thermoelectric film. Following that, we systematically scrutinize these models using a combination of FEA simulations and actual prototypes. For theoretical simplicity, the theoretical model considers only the heat conduction within the substrate, neglecting impact from external, environmental factors on the test signal. Hence, our approach does not account for fluctuations in the ambient temperature or electromagnetic fields affecting the substrate's temperature and obtained electrical potential distribution, respectively. However, subsequent experimental validation proves the model’s reliability and accuracy under stable temperature and electromagnetic field conditions.

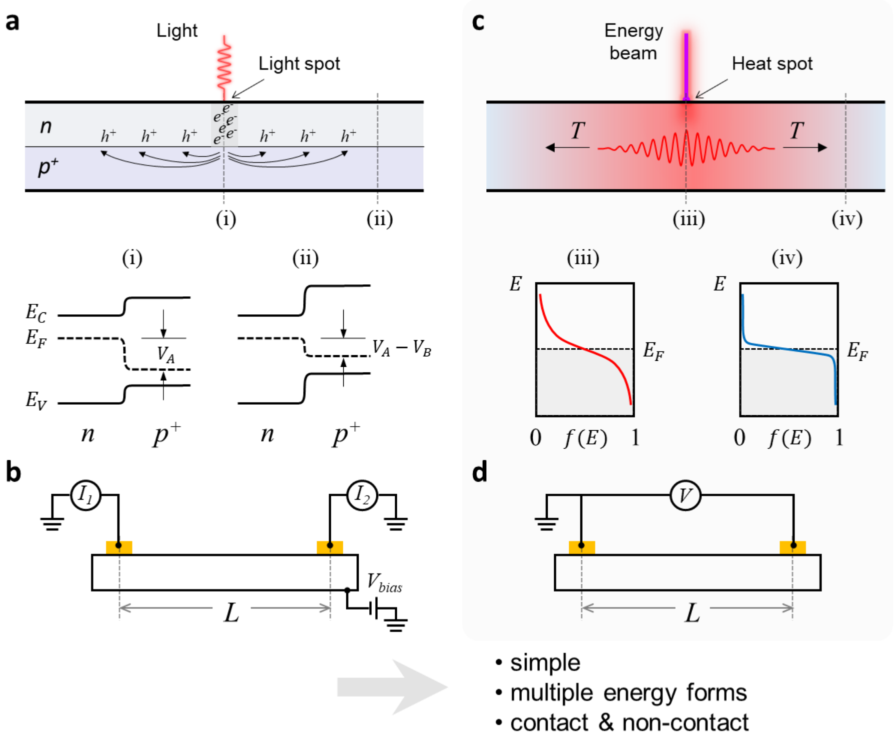

Figure 5.1. Comparison of conventional PSD and our T-PSD. (a) The working principle of conventional PSD based on the lateral photoelectric effect, exemplified by the junction between an n-type region (*n*) and another more heavily doped p-type region (*p*+). When a beam of light illuminates the junction, hole-electron pairs are generated, establishing a new steady-state condition where most of the injected holes accumulate in the *p*+ region and most of the injected electrons reside in the n region. This results in a shift in the Fermi levels (i) at the light spot and (ii) away from the light spot, leading to a transverse photovoltage$V_A - V_B$ between the two positions. (b) A simplified photocurrent circuit for light spot position estimation. (c) The working principle of our T-PSD. In the presence of a HS on the detector surface, phonons are continuously excited and propagate through the detector, making that the Fermi distribution (iii) at the HS is "softer" than that (iv) at the cooler surrounding area. This non-equilibrium distribution of hot electrons and holes results in thermoelectric voltage which is solely dependent on the temperature difference between two points within the detector. Importantly, the HS can be generated by various forms of energy. (d) The simplified circuit to detect the thermoelectric voltage for HS position estimation.

5.3.2. Implementation and multiple energy forms verification for 1D T-PSD

The 1D T-PSD design, depicted in Figure 5.2a, consists of a homogeneous substrate, a thermoelectric film on top, and two electrodes positioned at each end. According to the theoretical derivation outlined in Section 5.6.1.1, a HS located at x with a constant temperature T_0 leads to a thermoelectric voltage $V_{diff} = V_{right} - V_{left}$ between the two terminal electrodes, which can be expressed as

$$V_{diff} = \frac{qS}{kwd} \times 2x. \tag{5.3}$$

where, q is the heat flux density and S denotes the Seebeck coefficient of the thermoelectric thin film. k, w, and d correspond to the thermal conductivity, width, and thickness of the substrate, respectively. x is the position of the HS. To provide more evidence and clarify our concept, an FEA model is constructed (Figure S5.1.1). Upon introducing a HS, for example, a laser beam, i.e., typically applied in laser cutting, to the sensor area, the temperature distribution becomes uneven, resulting in a temperature difference, $\Delta T = T_{right} - T_{left}$, between the two terminals (Figure 5.2b). The change in this ΔT is a power dependent, linear function of the position as displayed in Figure 5.2c. This change also results in a linear relationship between the corresponding measurable V_{diff} and the HS position (Figure S5.1.2). V_{diff} is zero when the HS is at the center of the 1D T-PSD, *i.e.*, $x = 0$. When the HS deviates in one direction from the center, it yields a signal of one polarity, while a signal of the opposite polarity is produced when the HS is displaced in the opposite direction. As a result, the 1D sensor is capable of precisely detecting the center position of a HS by probing the null signal.

To support our analytical and simulation results, we fabricated 1D T-PSDs and evaluated them using a custom-built setup (Figure S5.1.3). Note, all characterizations were performed in an electromagnetic-shielded, clean, and dry environment with a controlled, stable ambient temperature. The measured V_{diff} reveals a sensitive response to a CO_2 laser spot serving as a HS on the sensing surface. The sensitivity is evident in the signal derived from the laser's different pulse width modulation (PWM) values (Figure 5.2d) and across various positions (Figure 5.2e). Note that a smaller PWM in the CO_2 laser system corresponds to a lower laser power output, thus leading to actual lower temperatures on the T-PSD. The detected signal exhibits minor fluctuations during the laser's ON state owing to the intermittent nature of the laser (Figure S5.1.4). The ability to detect these fluctuations showcase our sensor's exceptional sensitivity. The measured V_{diff} exhibits a linear relationship with the position on the T-PSD, as shown in Figure 5.2f. The minor deviations in the central position at V_{diff} = 0 are primarily attributed to the influence of the temperature distribution of the imperfect geometry of the substrate. The most noteworthy finding is the high reproducibility of these measurements for different PWM values, namely, 4%, 5%, and 6%, with corresponding central offsets of x = (-0.46 ± 0.03), (-0.47 ± 0.02) and (-0.50 ± 0.01) mm, respectively. These results indicate that the central position remains constant irrespective of the absolute temperature or fluctuation of the HS. This consistency aligns with the predictions made by the theoretical models. The position sensitivity of the T-PSD is quantified by the slope of the line, expressed in units of $V \cdot mm^{-1}$:

$$\frac{dV_{diff}}{dx} = -\frac{2qS}{kwd}. \tag{5.4}$$

Our 1D T-PSD has a positional sensitivity of 0.313 mV·mm^{-1} at a PMW value of 6%. Based on the multimeter's resolution of 100 nV and the specific parameters of the materials used, the detection resolution for the HS's central position is estimated to be 0.319 µm. Note, the resolution may be further enhanced by employing a thermoelectric film with a higher S, a substrate with lower k, a thinner d, and a narrower w, as indicated by equation (5.4).

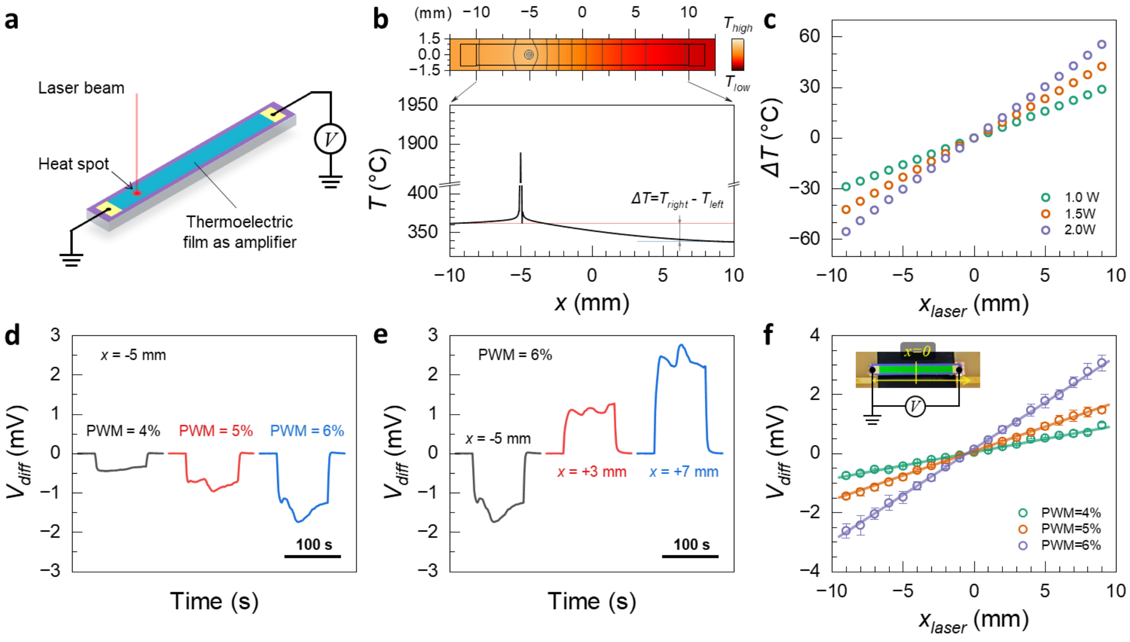

Figure 5.2. 1D T-PSD simulation and experimental results. (a) Working principal sketch of a 1D T-PSD using a laser as a HS. (b) The simulated temperature distribution on the 1D T-PSD with a HS at $x = -5$ mm and its distribution along the detector. A temperature difference, $\Delta T = T_{right} - T_{left}$, between the left terminal and the right terminal exists upon irradiating with a HS. (c) Simulated ΔT as a function of the HS position on the 1D T-PSD surface. (d) Experimentally derived V_{diff} when the laser spot is located at $x = -5$ mm for different PWM values of 4%, 5%, and 6% of a CO2 laser. (e) Measured V_{diff} at a laser PWM = 6% at different positions, $x = -5, +3$ and $+7$ mm. (f) Measured V_{diff} using different PWM values along the detector. The lines are linear fits with $R^2 \approx 0.94, 0.92,$ and 0.88. Inset shows the photograph of the testing 1D T-PSD prototype.

The generality of our methodology is demonstrated by using a hot soldering iron tip (Figure 5.3a~c) as a HS and an electron beam (Figure 5.3d~e) instead of a laser beam. A different substrate, *i.e.*, glass, is used to fabricate another prototype (Figure S5.1.5), verifying that the T-PSD does not rely on a semiconducting substrate. These results also reveal a robust position-dependent response behavior of the T-PSDs.

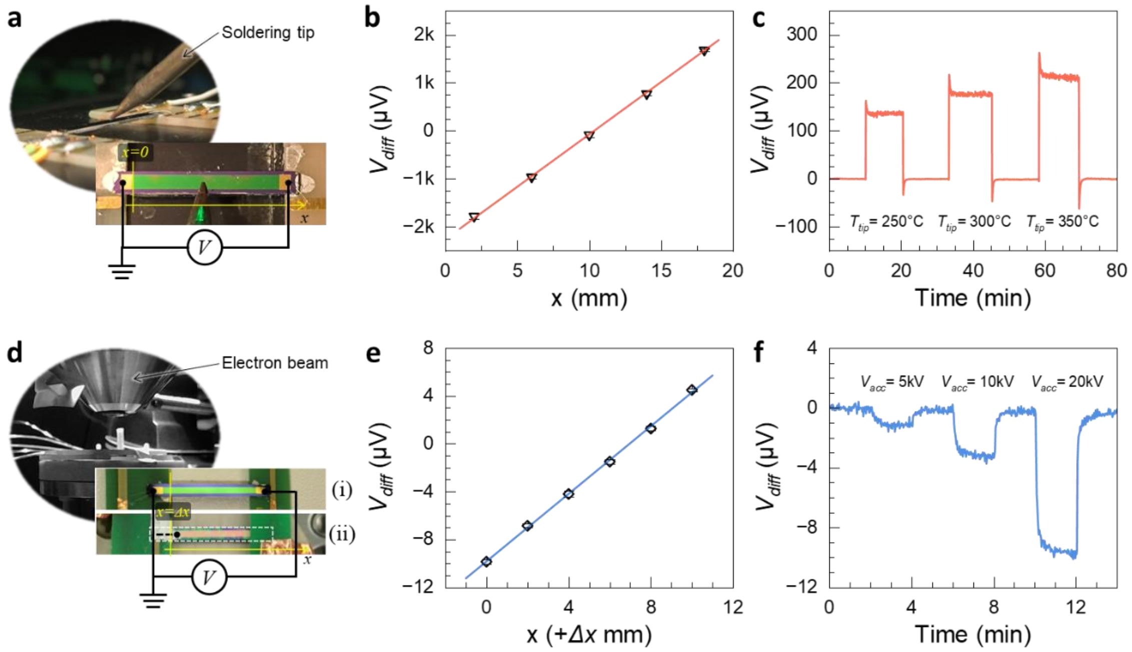

Figure 5.3. T-PSD under multiple energy forms. (a) Photographs of a 1D T-PSD prototype working under a hot soldering tip as a HS. This device is 25 mm in length with a 20 mm active area. (b) Measured V_{diff} at different positions along the detector using a hot soldering tip at 400 °C as a HS. (c) The measured V_{diff} as a response to different soldering tip temperature at $x \approx 11.5$ mm). The line is a linear fit with $R^2 \approx 1.0$. (d) Photographs of a 1D T-PSD prototype working under an electron beam as a HS in a scanning electron microscope chamber. Top view (i) and bottom view (ii) of the prototype. To prevent incident electrons from affecting the detected signal, the back side of the detector is used to detect the electron beam. Besides, the rear surface has been coated with a 2 nm Au layer and is grounded with silver glue to prevent the impact of charge accumulation. This device is 20 mm in length with a 15 mm active area. (e) Measured V_{diff} at different positions along the detector. Since the position $x = 0$ cannot be determined accurately, the position of the electron beam, $x + \Delta x$, means the distance Δx between the initial electron beam position and position $x = 0$, plus the distance x between the initial electron beam position and the current electron beam position. The line is a linear fit with $R^2 \approx 1.0$. (f) The measured V_{diff} as a response to different electron acceleration voltages at $x = 0 + \Delta x$ mm.

5.3.3. Implementation of 2D T-PSD

The 1D T-PSD can be expanded into a 2D T-PSD by changing the geometry of the thermoelectric thin film from a strip to a cross and integrating two additional voltage-probe terminals, as shown in Figure 5.4a and Figure S5.2.1. A mathematical model for 2D T-PSD is derived by extending Fourier's law of heat conduction (Section 5.6.2.1). The following set of equations can be derived to express the probed thermoelectric voltage signals at the terminals

$$\begin{cases} V_1 = -\frac{qS}{4\pi kd}\, ln\left(\frac{(x+L/2)^2+y^2}{x^2+(y+L/2)^2}\right) \\ V_2 = -\frac{qS}{4\pi kd}\, ln\left(\frac{x^2+(y-L/2)^2}{x^2+(y+L/2)^2}\right). \\ V_3 = -\frac{qS}{4\pi kd}\, ln\left(\frac{(x-L/2)^2+y^2}{x^2+(y+L/2)^2}\right) \end{cases} \tag{5.5}$$

where V_1, V_2, and V_3 represent the detected signals at the different electrodes. L is the side length of the square substrate. The corresponding position of the HS is denoted by (x, y). The magnitude of the probed voltage signals is determined by the coefficient, $-\frac{qS}{4\pi kd}$, in equation (5.5), which depends on the material properties and detector size, namely, S, k, and d as well as the heat flux q generated from the HS. According to the equation group, three special lines, where V_1, V_2, and V_3 are equal to zero, can be highlighted. In detail, when the HS is positioned on the x-axis, *i.e.*, $y = 0$, $V_2 = 0$. Also, when the HS is located on the diagonal, *i.e.*, $y = x$ or $y = -x$, the measured signal is $V_1 = 0$ or $V_3 = 0$, respectively. If any of the three signals equals zero, it indicates that the HS is located on the diagonals or $y = 0$ line. Additionally, the center of the 2D T-PSD serves as a unique point because all signals are equal to zero. This feature can be used for precise centering scenarios. Furthermore, these three lines divide the detection area into six sections as displayed in Figure 5.4b. The combination of the positive and negative signs of the measured voltage signals V_1, V_2, and V_3, as listed in Table S5.1, can be used to roughly decode the position of the HS. Besides, the signal distribution within the x-y coordinate system can be analyzed in a predictive manner, as depicted in Figure S5.2.2.

Similar to the 1D case, we developed a FEA model to validate the voltage distribution patterns of the 2D T-PSD design (Figure S5.2.3). A spatial temperature distribution is observed when the sensor region is exposed to a HS, as seen in Figure 5.4c. Depending on the HS position, the temperatures of the different electrode terminals vary. The simulated V_1, V_2, and V_3 distributions (Figure S5.2.4 and Figure S5.2.5a) align well with the mathematical plots (Figure S5.2.2). Afterwards, we manufactured and assembled 2D T-PSD prototypes (Figure 5.4a and Figure S5.2.6) with a detection area of 18 x 18 mm^2. When a CO_2 laser beam, serving as a HS, is directed over the sensor's surface, it induces a localized temperature increase. This rise in temperature generates corresponding voltage signals at the different electrodes. A comprehensive comparison was conducted, illustrating the signal distributions from numerical calculations (Figure S5.2.2), FEA simulation (Figure S5.2.4), and experimental result (Figure 5.4d-f and Figure S5.2.5b) for V_1, V_2, and V_3. The distributions of both experimental and FEA results exhibit slight asymmetry and irregularity, primarily due to the influence of sensor geometry. Quantitative analysis reveals that the center of the experimental signal distribution is at (0.302, -0.453), which differs slightly from the numerical calculation and simulated signal centers, both located at (0, 0). Given the well-controlled testing environment, we attribute this deviation mainly to imperfections of the sample itself, such as geometric irregularities from manual cutting, bonding connection defects, and contamination during the sample preparation process. A hot soldering iron tip is also used as a HS (Figure S5.2.7) to prove the versatility of the T-PSD in detecting diverse kinds of HSs, including but not limited to, laser beams, electrons, ions, to name a few.

To ensure the robustness and accuracy of the T-PSD in practical scenarios, it is crucial to consider and mitigate the effects of various real-world factors. Firstly, external environmental influences, such as ambient temperature fluctuations caused by airflow, convection, radiation exposure, uneven illumination, or nearby heat sources, can alter temperature gradients and lead to variations in the measured V_{diff}. Besides, electromagnetic fields can also interfere with electron transport in the AZO film, causing noise and signal distortion. Such external factors can compromise the accuracy of the voltage signals. To mitigate these influences, experiments were conducted in controlled environments with constant temperature and electromagnetic shielding (Figure S5.2.8). Secondly, experimental measurements often introduce noise and signal instability from electronic components, power supply fluctuations, or environmental electromagnetic interference, which can degrade voltage signal accuracy and lead to incorrect HS position detection. For this reason, it is necessary to collect the reference signal in advance to perform the necessary drift compensation. Our drift compensation strategy is illustrated in Figure S5.2.9.

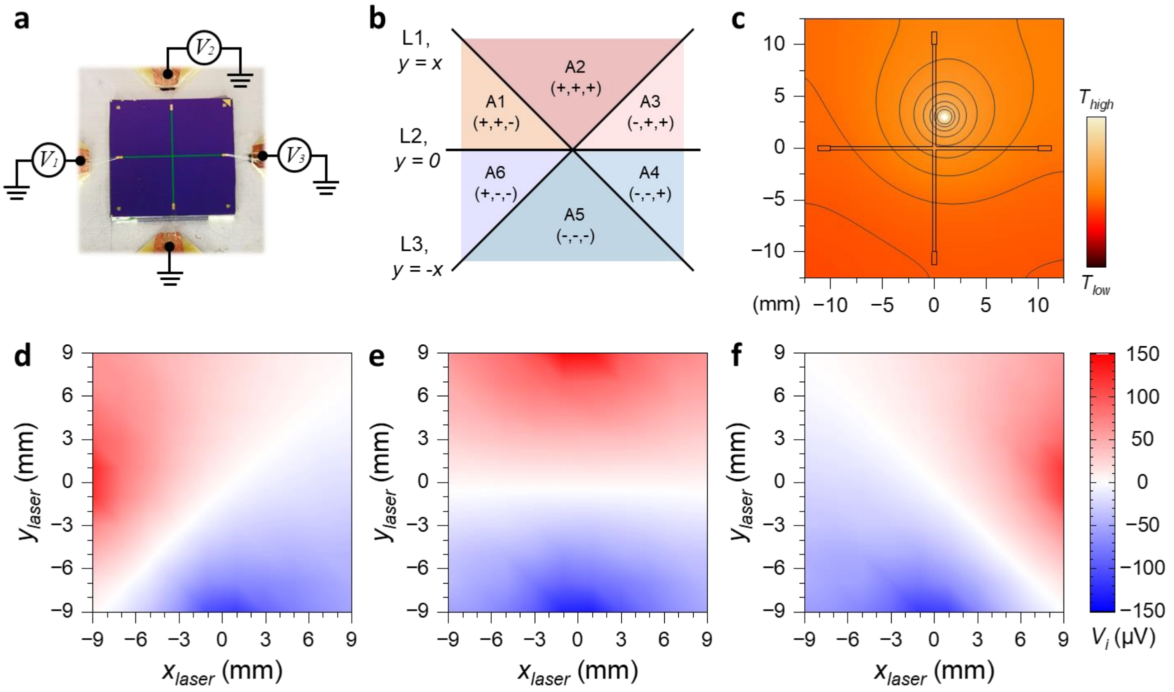

Figure 5.4. 2D T-PSD simulation and experimental results. (a) Photograph of a 2D T-PSD prototype, and corresponding circuit connection. (b) The segmentation of the location area on the 2D T-PSD for rough decoding. The position of the HS can be roughly judged by the sign combination of V_i. (c) The simulated temperature distribution on the substrate surface when a laser beam as HS is induced at the position (+1, +3). The prototype and the simulated model share the same size. (d-f) The measured voltage signals V_i from the three voltage terminals, V1, V2, and V3 (as denoted in (a)), when the laser spot with PWM = 6% is located at different positions on the detector.

5.3.4. Decoding pathways for 2D T-PSD

In addition to the above control of the external environment and calibration during the measurement process, we developed two tailored decoding strategies for 2D T-PSD. The decoding process can be generally categorized into two levels: rough decoding and accurate decoding. The varied sign combination of V_1, V_2, and V_3 can be used to locate the HS (Figure 5.4b). For example, if the signs of V_1, V_2, and V_3 are -, -, and +, respectively, indicating that the HS is situated in the A4 sector. One cannot derive the specific coordinate from this estimation except the center point. However, accurate decoding can be achieved through the "ratio strategy" we developed. The coefficient, $-\frac{qS}{4\pi kd}$, in equation (5.5) affects the signal's amplitude, whereas the natural logarithm component governs the signal distribution and is only associated with the position (x, y). The ratios, e.g., $\frac{V_1}{V_2}$, enable the elimination of the coefficients, making them independent of material properties and the local temperature rise due to the HS. Here, the following two ratios, R_a and R_b, are selected for accurate decoding since both contain information about all three voltages:

$$\begin{cases} R_a = \frac{V_1}{V_2+(V_1-V_3)} \\ R_b = \frac{V_3}{V_2-(V_1-V_3)} \end{cases}. \tag{5.6}$$

Note, other ratios and combinations might be used as well if they lead to distinct solutions for the position (x,y). Practically, the accuracy of HS position detection can be compromised by signal inconsistencies due to variations in sensor performance, sensor shape, or external disturbances. Therefore, each T-PSD should undergo complete offset calibration using reference HS positions to correct for systematic biases. This calibration ensures long-term stability and accurate performance. The calibration procedure involves probing the entire detector surface first to obtain the line segment with the measured value $V_i = 0$, $(i = 1, 2, 3)$. Then, the measured positions are compared to the corresponding line segment with the theoretical value $V_{i,\text{theoretical}} = 0$ to obtain the offset data x_{offset} and y_{offset}. For instance, according to the analysis in Figure S5.2.5, the offset values are calibrated as., x_{offset} = 0.302 mm, y_{offset} = -0.453 mm for 2D T-PSD in the Figure 5.4. Then, the following formulas are used to correct the actual x and y in V_1, V_2, and V_3 in equation (5.5) and equation (5.6),

$$\begin{cases} x_{i,update} = x + x_{offset}, & (i = 1, 2, 3) \\ y_{i,update} = y + y_{offset}, & (i = 1, 2, 3) \end{cases}. \tag{5.7}$$

Note that the equation group can contain multiple solutions, *i.e.*, several coordinates. During actual decoding, an important criterion for judging the correctness of the decoding result and the data quality is the proximity of these coordinate positions. We can anticipate a better decoding result the smaller the area of the coordinate groups present. From the coordinate set solved by V_1, V_2, and V_3, take the average of all the solutions in the intersection set as the true solution. Then, calculate the mean and standard error of x and y, respectively, to get the coordinates $(\bar{x} \pm s_x, \bar{y} \pm s_y)$. These coordinates represent the actual location of the HS.

These measures help to normalize the influence of signal amplitude variations, ensure stable measurements, and correct for systematic biases. By considering these factors, the T-PSD can achieve reliable and precise heat spot location identification even under non-ideal conditions. The reliability of the decoding is proven via a set of detected voltage signals at one position, *i.e.*, (6, -2), under varying PWM values, as depicted in Figure 5.5a-b. As predicted, the two ratios are independent of the characteristics of the HS, converting a fluctuating signal output into stable ratios for accurate decoding (Figure 5.5c and S5.3.1). Each position in the detection area corresponds to a unique ratio pair, indicating that precise position decoding is feasible, as it is obvious in the contour diagrams of the two ratios (Figure 5.5d and S5.3.2). To verify the reliability of the derived ratio strategy, several positions were randomly selected on the surface of the detector. The CO_2 laser beam was used as the HS for this experiment. The actual positions ((-3, -5), (-3, 1), (1, -3), (5, 1), (6, -2)) and the decoded positions ((-2.66 ± 0.36, -5.13 ± 0.99), (-2.75 ± 0.36, 1.12 ± 0.38), (1.13 ± 0.28, -3.16 ± 0.53), (4.75 ± 0.15, 1.31 ± 0.18), (5.55 ± 0.11, -1.7 ± 0.12)) correspond well to each other, as shown in the Figure 5.5e. Factors such as the detector's geometry, the air's convection, and the thermal radiation will be relatively weakened, when the temperature is higher. As predicted, the decoding is more accurate when the temperature rise induced by the laser's power is higher (Figure S5.3.3). The results of the conducted experiments demonstrate the reliability, consistency, and stability in detecting a HS position using our T-PSD concept.

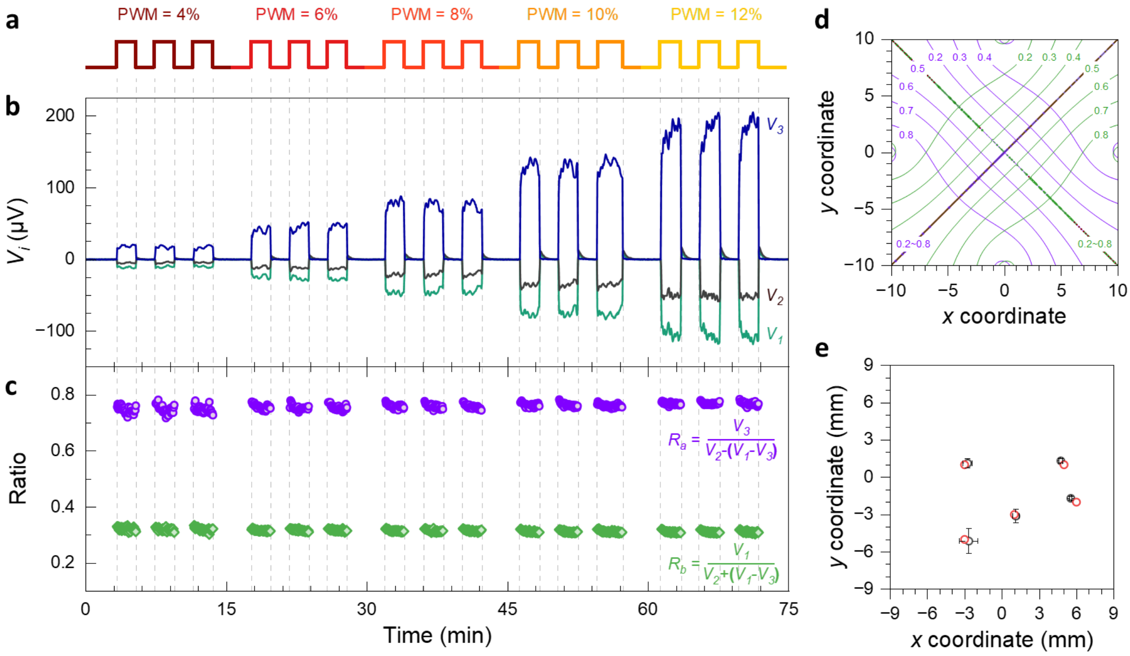

Figure 5.5. Demonstration of a method for accurate decoding the V_i into corresponding positions in 2D T-PSD. (a) Laser HS pulses setup. The laser spot is located at the position (6, -2) and a varying PWM values of 4, 6, 8, 10, and 12% are used. (b) The corresponding V_i signal. (c) The derived ratios of R_a and R_b. The ratio values remain almost unchanged despite changing the PWM values, suggesting their only position-dependent character. (d) Contour map of the calculated ratio values, R_a (green) and R_b (violet), over the detection area for accurate decoding. The precise position of the HS can be determined by comparison with this distribution. (e) Comparison of several actual laser spot positions (red) with the corresponding decoded positions (black) using PWM=6%.

5.4. Conclusions

In this study, we have introduced a new detector concept, termed the T-PSD, designed for the precise position detection of a single HS through the analysis of generated thermoelectric voltages. Correspondingly, a reliable and precise decoding method, the "ratio strategy", was proposed and demonstrated for extracting the spatial position information from the measured voltage signals. The fabricated prototypes have exhibited the capability to accurately detect HSs generated by various heat sources such as a laser beam, an electron beam, and a soldering iron tip. The comprehensive results highlight the T-PSD's outstanding features, including high precision, exceptional sensitivity, robust repeatability, and positional stability. These characteristics have also been validated through analytical descriptions and FEA simulations. Nevertheless, potential enhancements for the T-PSD encompass but are not limited to: (1) employing thermoelectric thin films with higher Seebeck coefficients; (2) considering the effects of heat convection, radiation, geometry effect of the substrate, and potential variations in the S and k with temperature; (3) incorporating additional electrode configurations for temperature reference or calibration. Throughout history, the introduction of new sensors has often facilitated advancements in various fields. The T-PSD concept, characterized by its simplicity and solid grounding in physical principles, holds the promise of positively impacting various industrial domains in the near future.

5.5. Materials and methods

AZO film deposition by ALD: The AZO films were deposited in a super-cycle ALD approach in exposure mode on SiO_2 (300 nm)/Si wafers (SIEGERT WAFER GmbH) using a Savannah^{TM}100 reactor (Cambridge Nanotech). The deposition was performed at 200 °C with 30 sccm nitrogen as the carrier gas and a working pressure of ca. 1.5 Torr. The precursors, namely, deionized water (DIW), diethylzinc (DEZ, Strem Chemicals, Inc., USA), and trimethylaluminum (TMA, Strem Chemicals, Inc., USA), were used as the source of O, Zn, and Al, respectively. All precursors were contained in stainless-steel bottles and held at room temperature. An ALD super-cycle was set as $[(\mathrm{DEZ\text{-}DIW})_a + (\mathrm{TMA\text{-}DIW})_b + (\mathrm{DEZ\text{-}DIW})_c]_x$, to synthesize uniformly doped AZO film with a ratio of DEZ:TMA = $(a+c):b$ = 20:1. The film thickness was adjusted to about 30 nm by running x = 30 super-cycles.

The T-PSD device preparation: Standard lithography processing was used to define the patterns, *i.e.*, strip or cross for 1D and 2D, respectively, on the ALD-deposited AZO film. Next, diluted HCl solution (HCl: H_2O = 2:100 $v \cdot v^{-1}$) was used to etch the film, leaving the desired pattern on the substrate. Subsequently, after removing the photoresist by acetone, another standard lithography process was used to define the electrode contact patterns, followed by sputtering Cr (10 nm) / Au (100 nm) as contacts.

Characterization: Seebeck coefficient of the AZO film was measured using a Potential-Seebeck microprobe (PSM II, PANCO GmbH). The experimental tests using a CO_2 laser (48-2SWM, SYNRAD), whose machining resolution is smaller than 1µm, and a hot soldering iron tip, as HSs were performed in a laser micromachining system (MM200-Flex, OPTEC) within a metal protective cover. The power output is 25 W with a wavelength of 10.2-10.8 µm. The tests using an electron beam as HS were performed within the scanning electron microscope (Quanta FEG-250). The average thermoelectric voltage signal from the PSD is measured using digital multimeters (34401A, HEWLETT PACKARD HP) with an integration time of 1 s.

FEA simulation: FEA conducted by COMSOL Multiphysics software was adapted to study the temperature and potential distribution on the T-PSD. The three-dimensional model was established using an almost one-to-one configuration (same size, same geometry) of the real T-PSDs. A gaussian beam profile was represented by the equation for the irradiance (intensity) distribution, $I(r) = \frac{P_{laser}}{2\pi r_{spot}^2} exp\left(-\frac{r_{focus}^2}{2r_{spot}^2}\right)$, where P_{laser} is the laser power, r_{spot} is the spot radius, and r_{focus} is the radius of the laser at the focus point. The experimentally measured Seebeck coefficient of -72.1 µV/K was assigned to the AZO film. In contrast to analytical description, a surface-to-ambient radiation was set to 0.8.

5.6. Supporting Information

5.6.1. 1D T-PSD

5.6.1.1. 1D T-PSD theoretical framework

When a HS, e.g., a laser beam or a soldering iron tip, is present on the sensor surface, the heat transfer within the sensor can be described by Fourier's law of heat conduction. This fundamental law states that the rate of heat transfer through a solid is proportional to the temperature gradient, and can be mathematically expressed as

$$q = -kA_{1D}\frac{dT}{dx} = -kwd\frac{dT}{dx}, \qquad \text{(S5.1-1)}$$

where q is the heat flux density, k is the material's thermal conductivity, and is considered a constant here, A_{1D} is the area for the heat flow. To simplify the calculation, we neglected the thickness of the thermoelectric film as it is very thin (<100 nm). So, the A_{1D} is the cross-section area of the substrate along the x-axis, i.e., $A_{1D} = wd$, where w and d are the width and thickness of the substrate, respectively. dT/dx is the temperature gradient, i.e., the change in temperature with respect to the distance in the direction of the heat flow. We also neglected the convection and radiation between the environment and the sensor, and only consider the lateral heat transfer within the substrate. This equation shows that the temperature distribution in a 1D system with a constant HS is linearly proportional to the distance from the HS. Combining equation (S5.1-1) and the Seebeck effect expression, equation (5.2), we have

$$\frac{dV}{dx} = \frac{qS}{kA_{1D}}. \qquad \text{(S5.1-2)}$$

Assuming a steady-state condition, where a HS with a constant temperature T_0 is located at $x = x_0$, the temperature distribution does not change with time. Two defined temperatures, T_1 and T_2, occur at the two ends of the sensor, i.e., at points $x(P_1) = -L/2$ and $x(P_2) = L/2$, respectively. The thermoelectric voltage, V_{diff}, generated by the temperature difference can be described as

$$V_{diff} = \frac{qS}{kA_{1D}}\left(\left(\frac{L}{2} + x_0\right) - \left(\frac{L}{2} - x_0\right)\right) = \frac{qS}{kwd}(2x_0). \qquad \text{(S5.1-3)}$$

Consequently, V_{diff} reflects the position of the HS. This potential can be probed easily by a multimeter connected between the terminals.

5.6.1.2. 1D T-PSD simulation

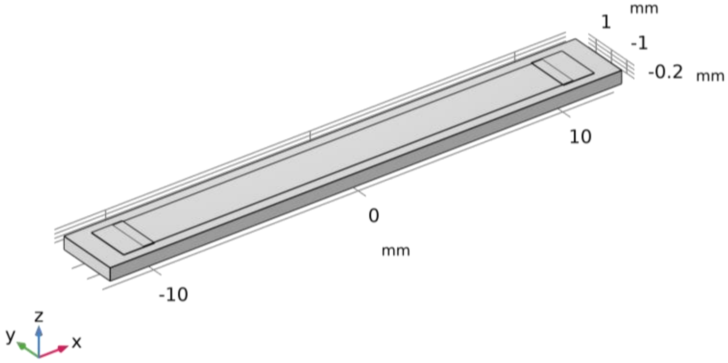

Figure S5.1.1. The simulation model geometry for the 1D T-PSD.

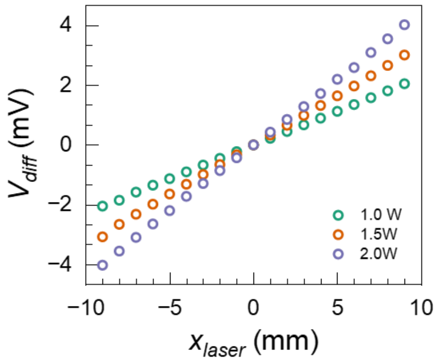

Figure S5.1.2. Simulated V_{diff} at different laser powers on the 1D T-PSD. They all reveal a linear relationship with the x-coordinate.

5.6.1.3. 1D T-PSD experiments

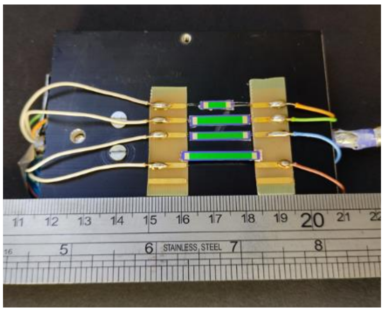

Figure S5.1.3. Photograph of several 1D T-PSDs on the test holder. Note that the longest T-PSD is elevated on the printed circuit board to prevent the holder's influence.

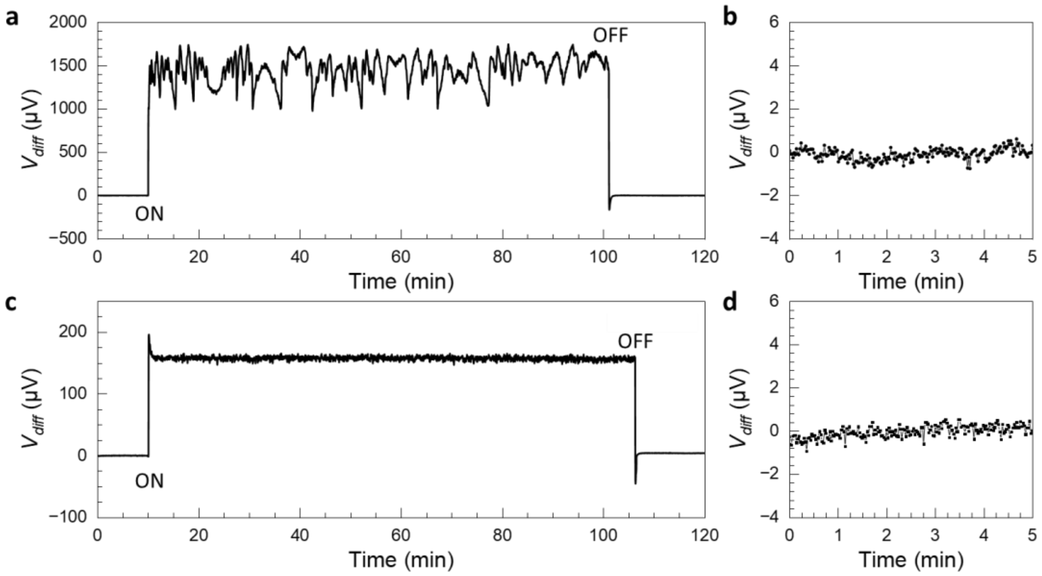

Figure S5.1.4. Comparison of the V_{diff} using different HS. (a) Overview of the probed V_{diff} from a long-time measurement using a CO2 laser beam with PWM=6% as a HS. (b) Zoomed-in base signal in (a). (c) Overview of the probed V_{diff} from a long-time measurement using a hot soldering iron tip with the temperature set to 300 °C as a HS. (d) Zoomed-in base signal in (c). The small fluctuation in (b) and (d) is the noise from the multimeter, while the stronger fluctuation in (a) when the laser is ON comes from the unstable laser output. The applied CO2 laser is a cutting laser with a power stability of ±5% without a voltage regulator.

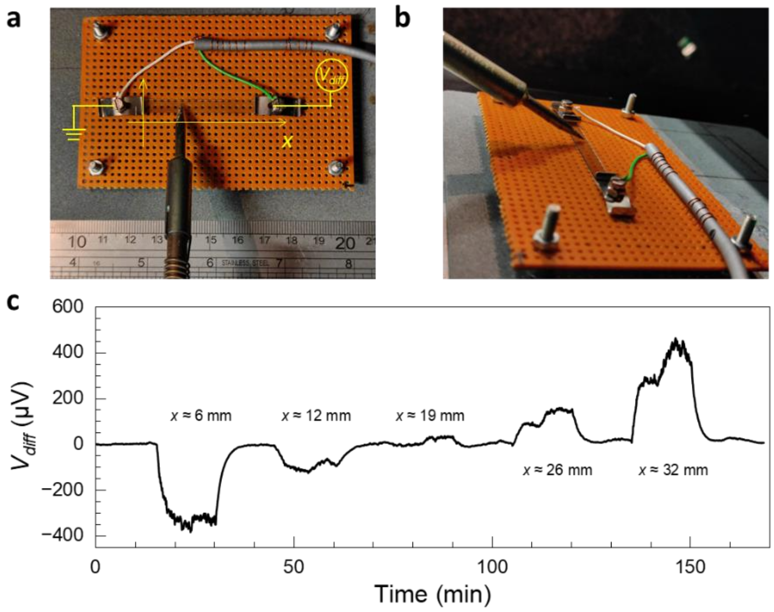

Figure S5.1.5. Glass substrate with an AZO film on top for a 1D T-PSD. (a) Top view and (b) bottom view of the glass-based 1D T-PSD device using a hot soldering iron tip as a HS. This device is 50 mm in length with a 38 mm active area. (c) The measured V_{diff} when the soldering iron tip with a temperature of 400 °C is located at different positions.

5.6.2. 2D T-PSD

5.6.2.1. 2D T-PSD theoretical framework

Expanding the substrate of the 1D T-PSD and distancing the HS away from the thin thermoelectric film strip will lead to diminished accuracy in position detection. This reduction in sensitivity occurs because a variation in the distance between the electrodes at both ends is more sensitive to movements of the HS along the linear axis defined by the two probe electrodes, as opposed to movements perpendicular to this axis. To address this limitation, a cross-shaped thermoelectric film is introduced, transforming the 1D T-PSD into a 2D T-PSD. We still ignore the thickness of the thermoelectric film and the convection between the environment and the sensor as well as its own thermal radiation. Only the lateral heat transfer is considered within the substrate. Furthermore, we assume the 2D sensor as an infinite 2D plate. Within this 2D space, the temperature distribution, as shown in Figure S5.2.1a, is a function only of radial distance r between the point heat source (x, y) and the probe points (x_i, y_i), with $i = 1, 2, 3$, and is independent of azimuth angle when using the polar coordinates, which can be expressed as

$$r = \sqrt{(x - x_i)^2 + (y - y_i)^2}. \tag{S5.2-1}$$

Again, Fourier's law is used by inserting the proper area relation A_r, taking the substrate thickness d into account. The heat transfer can be considered as a radial transfer mode within a 2D plate. The area for the heat flow can be written as $A_r = 2\pi r d$. The radial heat flux q_r from the HS is then written as

$$q_r = -kA_r \frac{\partial T}{\partial r} = -2\pi k r d \frac{\partial T}{\partial r}, \tag{S5.2-2}$$

with the boundary conditions $T = T_i$ at $r = r_i$, and the HS temperature $T = T_0$ at the HS edge $r = r_0$. The solution to the above equation is

$$q = -2\pi k d \frac{(T_i - T_0)}{ln(r_0/r)}. \tag{S5.2-3}$$

Then temperature $T(x, y)$ at any point (x, y) on the surface with a HS at position (x_0, y_0) and a constant temperature T_0 can be expressed using the below equation

$$T(x, y) = T_0 - \frac{q}{2\pi k d}\, ln(\frac{r_0}{r_i}), \tag{S5.2-4}$$

Where r_0 is the radius of the HS. According to equation (S5.2-4), the temperature distribution is relatively insensitive to small variations in the value of r_0. The T-PSD detects the position but not the shape of the HS.

As shown in Figure S5.2.1b, the 2D T-PSD has one ground and three probe terminals at $P_1(-L/2, 0)$, $P_2(0, L/2)$, and $P_3(L/2,0)$, respectively. The temperature difference between the three points and the ground point $P_4(0, -L/2)$ can be written as

$$\begin{cases} \Delta T_{1-4} = T_1 - T_4 = T(-L/2, 0) - T(0, -L/2) = \frac{q}{2\pi k d}\, ln(\frac{r_1}{r_4}) \\ \Delta T_{2-4} = T_2 - T_4 = T(0, L/2) - T(0, -L/2) = \frac{q}{2\pi k d}\, ln(\frac{r_2}{r_4}) \\ \Delta T_{3-4} = T_3 - T_4 = T(L/2,0) - T(0, -L/2) = \frac{q}{2\pi k d}\, ln(\frac{r_3}{r_4}) \end{cases}. \tag{S5.2-5}$$

Combining equation (S5.2-1) and equation (S5.2-5), we have

$$\begin{cases} V_1 = -S\Delta T_{1-4} = -\frac{qS}{2\pi kd}\, ln\left(\frac{r_1}{r_4}\right) = -\frac{qS}{4\pi kd}\, ln\left(\frac{(x+L/2)^2+(y)^2}{(x)^2+(y+L/2)^2}\right) \\ V_2 = -S\Delta T_{2-4} = -\frac{qS}{2\pi kd}\, ln\left(\frac{r_2}{r_4}\right) = -\frac{qS}{4\pi kd}\, ln\left(\frac{(x)^2+(y-L/2)^2}{(x)^2+(y+L/2)^2}\right). \\ V_3 = -S\Delta T_{3-4} = -\frac{qS}{2\pi kd}\, ln\left(\frac{r_3}{r_4}\right) = -\frac{qS}{4\pi kd}\, ln\left(\frac{(x-L/2)^2+(y)^2}{(x)^2+(y+L/2)^2}\right) \end{cases} \tag{S5.2-6}$$

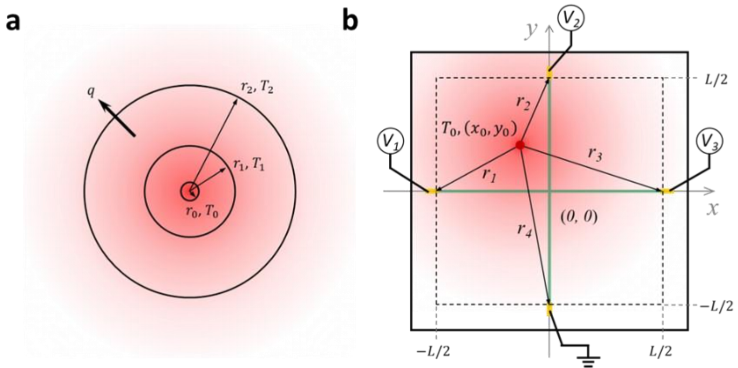

Figure S5.2.1. Heat conduction sketch in 2D space. (a) Polar coordinates. (b) The calculation in 2D T-PSD.

When the three thermoelectric voltages, V_1, V_2 and V_3, are measured, the above equation group can be utilized to derive the HS position (x, y) and the heat flow q. In equation (S5.2-6), the coefficient, $-\frac{qS}{2\pi kd}$, remains independent of the position and is solely related to the sensor material. Hence, the coefficient can be normalized to a constant, e.g., 1, for studies focusing solely on position dependence. By plotting the mathematical model with a normalized coefficient, as illustrated in Figure S5.2.2, the resulting patterns of the graphs closely align with the experimental data displayed in Figure 5.4d-f. These agreements provide compelling evidence that our proposed fitting model is accurate.

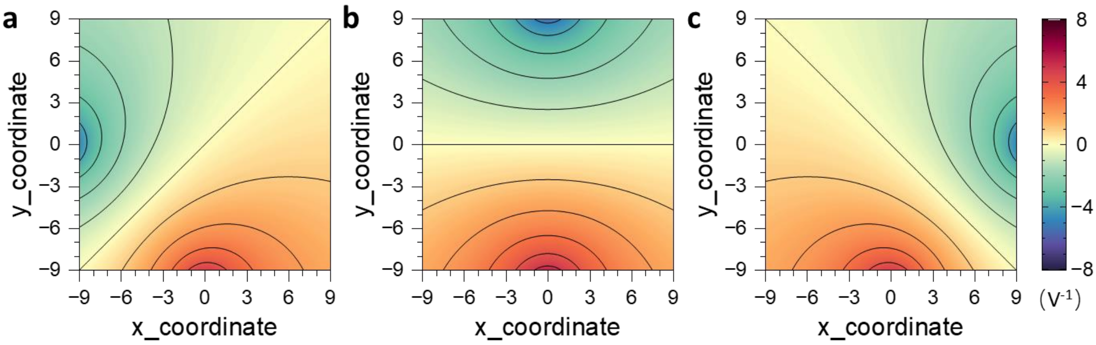

Figure S5.2.2. The analytical calculated V_i signal. They are the function graphs pictured from the mathematical model for (a) V_1, (b) V_2, and (c) V_3, respectively, in equation (S5.3-5.6).

5.6.2.2. 2D T-PSD simulation

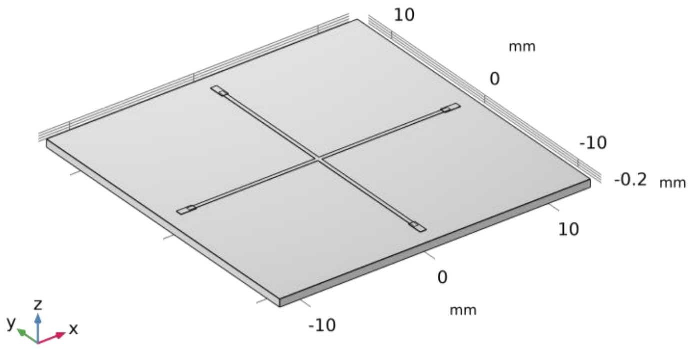

Figure S5.2.3. The simulation model geometry for 2D T-PSD.

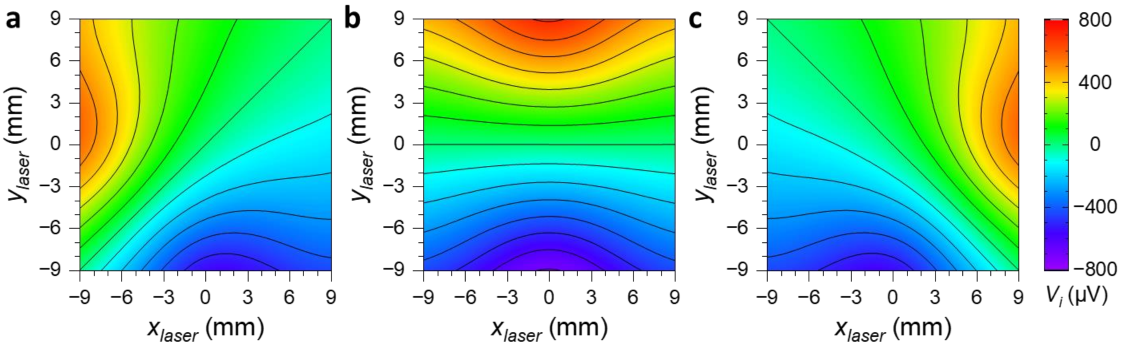

Figure S5.2.4. The simulated V_i signal. Simulated voltages, V_1, V_2, and V_3, (panel (a), (b), and (c), respectively) when the laser is located at different points on the 2D T-PSD surface. The laser power used for the simulation is 2W.

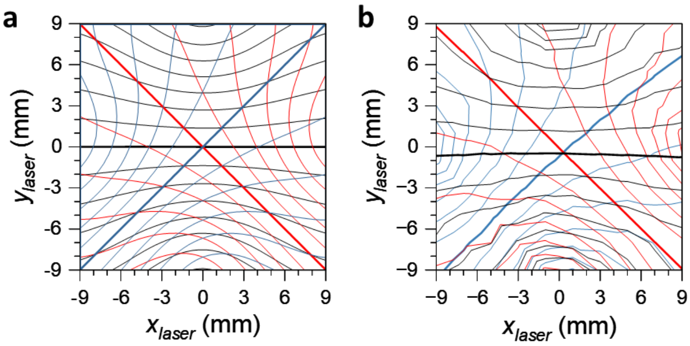

Figure S5.2.5. Contour plot comparison of simulated and experimental data. (a) Contour plot integration of voltage distribution obtained from FEA simulation. (b) Integration of contour maps of experimental voltage distributions. In these plots, the blue, black, and red lines represent the corresponding distributions of V_1, V_2 and V_3 respectively. The thick blue, black, and red lines represent the corresponding distributions, where $V_1 = 0$, $V_2 = 0$ and $V_3 = 0$ respectively. In the simulated distribution, the center point, where $V_1 = V_2 = V_3 = 0$, is located at the exact center of T-PSD, at coordinates (0, 0). However, due to imperfect sample cutting, the distribution obtained from experimental testing does not exactly match the simulated distribution. The intersection points between the three lines in the experimental distribution are (0.302, -0.400), (0.223, -0.479), and (0.380, -0.479). The center point of these three intersections, (0.302, -0.453), is taken as the distribution center of the measured signal. These coordinates are used for data correction offsets, i.e., x_{offset} = 0.302 mm, y_{offset} = -0.453 mm.

5.6.2.3. 2D T-PSD experimental realization

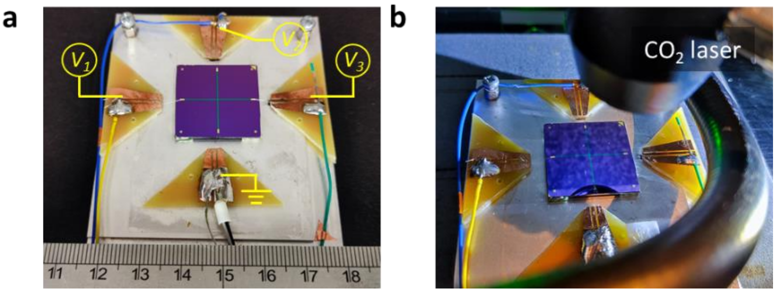

Figure S5.2.6. Photograph of a 2D T-PSD prototype. The 2D T-PSD is (a) integrated onto the test holder and (b) implemented in the test environment using a CO_2 laser beam as a HS.

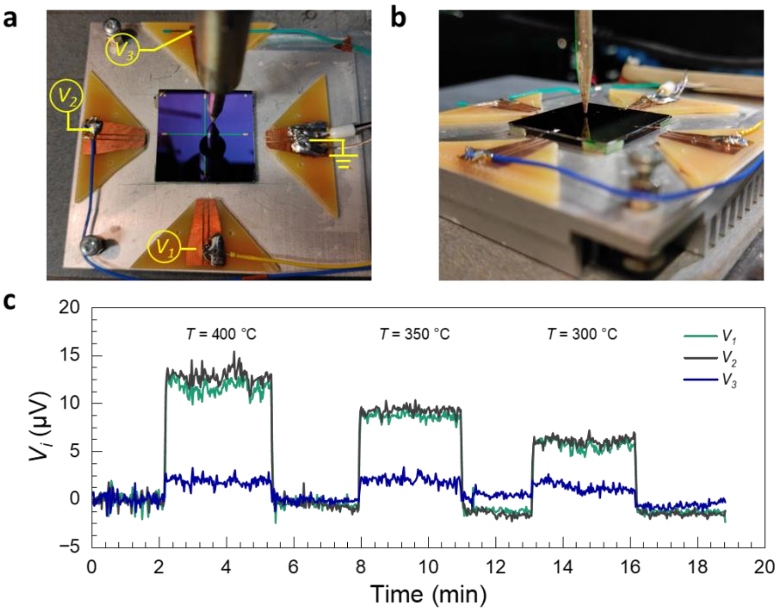

Figure S5.2.7. Hot soldering iron tip as a HS for 2D T-PSD. (a) Top view and (b) side view of the 2D T-PSD device. This device is the same 2D T-PSD device used in Figure S5.2.6. (c) The measured V_{diff} under different temperatures when the soldering iron tip is located near (-7, 7) mm.

5.6.3. 2D T-PSD signals decoding

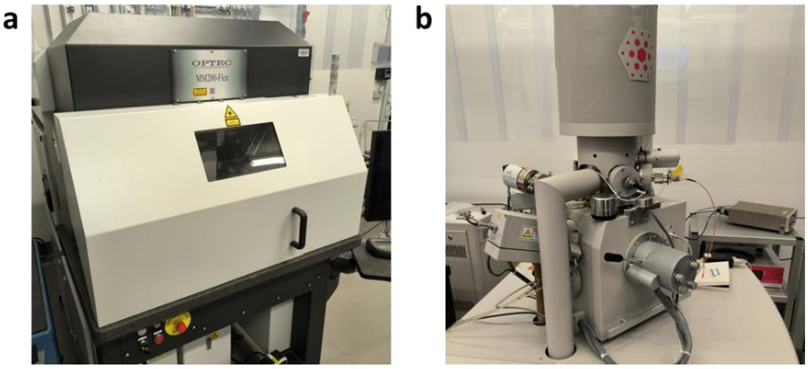

Figure S5.3.1. Protection of test environment. (a) All tests using the CO_2 laser beam and the hot soldering iron tip as HS were conducted within the metal protective cover of the laser micromachining system. (b) All tests using the electron beam as the heat source were performed in the high vacuum metal chamber of the scanning electron microscope. These tests were conducted in a laboratory with constant temperature and humidity to ensure the stability of the experimental environment.

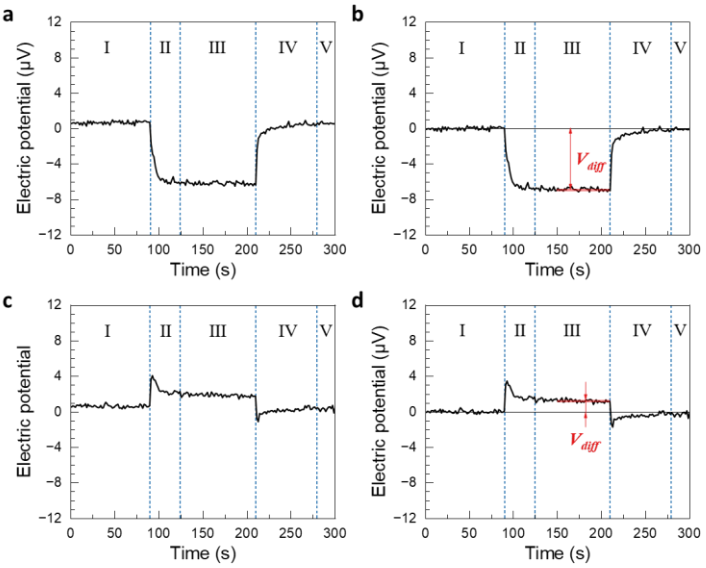

Figure S5.3.2. Typical signal analysis to show the drift compensation strategy. (a) and (c) are the signals when the electron beam is located at x=2+Δx mm and x=8+Δx mm respectively. They are representative thermoelectric DC signals for stable HS measurements. Here, a single test takes about 5 minutes. The HS is not on the detector for the first 1.5 minutes (Phase I). The temperature is the same everywhere in the detector, and the measured signal can be used as a reference baseline to correct the drift of the voltmeter. After activating HS, the temperature gradient begins to build and the signal of the sample begins to change. However, because it takes time to stabilize the temperature gradient, the measured signal also takes a period of time (stage II) to relax and reach a stable state (stage III). After removing the HS, the temperature of the sensor takes some time to cool down (stage IV) to room temperature (stage V). Oscillations in the baseline are caused by noise in the test. In order to improve the accuracy of decoding, the average value of the baseline is taken as the drift of the voltmeter, and the overall signal is shifted and corrected based on this drift value. The translationally corrected signals when the electron beam is located at x=2+Δx mm and x=8+Δx mm are shown in (b) and (d) respectively. In order to ensure the accuracy of the measured signal as much as possible, the average value of the last segment of data in the stage III signal is taken as V_{diff} for position decoding. For example, for these two data, we select the average value of the data one minute before removing HS as V_{diff}.

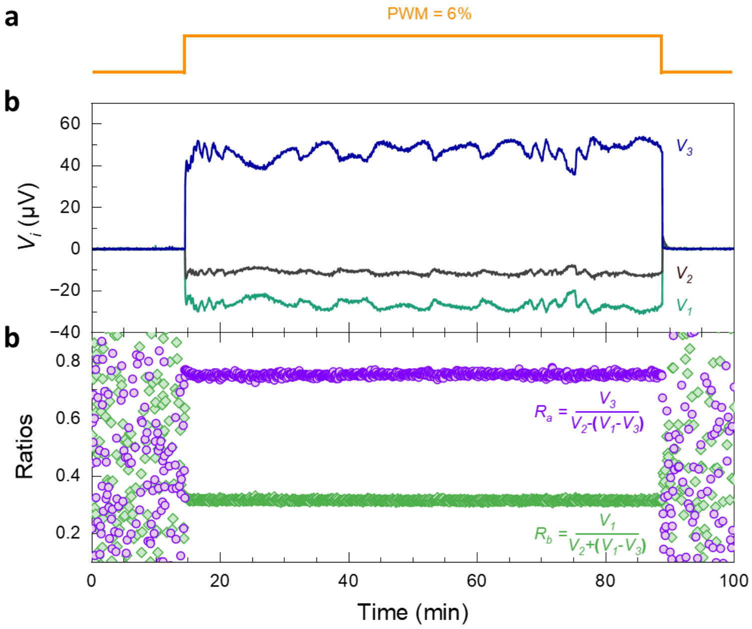

Figure S5.3.3. Long-time measurement for a 2D T-PSD at the position (6, -2) to highlight the stability of the ratios. (a) Laser pulse sketch. (b) The corresponding V_i signala. (c) The corresponding derived ratios of R_a and R_b . The ratio remains stable throughout the measurement. The position determination is independent of the form of the HS and can even attenuate the instability of the HS. These ratios are offset by the coefficient, $-\frac{qS}{2\pi kd}$, that allow them to be independent of material properties, the local temperature of the HS, and even its inherent fluctuations.

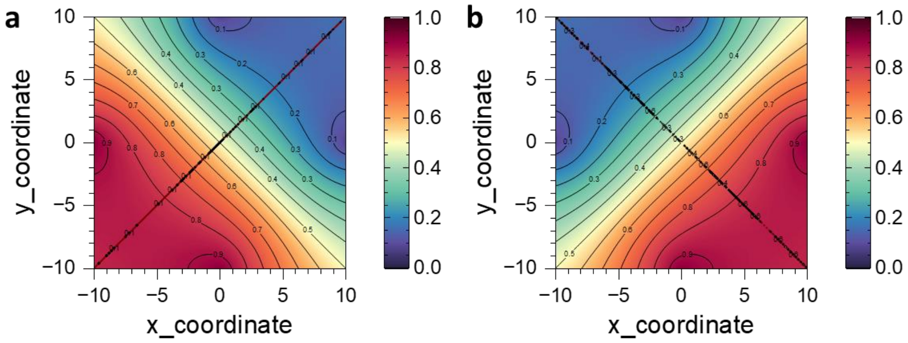

Figure S5.3.4. The graphs from the mathematical model for (a) R_a and (b) R_b.

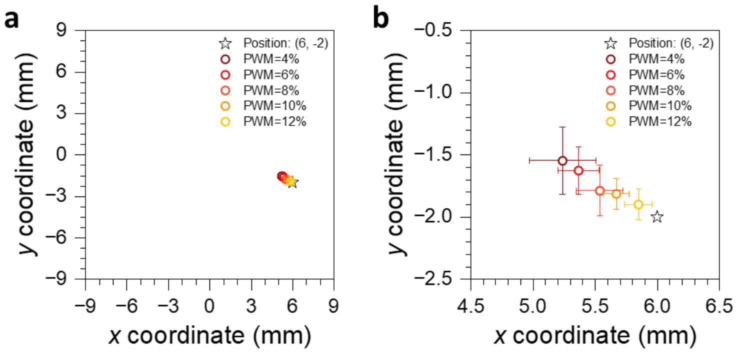

Figure S5.3.5. The decoded result comparison for different PWM values in Figure 5.4b. The signal of the second laser pulse under each PWM setting is used. within (a) the whole detecting area and (b) the zoomed-in area. Although position (6, -2) is already on the edge of the accurate area, a higher PWM will make the decoding more accurate due to the weakened environment influence.

Table S5.3.1. The sign combination of the measured signals.

Region/Line	V_1	V_2	V_3
L1	0		
L2		0	
L3			0
A1	+	+	-
A2	+	+	+
A3	-	+	+
A4	-	-	+
A5	-	-	-
A6	+	-	-
Center point	0	0	0

5.7. Cover art

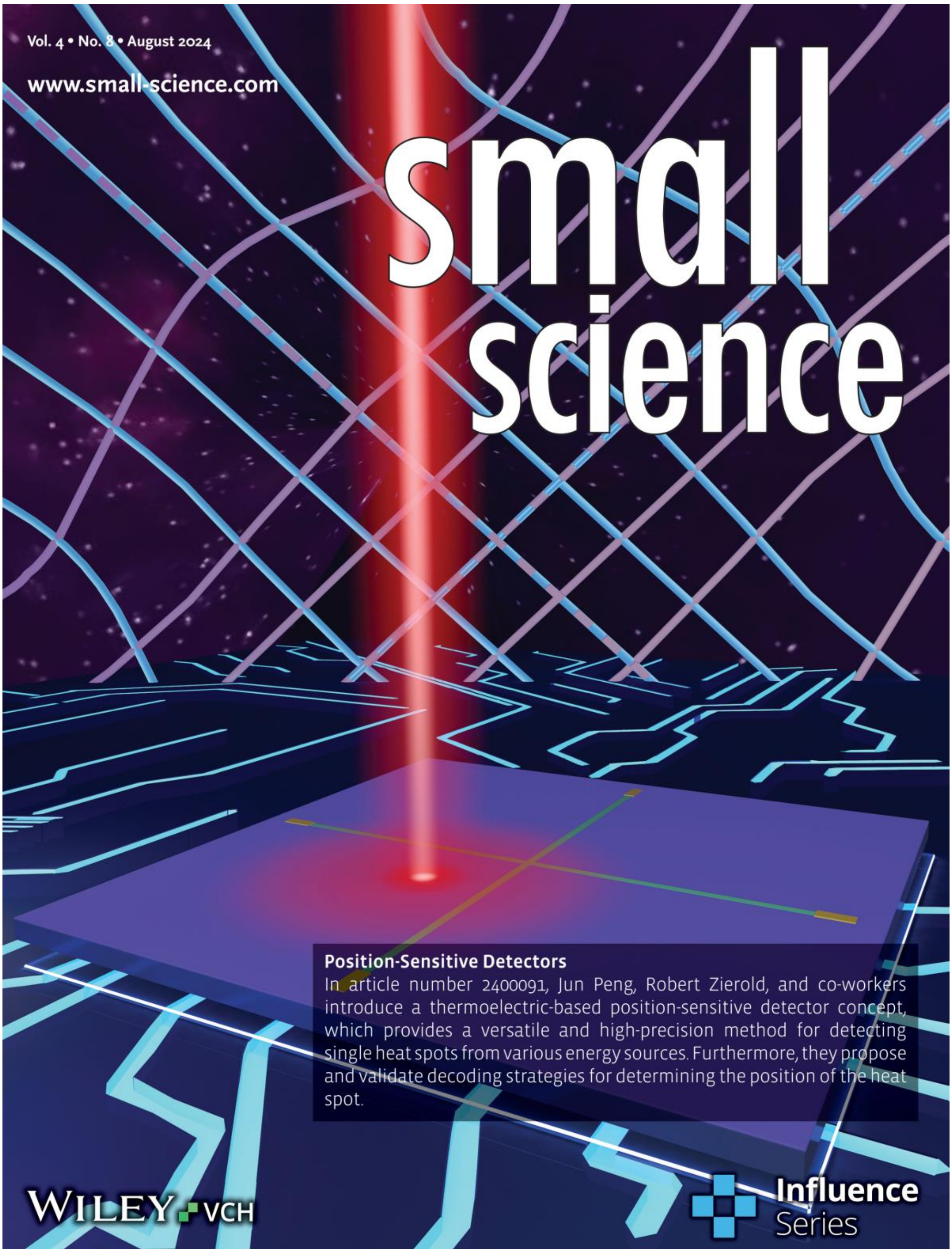

Position-Sensitive Detectors

In article number 2400091, Jun Peng, Robert Zierold, and co-workers introduce a thermoelectric-based position-sensitive detector concept, which provides a versatile and high-precision method for detecting single heat spots from various energy sources. Furthermore, they propose and validate decoding strategies for determining the position of the heat spot.

The cover design is featured on a frontispiece in Small Science.

6. Atomic layer etching of SiO_2 via sequential SF_6 gas and Ar plasma

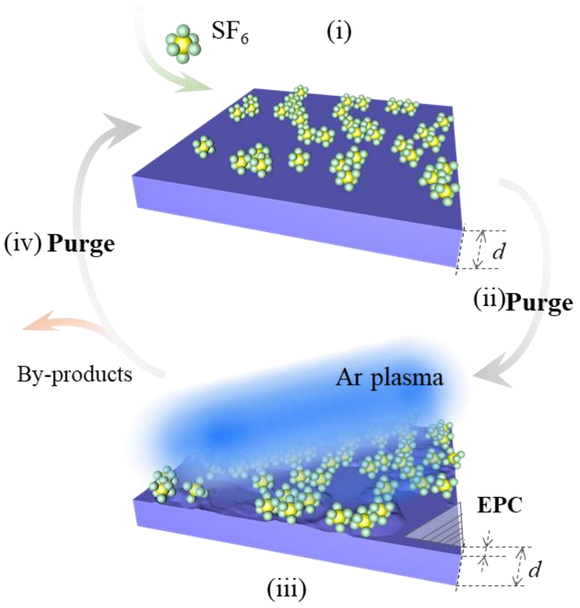

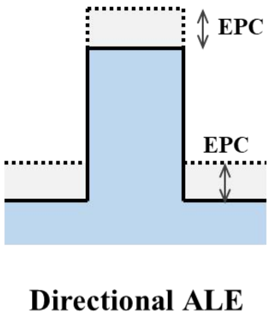

This work demonstrates an atomic layer etching process on silicon dioxide using sequential SF_6 gas and Ar plasma at room temperature, achieving a stable and consistent etching rate of approximately 1.4 Å/cycle. The systematic study confirms its 100% synergy and reveals its directional etching characteristics.

This chapter is adapted from a submitted first author's peer-reviewed article which has been uploaded on arXiv, with only the formatting changed, and the content remains unchanged.

J. Peng, R. Venugopal, R. Blick, R. Zierold, *Atomic layer etching of SiO_2 using sequential SF_6 gas and Ar plasma*. arXiv:2412.20653. DOI: 10.48550/arXiv.2412.20653.

Manuscript title

Atomic layer etching of SiO_2 via sequential SF_6 gas and Ar plasma

Author list

Jun Peng, Rakshith Venugopal, Robert Blick, Robert Zierold**

Center for Hybrid Nanostructures, Universität Hamburg, 22761 Hamburg, Germany

Keywords

atomic layer etching, synergy, silicon dioxide, sulfur hexafluoride, plasma, directional etching

Author contributions

J.P. proposed the concepts and designed the experiments; V.R. and J.P. performed the experiments and analyzation; R.Z. supervised the study; R.B. provided infrastructure to conduct the experiments; J.P., V.R. and R.Z. co-wrote the manuscript. All authors discussed the experimental and theoretical results and commented on the manuscript. All authors have approved the final version of the manuscript.

Acknowledgements

This work was funded by the Deutsche Forschungsgemeinschaft (DFG, German Research Foundation) – Projektnummer 192346071 – SFB 986 “Tailor-Made Multi-Scale Materials Systems”.

6.1. Abstract

In the relentless pursuit of advancing semiconductor technologies, the demand for atomic layer processes has given rise to innovative processes, which have already played a significant role in the continued miniaturization features. Among these, atomic layer etching (ALE) is gaining increasing attention, offering precise control over material removal at the atomic level. Despite some thermal ALE achieved sub-nm etching controllability, the currently practical ALE processes that involve plasmas steps often suffer from high etch rates due to the scarcity of highly synergistic ALE half-reactions. To overcome this limitation, we developed an ALE process of silicon dioxide (SiO_2) on a silicon wafer using sequential pure sulfur hexafluoride (SF_6) gas exposure half-reaction and argon (Ar) plasma etching half-reaction near room temperature, achieving a stable and consistent etching rate of approximately 1.4 Å/cycle. In this process, neither of the two half-cycle reactions alone produces etching effects, and etching only occurs when the two are repeated in sequence, which means a 100% synergy. The identification of temperature and plasma power windows further substantiates the high synergy of our ALE process. Moreover, detailed morphology characterization over multiple cycles reveals a directional etching effect. This study provides a reliable, reproducible, and highly controllable ALE process for SiO_2 etching, which is promising for nanofabrication processes.

6.2. Introduction

Atomic layer processing technologies, including atomic layer deposition (ALD) and ALE, have emerged as key techniques in the semiconductor industry,[46, 142, 278, 279] and have further been instrumental in fabricating recent generations of nanoelectronics such as quantum devices.[280-284] They offer true atomic-level control on the processing thickness, pushing the limits of feature size, three-dimensional scaling, and overall device performance, while also being compatible with wafer-scale fabrication and high-volume manufacturing.[5, 146, 285] The concept of ALE first appeared in a 1988 patent, which described the removal of single atomic layers of crystalline diamond by alternating exposure to nitrogen dioxide and bombardment with inert gas ions in a plasma.[3] However, due to the limited demand for such precise etching techniques at the time, it did not raise much attention. As Moore's Law has reached its limits in the past decade, ALE has gained more attention and has even been used in logic devices at the 10 nm technology node.[5] And in 2015, Lee and George[286] reported the first isotropic etching of Al_2O_3 using a thermal ALE process, inspiring further exploration of ALE as a unique dry etch technique. However, plasma-related ALEs, which is more practical and widely used, still suffer from excessively high etching rates due to non-ideal synergy between half-reactions, where other etching reactions such as physical sputtering occur. ALE synergy, S, can be used to check the purity of the ALE process and is quantified as a percentage relative to the total amount of material etched per cycle (EPC), $S = \frac{\mathrm{EPC}-(\alpha+\beta)}{\mathrm{EPC}} \times 100\%$, where the values of "$\alpha$" and "$\beta$" are undesirable contributions from the individual surface modification steps and the removal step, respectively.[146, 147]

SiO_2, a critical material in the semiconductor field, has been extensively explored using various ALE strategies.[148] These include thermal ALEs with trimethylaluminum as a precursor,[287, 288] plasma-related ALEs using fluorocarbons to modify the passivated surface,[289, 290] and ALE utilizing pure infrared thermal effects to etch the modified surface.[291] While thermal ALE obtained an EPC below 1 Å/cycle, its isotropic etching characteristics limit its applicability in an environment where directional etching remains the primary demand. Although plasma-involved ALE offers good directional etching results, challenges such as high etching rates and weak synergy persist in SiO_2 ALE. Here, we demonstrate an ALE strategy for SiO_2, whose ALE temperature window is near room temperature, using sequential SF_6 gas and Ar plasma, and achieving a constant EPC of approximately 1.4 Å/cycle. The 100% synergy of this strategy was confirmed through a systematic study involving plasma power, dose, and substrate temperature. Additionally, this ALE process was used to etch pillars and holes, exhibiting excellent directional etching effects. This work provides a competitive, reliable, and controllable directional etching option for high-precision micro-nanofabrication.

6.3. Results and discussion

6.3.1. Process of the proposed ALE

According to the consensus of the ALE community, an ALE process decomposes the whole etching process into two or more individually controlled, self-limiting, surface reaction steps that remove material only when run in sequence.[5] Our ALE process is designed based on this idea, which consists of four steps per cycle: (i) surface modification step, (ii) purge step, (iii) removal step, and (iv) purge step as shown in Figure 6.1a. In the modification step (Figure 6.1a(i)), the SF_6 molecules are introduced into the reactor and adsorbed on the exposed substrate surface in a self-limiting manner. After a purge step (Figure 6.1a(ii)), the Ar plasma is activated (Figure 6.1a(iii)), generating Ar+ ions and free electrons. The plasma products react with the modified silica surface, resulting in active substances, e.g., SF_5^+, SF_4^{2+}, and F-radicals.[292] These substances, especially F-radicals, are highly reactive and can react with SiO_2 to generate volatile byproducts such as SiF_4.[293] Because SF_6 is adsorbed on the substrate surface in a self-limiting manner, the quantity of SF_6 and the movement and range of action of the active substances are limited. This constraint ensures that only a single layer of the surface is etched after another purge step (Figure 6.1a(iv)). Note that the single "layer" etched in ALE, similar to ALD, refers to a fixed thickness etched in each cycle, typically in the sub-nm range. If the material being etched is crystalline, this thickness is usually equal to or slightly less than a crystalline monolayer thickness. In addition, in practical applications, the etched material is often amorphous, removing the monolayer concept not strictly applicable. In ALE, the thickness etched in each cycle is defined as EPC. Figure 6.1b shows the etch thickness for different cycle numbers. The EPC obtained by linear fitting is 1.4 Å/cycle with $R^2 \approx 0.999$. The characterization was conducted using the standard loop recipe for this work: a pulse of SF6 gas molecules (20 sccm, 5 s) for the modification step, followed by 30 s purge; then a pulse of Inductively Coupled Plasma (ICP) (100 W, 60 s) for the removal step, with another purge for 30 s. Throughout the process, Ar served as a carrier gas with a flow rate of 100 sccm. The reactor was maintained at room temperature and 1 Pa pressure. Figure 6.1c and Table S6.1 compare the EPC between this work and previous explorations over the past decade,[287-289, 291, 294-303] demonstrating the superiority of our "sequential SF_6 gas and Ar plasma" ALE strategy in accuracy. Our approach has achieved an EPC on par with thermal ALE, showcasing its potential in further research and practical applications.

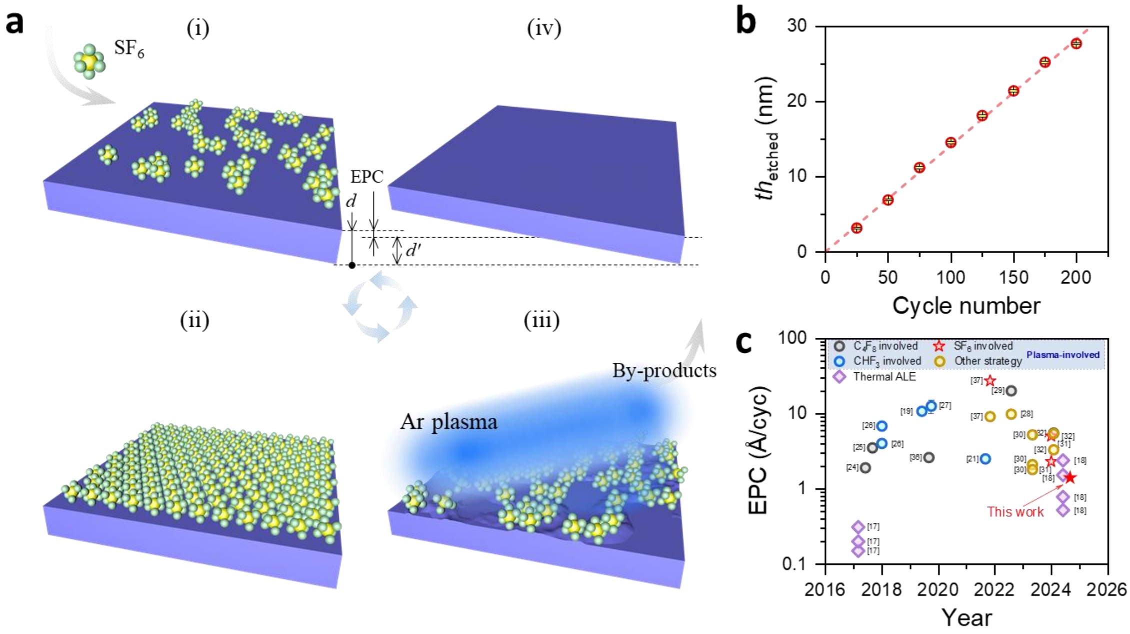

Figure 6.1. ALE process. (a) Schematic diagram of the ALE strategy using sequential SF_6 gas and pulsed Ar plasma. The process consists of two half-reactions, with the total cycle divided into four steps: (i) In the surface modification step, a pulse of SF_6 molecules is adsorbed on the exposed substrate surface in a self-limiting manner. (ii) A purge step follows to remove excess molecules, leaving a thin SF_6 layer on the exposed silica surface. (iii) In the removal step, a pulse of Ar plasma is applied, breaking the bonds and removing the surface atomic layer. (iv) Subsequently, the reaction chamber is purged again, leaving a new, fresh SiO_2 surface. Each cycle removes a thin layer of silicon dioxide from the surface, termed Etch Per Cycle (EPC). (b) When using the standard loop recipe, the EPC is defined 1.4 Å/cycle from the etched thickness, th_{etched}, over cycle numbers by linear fitting with $R^2 \approx 0.999$. (c) Comparison of the EPC from this work with the state-of-the-art plasma-involved SiO_2 ALE in the past decade. The numbers next to the data points represent the corresponding reference number in Table S6.1. The precision of our plasma-involved process is comparable to thermal ALE processes.

6.3.2. ALE synergy characterization

In ALE, the modification and removal steps are separated by two purge steps in the loop setup as displayed in Figure 6.2a. Ideally, no step in ALE will produce etching effect alone. In order to better understand the etching mechanism of this ALE process, it is worthwhile to conduct a more careful and systematic study of the control variables of the surface modification step and the removal step, and characterize their ALE synergy effect S simultaneously. First, the modification step is removed from the standard process, and the effect of ICP power (removal step) on etching is studied separately. Such a process can be seen as pure Ar^+ sputtering process. From the results shown in Figure 6.2b, it can be seen that the EPC corresponding to the four ICP powers fluctuates around zero. This fluctuation is caused by the error of the ellipsometer measurement. Therefore, within the tested ICP power range (50~100 W), β equals zero. Next, the etching step is removed from the cycle and the SF_6 dose (modification step) is studied. Obviously, SF_6 alone does not produce any etching (Figure 6.2c), which means α

equals zero. It can be calculated that the ALE synergy of the standard process in this work is *S* = 100%. Such a result is much better than the synergy (~80%) of the ALE using alternating fluorocarbon plasma and argon ions that has been used in the production of logic devices at the 10 nm technology node.[147] ALE has an important characteristic, self-limitation, which can be verified by controlling the dose of the precursor. As shown in Figure 6.2d, gradually increasing the dose of SF_6 results in a gradual increase in EPC, which reaches saturation at around 25 sccm·s. Beyond this point, the EPC no longer changes significantly with further increases in the dose. Note that lower doses cannot be set by the instrument used.

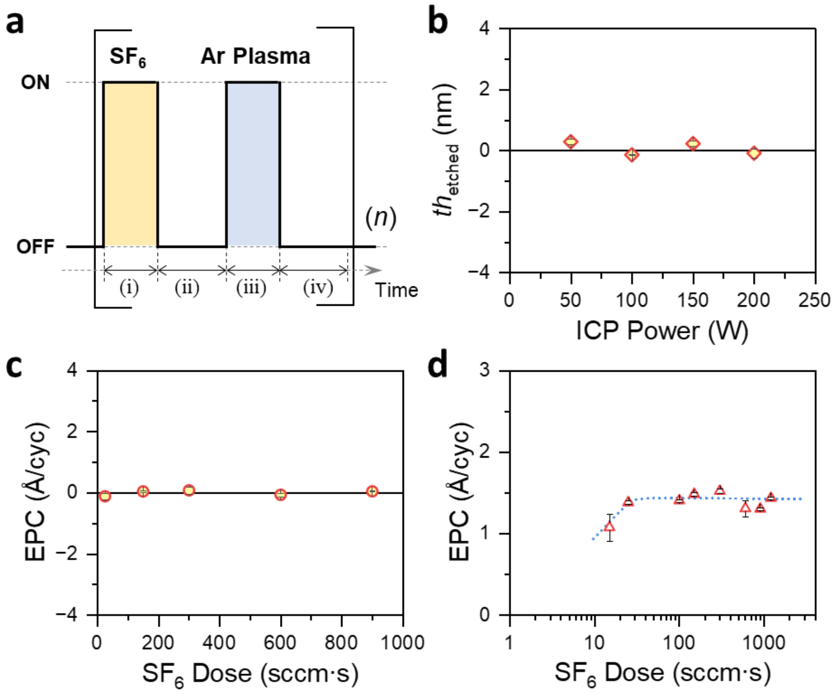

Figure 6.2. The process setup and synergy verification. (a) Process setup. By controlling the variables, the synergistic effect can be verified to show how "pure" our ALE process is. Steps (i) to (iv) correspond to (i) to (iv) in Figure 6.1a. (b) Process tests without (i) SF_6 modification step. (c) Process tests without (iii) Ar plasma removal step. These two tests were performed based on the standard process, changing only the corresponding parameter amounts shown on the x-axis, namely ICP power and SF_6 dose, respectively. (d) Effect of SF_6 dose on etching effect when setting the ICP power at 100 W. This shows that the adsorption of SF_6 on the substrate surface is self-limiting.

6.3.3. ALE windows exploration

Based on the above data, it can be confirmed that the "sequential SF_6 gas and Ar plasma" ALE process demonstrates pure ALE with 100% synergy. As ALD and ALE share many similarities, an ideal ALE should also exhibit an ALE window like that ALD has an ALD window. Figure 6.3a shows the effect of the wafer holder temperature on the etching rate. From room temperature to about 40 °C, the EPC remains stable, indicating the ALE window location. While beyond this range until 160 °C, the EPC gradually decreases. According to the adsorption principle, this decrease in EPC may be due to SF_6 molecules at higher thermal energy, leading to easier desorption from the surface and thus reducing effective etching. In addition to the temperature window, an ICP power window is also identified. As ICP power increases, the ionization rate of the gas increases, resulting in higher ion density, higher electron temperature, and more energetic plasma. When the energy of incident active particles is sufficient to remove the SF_6-modified surface but not the underlying SiO_2, it falls within the ALE power window, such as the 50-100 W range in Figure 6.3b. Below this window, the energy of incident particles is insufficient to remove all the modified surface, causing a decreasing EPC. However, contrary to previous reports on plasma-related ALE of SiO_2, our EPC decreases as the ICP power increases beyond the window. Typically the EPC rises due to the onset of physical sputtering.[304] This difference may be explained by the increased concentration of various particles at higher ICP power, diluting the concentration of dissociated F-radicals and reducing EPC. Additionally, higher energy active particles and elevated temperatures may cause more intense collisions, leading to elastic scattering and desorption of SF_6 from the surface, thereby diminishing effective etching. Note that the tested ICP power has not yet reached the threshold of physical sputtering in this condition as shown in Figure 6.2b.

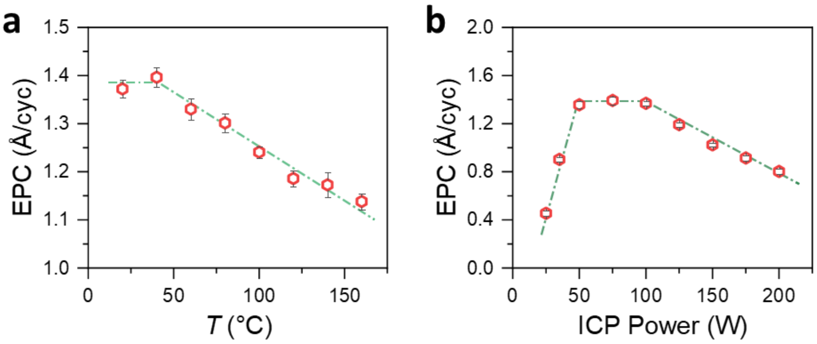

Figure 6.3. Characteristics of the ALE windows. (a) Temperature window. (b) Plasma power window. The standard process parameters are controlled as a continuous flow of 100 sccm of Ar, 5 sccm of SF_6 for 5 seconds, and a plasma time of 60 seconds. Only the corresponding quantities are changed during the study.

6.3.4. Directional etching

Unlike the unparalleled conformality of ALD, ALE can be categorized into directional etching and isotropic etching, each required for different applications. Therefore, verifying the type of etching in the ALE process is crucial. A substrate with pillars with 600 nm in diameter is used for testing. Figure 6.4a and Figure 6.4b show optical microscope images and atomic force microscope (AFM) images of the sample at different stages. The color variations in the optical images result from changes in the overall film thickness due to etching. The AFM image and detailed interface profile analysis (Figure 6.4c) reveal that the three-dimensional surface morphology of the sample does not change significantly as the etching proceeds. This observation indicates that our ALE process is directional and does not etch the side facets of the pillars (Figure 4d). In isotropic etching, besides the pillar height remaining unchanged, the pillar diameter should uniformly reduce (Figure S6.2). For this sample, the entire sample was uniformly etched by 62 nm (Figure 6.4e). If the process were isotropic, the diameter of the pillar should have reduced by about 27%, but the actual diameter remained constant. The directional etching in our ALE process is likely the result of the bias voltage generated by factors such as the self-bias effect and potential capacitive coupling from the ICP power. Although the bias voltage was not deliberately activated during the experiment, it is still observed when the Ar plasma pulse is initiated (Figure S6.3). This bias voltage creates an electric field in the plasma sheath near the substrate surface, accelerating ions toward the substrate. Therefore, the bombardment of charged particles in the plasma, including Ar^+ ions, on the substrate is directional, enhancing the perpendicular component of their interaction with the substrate plane. For different incident angles, the energy of the particles varies significantly. The higher the incident angle, the smaller the particle energy, and the less likely it is to etch the micro-nano pillars and hole sidewalls.[305, 306] At low pressure, particles also have a larger mean free path. This directional movement and angle-dependent energy ensure that etching primarily affects the vertical dimensions of the sample rather than the horizontal. Furthermore, this directional etching also shows high repeatability in hole samples (Figure S6.4). Additionally, after ALE etching, the sample's roughness (Ra) remained around 0.7 nm, confirming the gentle etching nature of the etching process.

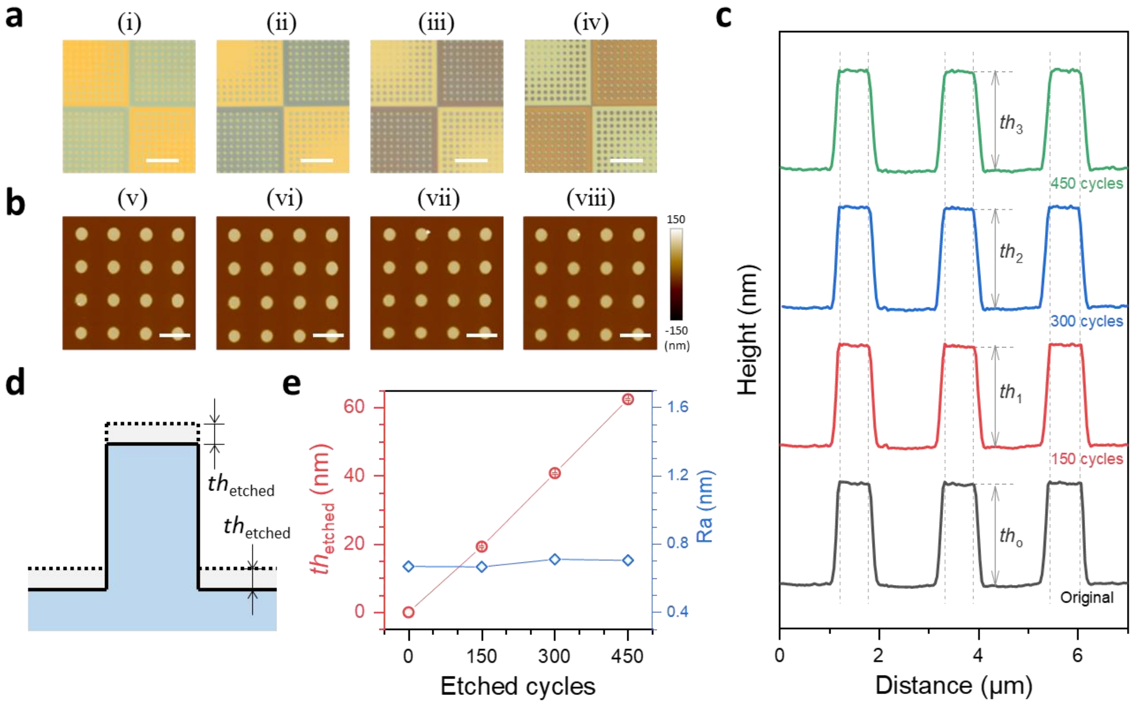

Figure 6.4. Directional ALE etching. Pillars are prepared for this characterization. (a) Optical microscope images and (b) the corresponding AFM images of the original pillar sample (i, v), the same position after 150 ALE cycles (ii, vi), the same position after 300 ALE cycles (iii, vii), and the same position after 450 ALE cycles (iv, viii). The color difference is due to the different thicknesses of SiO_2 after etching. The scalebar for (a), (b) are 10 μm and 2 μm. (c)The analysis of the same three consecutive pillars in their original state and after 150, 300, and 450 ALE cycles. The corresponding pillar heights th_0, th_1, th_2, and th_3 are 91.4 ± 1.17, 91.3 ± 0.86, 90.7 ± 0.91, 89.6 ± 1.00 nm, which keeps the same during the etching. (d) Sketch of the directional etching result. (e) Corresponding etched thickness th_{etched} and roughness *Ra* during the test. The stable and low *Ra* suggests a damage-free surface.

6.4. Conclusions

In summary, we have developed an ALE process for SiO_2 using sequential pure SF_6 gas exposure and Ar plasma etching near room temperature, achieving a stable and consistent etching rate of approximately 1.4 Å/cycle. No etching effect was observed in the individual half-reaction cycles, and we identified both an ALE temperature window near room temperature and an ALE plasma power window, indicating 100% synergy between the half-reactions. Additionally, the diameter of the micro-nano pillars and holes on the plane remained unchanged during the etching process, confirming that the process is directional. Our etching process is performed using commercial RIE equipment with commonly used gases in the semiconductor field, offering good scalability and versatility. While we used SiO_2 as an example to demonstrate the precise etching capability of this method, the process described here can potentially be extended to other materials that are reactive to an etching gas's plasma but unreactive to its pure gas.

6.5. Material and methods

The samples used were cut from a 4-inch SiO_2 (300 nm)/Si wafers (SIEGERT WAFER GmbH). Each sample was cut into approximately 1×1 cm. The samples were cleaned in acetone, isopropanol and deionized water. The etching was done in a commercial reactive ion etching (RIE) System (SenTech SI 500). The samples were inserted into the chamber under vacuum. The standard process of the ALE process is a cyclic process performed at a constant 23 °C with a continuous flow of 100 sccm of Ar at a working pressure of 1 Pa. SF_6 is injected into the reaction chamber at a rate of 20 sccm for 5 seconds alongside 100 sccm Ar, then the injection of SF_6 is stopped. The excess SF_6 is purged away by the Ar gas, for 30 seconds. This is termed the Purge Process. After which the plasma is activated by applying an ICP power of 100 W for 60 seconds. After turning off the ICP power, another Purge Process occurs for 30 seconds. This constitutes one ALE process. It was found that the etch rate is ~1.4 Å/cyc. The thickness of the samples was measured with an *ex-situ* ellipsometer (SenTech). The thickness is determined by using a Cauchy Model for SiO_2. The film thickness was measured before and after etching. For the pillars, positive e-beam resist ARP661.09 was used. The pattern was defined by an electron beam lithography system (Raith). The resulting sample was then subjected to a deep ion etching in the RIE system, with a continuous flow of 60 sccm SF_6, a plasma was generated with an ICP power of 300W and a radio frequency (RF) bias of 60 W. The etching was carried out for 70 seconds. Then, the samples were cleaned with an Ar plasma of 300 W of ICP power for 120 seconds in the same RIE system. Scanning Electron Microscope images were taken from SEM (Zeiss Crossbeam 550), and the roughness was measured by Atomic Force Microscope (AFM, Dimension).

6.6. Supporting Information

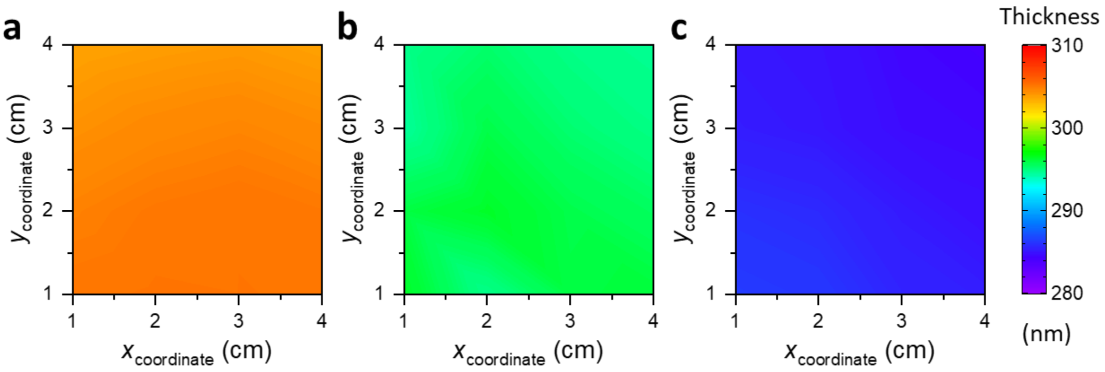

Figure S6.1. Uniformity test on the same SiO_2/Si wafer with a 4.5 cm × 4.5 cm size. (a) The thickness of the SiO_2 layer of the original sample is 304.7 ± 0.54 nm. (b) The thickness of the SiO_2 layer after 75 cycles is 295.5 ± 0.67 nm, and 9.2 ± 0.51 nm is etched. (c) The thickness after another 75 cycles, in total of 150 cycles, is 285.2 ± 0.61 nm, and 19.5 ± 0.50 nm is etched. The test was performed at a 4 cm × 4 cm area with a spacing of 1 cm. Each measurement was made at the same location. The standard deviations of the etched thickness after 75 cycles and 150 cycles are all around 0.5 nm, indicating good intra-wafer uniformity of the etching.

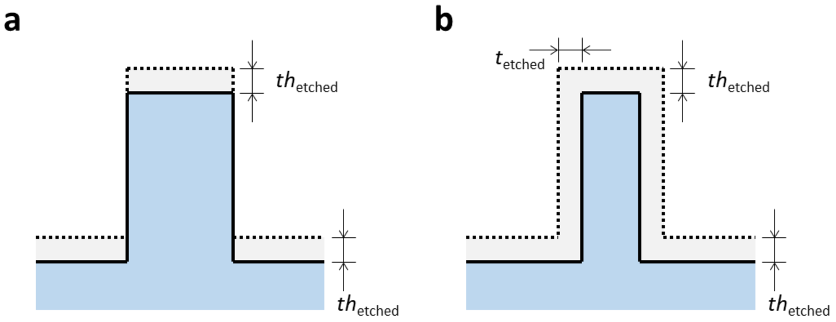

Figure S6.2. Comparison of directional etching and isotropic etching. (a) Directional etching will only etch in the vertical direction, not in the horizontal direction. (b) However, in isotropic etching, the cylinder will be uniformly etched in both the vertical and horizontal directions, resulting in a reduction in diameter.

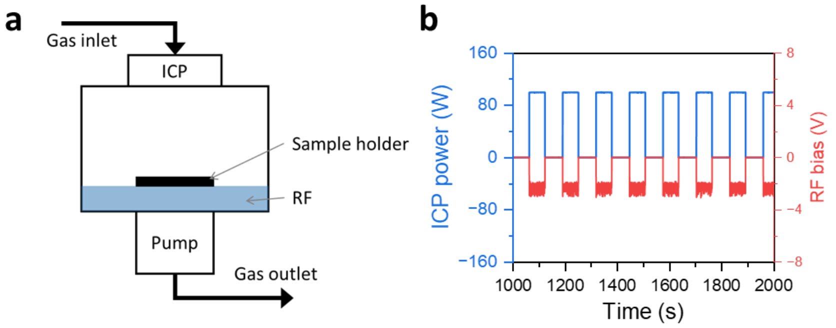

Figure S6.3. Indirect bias voltage. (a) The sketch of the reactor. (b) Part of the instrument log showing the detected ICP power and RF power during the experiment. During the experiment, only the ICP on the top of the sample was activated in the form of pulses, and the RF power was set to zero. Every time the ICP was activated, a passively generated RF bias was recorded. This bias will make the plasma directional.

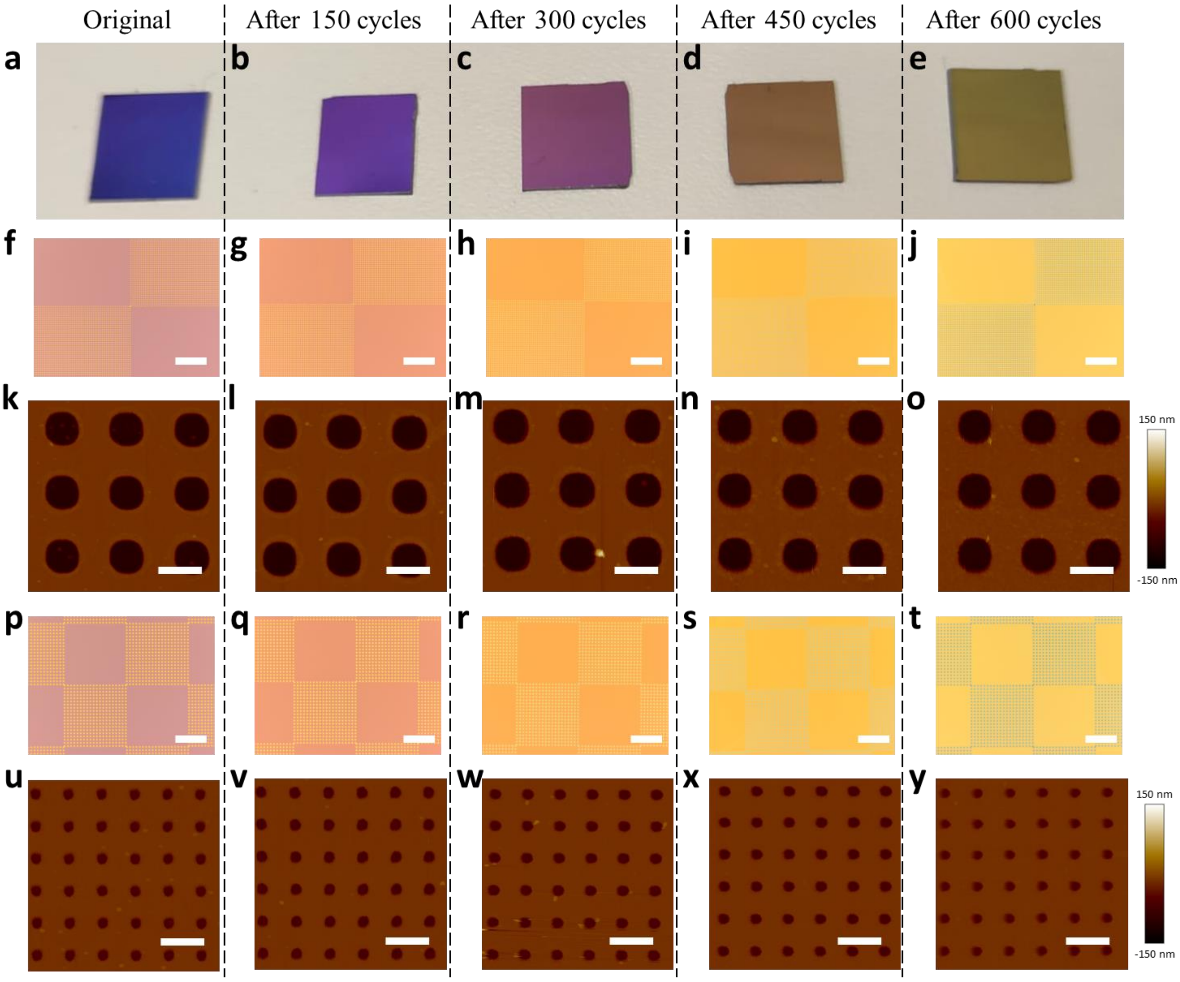

Figure S6.4. Holes sample for the etching effect test. (a~e) Photo of the etching reference samples. The size of the five reference samples is about 1 cm × 1 cm. Samples (b)~(e) were placed in the reaction chamber at the first batch and taken out after the corresponding etching batch in turns. (f~j) Optical images of the same sample, with a hole diameter of about 1.2 µm, at the same position after different number of etching cycles. (k~o) AFM images of the same sample after different number of etching cycles corresponding to the sample in (f~j). (p~t) Optical images of the same sample, with a hole diameter of about 0.6 µm, at the same position after different number of etching cycles. (u~y) AFM images of the same sample after different number of etching cycles corresponding to the sample in (p~t). Etching reduces the thickness of the SiO_2 film, causing the color of the film to change, but the diameter of the pores does not change. The scalebar for (f~j), (k~o), (p~t), and (u~yt) are 20 µm, 2 µm, 20 µm, and 2 µm.

Table S6.1. EPC comparisons of reported SiO_2 etching using ALE manner.

#	Time	Reactant A	Reactant B	Further reactants	EPC (Å/cyc)	ref
1	2017-02	Trimethylaluminum ($Al(CH_3)_3$)	HF	--	0.027 (0.1 Torr) 0.15 (0.5 Torr) 0.2 (1 Torr) 0.31 (4 Torr)	[287]
2	2017-05	C_4F_8 plasma	Ar plasma	--	1.9	[294]
3	2017-08	C_4F_8/Ar plasma	Ar plasma	--	3 ~ 4	[295]
4	2017-12	CHF_3 plasma	O_2 or Ar plasma	--	6.8 (O_2 plasma) 4.0 (Ar plasma)	[296]
5	2019-05	Ar plasma	CHF_3	--	10.7	[289]
6	2019-08	C_4F_8/Ar plasma	Ar plasma	--	2.6	[307]
7	2019-09	CHF_3	Ar Plasma	--	10 ~ 15	[297]
8	2021-08	CHF_3/O_2 plasma	infrared annealing		2.5	[291]
9	2021-10	HF	NH_3	infrared annealing	9.09	[303]
10	2021-10	H_2, SF_6 plasma	NH_3	infrared annealing	27.0	[303]
11	2022-07	CF_3I plasma	O_2 plasma	--	9.8	[298]
12	2022-07	C_4F_8	Ar Plasma	--	20	[299]
13	2023-04	Heptafluoropropyl methyl ether (HFE-347mcc3)	Ar plasma	--	2.1	[300]
14	2023-04	Heptafluoroisopropyl methyl ether (HFE-347mmy)	Ar plasma	--	1.8	[300]
15	2023-04	Perfluoro propyl carbinol (PPC)	Ar plasma	--	5.2	[300]
16	2023-12	SF_6 plasma	Ar plasma	--	2.3 (without bias) 5 (with bias)	[301]
17	2024-01	C_4F_8	Ar plasma	--	5.5	[302]
18	2024-01	perfluoroisopropyl vinyl ether (PIPVE)	Ar plasma	--	3.3	[302]
19	2024-01	perfluoropropyl vinyl ether (PPVE)	Ar plasma	--	5.4	[302]
20	2024-05	Trimethylaluminum ($Al(CH_3)_3$)	$Ar/H_2/SF_6$ plasma	--	0.52 (SiO_2) 0.78 (ALD SiO_2) 1.52 (PECVD) 2.38 (Sputtered)	[288]
	★	SF_6	Ar plasma	--	1.4	This work

7. Concluding Remarks

7.1. Main results

This dissertation revolves around the theme of ALP. A fabrication route for ALD assisted VO_2 synthesis was developed (Chapter 3), and its applications in the fields of memristors (Chapter 3) and photonic crystals (Chapter 4) were explored. Additionally, a novel T-PSD, was proposed based on the unique interface characteristics of ALD films (Chapter 5). Finally, building on the understanding of ALD, ALE process for SiO_2 etching was further developed (Chapter 6). The specific key contributions are summarized as follows:

(1) ALD-assisted strategy for the synthesis of VO_2.

A pure thermal ALD process is developed to deposit non-stoichiometric VO_x using TDMAV and water as precursors. A subsequent tailored annealing process effectively tunes the VO_x into the VO_2 phase. The optimal annealing conditions is 450 °C for 10 minutes in a nitrogen atmosphere with an oxygen partial pressure of 4% at approximately 1.4 Torr.

(2) ALD-assisted VO_2 for the memristor application.

ALD-assisted VO_2 for 2D and 3D memristor applications is explored. Specifically, the VO_2 thin-film memristors and Si-Al_2O_3/VO_2 core/shell memristors fabricated through this ALD-assisted VO_2 process demonstrated excellent switching performance and displayed tunability that was highly sensitive to temperature. The results highlight the 3D scalability of ALD-assisted VO_2 deposition in memristor applications, particularly when integrated with micro- and nanostructures.

(3) ALD-assisted VO_2 for the photonics application.

By leveraging the conformality of ALD coatings on three-dimensional complex structures and combining this with the IMT of VO_2, we have constructed a switchable 3D PhC. We introduce a fabrication strategy for switchable 3D PhCs, utilizing sacrificial templates and ALD of VO_x, along with precisely controlled annealing. The resulting VO_2 IO PhC demonstrates significant control over the PBG in the NIR region, which can be reversibly switched by adjusting the external temperature. Additionally, we reveal a temperature-dependent transition from a narrow-band NIR reflector to a broad-band absorber.

(4) T-PSD detector.

A kind of novel PSD, the T-PSD is proposed to detect single heat spots arising from various energy sources, including electromagnetic radiation, electrons, and macroscopic mechanical heat. The T-PSD concept is derived mathematically from fundamental principles of heat conduction and the Seebeck effect. This concept is validated through finite element simulations in both 1D and 2D configurations. Subsequently, T-PSD prototypes are fabricated and tested for positional detection using stimuli such as CO_2 laser beams, hot soldering tips, and electron beams. The prototypes, which feature structured AZO thermoelectric thin films prepared via ALD, are equipped with voltage probes to measure thermoelectric voltages as a function of the position and intensity or temperature of the heat spot. Practical decoding strategies are introduced to determine the position of the measured signals.

(5) ALE of SiO_2.

A new ALE process is developed for SiO_2 etching using SF_6 gas and Ar plasma near room temperature, achieving a stable and consistent etching rate of approximately 1.4 Å/cycle. The self-limiting nature and 100% synergy are verified through systemic parameters tests. Moreover, detailed morphology characterization over multiple cycles reveals directional etching. Additionally, the diameter of the micro-nano pillars and holes on the plane remained unchanged during the etching process, confirming the directional etching character.

7.2. Challenges and chances

So where are we going next? Throughout the completion of this dissertation, numerous new questions and ideas emerged and I cannot possibly cover them all here. However, further exploration in the following directions would be both interesting and promising based on the progress made so far.

Further studies for the ALE

Over the past decade, ALE has begun to gain significant attention, though examples of highly synergistic ALE remain limited. Theoretical studies are therefore limited. Our experimental results, which demonstrate 100% synergy, offer a promising basis for further fundamental research that could either validate existing theories or lead to the development of new theoretical concepts. Several key questions require deeper understanding: What are the specific adsorption properties of SF_6 on the SiO_2 surface? How exactly are fluorine radicals generated - are they the result of collision mechanisms or other processes? Furthermore, what is the extent of diffusion for these generated fluorine radicals? In addition, the ALE process developed in this study currently displays directional etching, attributed to the parasitic bias voltage introduced by the ICP power in the equipment. As discussed in Figure 2.15, if this bias were eliminated, then all involved reactions should be isotropic, it is possible to achieve isotropic ALE. Pursuing further theoretical research and addressing these questions will be essential for advancing both ALE and area-selective ALP.

Area-selective ALP

A promising direction for ALP lies in the development of area-selective ALP. One of the significant advantages of area-selective ALP is its potential to simplify the preparation steps required for pattern definition on substrates in semiconductor fabrication. Traditionally, this process necessitates a minimum of five steps: spin coating, exposure, development, deposition or etching, and stripping. The complexity arises primarily from the current pursuit of achieving large-area uniformity, whether in deposition or etching, making the protection of non-target areas necessary. The concept of area-selective ALP seeks to confine reaction processes to specific target areas, thereby preventing these processes from occurring in non-target regions. Recent reports on selective ALD [308-311] and selective ALE [312, 313] have primarily focused on modifying and delineating areas using inhibitors. However, a different approach emerges through the analysis of Figures 2.12, Figure 2.14, and Figure 2.15, suggesting that physical methods, such as electron exposure, temperature control, photons, or even electromagnetic fields, can be employed during the modification or activation steps to define the target regions. These methods adjust the surface energy of specific areas, allowing surface reactions to either enter or exit the ALP window, thereby achieving area-selective ALP. For example, the ALE process developed in this study exhibits a well-defined and steep temperature window (Figure 6.3a), which is particularly conducive to area-selective ALE. The reaction mechanisms need to be further investigated, but generally speaking, the temperature predominantly influences the adsorption process of SF_6 on the SiO_2 surface. From this perspective, a feasible approach to area-selective ALE could involve an additional modification process performed after the modification step and right before the activation step. For instance, by using laser scanning to heat areas where etching is undesired, SF6 can be desorbed from the SiO_2 surface in those regions. Consequently, during the removal step, only the SiO_2 surface that has adsorbed SF_6 will be etched, while the laser-treated, SF_6-free areas will remain unaffected.

Function tunability development of the ALD-assisted VO_2 applications

ALD is considered "the ultimate way to achieve high-density 3D synapses and memory arrays",[181] and Chapter 3 has already demonstrated the feasibility of ALD-assisted VO_2 as a later-added shell in core-shell memristor devices. The next step is to synthesize more controllable and ordered 3D templates to create truly functional 3D synaptic and memory arrays. The 3D photonic crystals presented in Chapter 4 further support the feasibility of this concept from a material preparation perspective, showcasing a large-area VO_2-based device with a complex 3D structure. Moreover, VO_2's IMT can be triggered by various external stimuli, including heat, light, stress, electric fields, and ion fields,[171, 177] offering numerous possibilities for tunability. For example, the current VO_2 IO PhC with a single-layer film structure can replaced by a multilayer structure, such as a "transparent conductive coating - VO_2 - transparent conductive film" system, entirely deposited by ALD. This would enable direct control of the 3D VO_2 PhC's band diagram via the electric field between the transparent conductive layers. Similarly, the tunability of VO_2-based memristors and thus hardware neural networks could be further explored. The VO_2 memristors synthesized in Chapter 3 exhibit temperature sensitivity, suggesting that hardware neural networks based on these memristors could also be tunable. Although this has not been studied to our knowledge, consider the following scenario: In a hardware neural network used to process large data arrays, different sensitivity levels might be needed at various points where data is introduced into the algorithm. This sensitivity could be controlled by adding temperature controllers near the VO_2-based memristor units. As shown in Figure 3.3, increasing the temperature lowers the threshold voltage, making the network more sensitive to input signal fluctuations; conversely, it becomes less responsive at lower temperatures. Just as memristors mimic neurons, the stimuli affecting ALD-assisted VO_2 properties could be artificially manipulated to simulate various neural states and environments.

Broader implications of T-PSD

In a broader context, I believe that the T-PSD serves not only as a position sensor but also as a versatile platform for studying thermoelectric thin films and heat transfer phenomena, with potential applications across various fields. For instance, accurately measuring the thermal conductivity of thin films remains a significant challenge in the field of thermoelectric materials and devices.[314-316] Environmental factors, particularly those related to the test system itself, can easily affect the measured signal. It is important to note that heat exchange occurs at the interface used to support the test material during thermal conductivity measurements.[317, 318] By employing T-PSD as a methodological platform, there is an opportunity to quickly isolate the impact of the testing environment on the substrate and obtain thermoelectric information about the material more straightforwardly and efficiently. Furthermore, while traditional PSDs have seen substantial success in everyday applications, they still encounter issues related to nonlinearity. An increasing number of researchers have observed thermal effects within the detection signal and have reported phenomena related to the photothermoelectric effect.[319-325] The T-PSD mathematical models, based purely on thermoelectric phenomena and heat conduction laws, accurately describe the experimental data, aligning well with FEA simulation results. Impressively, when carefully examining the distribution of decoding signals and positions in traditional PSDs based on photoelectric phenomena, a noticeable similarity emerges with the distribution or evolution of signals and positions in T-PSD. This observation suggests that the essence of the photothermoelectric phenomenon may actually lie in the coupling between photoelectric and thermoelectric phenomena. This raises important questions: How exactly are these two phenomena coupled? Is it a simple additive relationship, or is there a more complex interaction between photo-generated and thermally excited electrons? By integrating an additional set of traditional PSDs based on the photoelectric effect into the T-PSD framework, it may be possible to separate and study the photothermal and photoelectric effects within the photothermoelectric phenomenon, thereby addressing these questions.

Driven by the rapid development of cutting-edge hardware technologies such as advanced semiconductor chips, photonic chips, and quantum devices, ALP is becoming increasingly critical, in both enhancing hardware performance and energy efficiency perspectives across various applications. It is also foreseeable that the specific features associated with ALP, such as interface performance, will gain increased attention and spur further advancements. In conclusion, ALP is evolving into a highly exciting and dynamic field, offering a unique convergence of physics, materials science, and engineering. While many challenges and unresolved issues remain, these challenges also present significant opportunities for innovation and discovery.

References

1. Suntola, T. and J. Antson, *Method for producing compound thin films*. 1977, Google Patents.
2. Aleskovskii, V. and S. Koltsov. *Some characteristics of molecular layering reactions*. in *Abstract of Scientific and Technical Conference of the Leningrad Technological Institute by Lensovet*. 1965.
3. Yoder, M.N., *Atomic layer etching*. 1988, Google Patents.
4. Kessels, E., *ALDALE2020 – The prime conference in the field of atomic scale processing brought to your home*. 2020: AtomicLimits.
5. Kanarik, K.J., S. Tan, and R.A. Gottscho, *Atomic layer etching: rethinking the art of etch.* The Journal of Physical Chemistry Letters, 2018. **9**(16): p. 4814-4821.
6. Oehrlein, G.S., et al., *Future of plasma etching for microelectronics: Challenges and opportunities.* Journal of Vacuum Science & Technology B, 2024. **42**(4): p. 041501.
7. Yan, Z., et al., *Atomic layer deposition technology for the development of high-quality, full-colour micro-LED displays.* Next Nanotechnology, 2024. **5**: p. 100051.
8. Zhang, J., et al., *Advances in Atomic Layer Deposition.* Nanomanufacturing and Metrology, 2022. **5**(3): p. 191-208.
9. Hossain, M.A., et al., *Atomic layer deposition enabling higher efficiency solar cells: A review.* Nano Materials Science, 2020. **2**(3): p. 204-226.
10. Seo, S., et al., *Atomic layer deposition for efficient and stable perovskite solar cells.* Chemical Communications, 2019. **55**(17): p. 2403-2416.
11. Shearrow, A., et al., *Atomic layer deposition of titanium nitride for quantum circuits.* Applied Physics Letters, 2018. **113**(21): p. 212601.
12. Knehr, E., et al., *Wafer-level uniformity of atomic-layer-deposited niobium nitride thin films for quantum devices.* Journal of Vacuum Science & Technology A, 2021. **39**(5): p. 052401.
13. Lu, R., et al., *Fabrication of Nb/*Al_2O_3*/Nb Josephson junctions using in situ magnetron sputtering and atomic layer deposition.* IEEE Transactions on Applied Superconductivity, 2013. **23**(3): p. 1100705-1100705.
14. Baum, P., D.-S. Yang, and A.H. Zewail, *4D visualization of transitional structures in phase transformations by electron diffraction.* Science, 2007. **318**(5851): p. 788.
15. Jeong, J., et al., *Suppression of Metal-Insulator Transition in* VO_2 *by Electric Field-Induced Oxygen Vacancy Formation.* Science, 2013. **339**(6126): p. 1402-1405.
16. Qazilbash, M.M., et al., *Mott Transition in* VO_2 *Revealed by Infrared Spectroscopy and Nano-Imaging.* Science, 2007. **318**(5857): p. 1750-1753.
17. Wang, S., et al., *Scalable thermochromic smart windows with passive radiative cooling regulation.* Science, 2021. **374**(6574): p. 1501-1504.
18. Yoon, H., et al., *Reversible phase modulation and hydrogen storage in multivalent* VO_2 *epitaxial thin films.* Nature Materials, 2016. **15**(10): p. 1113-1119.
19. Aetukuri, N.B., et al., *Control of the metal–insulator transition in vanadium dioxide by modifying orbital occupancy.* Nature Physics, 2013. **9**(10): p. 661-666.

20. Shi, R., et al., *Recent advances in fabrication strategies, phase transition modulation, and advanced applications of vanadium dioxide.* Applied Physics Reviews, 2019. **6**(1): p. 011312.
21. Zhang, Y., et al., *Recent Progress on Vanadium Dioxide Nanostructures and Devices: Fabrication, Properties, Applications and Perspectives.* Nanomaterials, 2021. **11**(2): p. 338.
22. Puurunen, R.L., *Surface chemistry of atomic layer deposition: A case study for the trimethylaluminum/water process.* Journal of Applied Physics, 2005. **97**(12): p. 121301.
23. Miikkulainen, V., et al., *Crystallinity of inorganic films grown by atomic layer deposition: Overview and general trends.* Journal of Applied Physics, 2013. **113**(2): p. 021301.
24. Mackus, A.J.M., A.A. Bol, and W.M.M. Kessels, *The use of atomic layer deposition in advanced nanopatterning.* Nanoscale, 2014. **6**(19): p. 10941-10960.
25. Grillo, F., et al., *Understanding and controlling the aggregative growth of platinum nanoparticles in atomic layer deposition: an avenue to size selection.* The Journal of Physical Chemistry Letters, 2017. **8**(5): p. 975-983.
26. George, S.M., *Atomic Layer Deposition: An Overview.* Chemical Reviews, 2010. **110**(1): p. 111-131.
27. Puurunen, R.L., *A Short History of Atomic Layer Deposition: Tuomo Suntola's Atomic Layer Epitaxy.* Chemical Vapor Deposition, 2014. **20**(10-11-12): p. 332-344.
28. Ahvenniemi, E., et al., *Review Article: Recommended reading list of early publications on atomic layer deposition—Outcome of the "Virtual Project on the History of ALD".* Journal of Vacuum Science & Technology A: Vacuum, Surfaces, and Films, 2017. **35**(1).
29. Knez, M., K. Nielsch, and L. Niinistö, *Synthesis and Surface Engineering of Complex Nanostructures by Atomic Layer Deposition.* Advanced Materials, 2007. **19**(21): p. 3425-3438.
30. Bae, C., H. Shin, and K. Nielsch, *Surface modification and fabrication of 3D nanostructures by atomic layer deposition.* MRS Bulletin, 2011. **36**(11): p. 887-897.
31. Detavernier, C., et al., *Tailoring nanoporous materials by atomic layer deposition.* Chemical Society Reviews, 2011. **40**(11): p. 5242-5253.
32. Suntola, T. and J. Hyvarinen, *Atomic Layer Epitaxy.* Annual Review of Materials Research, 1985. **15**(Volume 15): p. 177-195.
33. Profijt, H.B., et al., *Plasma-assisted atomic layer deposition: basics, opportunities, and challenges.* Journal of Vacuum Science & Technology A, 2011. **29**(5): p. 050801.
34. Knoops, H.C.M., et al., *Status and prospects of plasma-assisted atomic layer deposition.* Journal of Vacuum Science & Technology A, 2019. **37**(3): p. 030902.
35. Poodt, P., et al., *Low temperature and roll-to-roll spatial atomic layer deposition for flexible electronics.* Journal of Vacuum Science & Technology A, 2011. **30**(1): p. 01A142.
36. *Atomic Layer Deposition for Semiconductors*, ed. C.S. Hwang. 2014, Boston, MA: Springer US. 3-12.
37. Coll, M. and M. Napari, *Atomic layer deposition of functional multicomponent oxides.* APL Materials, 2019. **7**(11): p. 110901.
38. Hiltunen, L., et al., *Nitrides of titanium, niobium, tantalum and molybdenum grown as thin films by the atomic layer epitaxy method.* Thin Solid Films, 1988. **166**: p. 149-154.

39. Hagen, D.J., M.E. Pemble, and M. Karppinen, *Atomic layer deposition of metals: Precursors and film growth.* Applied Physics Reviews, 2019. **6**(4): p. 041309.
40. Zhang, H., et al., *Atomic layer deposition of cobalt phosphide for efficient water splitting.* Angewandte Chemie International Edition, 2020. **59**(39): p. 17172-17176.
41. Mackus, A.J.M., et al., *Synthesis of doped, ternary, and quaternary materials by atomic layer deposition: a review.* Chemistry of Materials, 2019. **31**(4): p. 1142-1183.
42. Vandalon, V. *Ternary materials and multi-step ALD processes are trending!* 2020.
43. Devloo-Casier, K., et al., *In situ synchrotron based x-ray techniques as monitoring tools for atomic layer deposition.* Journal of Vacuum Science & Technology A, 2013. **32**(1): p. 010801.
44. Knapas, K. and M. Ritala, *In Situ Studies on Reaction Mechanisms in Atomic Layer Deposition.* Critical Reviews in Solid State and Materials Sciences, 2013. **38**(3): p. 167-202.
45. Dendooven, J. and C. Detavernier, *Basics of Atomic Layer Deposition: Growth Characteristics and Conformality,* in *Atomic layer deposition in energy conversion applications*. 2017. p. 1-40.
46. Cremers, V., R.L. Puurunen, and J. Dendooven, *Conformality in atomic layer deposition: Current status overview of analysis and modelling.* Applied Physics Reviews, 2019. **6**(2): p. 021302.
47. Harberts, J., et al., *Toward brain-on-a-chip: human induced pluripotent stem cell-derived guided neuronal networks in tailor-made 3D nanoprinted microscaffolds.* ACS Nano, 2020. **14**(10): p. 13091-13102.
48. Weimer, A.W., *Particle atomic layer deposition.* Journal of Nanoparticle Research, 2019. **21**(1).
49. Niu, W., et al., *Applications of atomic layer deposition in solar cells.* Nanotechnology, 2015. **26**(6): p. 064001.
50. Guan, C. and J. Wang, *Recent Development of Advanced Electrode Materials by Atomic Layer Deposition for Electrochemical Energy Storage.* Advanced Science, 2016. **3**(10): p. 1500405.
51. Eswar, N.K.R., S.A. Singh, and J. Heo, *Atomic layer deposited photocatalysts: comprehensive review on viable fabrication routes and reactor design approaches for photo-mediated redox reactions.* Journal of Materials Chemistry A, 2019. **7**(30): p. 17703-17734.
52. Shim, J.H., et al., *Atomic layer deposition for surface engineering of solid oxide fuel cell electrodes.* International Journal of Precision Engineering and Manufacturing-Green Technology, 2019. **6**(3): p. 629-646.
53. Karimaghaloo, A., et al., *Nanoscale surface and interface engineering of solid oxide fuel cells by atomic layer deposition.* International Journal of Precision Engineering and Manufacturing-Green Technology, 2019. **6**(3): p. 611-628.
54. Marichy, C. and N. Pinna, *Atomic layer deposition to materials for gas sensing applications.* Advanced Materials Interfaces, 2016. **3**(21): p. 1600335.
55. Wang, C.-M., et al., *Surface engineering of synthetic nanopores by atomic layer deposition and their applications.* Frontiers of Materials Science, 2013. **7**(4): p. 335-349.
56. Yang, H.-C., et al., *Atomic layer deposition for membrane interface engineering.* Nanoscale, 2018. **10**(44): p. 20505-20513.
57. Skoog, S.A., J.W. Elam, and R.J. Narayan, *Atomic layer deposition: Medical and biological applications.* International Materials Reviews, 2013. **58**(2): p. 113-129.

58. Mackus, A.J.M., M.J.M. Merkx, and W.M.M. Kessels, *From the bottom-up: toward area-selective atomic layer deposition with high selectivity.* Chem. Mater., 2019. **31**: p. 2.
59. Kanarik, K.J., et al., *Overview of atomic layer etching in the semiconductor industry.* Journal of Vacuum Science and Technology A: Vacuum, Surfaces and Films, 2015. **33**(2).
60. Fischer, A., et al., *Thermal atomic layer etching: A review.* Journal of Vacuum Science and Technology A: Vacuum, Surfaces and Films, 2021. **39**(3).
61. Sundberg, P. and M. Karppinen, *Organic and inorganic–organic thin film structures by molecular layer deposition: A review.* Beilstein Journal of Nanotechnology, 2014. **5**: p. 1104-1136.
62. Meng, X., *An overview of molecular layer deposition for organic and organic-inorganic hybrid materials: Mechanisms, growth characteristics, and promising applications.* Journal of Materials Chemistry A, 2017. **5**(35): p. 18326-18378.
63. Graniel, O., J. Puigmartí-Luis, and D. Muñoz-Rojas, *Liquid atomic layer deposition as emergent technology for the fabrication of thin films.* Dalton Transactions, 2021. **50**(19): p. 6373-6381.
64. Jeong, H. and L. Shi, *Memristor devices for neural networks.* Journal of Physics D: Applied Physics, 2019. **52**(2): p. 023003.
65. Scott, J.F. and C.A.P.D. Araujo, *Ferroelectric Memories.* Science, 1989. **246**: p. 1400-1405.
66. Thakare, P.V. and S. Tembhurne, *A power analysis of SRAM cell using 12T topology for faster data transmission.* International Journal of Science Technology & Engineering, 2016. **2**: p. 441-446.
67. Park, S.-K., *Technology scaling challenge and future prospects of DRAM and NAND flash memory.* IEEE Circuits and Devices Magazine, 2015. **0**: p. 1-4.
68. agan Singh Meena, et al., *Overview of emerging nonvolatile memory technologies.* Nanoscale Research Letters 2014. **9**: p. 1-13.
69. Pan, F., et al., *Recent progress in resistive random access memories: Materials, switching mechanisms, and performance.* Materials Science and Engineering: R: Reports, 2014. **83**: p. 1-59.
70. Zahoor, F., T.Z. Azni Zulkifli, and F.A. Khanday, *Resistive random access memory (RRAM): an overview of materials, switching mechanism, performance, multilevel cell (mlc) storage, modeling, and applications.* Nanoscale Res Lett, 2020. **15**(1): p. 90.
71. Wong, H.S.P., et al., *Metal–Oxide RRAM.* Proceedings of the IEEE, 2012. **100**(6): p. 1951-1970.
72. Abedin, M., et al., *Material to system-level benchmarking of CMOS-integrated RRAM with ultra-fast switching for low power on-chip learning.* Scientific Reports, 2023. **13**(1): p. 14963.
73. Peters, C., et al. *Reliability of 28nm embedded RRAM for consumer and industrial products*. in *2022 IEEE International Memory Workshop (IMW)*. 2022.
74. Coughlin, T., *MRAM Coming to Consumer Products.* IEEE Consumer Electronics Magazine, 2021. **10**(2): p. 51-52.
75. Gao, B., et al., *A Unified PUF and TRNG Design Based on 40-nm RRAM With High Entropy and Robustness for IoT Security.* IEEE Transactions on Electron Devices, 2022. **69**(2): p. 536-542.
76. Wang, J., et al., *Design of RRAM with high storage capacity and high reliability for IoT applications.* Solid-State Electronics, 2022. **194**: p. 108292.

77. Wan, W., et al., *A compute-in-memory chip based on resistive random-access memory.* Nature, 2022. **608**(7923): p. 504-512.

78. Chen, W., et al. *Resistive-RAM-based in-memory computing for neural network: a review*. Electronics, 2022. **11**, DOI: 10.3390/electronics11223667.

79. Huo, Q., et al., *A computing-in-memory macro based on three-dimensional resistive random-access memory.* Nature Electronics, 2022. **5**(7): p. 469-477.

80. Wang, C., et al., *Research progress in architecture and application of RRAM with computing-in-memory.* Nanoscale Advances, 2023. **5**(6): p. 1559-1573.

81. Arumí, D., et al. *RRAM based random bit generation for hardware security applications*. in *2016 Conference on Design of Circuits and Integrated Systems (DCIS)*. 2016.

82. Peng, B., et al., *A RRAM-based true random number generator with 2T1R architecture for hardware security applications.* Micromachines, 2023. **14**(6).

83. Dongre, A. and G. Trivedi, *Variation Tolerant RRAM Based Synaptic Architecture for On-Chip Training.* IEEE Transactions on Nanotechnology, 2023. **22**: p. 436-444.

84. Schuman, C.D., et al., *Opportunities for neuromorphic computing algorithms and applications.* Nature Computational Science, 2022. **2**(1): p. 10-19.

85. Sun, Z., et al., *One-step regression and classification with cross-point resistive memory arrays.* Science Advances, 2020. **6**(5): p. eaay2378.

86. Sun, P., et al., *Thermal crosstalk in 3-dimensional RRAM crossbar array.* Scientific Reports, 2015. **5**(1): p. 13504.

87. Sun, Z., et al., *Solving matrix equations in one step with cross-point resistive arrays.* Proceedings of the National Academy of Sciences, 2019. **116**(10): p. 4123-4128.

88. Hickmott, T.W., *Low‐Frequency Negative Resistance in Thin Anodic Oxide Films.* Journal of Applied Physics, 1962. **33**(9): p. 2669-2682.

89. GIBBONS, J.F. and W.E. BEADLEt, *switching properties of thin NiO films.* Solid State Electron, 1964. **7**: p. 785-797.

90. PINTO, R., *Filamentary switching and memory action in thin anodic oxides.* Phys. Lett.A, 1971. **35**: p. 155-156.

91. Waser, R., et al., *Redox-Based Resistive Switching Memories - Nanoionic Mechanisms, Prospects, and Challenges.* Advanced Materials, 2009. **21**(25-26): p. 2632-2663.

92. Menzel, S., Eike Linn, and R. Waser, *Redox-based Resistive Memory.* Emerging Nanoelectronic Devices, 2014: p. 137-161.

93. Nandakumar, S.R., et al., *A 250 mV Cu/SiO_2/W memristor with half-integer quantum conductance states.* Nano Lett, 2016. **16**(3): p. 1602-8.

94. Valov, I. and T. Tsuruoka, *Effects of moisture and redox reactions in VCM and ECM resistive switching memories.* Journal of Physics D: Applied Physics, 2018. **51**(41).

95. Lee, S.H., et al., *Interfacial triggering of conductive filament growth in organic flexible memristor for high reliability and uniformity.* ACS Appl Mater Interfaces, 2019. **11**(33): p. 30108-30115.

96. L. Goux, et al., *On the gradual unipolar and bipolar resistive switching of TiN/HfO_2/Pt memory systems.* Electrochemical and Solid-State Letters, 2010. **13**: p. 54-56.

97. Hubbard, W.A., et al., *Nanofilament formation and regeneration during Cu/Al_2O_3 resistive memory switching.* Nano Lett, 2015. **15**(6): p. 3983-7.

98. Egorov, K.V., et al., *In situ control of oxygen vacancies in TaO_x thin films via plasma-enhanced atomic layer deposition for resistive switching memory applications.* ACS Appl Mater Interfaces, 2017. **9**(15): p. 13286-13292.

99. Shalu Saini, Anurag Dwivedi, and S.P. Tiwari, *Enhanced resistive switching in flexible hybrid RRAM devices with PVK: MoS_2/TiO_2 Bilayer.* IEEE Transactions on electron devices, 2023. **70**: p. 53.

100. Wang, X.F., et al., *Interface engineering with MoS_2-Pd nanoparticles hybrid structure for a low voltage resistive switching memory.* Small, 2018. **14**(2).

101. Hao, C., et al., *Liquid-Exfoliated Black Phosphorous Nanosheet Thin Films for Flexible Resistive Random Access Memory Applications.* Advanced Functional Materials, 2016. **26**(12): p. 2016-2024.

102. Liu, J., et al., *Fabrication of flexible, all-reduced graphene oxide non-volatile memory devices.* Adv Mater, 2013. **25**(2): p. 233-8.

103. Liu, J., et al., *Preparation of MoS_2-polyvinylpyrrolidone nanocomposites for flexible nonvolatile rewritable memory devices with reduced graphene oxide electrodes.* Small, 2012. **8**(22): p. 3517-22.

104. Jeong, H.Y., et al., *Graphene oxide thin films for flexible nonvolatile memory applications.* Nano Lett, 2010. **10**(11): p. 4381-6.

105. B. J. Choi, et al., *Resistive switching mechanism of TiO_2 thin films grown by atomic-layer deposition.* Journal of applied physics, 2005. **98**: p. 033715.

106. D. C. Kim, et al., *Electrical observations of filamentary conductions for the resistive memory switching in NiO films.* APL, 2006. **88**: p. 202102.

107. Waser, R. and M. Aono, *Nanoionics-based resistive switching.* Nature Materials, 2007. **6**: p. 833-840.

108. Zhirnov, V.V., et al., *Memory Devices: Energy-Space-Time Tradeoffs.* Proceedings of the IEEE, 2010. **98**(12): p. 2185-2200.

109. Kim, K.M., D.S. Jeong, and C.S. Hwang, *Nanofilamentary resistive switching in binary oxide system; a review on the present status and outlook.* Nanotechnology, 2011. **22**(25): p. 254002.

110. Rozenberg, M.J., I.H. Inoue, and M.J. Sanchez, *Nonvolatile memory with multilevel switching: a basic model.* Phys Rev Lett, 2004. **92**(17): p. 178302.

111. Guan, X., S. Yu, and H.S.P. Wong, *On the switching parameter variation of metal-oxide RRAM—Part I: Physical modeling and simulation methodology.* IEEE Transactions on Electron Devices, 2012. **59**(4): p. 1172-1182.

112. Ansh and M. Shrivastava, *Superior resistance switching in monolayer MoS_2 channel-based gated binary resistive random-access memory via gate-bias dependence and a unique forming process.* Journal of Physics D: Applied Physics, 2022. **55**(8): p. 085102.

113. Das, U., et al., *Uniform, large-scale growth of WS_2 nanodomains via CVD technique for stable non-volatile RRAM application.* Materials Science in Semiconductor Processing, 2020. **107**: p. 104837.

114. Zhirnov, V.V., et al., *Scaling limits of resistive memories.* Nanotechnology, 2011. **22**(25): p. 254027.

115. Cavin, R.K., P. Lugli, and V.V. Zhirnov, *Science and Engineering Beyond Moore's Law.* Proceedings of the IEEE, 2012. **100**(Special Centennial Issue): p. 1720-1749.

116. Min-Che Hsieh, et al., *Ultra high density 3D Via RRAM in pure 28nm CMOS process.* Tech. Dig. - Int. Electron Devices Meet. IEDM, 2013. **1**: p. 260–263.

117. Peng, J. and R. Zierold, *Encyclopedia of condensed matter physics*. Atomic layer deposition of materials, ed. T. Chakraborty. Vol. 5. 2024, Oxford: Elsevier.

118. Joannopoulos, J.D., et al., *Photonic crystals: molding the flow of light*. Second Edition ed. 2008: Princeton University Press.

119. Joannopoulos, J.D., et al., *Photonic Crystals: Molding the Flow of Light - Second Edition*. 2011: Princeton University Press.

120. Born, M. and E. Wolf, *Principles of Optics: Electromagnetic Theory of Propagation, Interference and Diffraction of Light*. 7 ed. 1999, Cambridge: Cambridge University Press.

121. Armstrong, E. and C. O'Dwyer, *Artificial opal photonic crystals and inverse opal structures – fundamentals and applications from optics to energy storage.* Journal of Materials Chemistry C, 2015. **3**(24): p. 6109-6143.

122. von Freymann, G., et al., *Bottom-up assembly of photonic crystals.* Chemical Society Reviews, 2013. **42**(7): p. 2528-2554.

123. Collet, M., et al., *Floquet–Bloch decomposition for the computation of dispersion of two-dimensional periodic, damped mechanical systems.* International Journal of Solids and Structures, 2011. **48**(20): p. 2837-2848.

124. Gómez-León, A. and G. Platero, *Floquet-Bloch Theory and Topology in Periodically Driven Lattices.* Physical Review Letters, 2013. **110**(20): p. 200403.

125. Gaillot, D.P. and C.J. Summers, *Inverse Opal Photonics*, in *Atomic Layer Deposition of Nanostructured Materials*, N. Pinna and M. Knez, Editors. 2011, John Wiley and Sons. p. 345-376.

126. Ge, J. and Y. Yin, *Responsive photonic crystals.* Angewandte Chemie International Edition, 2011. **50**(7): p. 1492-1522.

127. Wallmark, J.T., *A new semiconductor photocell using lateral photoeffect.* Proceedings of the IRE, 1957. **45**(4): p. 474-483.

128. Streetman, B.G. and S. Banerjee, *Solid State Electronic Devices*. 2000: Prentice Hall.

129. *p-n Junctions*, in *Physics of Semiconductor Devices*. 2006. p. 77-133.

130. Andersson, H., *Position sensitive detectors: device technology and applications in spectroscopy*, in *Department of Information Technology and Media*. 2008, Mid Sweden University.

131. Shen, C.B., et al. *Research of signal-processing methods in four-quadrant photodetector*. in *2008 International Conference on Electrical Machines and Systems*. 2008.

132. Esper-Chaín, R., et al., *Configurable quadrant photodetector: an improved position sensitive device.* IEEE Sensors Journal, 2016. **16**(1): p. 109-119.

133. Zhang, W., et al., *Design of Small Laser Tracking System Based on Four-Quadrant Detector.* Applied Mechanics and Materials, 2013. **300-301**: p. 393-399.

134. Bergman, T.L., *Fundamentals of heat and mass transfer*. 2011: John Wiley & Sons.

135. Holman, J.P., *Heat Transfer*. 10th ed. 2010: McGraw-Hill Education.

136. Zaidi, S.J.A., et al., *Interfaces in atomic layer deposited films: opportunities and challenges.* Small Science, 2023. **3**(10): p. 2300060.

137. Yu, Y., et al., *Thin-film deposition techniques in surface and interface engineering of solid-state lithium batteries.* Next Nanotechnology, 2023. **3-4**: p. 100028.

138. Losego, M.D., et al., *Effects of chemical bonding on heat transport across interfaces.* Nature Materials, 2012. **11**(6): p. 502-506.

139. Lee, S.M. and D.G. Cahill, *Heat transport in thin dielectric films.* Journal of Applied Physics, 1997. **81**(6): p. 2590-2595.

140. Gundrum, B.C., D.G. Cahill, and R.S. Averback, *Thermal conductance of metal-metal interfaces.* Physical Review B, 2005. **72**(24): p. 245426.

141. *AtomicLimits*, in *AtomicLimits*. www.AtomicLimits.com.

142. Faraz, T., et al., *Atomic Layer Etching: What Can We Learn from Atomic Layer Deposition?* ECS Journal of Solid State Science and Technology, 2015. **4**(6): p. N5023.

143. Coburn, J.W. and H.F. Winters, *Ion‐ and electron‐assisted gas‐surface chemistry—An important effect in plasma etching.* Journal of Applied Physics, 1979. **50**(5): p. 3189-3196.

144. Aleksandrov, N.L. and D.A. Novitskii, *Synergistic effect in the rate of three-body ion - ion recombination in gas mixtures.* Journal of Physics B: Atomic, Molecular and Optical Physics, 1997. **30**(1): p. 125.

145. Barone, M.E. and D.B. Graves, *Chemical and physical sputtering of fluorinated silicon.* Journal of Applied Physics, 1995. **77**(3): p. 1263-1274.

146. Kanarik, K.J., et al., *Overview of atomic layer etching in the semiconductor industry.* Journal of Vacuum Science & Technology A, 2015. **33**(2): p. 020802.

147. Kanarik, K.J., et al., *Predicting synergy in atomic layer etching.* Journal of Vacuum Science & Technology A, 2017. **35**(5).

148. Lill, T., *Atomic Layer Processing: Semiconductor Dry Etching Technology*. 2021.

149. Lill, T.B., et al., *Abundance and Depth of Origin of Neutral and Ionic Clusters Sputtered from a Liquid Gallium-Indium Eutectic Alloy.* Physical Review Letters, 1994. **73**(12): p. 1719-1722.

150. *DFT Calculations for Surfaces of Solids*, in *Density Functional Theory*. 2009. p. 83-112.

151. Lill, T., et al., *Directional Atomic Layer Etching*, in *Encyclopedia of Plasma Technology*, J.L. Shohet, Editor. 2016, Taylor & Francis Group.

152. Metzler, D., et al., *Fluorocarbon assisted atomic layer etching of SiO_2 using cyclic Ar/C_4F_8 plasma.* Journal of Vacuum Science & Technology A, 2013. **32**(2): p. 020603.

153. T. Carver, C., et al., *Atomic Layer Etching: An Industry Perspective.* ECS Journal of Solid State Science and Technology, 2015. **4**(6): p. N5005.

154. Park, S.D., D.H. Lee, and G.Y. Yeom, *Atomic Layer Etching of Si(100) and Si(111) Using Cl_2 and Ar Neutral Beam.* Electrochemical and Solid-State Letters, 2005. **8**(8): p. C106.

155. Tamirisa, P.A., et al., *Plasma etching of copper films at low temperature.* Microelectronic Engineering, 2007. **84**(1): p. 105-108.

156. George, S.M., *Mechanisms of thermal atomic layer etching.* Accounts of Chemical Research, 2020. **53**(6): p. 1151-1160.

157. Mameli, A., et al., *Isotropic Atomic Layer Etching of ZnO Using Acetylacetone and O_2 Plasma.* ACS Applied Materials & Interfaces, 2018. **10**(44): p. 38588-38595.

158. Wang, H., et al., *Isotropic plasma-thermal atomic layer etching of aluminum nitride using SF_6 plasma and $Al(CH_3)_3$.* Journal of Vacuum Science & Technology A, 2023. **41**(3): p. 032606.

159. Zahoor, F., T.Z. Azni Zulkifli, and F.A. Khanday, *Resistive random access memory (RRAM): an overview of materials, switching mechanism, performance, multilevel cell (mlc) storage, modeling, and applications.* Nanoscale Research Letters, 2020. **15**(1): p. 90.

160. Li, H., et al., *Memristive crossbar arrays for storage and computing applications.* Advanced Intelligent Systems, 2021. **3**(9): p. 2100017.

161. Ke, Y., et al., *Vanadium dioxide: the multistimuli responsive material and its applications.* Small, 2018. **14**(39): p. 1802025.

162. Crunteanu, A., et al., *Voltage- and current-activated metal–insulator transition in VO_2-based electrical switches: a lifetime operation analysis.* Science and Technology of Advanced Materials, 2010. **11**(6): p. 065002.

163. Li, G., et al., *Photo-induced non-volatile VO_2 phase transition for neuromorphic ultraviolet sensors.* Nature Communications, 2022. **13**(1): p. 1729.

164. Khan, Z., et al., *VO2 Nanostructures for Batteries and Supercapacitors: A Review.* Small, 2021. **17**(4): p. 2006651.

165. Peng, J., et al., *Switchable 3D Photonic Crystals Based on the Insulator-to-Metal Transition in VO_2.* ACS Applied Materials & Interfaces, 2024.

166. Hu, P., et al., *Vanadium oxide: phase diagrams, structures, synthesis, and applications.* Chemical Reviews, 2023. **123**(8): p. 4353-4415.

167. Schofield, P., et al., *Harnessing the metal–insulator transition of VO_2 in neuromorphic computing.* Advanced Materials, 2023. **35**(37): p. 2205294.

168. Goi, E., et al., *Perspective on photonic memristive neuromorphic computing.* PhotoniX, 2020. **1**(1): p. 3.

169. Feng, C., et al., *Quantum imaging of the reconfigurable VO_2 synaptic electronics for neuromorphic computing.* Science Advances, 2023. **9**(40): p. eadg9376.

170. Ying, J., F. Min, and G. Wang, *Neuromorphic behaviors of VO_2 memristor-based neurons.* Chaos, Solitons & Fractals, 2023. **175**: p. 114058.

171. Yang, Z., C. Ko, and S. Ramanathan, *Oxide electronics utilizing ultrafast metal-insulator transitions.* Annual Review of Materials Research, 2011. **41**(1): p. 337-367.

172. Yuan, R., et al., *A neuromorphic physiological signal processing system based on VO_2 memristor for next-generation human-machine interface.* Nature Communications, 2023. **14**(1): p. 3695.

173. Duan, Q., et al., *Artificial multisensory neurons with fused haptic and temperature perception for multimodal in-sensor computing.* Advanced Intelligent Systems, 2022. **4**(8): p. 2200039.

174. Han, C.Y., et al., *Characterization and Modelling of Flexible VO_2 Mott Memristor for the Artificial Spiking Warm Receptor.* Advanced Materials Interfaces, 2022. **9**(19): p. 2200394.

175. Xu, Y., et al., *Adaptive Hodgkin–Huxley neuron for retina-inspired perception.* Advanced Intelligent Systems, 2022. **4**(12): p. 2200210.

176. Yi, W., et al., *Biological plausibility and stochasticity in scalable VO_2 active memristor neurons.* Nature Communications, 2018. **9**(1): p. 4661.

177. Chen, S., et al., *Gate-controlled VO_2 phase transition for high-performance smart windows* Science Advances, 2019. **5**(3): p. eaav6815.

178. Cao, C., et al., *Sputtering flexible VO_2 films for effective thermal modulation.* ACS Applied Materials & Interfaces, 2022. **14**(24): p. 28105-28113.

179. Yuan, R., et al., *A calibratable sensory neuron based on epitaxial VO_2 for spike-based neuromorphic multisensory system.* Nature Communications, 2022. **13**(1): p. 3973.

180. Hao, C., et al., *Atomic layer deposition films for resistive random-access memories.* Advanced Materials Technologies, 2024. **n/a**(n/a): p. 2301762.

181. Hudec, B., C.C. Chang, and T.H. Hou. *Memristive devices by ALD: design aspects for high density 3D arrays for memory and neuromorphic applications*. in *2018 14th IEEE International Conference on Solid-State and Integrated Circuit Technology (ICSICT)*. 2018.

182. Shvets, P., et al., *A review of Raman spectroscopy of vanadium oxides.* Journal of Raman Spectroscopy, 2019. **50**(8): p. 1226-1244.

183. Dubberley, S.R., B.R. Tyrrell, and P. Mountford, *Tetrakis(dimethylamido)vanadium(IV).* Acta Crystallographica Section C, 2001. **57**(8): p. 902-904.

184. Wang, X., et al., *Atomic layer deposition of vanadium oxide thin films from tetrakis(dimethylamino)vanadium precursor.* Journal of Materials Research, 2017. **32**(1): p. 37-44.

185. Rampelberg, G., et al., *Semiconductor-metal transition in thin VO_2 films grown by ozone based atomic layer deposition.* Applied Physics Letters, 2011. **98**(16): p. 162902.

186. Blanquart, T., et al., *Atomic layer deposition and characterization of vanadium oxide thin films.* RSC Advances, 2013. **3**(4): p. 1179-1185.

187. Lv, X., et al., *Atomic layer deposition of VO2 films with Tetrakis-dimethyl-amino vanadium (IV) as vanadium precursor.* Applied Surface Science, 2017. **396**: p. 214-220.

188. Wei, J., et al., *Hydrogen stabilization of metallic vanadium dioxide in single-crystal nanobeams.* Nature Nanotechnology, 2012. **7**(6): p. 357-362.

189. Park, H.H., et al., *Tunable electrical properties of vanadium oxide by hydrogen-plasma-treated atomic layer deposition.* ACS Omega, 2017. **2**(4): p. 1259-1264.

190. Chouteau, S., et al., *Investigation of the metal-to-insulator transition of N-doped VO_2 (M1) thin films.* Applied Surface Science, 2021. **554**: p. 149661.

191. Baltakesmez, A., C. Aykaç, and B. Güzeldir, *Phase transition and changing properties of nanostructured V_2O_5 thin films deposited by spray pyrolysis technique, as a function of tungsten dopant.* Applied Physics A, 2019. **125**(6): p. 441.

192. Rampelberg, G., et al., *Crystallization and semiconductor-metal switching behavior of thin VO_2 layers grown by atomic layer deposition.* Thin Solid Films, 2014. **550**: p. 59-64.

193. Guan, S., et al., *Toward Room-Temperature Thermochromism of VO_2 by Nb Doping: Magnetic Investigations.* Chemistry of Materials, 2019. **31**(23): p. 9819-9830.

194. Lee, D., et al., *Isostructural metal-insulator transition in VO_2.* Science, 2018. **362**(6418): p. 1037-1040.

195. Sakai, J., et al., *Impact of thermal expansion of substrates on phase transition temperature of VO_2 films.* Journal of Applied Physics, 2014. **116**(12): p. 123510.

196. Muraoka, Y. and Z. Hiroi, *Metal–insulator transition of VO_2 thin films grown on TiO_2 (001) and (110) substrates.* Applied Physics Letters, 2002. **80**(4): p. 583-585.

197. Chen, H.-W., et al., *Strain engineering of optical properties in transparent VO_2/muscovite heterostructures.* Physical Chemistry Chemical Physics, 2021. **23**(14): p. 8908-8915.

198. Cao, J., et al., *Strain engineering and one-dimensional organization of metal–insulator domains in single-crystal vanadium dioxide beams.* Nature Nanotechnology, 2009. **4**(11): p. 732-737.

199. Crunteanu, A., et al., *Electric field-assisted metal insulator transition in vanadium dioxide (VO_2) thin films: optical switching behavior and anomalous far-infrared emissivity variation*. SPIE OPTO. Vol. 9364. 2015: SPIE.

200. He, H.-K., H.-M. Huang, and R. Yang, *Two-Terminal Neuromorphic Memristors*, in *Neuromorphic Devices for Brain‐Inspired Computing*. 2022. p. 1-46.

201. Bohaichuk, S.M., et al., *Fast Spiking of a Mott VO2–Carbon Nanotube Composite Device.* Nano Letters, 2019. **19**(10): p. 6751-6755.

202. del Valle, J., et al., *Subthreshold firing in Mott nanodevices.* Nature, 2019. **569**(7756): p. 388-392.

203. Harberts, J., et al., *Generation of human iPSC-derived neurons on nanowire arrays featuring varying lengths, pitches, and diameters.* Advanced Materials Interfaces, 2022. **9**(24): p. 2200806.

204. Joannopoulos, J.D., P.R. Villeneuve, and S.H. Fan, *Photonic crystals: Putting a new twist on light.* Nature, 1997. **386**(6621): p. 143-149.

205. Lee, G.-H., et al., *Multifunctional materials for implantable and wearable photonic healthcare devices.* Nature Reviews Materials, 2020. **5**(2): p. 149-165.

206. Li, G., S. Zhang, and T. Zentgraf, *Nonlinear photonic metasurfaces.* Nature Reviews Materials, 2017. **2**(5): p. 17010.

207. Bogaerts, W., et al., *Programmable photonic circuits.* Nature, 2020. **586**(7828): p. 207-216.

208. Ko, J.H., et al., *A review of tunable photonics: Optically active materials and applications from visible to terahertz.* iScience, 2022. **25**(8): p. 104727.

209. Zheng, C., et al., *Enabling active nanotechnologies by phase transition: from electronics, photonics to thermotics.* Chemical Reviews, 2022. **122**(19): p. 15450-15500.

210. Wuttig, M., H. Bhaskaran, and T. Taubner, *Phase-change materials for non-volatile photonic applications.* Nature Photonics, 2017. **11**(8): p. 465-476.

211. Neubrech, F., X. Duan, and N. Liu, *Dynamic plasmonic color generation enabled by functional materials.* Science Advances, 2020. **6**(36): p. eabc2709.

212. Morin, F.J., *Oxides which show a metal-to-insulator transition at the Neel temperature.* Physical Review Letters, 1959. **3**(1): p. 34-36.

213. Adler, D., et al., *Semiconductor-to-metal transitions in transition-metal compounds.* Physical Review, 1967. **155**(3): p. 851-860.

214. Zylbersztejn, A. and N.F. Mott, *Metal-insulator transition in vanadium dioxide.* Physical Review B, 1975. **11**(11): p. 4383-4395.

215. Sood, A., et al., *Universal phase dynamics in VO_2 switches revealed by ultrafast operando diffraction.* Science, 2021. **373**(6552): p. 352.

216. Cueff, S., et al., *VO_2 nanophotonics.* APL Photonics, 2020. **5**(11).

217. Wen, C., et al., *A review of the preparation, properties and applications of VO_2 thin films with the reversible phase transition.* 2024. **11**.

218. Armstrong, E., et al., *3D Vanadium Oxide Inverse Opal Growth by Electrodeposition.* Journal of The Electrochemical Society, 2015. **162**(14): p. D605.

219. Ke, Y., et al., *Two-dimensional SiO_2/VO_2 photonic crystals with statically visible and dynamically infrared modulated for smart window deployment.* ACS Applied Materials & Interfaces, 2016. **8**(48): p. 33112-33120.

220. Muskens, O.L., et al., *Antenna-assisted picosecond control of nanoscale phase transition in vanadium dioxide.* Light: Science & Applications, 2016. **5**(10): p. e16173-e16173.

221. King, J., et al., *Electrically tunable VO_2–metal metasurface for mid-infrared switching, limiting and nonlinear isolation.* Nature Photonics, 2024. **18**(1): p. 74-80.

222. Golubev, V.G., et al., *Hysteresis of the photonic band gap in VO_2 photonic crystal in the semiconductor-metal phase transition.* Semiconductors, 2002. **36**(9): p. 1043-1047.

223. Ibisate, M., D. Golmayo, and C. López, *Vanadium dioxide thermochromic opals grown by chemical vapour deposition.* Journal of Optics A: Pure and Applied Optics, 2008. **10**(12): p. 125202.

224. Pemble, M., I. Povey, and F. Chalvet, *Developments in the understanding of ALD processes and applications of ALD in critical technologies.* ECS Transactions, 2007. **11**(7): p. 155.

225. Peter, A.P., et al., *Metal-insulator transition in ALD VO_2 ultrathin films and nanoparticles: morphological control.* Advanced Functional Materials, 2015. **25**(5): p. 679-686.

226. Mattelaer, F., et al., *Atomic layer deposition of vanadium oxides for thin-film lithium-ion battery applications.* RSC Advances, 2016. **6**(115): p. 114658-114665.

227. Bai, G., K.M. Niang, and J. Robertson, *Preparation of atomic layer deposited vanadium dioxide thin films using tetrakis(ethylmethylamino) vanadium as precursor.* Journal of Vacuum Science & Technology A, 2020. **38**(5): p. 052402.

228. Prasadam, V.P., et al., *Atomic layer deposition of vanadium oxides: process and application review.* Materials Today Chemistry, 2019. **12**: p. 396-423.

229. Lee, W.-J. and Y.-H. Chang, *Growth without postannealing of monoclinic VO_2 thin film by atomic layer deposition using VCl_4 as precursor.* Coatings, 2018. **8**(12).

230. Gao, Y., et al., *Efficient charge injection in organic field-effect transistors enabled by low-temperature atomic layer deposition of ultrathin VO_x interlayer.* Advanced Functional Materials, 2016. **26**(25): p. 4456-4463.

231. Hausmann, D.M., et al., *Atomic layer deposition of hafnium and zirconium oxides using metal amide precursors.* Chemistry of Materials, 2002. **14**(10): p. 4350-4358.

232. Li, J., et al., *Atomic layer deposition mechanism of hafnium dioxide using hafnium precursor with amino ligands and water.* Surfaces and Interfaces, 2024. **44**: p. 103766.

233. Blankenship, B.W., et al., *Photothermally activated artificial neuromorphic synapses.* Nano Letters, 2023. **23**(19): p. 9020-9025.

234. Evlyukhin, E., et al., *Directly measuring the structural transition pathways of strain-engineered VO_2 thin films.* Nanoscale, 2020. **12**(36): p. 18857-18863.

235. Moatti, A., et al., *Electrical transition in isostructural VO_2 thin-film heterostructures.* Scientific Reports, 2019. **9**(1): p. 3009.

236. Petrov, G.I., V.V. Yakovlev, and J. Squier, *Raman microscopy analysis of phase transformation mechanisms in vanadium dioxide.* Applied Physics Letters, 2002. **81**(6): p. 1023-1025.

237. Angel, R.J., et al., *Stress, strain and Raman shifts.* 2019. **234**(2): p. 129-140.

238. Parker, J.C., *Raman scattering from VO_2 single crystals: A study of the effects of surface oxidation.* Physical Review B, 1990. **42**(5): p. 3164-3166.

239. Kubrin, R., et al., *Bottom-up fabrication of multilayer stacks of 3D photonic crystals from titanium dioxide.* ACS Applied Materials & Interfaces, 2016. **8**(16): p. 10466-10476.

240. Cueff, S., et al., *VO_2 nanophotonics.* APL Photonics, 2020. **5**(11): p. 110901.

241. Guo, Y., et al., *Study of the phase transition properties and electronic band structures of VO_2 thin films grown on different substrates.* Materials Research Express, 2019. **6**(2): p. 026409.

242. Oguntoye, I.O., et al., *Continuously tunable optical modulation using vanadium dioxide Huygens metasurfaces.* ACS Applied Materials & Interfaces, 2023. **15**(34): p. 41141-41150.

243. Wan, C., et al., *On the optical properties of thin-film vanadium dioxide from the visible to the far infrared.* Annalen der Physik, 2019. **531**(10): p. 1900188.

244. Mackay, T.G. and A. Lakhtakia, *The transfer-matrix method in electromagnetics and optics*. 1 ed, ed. T.G. Mackay and A. Lakhtakia. 2020, Cham: Springer Cham. XIII, 112.

245. Maier, S.A., *Plasmonics: Fundamentals and applications*. 1 ed. 2007, New York, NY: Springer US.

246. Gehensel, R.J., et al., *Improved thermal stability of zirconia macroporous structures via homogeneous aluminum oxide doping and nanostructuring using atomic layer deposition.* Journal of the European Ceramic Society, 2021. **41**(7): p. 4302-4312.

247. Pasquarelli, R.M., et al., *Enhanced structural and phase stability of titania inverse opals.* Journal of the European Ceramic Society, 2015. **35**(11): p. 3103-3109.

248. Furlan, K.P., et al., *Photonic materials for high-temperature applications: Synthesis and characterization by X-ray ptychographic tomography.* Applied Materials Today, 2018. **13**: p. 359-369.

249. Furlan, K.P., et al., *Low-temperature mullite formation in ternary oxide coatings deposited by ALD for high-temperature applications.* Advanced Materials Interfaces, 2017. **4**(23): p. 1700912.

250. Fujiwara, H., *Spectroscopic Ellipsometry: Principles and Applications*. 2007: Wiley.

251. Liu, K., et al., *Graphene-based infrared position-sensitive detector for precise measurements and high-speed trajectory tracking.* Nano Letters, 2019. **19**(11): p. 8132-8137.

252. Liu, K., et al., *A time-division position-sensitive detector image system for high-speed multitarget trajectory tracking.* Advanced Materials, 2022. **34**(47): p. 2206638.

253. Vora, H.D. and S. Sanyal, *A comprehensive review: metrology in additive manufacturing and 3D printing technology*. Progress in Additive Manufacturing, 2020. **5**(4): p. 319-353.

254. Liu, S.-F., et al., *3D nanoprinting of semiconductor quantum dots by photoexcitation-induced chemical bonding.* Science, 2022. **377**(6610): p. 1112-1116.

255. Kim, T., et al., *Dynamic tactility by position-encoded spike spectrum.* Science Robotics, 2022. **7**(63): p. eabl5761.

256. Fang, G., et al., *Soft robotic manipulator for intraoperative MRI-guided transoral laser microsurgery.* Science Robotics, 2021. **6**(57): p. eabg5575.

257. Mou, J. and C. Richard Liu, *A method for enhancing the accuracy of CNC machine tools for on-machine inspection.* Journal of Manufacturing Systems, 1992. **11**(4): p. 229-237.

258. Gu, D., et al., *Material-structure-performance integrated laser-metal additive manufacturing.* Science, 2021. **372**(6545): p. eabg1487.
259. Strauß, M., et al., *Highly sensitive single-molecule detection of macromolecule ion beams.* Science Advances, 2023. **9**(48): p. eadj2801.
260. Aad, G., et al., *A detailed map of Higgs boson interactions by the ATLAS experiment ten years after the discovery.* Nature, 2022. **607**(7917): p. 52-59.
261. Tumasyan, A., et al., *A portrait of the Higgs boson by the CMS experiment ten years after the discovery.* Nature, 2022. **607**(7917): p. 60-68.
262. Henry, J. and J. Livingstone, *Thin-film amorphous silicon position-sensitive detectors.* Advanced Materials, 2001. **13**(12-13): p. 1022-1026.
263. Hu, C., X. Wang, and B. Song, *High-performance position-sensitive detector based on the lateral photoelectrical effect of two-dimensional materials.* Light: Science & Applications, 2020. **9**(1): p. 88.
264. Wang, W., J. Lu, and Z. Ni, *Position-sensitive detectors based on two-dimensional materials.* Nano Research, 2021. **14**(6): p. 1889-1900.
265. Robinson, A.L., *Position-sensitive detectors: an "electronic film" for X-rays.* Science, 1978. **199**(4324): p. 39-42.
266. Krieg, M., et al., *Atomic force microscopy-based mechanobiology.* Nature Reviews Physics, 2019. **1**(1): p. 41-57.
267. Zeng, J., et al., *Direct detection of photoinduced magnetic force at the nanoscale reveals magnetic nearfield of structured light.* Science Advances, 2022. **8**(45): p. eadd0233.
268. Hong, S.Y., et al., *Stretchable active matrix temperature sensor array of polyaniline nanofibers for electronic skin.* Advanced Materials, 2016. **28**(5): p. 930-935.
269. Ding, T., et al., *Scalable thermoelectric fibers for multifunctional textile-electronics.* Nature Communications, 2020. **11**(1): p. 6006.
270. Ren, X., et al., *A low-operating-power and flexible active-matrix organic-transistor temperature-sensor Array.* Advanced Materials, 2016. **28**(24): p. 4832-4838.
271. Mbarek, S.B., N. Alcheikh, and M.I. Younis, *Recent advances on MEMS based infrared thermopile detectors.* Microsystem Technologies, 2022. **28**(8): p. 1751-1764.
272. Siringo, G., et al., *The Large APEX BOlometer CAmera LABOCA.* A&A, 2009. **497**(3): p. 945-962.
273. Skipidarov, S. and M. Nikitin, *Novel thermoelectric materials and device design concepts*. 2019: Springer Cham.
274. Onsager, L., *Reciprocal relations in irreversible processes. I.* Physical Review, 1931. **37**(4): p. 405-426.
275. Jood, P., et al., *Al-doped zinc oxide nanocomposites with enhanced thermoelectric properties.* Nano Letters, 2011. **11**(10): p. 4337-4342.
276. Loureiro, J., et al., *Transparent aluminium zinc oxide thin films with enhanced thermoelectric properties.* Journal of Materials Chemistry A, 2014. **2**(18): p. 6649-6655.
277. Goodarzi, K., S.R. Ramezani, and S. Hajati, *Reducing thermal contact resistance using nanocoating.* Applied Thermal Engineering, 2014. **70**(1): p. 641-646.
278. Fischer, A., et al., *Thermal atomic layer etching: A review.* Journal of Vacuum Science & Technology A, 2021. **39**(3): p. 030801.

279. Peng, J. and R. Zierold, *Atomic layer deposition of materials*, in *Encyclopedia of Condensed Matter Physics (Second Edition)*, T. Chakraborty, Editor. 2024, Academic Press: Oxford. p. 716-728.
280. de Leon, N.P., et al., *Materials challenges and opportunities for quantum computing hardware.* Science, 2021. **372**(6539): p. eabb2823.
281. Lu, W., et al., *In Situ Thermal Atomic Layer Etching for Sub-5 nm InGaAs Multigate MOSFETs.* Nano Letters, 2019. **19**(8): p. 5159-5166.
282. Place, A.P.M., et al., *New material platform for superconducting transmon qubits with coherence times exceeding 0.3 milliseconds.* Nature Communications, 2021. **12**(1): p. 1779.
283. Chen, Z., et al., *Quantum interference enhances the performance of single-molecule transistors.* Nature Nanotechnology, 2024. **19**(7): p. 986-992.
284. Chen, C.Y., et al., *Tailoring amorphous boron nitride for high-performance two-dimensional electronics.* Nature Communications, 2024. **15**(1): p. 4016.
285. Chen, X., et al., *Atomic layer lithography of wafer-scale nanogap arrays for extreme confinement of electromagnetic waves.* Nature Communications, 2013. **4**(1): p. 2361.
286. Lee, Y. and S.M. George, *Atomic Layer Etching of Al_2O_3 Using Sequential, Self-Limiting Thermal Reactions with $Sn(acac)_2$ and Hydrogen Fluoride.* ACS Nano, 2015. **9**(2): p. 2061-2070.
287. DuMont, J.W., et al., *Thermal Atomic Layer Etching of SiO_2 by a "Conversion-Etch" Mechanism Using Sequential Reactions of Trimethylaluminum and Hydrogen Fluoride.* ACS Applied Materials & Interfaces, 2017. **9**(11): p. 10296-10307.
288. Catherall, D., A. Hossain, and A. Minnich, *Atomic layer etching of SiO_2 using sequential exposures of $Al(CH_3)_3$ and H_2/SF_6 plasma.* arXiv:2405.05491, 2024.
289. Dallorto, S., et al., *Atomic layer etching of SiO_2 with Ar and CHF_3 plasmas: A self-limiting process for aspect ratio independent etching.* Plasma Processes and Polymers, 2019. **16**(9): p. 1900051.
290. Metzler, D., et al., *Characterizing fluorocarbon assisted atomic layer etching of Si using cyclic Ar/C_4F_8 and Ar/CHF_3 plasma.* The Journal of Chemical Physics, 2016. **146**(5): p. 052801.
291. Miyoshi, N., et al., *Atomic layer etching of Si_3N_4 with high selectivity to SiO_2 and poly-Si.* Journal of Vacuum Science & Technology A, 2021. **39**(5): p. 052601.
292. Knizikevičius, R., *Simulations of Si and SiO_2 etching in SF_6+O_2 plasma.* Vacuum, 2009. **83**(6): p. 953-957.
293. Mankelevich, Y.A., et al., *Fluorine atoms interaction with the nanoporous materials: experiment and DFT simulation.* The European Physical Journal D, 2017. **71**(5): p. 126.
294. Kaler, S.S., et al., *Atomic layer etching of silicon dioxide using alternating C4F8 and energetic Ar+ plasma beams.* Journal of Physics D: Applied Physics, 2017. **50**(23): p. 234001.
295. Gasvoda, R.J., et al., *Surface Phenomena During Plasma-Assisted Atomic Layer Etching of SiO_2.* ACS Applied Materials & Interfaces, 2017. **9**(36): p. 31067-31075.
296. Koh, K., et al., *Quasi atomic layer etching of SiO_2 using plasma fluorination for surface cleaning.* Journal of Vacuum Science & Technology A, 2017. **36**(1): p. 01B106.
297. Dallorto, S., et al., *Balancing ion parameters and fluorocarbon chemical reactants for SiO_2 pattern transfer control using fluorocarbon-based atomic layer etching.* Journal of Vacuum Science & Technology B, 2019. **37**(5).

298. Kim, S.Y., I.-S. Park, and J. Ahn, *Atomic layer etching of SiO_2 using trifluoroiodomethane.* Applied Surface Science, 2022. **589**: p. 153045.
299. Lee, Y.S., et al., *Purgeless atomic layer etching of SiO_2.* Journal of Physics D: Applied Physics, 2022. **55**(36): p. 365203.
300. Kim, Y., et al., *Plasma Atomic Layer Etching of SiO_2 and Si_3N_4 with Low Global Warming $C_4H_3F_7O$ Isomers.* ACS Sustainable Chemistry & Engineering, 2023. **11**(16): p. 6136-6142.
301. Osonio, A., et al., *Topographically-selective atomic layer etching of SiO_2 using radical fluorination of the surface followed by Ar ion bombardment.* Japanese Journal of Applied Physics, 2023. **62**(12): p. 121001.
302. Kim, J., et al., *Low global warming $C_5F_{10}O$ isomers for plasma atomic layer etching and reactive ion etching of SiO_2 and Si_3N_4.* Plasma Processes and Polymers, 2024. **21**(5): p. 2300216.
303. Miyoshi, N., et al., *Atomic layer etching of SiO_2 with self-limiting behavior on the surface modification step using sequential exposure of HF and NH_3.* Journal of Vacuum Science & Technology A, 2021. **40**(1): p. 012601.
304. Faraz, T., et al., *Precise ion energy control with tailored waveform biasing for atomic scale processing.* Journal of Applied Physics, 2020. **128**(21): p. 213301.
305. Teichmann, M., et al., *Ripple coarsening on ion beam-eroded surfaces.* Nanoscale Research Letters, 2014. **9**(1): p. 439.
306. Winter, H., *Collisions of atoms and ions with surfaces under grazing incidence.* Physics Reports, 2002. **367**(5): p. 387-582.
307. Gasvoda, R.J., et al., *Surface prefunctionalization of SiO_2 to modify the etch per cycle during plasma-assisted atomic layer etching.* Journal of Vacuum Science & Technology A, 2019. **37**(5): p. 051003.
308. Dong, W., et al., *Application of three-dimensionally area-selective atomic layer deposition for selectively coating the vertical surfaces of standing nanopillars.* Scientific Reports, 2014. **4**(1): p. 4458.
309. Grillo, F., et al., *Area-Selective Deposition of Ruthenium by Area-Dependent Surface Diffusion.* Chemistry of Materials, 2020. **32**(22): p. 9560-9572.
310. Mackus, A.J.M., M.J.M. Merkx, and W.M.M. Kessels, *From the bottom-up: toward area-selective atomic layer deposition with high selectivity.* Chemistry of Materials, 2019. **31**: p. 2.
311. Cao, K., J. Cai, and R. Chen, *Inherently selective atomic layer deposition and applications.* Chemistry of Materials, 2020. **32**(6): p. 2195-2207.
312. Osonio, A.P., et al., *Area-selective plasma-enhanced atomic layer etching (PE-ALE) of silicon dioxide using a silane coupling agent.* Journal of Vacuum Science & Technology A, 2022. **40**(6): p. 062601.
313. Vos, M.F.J., et al., *Area-selective deposition of ruthenium by combining atomic layer deposition and selective etching.* Chemistry of Materials, 2019. **31**(11): p. 3878-3882.
314. Mason, S.J., et al., *Determining absolute Seebeck coefficients from relative thermopower measurements of thin films and nanostructures.* Journal of Applied Physics, 2020. **127**(8): p. 085101.
315. Isotta, E., et al., *Towards Low Cost and Sustainable Thin Film Thermoelectric Devices Based on Quaternary Chalcogenides.* Advanced Functional Materials, 2022. **32**(32): p. 2202157.
316. Ling, Y., et al., *Thermal conductivity measurement of thermoelectric films using transient Photo-Electro-Thermal technique.* Measurement, 2023. **217**: p. 113058.

317. Kim, P., et al., *Thermal Transport Measurements of Individual Multiwalled Nanotubes.* Physical Review Letters, 2001. **87**(21): p. 215502.
318. Linseis, V., et al., *Advanced platform for the in-plane ZT measurement of thin films.* Review of Scientific Instruments, 2018. **89**(1): p. 015110.
319. Lu, X., et al., *Progress of photodetectors based on the photothermoelectric effect.* Advanced Materials, 2019. **31**(50): p. 1902044.
320. Bianchi, C., A. Marques, and I. Ferreira, *Photothermoelectric AZO/SiO_2/NiO Device.* Advanced Materials Technologies, 2023. **8**(15): p. 2300133.
321. Chen, L.-D., et al., *Optimization of photo-thermoelectric performance in SnSe crystals via doping engineering.* Applied Physics Letters, 2023. **123**(4).
322. Lv, B., et al., *Local large temperature difference and ultra-wideband photothermoelectric response of the silver nanostructure film/carbon nanotube film heterostructure.* Nature Communications, 2022. **13**(1): p. 1835.
323. Dai, W., et al., *Giant photothermoelectric effect in silicon nanoribbon photodetectors.* Light: Science & Applications, 2020. **9**(1): p. 120.
324. Zhao, H., et al., *Conjuncted photo-thermoelectric effect in ZnO–graphene nanocomposite foam for self-powered simultaneous temperature and light sensing.* Scientific Reports, 2020. **10**(1): p. 11864.
325. Ouyang, W., et al., *Self-powered UV photodetectors based on ZnO nanomaterials.* Applied Physics Reviews, 2021. **8**(3): p. 031315.

Acknowledgements

I would like to express my deepest gratitude to everyone who supported me throughout my PhD journey at UHH. Thank you all so much!

First and foremost, I would like to thank Prof. Dr. Robert H. Blick and Dr. Robert Zierold, my supervisor and co-supervisor. Both have an incredibly open research philosophy, trusting, respecting, and supporting almost every idea I had—no matter how naive it seemed. They guided me to double-check these ideas from scientific perspectives and encouraged me to bring them to the real world. Without such support, I would not have been able to pursue so many interesting projects during this period. A special thanks to Prof. Dr. Robert H. Blick for his initial trust five years ago, allowing me to join this excellent team and embark on this research journey. And special thanks to Dr. Robert Zierold for his unwavering support, advice, and assistance, often around the clock, whether it was discussing and determining research directions, revising manuscripts, or responding to review comments, both big and small. Beyond research, I also learned invaluable soft skills from him, such as how to collaborate effectively with other scientists and communicate clearly.

I would also like to thank the SFB986 project and the structured doctoral program MGK for their support. For me, SFB was more than just a project providing financial backing, and MGK was more than a platform for enhancing project cooperation and communication. However, together, they gave me a sense of belonging. Through meetings, academic workshops, spring and summer schools, tutorial preparation and teaching, and retreats, I gained a wide range of knowledge in different fields, including but not limited to physics, chemistry, machine learning, artificial intelligence, and biology. There, I have also experienced a diversity of activities beyond science, including cultural exchanges and various soft skills workshops. I owe special thanks to Prof. Dr. Christian Kautz, Dr. Layla Tulimat, Clemens Schröter, and others for their organization efforts—without which, I would not have had such a rich experience.

Next, I want to thank all the outstanding individuals who worked closely with me during my doctoral studies.

I must thank Carina Hedrich, Vincent Strenzke, Isabel González Díaz-Palacio, Kristian Deneke, Dr. Pai Zhao, Dr. Stefanie Haugg, Dr. Jann Harberts, Dr. Chithra H. Sharma, and Malte Siegmund in the research group for their help and insightful discussions. This work is as much a result of their wisdom and efforts as it is mine.

Thank you, Daniel Hensel, Rakshith Venugopal, Lucas Rave, Colin Schormann, Sebastian Koch, and Heather Phillips, for choosing me as your co-supervisor for your master's thesis research, undergraduate thesis research, or overseas research projects. Thank you for their hard

work dedication to our research, and for the trust and support in my elementary supervision skills.

Thank you, Prof. Dr. Kaline P. Furlan, Laura G. Maragno, and Nithin T. James for their support with XRD measurement and analysis, as well as photonic crystal template preparation. Thank you, Prof. Dr. Manfred Eich, Dr. Alexander Y. Petrov, Julia Brandt, Maurice Pfeiffer, and Julius Henf for their assistance with optical measurements, and to Dr. Tobias Krekeler and Prof. Dr. Martin Ritter for their help with TEM characterization. I would also like to thank Dr. Lars Tiemann for his support with electrical measurements and equipment setup, and Dr. Christian Heyn for his help with Raman measurement analysis. Thanks also to Prof. Dr. Mathias Winterhalter for many enjoyable discussions.

My thanks go out as well to the administrators and technicians of the group—Thomas Finger, Katja Finger, Bojan Bosniak, and Mathias Hein—for their general assistance, including routine maintenance of experimental equipment and process discussions.

And, of course, my heartfelt thanks to my family and friends for their unwavering care and support throughout this journey!

List of publications

Publications related to the dissertation:

Book chapter:

[1] **Peng, J**. and R. Zierold, *Atomic layer deposition of materials*, in *Encyclopedia of Condensed Matter Physics (Second Edition)*, T. Chakraborty, Editor. 2024, Academic Press: Oxford. p. 716-728.

Article:

[2] **J. Peng**, D. Hensel, R. Venugopal, L. Rave, C. Schormann, S. Koch, R. H. Blick, R. Zierold, *ALD-assisted VO_2 for memristor application*. Advanced Engineering Materials, 2025. 2402614.

[3] **J. Peng**, J. Brandt, M. Pfeiffer, L. G. Maragno, T. Krekeler, N. T. James, J. Henf, C. Heyn, M. Ritter, M. Eich, A. Yu. Petrov, K. P. Furlan, R. H. Blick, R. Zierold, *Switchable 3D photonic crystals based on the insulator-to-metal transition in VO_2*. ACS Applied Materials & Interfaces, 2024. 16(49): p. 67106-67115.

[4] **J. Peng**, R. Venugopal, R. Blick, R. Zierold, *Atomic layer etching of SiO_2 using sequential SF_6 gas and Ar plasma*. submitted.

[5] **J. Peng**, P. Zhao, R. Venugopal, K. Deneke, S. Haugg, R. Blick, R. Zierold, *Thermal Sight: A Position-Sensitive Detector for a Pinpoint Heat Spot*. Small Science, 2024. 4(8): p. 2400091.

Review:

[6] C. Hao, **J. Peng**, R. Zierold, R. H. Blick, *Atomic layer deposition films for resistive random-access memories*. Advanced Materials Technologies, 2024. 9(16): p. 2301762.

Patent:

[7] Zierold, R., **J. Peng**, and R. Blick, *Ein einfacher, thermoelektrischer, ortsauflösender Dünnfilm-Temperatursensor*. 2024. (Patent priority statement)

Other publications

Article:

[8] C. Hedrich, D. Deduytsche, R. R. Petit, T. Krekeler, **J. Peng**, M. Ritter, J. Dendooven, C. Detavernier, R. H. Blick, R. Zierold, *Tuning the crystallization temperature of titanium dioxide thin films by incorporating silicon dioxide via supercycle atomic layer deposition*. Surfaces and Interfaces, 2025. 57: p. 105696.

[9] X. Yang, Y. Lu, Z. Liu, H. Ji, Z. Chen, **J. Peng**, Y. Su, Y. Zou, C. Wu, S. X. Dou, P. Gao, Z. Guo, J. Sun, *Facet-governed Zn homoepitaxy via lattice potential regulation*. Energy & Environmental Science, 2024. 17(15): p. 5563-5575.

[10] A. Alshaikh, **J. Peng**, R. Zierold, R. H. Blick, C. Heyn, *Vertical Electric-Field-Induced Switching from Strong to Asymmetric Strong–Weak Confinement in GaAs Cone-Shell*

Quantum Dots Using Transparent Al-Doped ZnO Gates. *Nanomaterials*, 2024. 14(21): p. 1712

[11] X. Yang, J. Lv, C. Cheng, Z. Shi, **J. Peng**, Z. Chen, X. Lian, W. Li, Y. Zou, Y. Zhao, M. H. Rümmeli, S. Dou, J. Sun, *Mosaic nanocrystalline graphene skin empowers highly reversible Zn metal anodes*. Advanced Science, 2023. 10(4): p. 2206077.

[12] X. Yang, W. Li, Z. Chen, M. Tian, **J. Peng**, J. Luo, Y. Su, Y. Zou, G. Weng, Y. Shao, S. Dou, J. Sun, *Synchronous dual electrolyte additive sustains Zn metal anode with 5600 h lifespan*. Angewandte Chemie International Edition, 2023. 62(10): p. e202218454.

[13] Y. Su, B. Liu, Q. Zhang, **J. Peng**, C. Wei, S. Li, W. Li, Z. Xue, X. Yang, J. Sun, *Printing-scalable* $Ti_3C_2T_x$ *MXene-decorated Janus separator with expedited* Zn^{2+} *flux toward stabilized Zn anodes*. Advanced Functional Materials, 2022. 32(32): p. 2204306.

[14] Z. Cao, J. Zhu, **J. Peng**, N. Meng, F. Bian, C. Luan, M. Zhang, Y. Li, K. Yu, J. Zeng, *Transformation pathway from CdSe nanoplatelets with absorption doublets at 373/393 nm to nanoplatelets at 434/460 nm*. The Journal of Physical Chemistry Letters, 2022. 13(18): p. 3983-3989.

[15] C. Wu, **J. Peng**, W. Pu, S. Lu, C. Zhang, N. Wu, Z. Sun, H. Zhang, H.-T. Wang, *Elastic properties of high-symmetry* Sb_4O_6 *cage-molecular crystal*. The Journal of Physical Chemistry Letters, 2021. 12(37): p. 9011-9019.

[16] **J. Peng**, W. Pu, S. Lu, X. Yang, C. Wu, N. Wu, Z. Sun, H.-T. Wang, *Inorganic low k cage-molecular crystals*. Nano Letters, 2021. 21(1): p. 203-208.

[17] X. Yang, S. Lu, **J. Peng**, X. Hu, N. Wu, C. Wu, C. Zhang, Y. Huang, Y. Yu, H.-T. Wang, *Ambipolar two-dimensional bismuth nanostructures in junction with bismuth oxychloride*. Nano Research, 2021. 14(4): p. 1103-1109.

Patent:

[18] H. Wang, **J. Peng**, S. Lu, X. Yang, N. Wu, C. Wu, W. Pu, Z. Sun, *Application of antimony trioxide material as a dielectric material between layers and between metals in semiconductor integrated circuits (三氧化二锑材料作为半导体集成电路层间或金属间的介电材料的应用)*. 2021: CN113764380B, PCT/CN2021/097622